Soil Behavior and Geo-Micromechanics

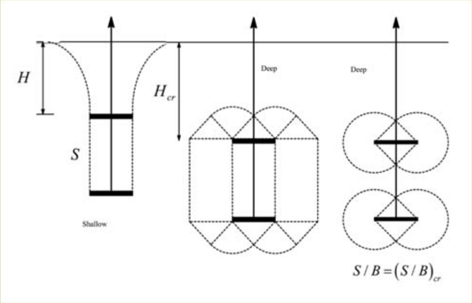

Geotechnical Special Publication No. 200

Edited by
Roger Meier
Andrew Abbo
Linbing Wang

ASCE
G-I
GEO-INSTITUTE

GEOTECHNICAL SPECIAL PUBLICATION NO. 200

SOIL BEHAVIOR AND GEO-MICROMECHANICS

PROCEEDINGS OF SESSIONS OF GEOSHANGHAI 2010

June 3–5, 2010
Shanghai, China

HOSTED BY
Tongji University
Shanghai Society of Civil Engineering, China
Chinese Institution of Soil Mechanics and Geotechnical Engineering, China

IN COOPERATION WITH
Alaska University Transportation Center, USA
ASCE Geo-Institute, USA
Deep Foundation Institute, USA
East China Architectural Design & Research Institute Company, China
Georgia Institute of Technology, USA
Nagoya Institute of Technology, Japan
Transportation Research Board (TRB), USA
The University of Newcastle, Australia
The University of Illinois at Urbana-Champaign, USA
The University of Kansas, USA
The University of Tennessee, USA
Vienna University of Natural Resources and Applied Life Sciences, Austria

EDITED BY
Roger Meier
Andrew Abbo
Linbing Wang

Published by the American Society of Civil Engineers

Library of Congress Cataloging-in Publication Data

GeoShanghai International Conference (2010)
Soil behavior and geo-micromechanics : proceedings of the GeoShanghai 2010 International Conference, June 3-5, 2010, Shanghai, China / edited by Roger Meier, Andrew Abbo, Linbing Wang.
p. cm. – (Geotechnical special publication ; no. 200)
Includes bibliographical references and index.
ISBN 978-0-7844-1101-8
1. Soil mechanics--Congresses. 2. Soil micromorphology--Congresses. I. Meier, Roger (Roger W.) II. Abbo, Andrew. III. Wang, Linbing, 1963- IV. Title.

TA710.A1G368 2010
624.1'5136--dc22 2010012084

American Society of Civil Engineers
1801 Alexander Bell Drive
Reston, Virginia, 20191-4400

www.pubs.asce.org

Any statements expressed in these materials are those of the individual authors and do not necessarily represent the views of ASCE, which takes no responsibility for any statement made herein. No reference made in this publication to any specific method, product, process, or service constitutes or implies an endorsement, recommendation, or warranty thereof by ASCE. The materials are for general information only and do not represent a standard of ASCE, nor are they intended as a reference in purchase specifications, contracts, regulations, statutes, or any other legal document. ASCE makes no representation or warranty of any kind, whether express or implied, concerning the accuracy, completeness, suitability, or utility of any information, apparatus, product, or process discussed in this publication, and assumes no liability therefore. This information should not be used without first securing competent advice with respect to its suitability for any general or specific application. Anyone utilizing this information assumes all liability arising from such use, including but not limited to infringement of any patent or patents.

ASCE and American Society of Civil Engineers—Registered in U.S. Patent and Trademark Office.

Photocopies and reprints.
You can obtain instant permission to photocopy ASCE publications by using ASCE's online permission service (http://pubs.asce.org/permissions/requests/). Requests for 100 copies or more should be submitted to the Reprints Department, Publications Division, ASCE, (address above); email: permissions@asce.org. A reprint order form can be found at http://pubs.asce.org/support/reprints/.

Copyright © 2010 by the American Society of Civil Engineers.
All Rights Reserved.
ISBN 978-0-7844-1101-8
Manufactured in the United States of America.

Preface

This special publication contains 41 technical papers addressing many different areas of soil behavior, constitutive modeling, and geo-micromechanics. The papers range from experimental studies of soil shear strength and compressibility to theoretical advances in Biot consolidation theory and constitutive modeling to numerical studies of shear banding and microstructure. The research described herein advances our understanding of soil as an engineering material and improves our ability to model the behavior of soil in slopes, foundations, and earth structures.

Each paper published in this ASCE Geotechnical Special Publication (GSP) was evaluated by two or more reviewers and the editors. The authors of the accepted papers have addressed all of the reviewers' comments to the satisfaction of the editors. All published papers are eligible for discussion in the *Journal of Geotechnical and Geoenvironmental Engineering* and are also eligible for ASCE awards.

The papers in this publication were presented during the GeoShanghai 2010 International Conference held in Shanghai, China, June 3-5, 2010. This conference was hosted by Tongji University, the Shanghai Society of Civil Engineering, and the Chinese Institution of Soil Mechanics and Geotechnical Engineering in cooperation with the ASCE Geo-Institute, the Transportation Research Board of the National Academies, the East China Architectural Design & Research Institute Company, the Deep Foundation Institute (USA), the University of Kansas, the University of Illinois at Urbana-Champaign, the Vienna University of Natural Resources and Applied Life Sciences (Austria), the Nagoya Institute of Technology (Japan), the Georgia Institute of Technology, the University of Newcastle (Australia), the Alaska University Transportation Center, and the University of Tennessee.

I would like to thank Professor Yongsheng Li, Conference Chair of GeoShanghai 2010, as well as his co-chairs Maosong Huang and Imad Al Qadi. I would also like to thank Baoshan Huang and Xian Liu, Secretaries General of the conference, and the rest of the Organizing Committee. Their leadership and hard work have made this conference possible.

Most importantly, I want to thank my co-editors, Andrew Abbo and Linbing Wang, for their tireless efforts bringing this publication to fruition. I could never have produced this volume without their extraordinary assistance.

Roger Meier
The University of Memphis, Tennessee, USA
January 6, 2010

Acknowledgements

The editors would like to thank the following individuals who reviewed one or more papers for this geotechnical special publication:

Khalid Alshibli
Kostas Anagnostopoulos
David Arellano
Ronaldo Borja
Sebastian Bryson
Jinchun Chai
Bo Chen
Rong-Her Chen
Xi Chen
Sun Dawei
Cristian Druta
Pendo Duku
Zhou Feng
Andy Fourie
Nurly Gofar
Peijun Guo
Suresh Gutta
A. Haddad
Jie Han
Pierre-Yves Hicher
Zhenshun Hong
Mohammad Hoseini
Yuxia Hu
Haiying Huang
Maosong Huang
Bujang Huat
Mehrab Jesmani
Edward Kavazanjian
Mamoru Kikumoto
Prabir Kolay
Liang Kong
Jyant Kumar
Osamu Kusakabe
Tommy Lee
Chunling Li
Jianzhong Li
Jianhua Liu
Han Eng Low
Ning Lu
Yang Lu
Hisham Mohamad
Soheil Nazarian
Majid Nazem
Tongyan Pan
Rohit Pant
Lysandros Pantelidis
Fangle Peng
K. K. Phoon
Luciano Picarelli
Tong Qui
Mehrdad Razavi
Richard Regueiro
Mohamed Rouainia
Cholachat Rujikiatkamjorn
Shihui Shen
Jack Shen
Yanping Sheng
Daichao Sheng
Han Shi
Jim Shiau
Tim Siegel
Kenichi Soga
Wojciech Solowski
Zhenhe Song
Ashley Stanford
Kiichi Suzuki
Yiqiu Tan
Chen Wan
Dariusz Wanatowski
Baojun Wang
Jeff Wang
Shanyong Wang
Dong Wang
Lei Wei
Haifang Wen
Zhang Wen
Kaiming Xia
Wenjing Xue
Xiao-Li Yang
Yangping Yao
Atsushi Yashima
Jian-hua Yin
Zhen-Yu Yin
Zhanping You
Sompote Youwai
Yuxia Kong
Xiong Zhang
Feng Zhang
Guoping Zhang
Mingming Zhang
Yu Zhou
Annan Zhou

Contents

Soil Behavior

Constitutive Modeling

Geo-Micromechanics

Indexes

This page intentionally left blank

One-Dimensional Consolidation of Saturated Clays Under Time-Dependent Loadings Considering Non-Darcy Flow

Zhongyu Liu[1], Liyun Sun[2], Jinchao Yue[3]

[1]Professor, School of Civil Engineering, Zhengzhou University, Zhengzhou, Henan 450001, China; zhyliu@zzu.edu.cn
[2]Ph.D Student, School of Water Conservancy and Environment Engineering, Zhengzhou University, Zhengzhou, Henan 450001, China; liyunjia@zzu.edu.cn
[3]Professor, School of Water Conservancy and Environment Engineering, Zhengzhou University, Zhengzhou, Henan 450001, China; yuejc@zzu.edu.cn

ABSTRACT: Hansbo's formula for non-Darcy flow was introduced to modify Terzaghi's 1-D consolidation equation, and the modified equation was generalized to account for the consolidation case under time-dependent loading. Numerical analysis was performed by using the finite volume method. The effects of the parameters of non-Darcy flow and the rate of loading on the consolidation process were investigated. The numerical results indicated that non-Darcy flow delays the dissipation of pore water pressure in saturated clay layers; thereby the rate of settlement of these soil layers is less than the solution based on Darcy flow. In addition, the influence of loading rate on the consolidation behaviors is remarkable in the construction period and in the initial stage after its completion of construction.

INTRODUCTION

Although the 1-D consolidation theory developed by Terzaghi in 1923 has had extensive use in practice, there sometimes exists notable difference between the solution based on Terzaghi's theory and the field settlement observations. This can be to some extent ascribed to the Terzaghi's assumptions that the external vertical load is constant in time and the flow of pore water follows Darcy's law.

In practice, since the external load gradually increases in the construction period and can be regarded as a constant with time only after its completion for a given building, the differential settlement of the foundation increases rapidly in the construction period and in the initial stage after its completion, which will possibly result in some cracks in the building. Therefore, the variation of the external load in the construction period should be important to estimate the settlement of foundation. Thus, Terzaghi's theory had been continuously modified to account for time-dependent loading by Biot (1941), Poskitt (1969), Mesri and Rokhsar (1974), Olson (1977), Lee et al (1992), Li et al (1999), Xie et al (2002) and Chen et al (2005). Almost all of these modified models were just based on the assumption that Darcy' law is valid. However, non-Darcy flow occurs in many fine-grained soils and can be divided into two types: pre-linear flow and post-linear flow. Experimental evidence (Hansbo, 1960; Deng et al, 2007; etc) indicates that the flow may obey an exponential relationship at low gradients for saturated clays, and it can be described by Hanbo's formula as

$$\left.\begin{aligned} q &= ci^{m}, & (i \le i_1) \\ q &= K(i - i_0), & (i > i_1) \end{aligned}\right\} \tag{1}$$

where q is the velocity of flow; i is the hydraulic gradient; i_1 is the threshold hydraulic gradient; c and K are the permeability parameters applied in the exponential and the linear parts respectively; i_0 is the computed threshold hydraulic gradient; m is the parameter described by experiment, and the relationships among these parameters are $i_0 = i_1(m-1)/m,\ c = K/(m i_1^{m-1})$. It can be seen that Darcy flow is a special case of non-Darcy flow with $m = 1$ and $i_0 = 0$.

By applying Eq. 1, Hansbo (1997) and Liu et al (2009) found the computed consolidation results matched better with the field observations, and Tee and Nie (2002) developed a coupled consolidation theory. In this paper, the non-Darcy flow described by Eq. 1 is incorporated in Terzaghi's 1-D consolidation equation and the modified equation is generalized to account for time-dependent loading. Then the influences of the parameters of non-Darcy flow and the rate of loading on the consolidation process are investigated by introducing the finite volume method to solve the presented equation.

GOVERNING EQUATIONS

The problem studied herein is shown in Fig. 1. A clay layer with thickness H, and with a pervious upper boundary and an impervious lower boundary, is subjected to an external vertical uniform constraction load $p(t)$ shown in Fig. 1(b), in which p_0 and p_u are the initial and the ultimate load, respectively, and t_c is the construction time.

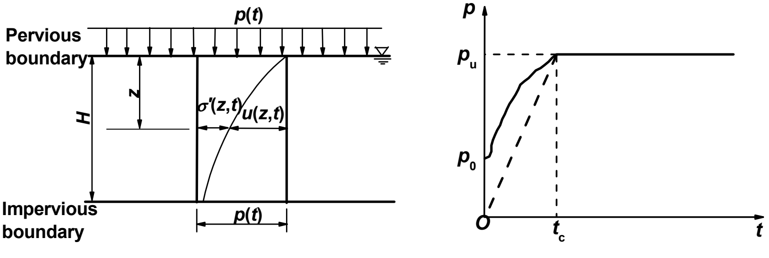

(a) (b)

Fig. 1. Process of consolidation in a clay layer. (a) Clay layer; (b) Loading curve.

Consider the assumptions that the soil properties such as the permeability and compressibility are constants. Then the differential equation governing the 1-D consolidation process of clay layer can be expressed as follows

$$\frac{C_{\mathrm{v}}}{\gamma_{\mathrm{w}}^{M-1} i_1^{M-1}} \left(\frac{\partial u}{\partial z} \right)^{M-1} \frac{\partial^2 u}{\partial z^2} = \frac{\partial u}{\partial t} - \frac{\partial p}{\partial t} \tag{2}$$

where $u(z,t)$ is the excess pore water pressure (EPWP); z is the depth; t is the time; γ_{w} is the unit weight of water; C_{v} is the coefficient of consolidation of soil, and $C_{\mathrm{v}} = K(1+e)/(a\gamma_{\mathrm{w}})$; a is the coefficient of compressibility; e is the void ratio of soil; $M = m$ if $i \le i_1$ and $M = 1$ if $i > i_1$.

The initial and boundary conditions are

$$u(z,0) = u_0 = p_0, \quad 0 \le z \le H \tag{3}$$

$$u(0,t) = 0, \quad \frac{\partial u}{\partial z}(H,t) = 0, \quad t > 0 \tag{4}$$

For the convenience, the dimensionless parameters are introduced as follows

$$U = \frac{u}{p_{\mathrm{u}}}, \quad Z = \frac{z}{H}, \quad T = \frac{C_{\mathrm{v}} t}{H^2}, \quad I = \frac{i\gamma_{\mathrm{w}} H}{p_{\mathrm{u}}}, \quad I_1 = \frac{i_1 \gamma_{\mathrm{w}} H}{p_{\mathrm{u}}}, \quad P(T) = \frac{p(t)}{p_{\mathrm{u}}} \tag{5}$$

Whereupon Eqs. 2-4 can be rewritten as

$$\frac{1}{I_1^{M-1}} \left(\frac{\partial U}{\partial Z} \right)^{M-1} \frac{\partial^2 U}{\partial Z^2} = \frac{\partial U}{\partial T} - \frac{\partial P}{\partial T} \tag{6}$$

$$U(Z,0) = U_0 = p_0 / p_{\mathrm{u}}, \quad 0 \le Z \le 1 \tag{7}$$

$$U(0,T) = 0, \quad \frac{\partial U}{\partial Z}(1,T) = 0, \quad T > 0 \tag{8}$$

NUMERICAL SOLUTIONS USING FINITE VOLUME METHOD

Discretization of equations

Divide the clay layer into N cells from the top down by the proportional spacing ΔZ, fix up a node at the midpoint of every cell, and let the time step equal to ΔT. Then the integral calculation for Eq. 6 is done in the jth cell during the kth time interval (from the time T_k to the time T_{k+1})

$$\int_{T_k}^{T_{k+1}}\left(\frac{1}{MI_1^{M-1}}\left(\frac{\partial U}{\partial Z}\right)^M\bigg|_{\mathrm{B}}-\frac{1}{MI_1^{M-1}}\left(\frac{\partial U}{\partial Z}\right)^M\bigg|_{\mathrm{T}}\right)\mathrm{d}T=\int_{\Delta Z}\left[\int_{T_k}^{T_{k+1}}\left(\frac{\partial U}{\partial T}-\frac{\partial P}{\partial T}\right)\mathrm{d}T\right]\mathrm{d}Z \tag{9}$$

where the subscripts B and T denote the bottom and top boundaries, respectively.

Let the backward difference substitute for the partial derivative of U and P with respect to T on the right side of Eq. 9, and let the central difference substitute for the partial derivative of U with respect to Z on the left side of Eq. 9. Thus

$$U_{j,k+1}=U_{j,k}+\frac{1}{MI_1^{M-1}}\frac{\Delta T}{\Delta Z^{M+1}}\left[\left(U_{j+1,k+1}-U_{j,k+1}\right)^M-\left(U_{j,k+1}-U_{j-1,k+1}\right)^M\right]+(P_{k+1}-P_k) \tag{10}$$

Initial and boundary conditions

The initial conditions described by Eq. 7 can be expressed as

$$U_{j,0}=U_0 \tag{11}$$

Since the gradient of EPWP on the top boundary of the first cell can be approximated as $\left.\frac{\partial U}{\partial Z}\right|_S=\frac{U_{1,k+1}}{\Delta Z/2}$, Eq. 9 for the first cell can be rewritten as

$$U_{1,k+1}=U_{1,k}+\frac{1}{MI_1^{M-1}}\frac{\Delta T}{\Delta Z^{M+1}}\left[\left(U_{2,k+1}-U_{1,k+1}\right)^M-2^M U_{1,k+1}^M\right]+(P_{k+1}-P_k) \tag{12}$$

In a similar way, Eq. 9 for the bottommost cell can be rewritten as

$$U_{N,k+1}=U_{N,k}-\frac{1}{MI_1^{M-1}}\frac{\Delta T}{\Delta Z^{M+1}}\left(U_{N,k+1}-U_{N-1,k+1}\right)^M+(P_{k+1}-P_k) \tag{13}$$

After $U(Z, T)$ is obtained, its average value U_a of the whole soil layer can be found as

$$U_\mathrm{a}(T_k)=\int_0^1 U(Z,T_k)\mathrm{d}Z=\sum_{i=1}^{N}U_{j,k}\Delta Z \tag{14}$$

NUMERICAL RESULTS

A constant loading rate as shown in Fig.1 (b) is assumed in the following analysis carried out with $N = 50$ and $\Delta T = 10^{-6}$.

Influence of non-Darcy flow properties

The influence of m or I_1 on the average excess pore water pressure (AEPWP) U_a are plotted in Fig. 2, where the corresponding curve based on Darcy flow is also depicted with a solid line for comparison. It is evident that the value of U_a based on non-Darcy flow is greater than that based on Darcy flow, and furthermore the greater the value of m or I_1, the greater the difference in AEPWP between values based on Darcy and non-Darcy flows. Therefore, the dissipation rate of EPWP based on non-Darcy flow is slower than that based on Darcy flow.

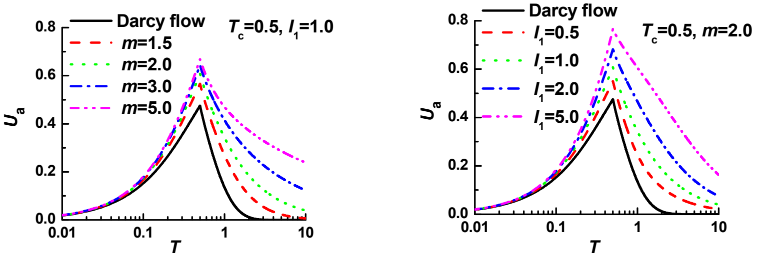

(a) (b)

Fig. 2. Influence of non-Darcy flow properties on AEPWP (a) with T_c=0.5 and I_1=1.0; (b) with T_c=0.5 and m=2.0

The curves of the average degree of consolidation (ADOC) U_t defined in terms of settlement versus the time T are plotted in Fig. 3. The figure shows that the rate of consolidation will slow down if the flow obeys non-Darcy's law compared with Darcy's law, and the difference will increase with the increasing m and I_1; that is, the time corresponding to a given ADOC U_t will be delayed. For example, the time based on non-Darcy flow with m=2.0 and I_1=5.0, as corresponding to U_t=80% and T_c=0.5, is 9.13 times that based on Darcy flow. Therefore, according to the definition of I_1, it can be obtained that the thicker the soil layer or the smaller the ultimate load p_u, the smaller the rate of consolidation; that is, the greater the deviation from the calculated value based on Darcy flow. Thus, the parameter I_1 is also important to characterize the consolidation of the soil layer besides the coefficient of consolidation C_v.

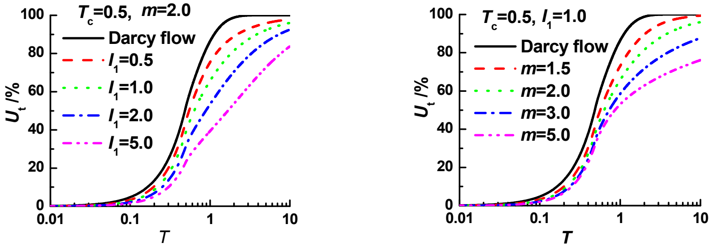

(a) (b)

Fig. 3. Influence of non-Darcy flow properties on ADOC. (a) with T_c=0.5 and I_1=1.0; (b) with T_c=0.5 and m=2.0

Influence of loading rate

The rate of loading can be denoted by the construction time T_c. Fig. 4 displays the influence of the loading rate on the AEPWP or ADOC, in which m=2.0 and I_1=1.0. It can be seen that (1) the value of the AEPWP increases with time and with the increase of loading rate as well (i.e., the decrease of T_c) in the construction period, while it decreases with time after its completion; and (2) the quicker the loading (i.e., the smaller T_c), the faster the consolidation in the construction period and in the initial stage after its completion. Therefore the value of ADOC will be overestimated if the rate of loading is not taken into account in these periods. However, since the influence of the loading rate on the consolidation will decrease after the completion of construction, the rate of loading can be ignored in estimating the final settlement.

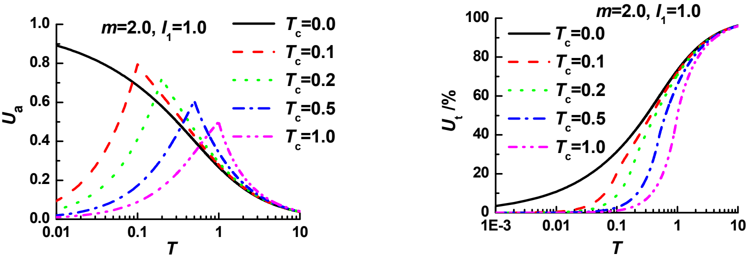

(a) (b)

Fig. 4. Influence of loading rate (*m*=2.0 and *I*₁=1.0). (a) on AEPWP; (b) on ADOC

CONCLUSIONS

By substituting Hansbo's equation for non-Darcy flow, Terzaghi's 1-D consolidation equation is modified and generalized to account for time-dependent loadings, and the finite volume method is introduced to solve the presented equation. Based on this research, the following conclusions can be drawn:

(1) Non-Darcy flow delays the dissipation of EPWP in the clay layer, and therefore the rate of consolidation is less than that of the solution based on Darcy flow.

(2) The rate of dissipation of EPWP and the rate of consolidation of the clay layer will decrease with the increase of m or I_1. Therefore, the parameter I_1 is important to characterize the consolidation of clay layer besides the coefficient of consolidation C_v.

(3) The influence of loading rate on the EPWP and the ADOC is remarkable in the construction period and in the initial stage after its completion. In addition, the rate of loading can be ignored in estimating the final settlement.

REFERENCES

Biot, A. (1941). "General theory of three-dimensional consolidational consolidation." *Journal of Applied Physics*, Vol. 12: 155-164.

Chen, R.P., Zhou, W.H., Wang, H.Z. and et al (2005). "One-dimensional nonlinear consolidation of multi-layered soil by differential quadrature method." *Computers and Geotechnics*, Vol. 32: 358-369.

Deng, Y.E., Xie, H.P., Huang, R.Q. and et al (2007). "Law of nonlinear flow in saturated clays and radial consolidation." *Applied Mathematics and Mechanics (English Edition)*, Vol. 28(11): 1427-1436.

Hansbo, S. (1960). "Consolidation of clay with special reference to influence of vertical sand drains." *Swedish Geotechnical Institute*, Vol.18: 45-50.

Hansbo S. (1997). "Aspects of vertical drain design: Darcian or non-Darcian flow." *Geotechnique*, Vol.47(5): 983-92.

Lee, P.K.K, Xie, K.H., Cheung, Y.K.(1992). "A study on one dimensional consolidation of layered systems." *International Journal of Numerical and Analytical Methods in Geomechanic*, Vol.16: 815-31.

Liu, Z., Sun, L.. Yue, J. and et al (2009). "One-dimensional consolidation theory of saturated clay based on non-Darcy flow." *Chinese Journal of Rock Mechanics and Engineering*, Vol.28(5): 973-979. (in Chinese)

Mesri, G., Rokhsar, A. (1974). Theory of consolidation for clays. *Journal of Geotechnical Engineering*, ASCE, Vol.100(GTB): 889-904.

Olson, R.E. (1977). "Consolidation under time-dependent loading." *Journal of Geotechnical Engineering Division*, ASCE, Vol. 103(GT1): 55-60.

Poskitt, T.J. (1969). "The consolidation of saturated clay with variable permeability and compressibility".*Geotechnique*, Vol.19(2):234-52.

Tee C.I., and Nie X. (2002). "Coupled consolidation theory with non-Darcian flow." *Computers and Geotechnics*, Vol. 29: 169-209.

Xie, K.H., Xie X.Y. and Wen J. (2002). "A study on one-dimensional nonlinear consolidation of double-layered soil." *Computers and Geotechnics*, Vol. 29: 151-168.

Applications of Adaptive Time Stepping in Analysis of Biot Consolidation

Andrew J. Abbo[1], Daichao C. Sheng[2], and Scott W. Sloan[3]

[1]Principal Researcher, Centre for Geotechnical and Materials Modeling, University of Newcastle, Callaghan, NSW, Australia, 2308; andrew.abbo@newcastle.edu.au
[2]Co-director, Centre for Geotechnical and Materials Modeling, University of Newcastle, Callaghan, NSW, Australia, 2308; daichao.sheng@newcastle.edu.au
[3]Director, Centre for Geotechnical and Materials Modeling, University of Newcastle, Callaghan, NSW, Australia, 2308; scott.sloan@newcastle.edu.au

ABSTRACT: The accuracy of finite element solutions for the consolidation of porous media is influenced by the number and size of the time increments used in the analysis. A solution algorithm for adaptively selecting time increments for the solution of elastic and elastoplastic coupled consolidation problems in finite element analysis has been developed by Sloan and Abbo (1999). By treating the governing consolidation relations as a system of 1st-order differential equations their algorithm utilized subincrementation to automatically adjust the size of time increments used in the analysis. Unlike other time stepping schemes, the procedure adjusts the time increments in order to control the error due to time stepping to lie near a specified tolerance. The algorithm was shown to be robust and to provide an efficient method for the solution of consolidation problems. In this paper the efficiency of the algorithm is further demonstrated through the analysis of the construction of an embankment on a deep layer of soft soil. The time increments required for the efficient and accurate analysis of the consolidation of porous media are shown to differ by orders of magnitude.

INTRODUCTION

Finite element analysis of the consolidation of soils requires a mixed formulation that couples displacements and excess pore pressures within the soil. These formulations generate a set of time-dependent, stiff, non-linear ordinary differential equations expressed in terms of the unknown nodal displacements and pore pressures. The solution of these equations requires the discretisation of the analysis within the time domain into small increments. The choice of time increments is an important factor in the accurate, stable and efficient solution of these equations. The selection of time increments for a coupled consolidation analysis is not a trivial task and requires a degree of expertise and experience. Even then an inefficient trial and error approach would typically be employed to ensure the results of an analysis are accurate. For complex problems involving many changes in boundary conditions or loads the choice of time steps becomes even more difficult.

Adaptive time stepping techniques have been developed that automatically select the size of the time increments used in an analysis. The automatic time stepping schemes developed by Abbo and Sloan (1999a), and subsequent variants by Sheng and Sloan (2003), were developed with the intent of providing an adaptive scheme that controls the global error in an analysis due to the discretisation of the analysis in the time domain. It was demonstrated that these schemes are able to control the global error to near a user specified tolerance (Abbo and Sloan, 1999b). Furthermore the adaptive schemes were shown to be both robust, efficient and implemented such that each time step requires little extra computational overhead as compared with traditional incremental solution schemes.

In this paper the consolidation of a deep soft soil layer due to the construction of an embankment is modeled using the finite element methods. The adaptive time stepping schemes of Sloan and Abbo (1999a) are used to advance the solution in the time domain. Results of the analysis show that these methods are able to adjust the size of time steps to control the global error in the settlement of the embankment to near a user specified tolerance.

GOVERNING EQUATIONS

The governing finite element equations for the consolidation of soils are formulated based upon equilibrium of the soil skeleton and continuity of flow of the pore fluid. The equations can be written in the form (see Abbo and Sloan,1999a)

$$\begin{bmatrix} \mathbf{K}_{ep} & \mathbf{L} \\ \mathbf{L}^{\mathrm{T}} & \mathbf{0} \end{bmatrix} \begin{Bmatrix} \dot{\mathbf{U}} \\ \dot{\mathbf{P}} \end{Bmatrix} + \begin{bmatrix} \mathbf{0} & \mathbf{0} \\ \mathbf{0} & \dot{\mathbf{H}} \end{bmatrix} \begin{Bmatrix} \mathbf{U} \\ \mathbf{P} \end{Bmatrix} = \begin{Bmatrix} \dot{\mathbf{F}}^{\mathrm{ext}} \\ \dot{\mathbf{Q}}^{\mathrm{ext}} \end{Bmatrix} \tag{1}$$

in which **U** are the nodal displacements, **P** and the pore pressures and in which the dot denotes the derivative with respect to time. These equations are more conveniently expressed in the form

$$\mathbf{C}\dot{\mathbf{X}} + \mathbf{K}\mathbf{X} = \dot{\mathbf{W}}^{\mathrm{ext}} \tag{2}$$

in which

$$\mathbf{C} = \begin{bmatrix} \mathbf{K}_{ep} & \mathbf{L} \\ \mathbf{L}^{\mathrm{T}} & \mathbf{0} \end{bmatrix}, \quad \mathbf{K} = \begin{bmatrix} \mathbf{0} & \mathbf{0} \\ \mathbf{0} & \dot{\mathbf{H}} \end{bmatrix}, \quad \mathbf{X} = \begin{Bmatrix} \mathbf{U} \\ \mathbf{P} \end{Bmatrix}, \quad \dot{\mathbf{X}} = \begin{Bmatrix} \dot{\mathbf{U}} \\ \dot{\mathbf{P}} \end{Bmatrix}, \quad \dot{\mathbf{W}}^{\mathrm{ext}} = \begin{Bmatrix} \dot{\mathbf{F}}^{\mathrm{ext}} \\ \dot{\mathbf{Q}}^{\mathrm{ext}} \end{Bmatrix}$$

The solution of equation (2) using simple incremental schemes is described by Sheng & Sloan (2003).

ADAPTIVE TIME STEPPING

The automatic time stepping schemes developed by Abbo and Sloan (1999a), and subsequent variants by Sheng and Sloan (2003), were developed with the intent of providing an adaptive scheme that controls the global error in an analysis due to the discretisation of the time domain. The basis of these adaptive schemes is to solve equation (2) using both a first-order and a second-order accurate scheme. The two solutions are combined to estimate the local truncation error in each time increment. This error is then used to adaptively control the size of the next time increment by limiting the truncation error to a user specified tolerance. Sloan and Abbo applied the first-order accurate backward Euler method to the solution of the governing equations

$$\mathbf{C}\dot{\mathbf{X}}_n + \mathbf{K}\left\{\mathbf{X}_{n-1} + h\dot{\mathbf{X}}_n\right\} = \dot{\mathbf{W}}_n^{\text{ext}} \tag{3}$$

and a second-order accurate two stage single step method of Gladwell and Thomas (1988)

$$\mathbf{C}\left(\dot{\mathbf{X}}_{n-1} + h\mathbf{A}\right) + \mathbf{K}\left(\mathbf{X}_{n-1} + h\dot{\mathbf{X}}_{n-1} + h^2\mathbf{A}\right) = \dot{\mathbf{W}}_n^{\text{ext}} \tag{4}$$

These schemes solve an identical systems of equations if

$$\dot{\mathbf{X}}_n = \dot{\mathbf{X}}_{n-1} + h\mathbf{A} \tag{5}$$

This permits both first order and second order accurate solutions to an increment to be obtained using a single factorization of the global equations. In doing so the scheme maintains the same computational overhead in each time step as a traditional incremental scheme. With these two schemes the first order and second order accurate updates for the displacements are given by

$$\mathbf{X}_n = \mathbf{X}_{n-1} + h\dot{\mathbf{X}}_n \qquad \text{and} \qquad \mathbf{X}_n = \mathbf{X}_{n-1} + h\dot{\mathbf{X}}_{n-1} + \tfrac{1}{2}h^2\mathbf{A} \tag{6}$$

where

$$\mathbf{A} = \left(\dot{\mathbf{X}}_n - \dot{\mathbf{X}}_{n-1}\right)/\,h \tag{7}$$

Using the first-order and second-order accurate updates of the displacements the local truncation error is estimated as

$$\mathbf{E}_n^u = \frac{h}{2}\left(\dot{\mathbf{U}}_{n-1} - \dot{\mathbf{U}}_n\right) \qquad\qquad \mathbf{E}_n^P = \frac{h}{2}\left(\dot{\mathbf{P}}_{n-1} - \dot{\mathbf{P}}_n\right) \tag{8}$$

which is divided into two components measuring the error in the pore pressure and in the displacements. To adaptively control the step size a more practical relative measure of the error is calculated as

$$R_n = \max\left\{\frac{\left\|\mathbf{E}_n^u\right\|}{\left\|\mathbf{U}_n\right\|}, \frac{\left\|\mathbf{E}_n^p\right\|}{\left\|\mathbf{P}_n\right\|}\right\} \tag{9}$$

The adaptive scheme then controls the size of each step such that the relative error is maintained below a user specified tolerance DTOL. If the error is less than the specified tolerance the step is accepted and the solution is advanced. However, if the relative error exceeds the tolerance the step is rejected and a smaller increment size will be trialed. Irrespective of whether the step is accepted or rejected the size of the next step size is predicted by scaling the current step size

$$h \leftarrow qh \tag{10}$$

in which scaling factor q given by

$$q = 0.8\sqrt{DTOL / R_n} \qquad 0.1 \le q \le 2 \tag{11}$$

and where the factor of 0.8 is introduced to ensure the step size is selected conservatively. This ensures the number of failed steps is minimized and allows to solution to proceed efficiently. The additional constraints are imposed to limit the change is step size so that they do not grow or contract too rapidly.

APPLICATION

The effectiveness of the adaptive time stepping scheme is demonstrated by considering the consolidation of a deep profile of soft clays due to the construction of an embankment. The finite element mesh, shown in Figure 1, uses 546 plane strain triangular elements that combine quadratic displacement and linear pore pressure fields. The embankment is modeled as a distributed load with a maximum load of 36kPa. The soft soil beneath the embankment, modeled as 4 distinct layers, is represented using the generalized Cam-Clay model for which the properties of each layer are listed in Table 1.

Table 1. Soil properties

Layer	**Thickness (m)**	**OCR**	**ϕ**	**λ**	**κ**	***N***	***k*** **(10^{-4}m/d)**	**γ (kN/m^3)**
1	2	7.0	33.8	0.08	0.01	1.9	10.0	17.6
2	8	2.0	33.8	0.53	0.02	5.0	5.0	14.9
3	2	2.0	32.8	0.10	0.01	2.1	2.0	20.0
4	19	1.0	32.8	0.53	0.02	4.2	4.0	16.1

The analysis is conducted in 3 stages; establishing the initial stresses, construction of the embankment and the consolidation of the soil. In this paper results are only presented for the final stage.

The results demonstrating the performance of the adaptive methods are summarized in Figure 2 and Table 2. Data are presented for analyses in which the adaptive stepping was controlled using tolerances (DTOL) varied from 10^{-2} to 10^{-6}. The relative error in the displacement of the embankment is plotted in Figure 2. This relative error was computed using the results of an adaptive analysis with a very small tolerance of DTOL=10^{-7}. This error plot shows that the adaptive algorithm was able to control the error in the displacement of the footing throughout the consolidation stage of the analysis to just less than the specified displacement tolerance.

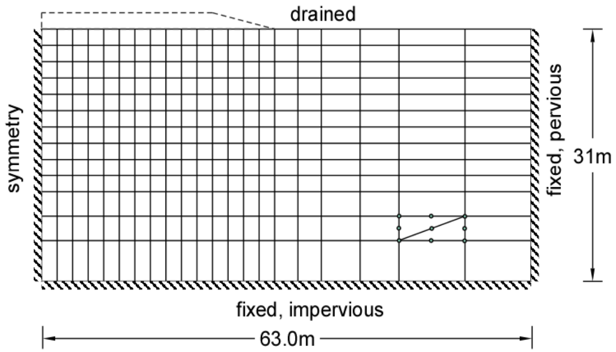

Figure 1. Finite element mesh modeling construction of embankment.

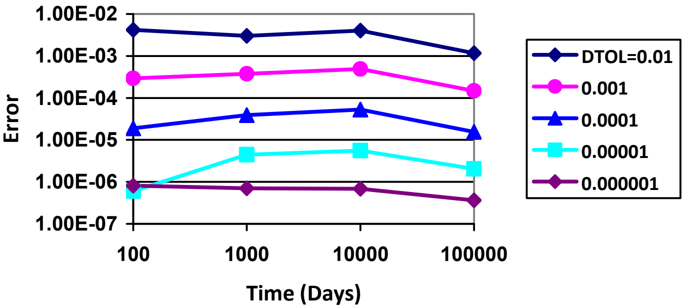

Figure 2. Temporal Discretisation error in displacement of footing versus time.

The number of time steps used by the adaptive scheme are listed in Table 2. These results show that slightly more than a 3 fold increase in the number of time increments is required to reduce the error in the analysis by an order of magnitude.

Table 2. Number of time increments

Tolerance	10^{-2}	10^{-3}	10^{-4}	10^{-5}	10^{-6}	10^{-7}
Number of increments	61	120	345	1045	3267	10307

Of more significance is the variation of the time increments during the analysis. A plot of the time increments used in the analysis with DTOL=10^{-5} is shown in Figure 3.

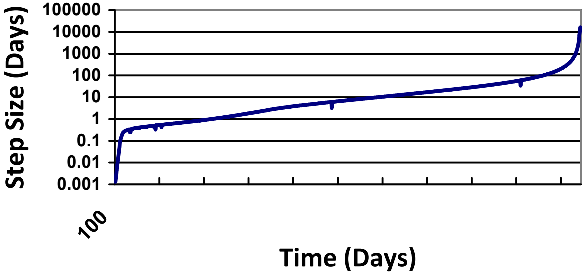

Figure 3. Variation of time increments during the analysis with DTOL=10^{-5}.

From Figure 3 it can be seen that size of increments used in the adaptive analysis varied by 8 orders of magnitude. During the initial stages of the analysis, when pore water gradients are high, very small increments were required to keep the local truncation errors below the required tolerance. This compares to the very large increments that could be used at the end of the analysis when consolidation of the embankment had essentially completed.

CONCLUSIONS

The advantages of adaptive time step integration have been demonstrated through the application of these schemes to modeling the consolidation of a deep layer of soft soil. The adaptive techniques of Sloan and Abbo (1999) are shown to be able to control the step size in order to maintain the temporal discretisation error to less than a user specified tolerance. Most importantly, the schemes enable a finite element analysis to be conducted efficiently by automatically choosing the appropriate number and size of time increments.

REFERENCES

Gladwell, I. and Thomas, R. M. (1988). "Variable-order variable-step algorithms for 2nd-order systems .2. The Codes." *International Journal for Numerical Methods in Engineering*, Vol. 26(1): 55-80.

Sheng, D., and Sloan, S. W. (2003). "Time stepping schemes for coupled displacement and pore pressure analysis." *Computational Mechanics*, Vol. 31(1-2): 122-134.

Sloan, S. W., and Abbo, A. J. (1999a). "Biot consolidation analysis with automatic time stepping and error control Part 1: Theory and implementation." *International Journal for Numerical and Analytical Methods in Geomechanics*, Vol. 23(6): 467-492.

Sloan, S. W., and Abbo, A. J. (1999b). "Biot consolidation analysis with automatic time stepping and error control Part 2: Applications." *International Journal for Numerical and Analytical Methods in Geomechanics*, Vol. 23(6): 493-529.

A Calculation Method of Secondary Compression Index for Natural Sedimentary Clays Using Void Index

Lingling ZENG[1], Songyu LIU[2]

[1]Ph.D Candidate, Institute of Geotechnical Engineering, Southeast University, Nanjing 210096, P. R. China; linglz413@126.com

[2]Professor, Institute of Geotechnical Engineering, Southeast University, Nanjing 210096, P. R. China; liusy@seu.edu.cn

ABSTRACT: A series of oedometer tests were performed on both undisturbed and remolded samples of Lianyungang clays to investigate the secondary compression behavior. The results of natural clays show that the coefficient of secondary compression, C_α, reaches the maximum dramatically in the vicinity of the consolidation yield stress. When the consolidation pressure is less than the yield stress (termed as pre-yield state), the creep can be neglected. But C_α decreases with the increase in consolidation stress in the post-yield state (i.e. the consolidation pressure being greater than the yield stress), similar to remolded samples. In addition, it is found that there is a unique relationship between the difference in coefficient of secondary compression, $(C_\alpha - C^*_\alpha)$, and the difference of void index (ΔI_v) between undisturbed and remolded samples. Furthermore, a simple method is proposed for predicting secondary compression index of natural clays.

INTRODUCTION

It is commonly accepted that clay exhibits creep at constant effective stresses, termed as secondary compression. Bjerrum (1967) proposed that the compression of a given clay can be divided into immediate and delayed compression. Mesri and Godlewski (1977; 1987) proposed that C_α / C_c is a constant. They (1977) also indicated that the compression index C_c changes with stress level, especially changing dramatically in the vicinity of the consolidation yield stress, for many natural sedimentary clays. Based on the concept of constant C_α / C_c, it can be inferred that C_α varies with effective stress. It should be pointed out that the e-log p curves of many natural sedimentary clays often exhibit an inverse “S” shape (Butterfield 1979). That is, the C_c varies with effective stress, consequently resulting in difficulty to determine C_α using C_c based on the constant C_α / C_c concept. The objective of this study is to develop a simple method of calculating the secondary compression index of natural clays with the concept of void index proposed by Burland (1990). With the proposed approach, the coefficient of secondary compression of natural sedimentary clays, C_α, can be easily determined by the secondary compression index of remolded clays, the intrinsic compression line (ICL), and the current void ratio.

SAMPLES AND TEST PROGRAM

The undisturbed samples were obtained by the thin-wall free-piston tube sampling method from a depth of 6.0 m below the ground surface in the city of Lianyungang. The basic physical properties are presented in Table 1. The secondary compression oedometer tests were performed on both undisturbed and remolded samples to investigate the secondary compression behavior, as shown in Table 2. The primary consolidation duration (t_p) is determined by the time when the pore pressure, u_b, measured at the base of the specimen is smaller than 1kPa. The conventional oedometer cell was modified as show in Fig 1 to perform the secondary compression test with one-way drainage at the top and a pore pressure transducer at the base.

Table 1. Sampling depth and basic physical indices

w_0 (%)	γ (g.cm^{-3})	e_0	CF (<2μm%)	w_L (%)	w_p (%)
81.6	15.48	2.22	31.8	80.3	30.9

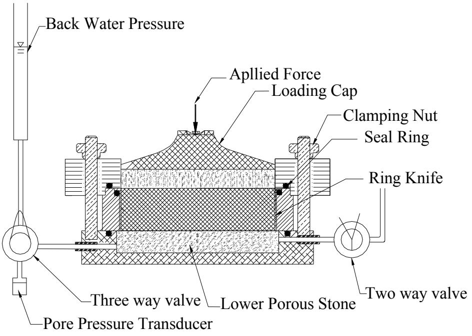

FIG. 1 Oedometer cell adapted for secondary consolidation test

Table 2. Secondary compression testing program

Sample	Load
Undisturbed	25-50-100-150-200-400-800-1200(kPa)
Remolded	12.5-25-50-100-200-400-800(kPa)

COMPRESSION BEHAVIOR OF LIANYUNGANG CLAY BASED ON VOID INDEX

Burland (1990) has proposed the intrinsic compression line (ICL) given in Eq. (1) which introduces the void index in Eq. (2).

$$I_v = 2.45 - 1.285x + 0.015x^3 \tag{1}$$

$$I_v = (e - e_{100}^*) / (e_{100}^* - e_{1000}^*) \tag{2}$$

Here $x = \log \sigma'_v$ and σ'_v is the effective vertical stress in kPa. The quantities e_{100}^* and e_{1000}^* are the void ratios of the remolded clays at the effective vertical stresses of 100 kPa and 1000 kPa, respectively.

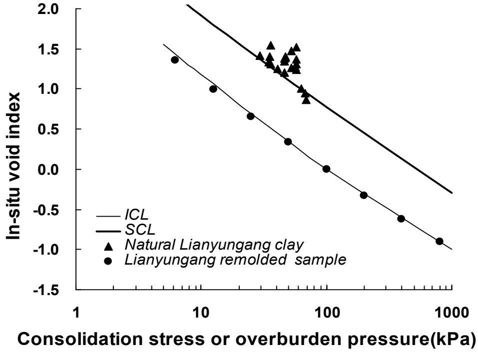

FIG. 2. Relationship between in-situ void index and overburden pressure for natural Lianyungang clay and the I_v -logσ'_v relationship of remolded sample

The compression curves of remolded samples are presented in Fig. 2. It can be seen that the normalized compression line of remolded Lianyungang clays is consistent with the ICL, indicating that the void index and the intrinsic compression line can be applied to remolded Lianyungang clays. In the same figure, it can be also seen that most natural data expressed in terms of natural void index versus effective overburden pressure lie above the SCL proposed by Burland (1990) based on the data of natural sedimentary soils published by Skempton (1970). This result shows the structure effects on natural Lianyungang clay.

Fig. 3 shows the typical I_v – log σ'_v compression curve of undisturbed samples. The values of I_v are calculated with Eq. (2) using the values of related void ratio at the end-of-primary consolidation (EOP). It can be seen in Fig. 3 that the difference of void index between the undisturbed specimen and the ICL at the same effective consolidation pressure (ΔI_v) changes with consolidation pressure. Fig. 4 gives the relationship of ΔI_v against σ'_v, indicating the maximum in the vicinity of the consolidation yield stress, σ'_{vy}. When $\sigma'_v < \sigma'_{vy}$ (termed as pre-yield state), the ΔI_v increases with σ'_v. But the ΔI_v decreases with increasing σ'_v in the post-yield state (i.e. $\sigma'_v > \sigma'_{vy}$). This phenomenon can be explained as follows. Hong et al. (2006) demonstrated that the microstructure of natural structured soils remains almost unchanged in the pre-yield state, but it changes significantly in the vicinity of σ'_{vy}. Furthermore, Hong et al. (2007) proposed that the effects of soil structure disappear completely when the applied stress is in the vicinity of σ'_{vy}. Hence, the soil structure resists the potential compression of undisturbed samples by applying consolidation stress in the pre-yield state. At the same time, the compression occurs for remolded soils without the effects of soil structure. Hence, ΔI_v between undisturbed and remolded samples increases with σ'_v in the pre-yield state. On the other hand, the compressibility of undisturbed sample is larger than that of the remolded sample because the former has a greater void ratio than the latter. Hence, the void index of undisturbed sample will gradually converge toward the ICL, consequently resulting in the decrease of the ΔI_v with increasing σ'_v in the post-yield state.

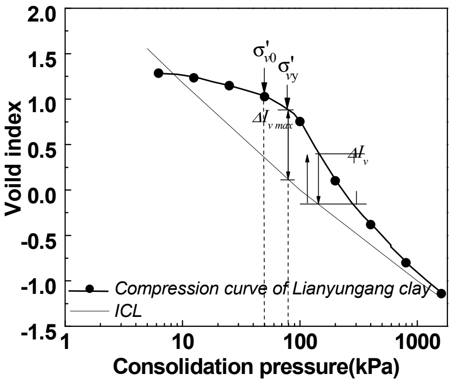

FIG. 3. Compression curve of natural Lianyungang clay in I_v-logσ'_v

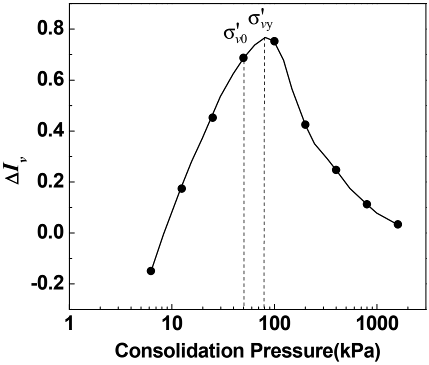

FIG. 4. Relationship of ΔI_v with consolidation pressure

CALCULATION OF SECONDARY COMPRESSION INDEX FOR NATURAL CLAYS USING VOID INDEX

Fig. 5 presents the relationship between C_α (defined as $C_\alpha = \Delta e/\log t$) and σ'_v for different durations of secondary compression. The results show that the secondary compression behavior of the undisturbed sample changes dramatically in the vicinity of σ'_{vy}. The creep can be neglected in the pre-yield state. However, C_α reaches a maximum sharply in the vicinity of σ'_{vy}. Then, C_α decreases with increasing σ'_v. On the other hand, the remolded sample shows a similar secondary compression behavior to the undisturbed sample in the post-yield state. The C_α decreases with the increase in σ'_v. But the curve of the remolded sample lies below that of the undisturbed sample in the post-yield state. It should also be pointed out that the decreasing ratio of C_α in the range of 25-50 kPa is somewhat less than that in the range of 50-100 kPa. This phenomenon is different from the common result for remolded clays. More study is necessary to explain this difference in the future.

The secondary compression behavior can be interpreted by the ΔI_v, as shown in Fig. 3. When the consolidation pressure exceeds the yield stress, the value of ΔI_v represents the unstable structure for the effects of soil structure disappearing completely. Hence, the creep is more significant as the ΔI_v is larger. Furthermore, the higher value of C_α results in the ΔI_v reducing more quickly. Consequently, ΔI_v reduces rapidly in the vicinity of the consolidation yield stress. Fig. 6 gives the relationship between the difference of void index (ΔI_v) and the effective consolidation stress for different secondary compression durations. It can be seen that the ΔI_v decreases with increase in secondary compression duration at the same consolidation stress.

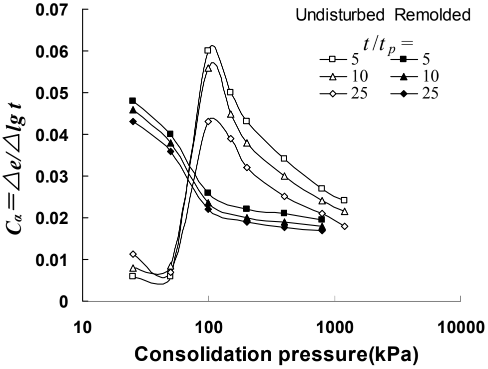

FIG. 5. Relationship between C_α and consolidation pressure for Lianyungang clay undergoing different duration of secondary compression

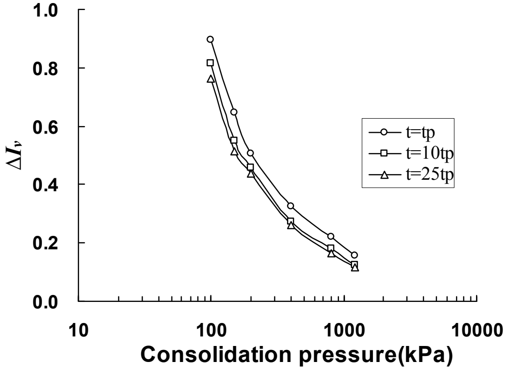

FIG. 6. Relationship of ΔI_v with consolidation pressure undergoing different secondary compression duration

Fig. 7 shows the relationships between C_α and ΔI_v. The secondary compression index increases linearly with the difference of void index (ΔI_v) at the same duration of secondary compression. Furthermore, the relationships of C_α against ΔI_v for different secondary compression durations can be normalized in terms of (C_α - C_α^*) versus ΔI_v, as shown in Fig. 8. The regression analysis gives the following equation:

$$C_a - C_\alpha^* = 0.0394\, \Delta I_v \tag{3}$$

where C_α^* is the secondary compression index value of the remolded sample. That is, we can get the relationship between $(C_a - C_\alpha^*)$ and ΔI_v as:

$$C_a = \eta \Delta I_v + C_\alpha^* \tag{4}$$

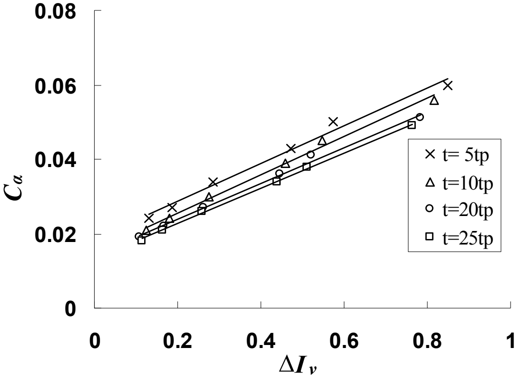

FIG. 7. Relationship of secondary compression index and the difference of void index (ΔI_v) undergoing different secondary compression duration

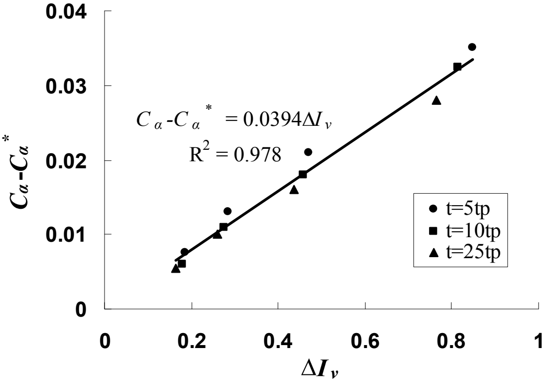

Fig. 8. Relationship of C_α- C_α^* and ΔI_v undergoing different secondary compression duration

The above equation indicates that the C_α of natural clays can be easily obtained using the void index. The η can be determined by the secondary compression oedometer tests. Compared with the traditional method using the compression index, the method proposed in this study can avoid the difficulty in obtaining the C_c of natural clays due to its change with consolidation time and stress level.

CONCLUSIONS

The main results obtained in this study are summarized as follows:

The difference of void index (ΔI_v) between undisturbed and remolded samples increases with applied stress in the pre-yield state, but decreases in the post-yield state. It has a good correlation relationship with the secondary compression coefficient of sedimentary structural clay.

The difference in C_α between natural and remolded clays increases linearly with the gap in void index between undisturbed and remolded samples at the same consolidation pressure in the post-yield state.

A simple method of predicting the secondary compression index for natural clays is proposed based on void index. The quantitative equation of the method can be expressed as: $C_\alpha = \eta\Delta I_v + C_\alpha^*$. The C_α of natural sedimentary structural clay can be simply assessed with the coefficient of secondary compression of remolded sample C_α^*, the constant η and the difference value of void index (ΔI_v) between the undisturbed specimen and the ICL at the same effective consolidation pressure.

REFERENCES

Bjerrum L. (1967). “Engineering geology of normally consolidated marine clays as related to the settlement of buildings.” *Geotechnique* , 17 (2) :83-118.

Burland, J. B. (1990). “On the compressibility and shear strength of natural clays.” *Geotechnique*, 40(3), 329-378.

Butterfield R. (1979). “A natural compression law for soils.” *Geotechnique*, 29(4): 469-480.

Hong, Z., Shen, S., Deng, Y. and Negami, T. (2007). Loss of soil structure for natural sedimentary clays. Geotechnical Engineering, Proceedings of ICE. 160 (3): 153 - 159.

Hong, Z., Tateishi, Y., and Han, J. (2006). “Experimental Study of Macro- and Microbehavior of Natural Diatomite.” *Geotechnical Engineering*, ASCE, 132(5): 603-610

Mesri, G., and Godlewski, P. M. (1977). “Time- and stress- compressibility interrelationship.” *Geotechnical Engineering*, ASCE, 1977, 103(5): 417-430.

Mesri, G., and Castro, A. (1987). “The C_α/C_c concept and K_0 during secondary compression.” *Geotechnical Engineering*, ASCE, 1987, 113(3): 230-247.

Skempton, A. W. (1970). “The consolidation of clays by gravitational compaction.” *Q. J. Geol. Soc.*, 125, 373–411.

Compressibility Behavior of Soft Clay Sediments

Mahdia Hattab[1-2], Tammam Hammad[2], Jean-Marie Fleureau[2]

[1]Laboratoire de Physique et Mécanique des Matériaux, CNRS FRE 3236, Université Paul Verlaine, Ile du Sauly, 57045 Metz Cedex1, France. ; mahdia.hattab@ecp.fr
[2]Laboratoire de Mécanique des Sols Structures et Matériaux, CNRS UMR 8579, Ecole Centrale Paris, Grande voie des vignes, 92295 Châtenay-Malabry, France.

ABSTRACT: The oedometric path of normally consolidated unremolded clay sediments evolves, in the ($\log \sigma'_v$ - I_L) plane, toward a maximum point located above the C_c line (which characterizes the compression of material that has been remolded and reconstituted) highlighting "apparent" overconsolidation. Then, the curve tends to join the C_c line indicating the beginning of destruction (failure) of bonds between particles. This progressive rupture of bonds becomes complete when the path rejoins the remolded behavior in the high stress domain. This gradual transition, from unremolded behavior towards remolded behavior, has been investigated on marine sediments extracted from the Gulf of Guinea. Oedometric tests were performed on both natural (unremolded) clay samples and remolded ones. The study is supported by several microscopic observations with SEM (Scanning Electron Microscope) and mercury intrusion porosimetry.

INTRODUCTION

The term "remolded reconstituted" indicates soil whose cementation, developed between particles throughout the process of sedimentation and consolidation, has been destroyed by a specific procedure of mixing performed in the laboratory. The behavior of the remolded reconstituted material (reconstituted at a water content of twice the liquid limit), will depend only on the applied stress tensor. Its study under normally consolidated conditions is fundamental, because it allows one to deduce the "intrinsic" mechanical properties (Burland, 1990) and thus to constitute a fixed reference framework in order to explain the behavior of unremolded clay (Biarez and Hicher, 1994). The present paper reports on an experimental analysis of the compressibility of deepwater marine sediments from the Gulf of Guinea characterized by a very high liquid limit. Our approach is based on two relations linking the overburden effective stress with the liquidity index: Biarez's relation and Burland's relation (where ICL is expressed as I_L parameter). Tests are performed on both natural (unremolded) clay samples and remolded reconstituted ones. The evolution of the behavior will be first examined at the macroscopic level using oedometric tests, then microstructure observations will be carried out at the local microscopic level. Two complementary techniques were used: scanning electron microscopy (SEM) for the fabric evolution, and mercury intrusion porosimetry (MIP) for evolution of porosity.

GoG SEDIMENT PROPERTIES

Tests were performed on clayey sediment samples taken in the Gulf of Guinea from an oil-bearing area. The available samples come from a core, 17 m long, taken at 700 m depth. Different authors (Favre & Hattab, 2006 ; De Gennaro et al., 2005) studied in detail the physical properties of the core samples. The material is a very plastic clay, dark grey, saturated and with many shell fragments visible by eye. The analyses performed by Thomas et al. (2005) highlight clay fraction amounts of 40 to 60% with approximately 50% of kaolinite and up to 15 to 25% of smectite. The organic content is 6% and the carbonate content is between 5 and 15%. The "grains" natural properties may be represented through the profiles of the liquid limit (w_L) and of the plastic limit (w_P). The liquid limit appears very high, especially at the surface where it reaches around 160% (Favre & Hattab, 2006). The results in Fig. 1, where Ip is the plasticity index, show that the sediments correspond to a usual smectite according to the classification of Biarez and Favre (1975). This is confirmed by spectrometry analyses conducted with SEM on different sub-sections of the core. The example shown in Fig. 1, which concerns a spectrometry analysis performed on a specimen taken at approximately 13 m depth, also indicates the presence of organic elements at this depth.

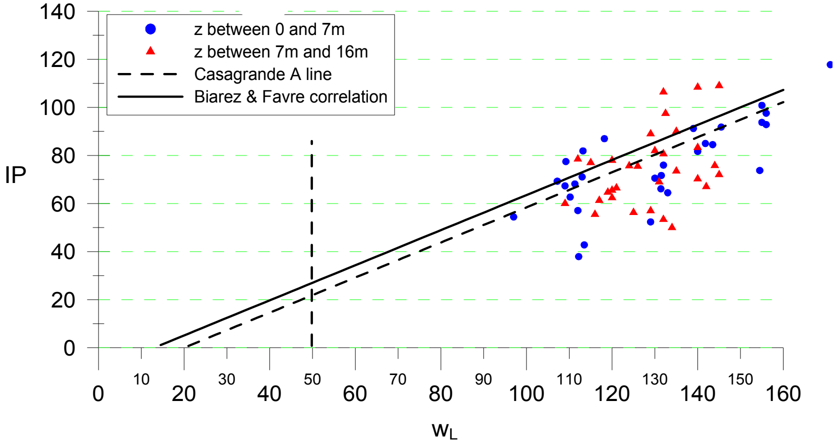

FIG. 1. Experimental results compared with Biarez (w_L- I_p) abacus.

The "grain" configuration and its evolution (structure) may be indicated by the natural water content w_{nat} (or void ratio e) variations, as well as by the axial effective stress σ'_v. The unit weight of the solid grains and sea water are γ_s = 26.5 kN/m^3 and γ_w = 10.2 kN/m^3, respectively. The measurements indicate very high values of w_{nat}, very close to the liquid limit and sometimes higher, especially at depths between 1 m and 5 m with values up to 180%.

COMPRESSIBILTY ANALYSIS ON THE OEDOMETRIC PATH

Biarez & Favre (1975) propose a unique abacus for all clayey soils for which the liquid limit is between 20 and 160%. The "arrangement of grains" seems to be directly linked to the consolidation stress tensor through the mineralogical properties. This relationship, defined by Equation 1, describes a normally consolidated remolded soil behavior which is represented in the ($\log \sigma'_v$- I_L) plane by a straight line called NCRS line (Normally Consolidated Remolded Simplified line), where I_L is the liquidity index and σ'_v(expressed in kPa) is the vertical effective stress.

$$I_L = 0.46\left(3 - \log \sigma'_v\right) \qquad (1)$$

More recently, Burland (1990) introduced the intrinsic compression line (ICL) to represent the one-dimensional compressibility behavior of remolded clays, a curve towards which the unremolded oedometric paths tend to converge in the high stress domain, after the rupture of the cementation between the "grains". This intrinsic state of the material is represented by the ICL curve and is expressed by Equation 2, where C_c^* is the intrinsic compression index (Eq. 4), defined according to two specific void ratios e_{100}^* and e_{1000}^* corresponding to the consolidation stresses of 100 and 1000 kPa respectively. I_v is the void index.

$$I_V = 2.45 - 1.285 \log \sigma'_v + 0.015 (\log \sigma'_v)^3 \qquad (2)$$

$$I_v = \frac{e - e_{100}^*}{C_c^*} \qquad (3)$$

$$C_c^* = e_{100}^* - e_{1000}^* \qquad (4)$$

Oedometric tests have been carried out systematically on each section of the core according to French Standard XP P 94-090-1. The sample height is h_0 = 24 mm and its diameter is d_0 = 70 mm. Loading is performed by steps of the vertical effective stress up to 80 kPa for the seven first layers noted [–7 m] depth, and up to 250 kPa for the layers below 7 m depth noted [+7 m], except for two sub-sections [5 9-10] (around 9 m depth) and [2 16-17] (around 16 m depth) for which the loading is conducted up to σ'_v= 1000 kPa, that is 17 times more than the in-situ effective stresses. All the oedometric paths are represented in the ($\log \sigma'_v$ - I_L) plane (Fig. 2). The ICL curve, which is a unique curve in the ($\log \sigma'_v$ - I_v) plane becomes, in the ($\log \sigma'_v$ - I_L) plane, dependent on the material (Favre & Hattab, 2008; Hattab & Favre, 2009); it is represented on Fig. 2 by ICL_{m-s} for remolded and reconstituted GoG sediments.

Oedometric curves were compared on one hand to the NCRS line, and on the other hand to the ICL_{m-s} line (this latter was calculated by taking into account the experimental values of the e_L and e_P parameters, according to depth). All the curves first evolve toward a peak which defines the "apparent overconsolidation stress" located above the NCRS line (sensitive clays). Afterwards, the paths gradually converge towards the ICL_{m-s} line. This is especially obvious in the case of the [5 9-10] and [2 16-17] samples, whose loading has been carried out up to σ'_v = 1000 kPa. The macroscopic level observations show that the oedometric loading of GoG sediment causes a gradual evolution of the material from an intact (unremolded) state, which is cemented and structured, to a remolded state which seems to be represented well by the $ICL_{m\text{-}s}$ curve (destructuration phenomenon by Leroueil et al., 1979). The question now is to examine, at the local level, the micro-fabric of the material before and after loading. Thus the porosity evolution was analyzed with the mercury intrusion porosimetry method, and the fabric evolution with scanning electron microscopy (SEM) observations.

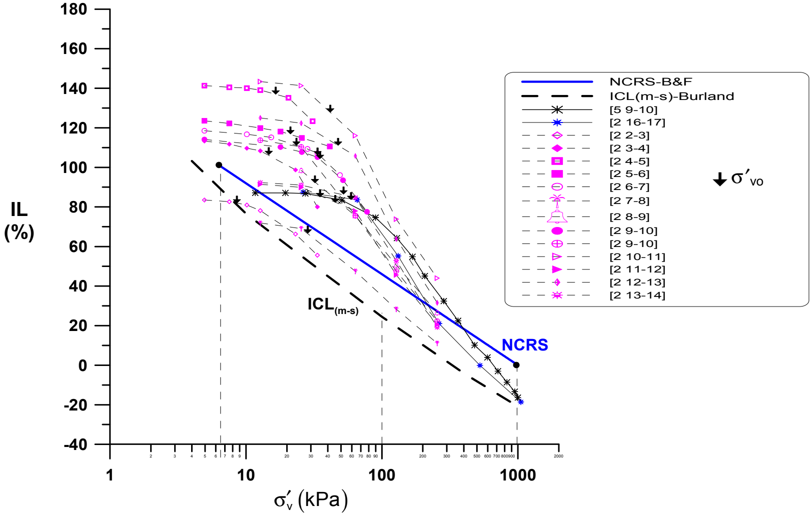

FIG. 2. Oedometric paths in the $(\acute{\sigma}_v, I_L)$ plane.

MICROSCOPIC ANALYSIS

MIP analysis allows to reach the local porosity of the sample as well as the pore size distribution. Fig. 3 shows the mercury intrusion incremental volume plotted versus the logarithm of pore diameter D. A high porosity is obtained in the initial state ([6 9-10] sample). The unremolded specimen features two families of pores: the first one may be described as inter-aggregate macropores around D = 1 µm; the second one corresponds to an intra-aggregate porosity around D = 0.06 µm. After oedometric loading (up to σ'_v = 1000 kPa on the intact sediment [5 9-10]), the macro-pores observed before the loading step between 3 µm and 1 µm have almost completely disappeared, leaving smaller pores located around D = 0.2 µm. For the remolded sample [2 9-10], which was loaded under the same conditions (oedometric loading to σ'_v= 1000 kPa), an peak with a similar pore diameter around D=0.2µm was obtained. This similarity between the two [5 9-10] and [2 9-10] sample responses confirms the previous macroscopic observations, especially by the fact that, after oedometric loading, the unremolded state joins the remolded one with the same peak value of pore diameter.

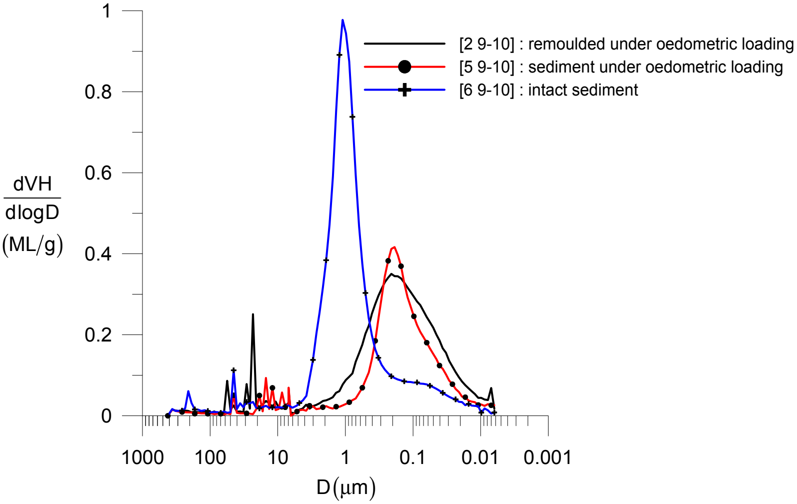

FIG. 3. Evolution of the porosity (MIP analysis).

Considering now the microstructural analyses, performed on the SEM pictures at the end of the loading, they seem to show a difference in the pore distributions between the natural sediment (after the breakage of the cementation) and the remolded sediment. In the first case, we obtain compressed clay zones crossed by a network of microcracks (Fig. 4a), whereas the second exhibits oriented clay particles observed by their edge view on the vertical plane (Fig. 4b).

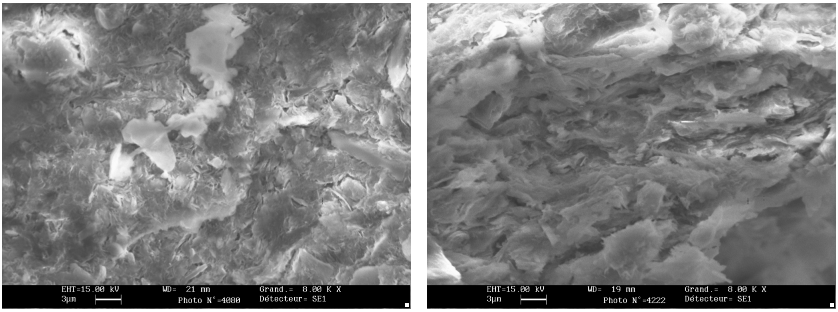

(a) GoG sediment [5 9-10] (b) Remolded GoG sediment [2 9-10]

FIG. 4. SEM pictures after oedometric loading – vertical plane.

CONCLUSIONS

Reference behaviors for remolded clays, proposed, on one hand, by Biarez (a simple statistical model based on the Atterberg limits) and, on the other hand, by Burland (a more complex but more precise experimental model), highlight sedimentation phenomenon (for samples) with (initial) high void ratio. This latter corresponds to self-compaction of “grains” prevented by a cohesion which is typically of physico-chemical nature. Rupture of this cohesion reveals a pronounced kink (sensitive clays) highlighted on oedometric paths. Beyond the kink, the clay, which, in the initial state, is structured and cemented, gradually tends towards the remolded state of the same material. This state seems to be well represented by the intrinsic compression line introduced by Burland and termed ICL_{m-s} in this paper. The evolution from an unremolded state towards a remolded one, analysed at macroscopic scale, was supported by mercury intrusion porosimetry analyses that showed that, at the end of the loading, identical pore diameters were obtained. Nevertheless, SEM investigations indicate that oedometric loading to $\sigma'_v = 1000$ kPa does not lead to the same microfabric (initially intact before loading as well as remolded) for both clay specimens.

ACKNOWLEDGMENTS

This work was conducted in the framework of the CLAROM "Deepwater sediments" project – on the site B Stacor core from the Gulf of Guinea. Project partners are: IFP, IFREMER, Fugro-France, Saipem-SA, Stolt Offshore, Technip and Total.

REFERENCES

Biarez, J. and Favre, J.-L. (1975). "Parameters filing and statistical analysis of data in soils mechanics." *Proc. 2 Int. Conf. Appl. Stat. Prob* Aix la Chapelle., 2 : 249.

Biarez, J. and Hicher, P-Y. (1994). "Elementary mechanics of soils behavior. Saturated remolded soils. " *A.A.Balkema / Rotterdam / Brookfield.*

Burland, J.B. (1990). "On the compressibility and shear strength of natural clays." *Géotechnique* 40 (3) : 329-378.

De Gennaro, V., Puech, A. and Delage, P. (2005). "On the compressibility of deepwater sediments of the Gulf of Guinea." Proc. Int. Symp. *On frontiers in Offshore Geotechnics,* Perth, Autralia.

Favre, J.L. and Hattab, M. (2006). "Properties of deepwater marine clays." *Revue Française de Geotechnique.* 116 : 3-13.

Favre, J-L. and Hattab, M. (2008). "Analysis of "Biarez-Favre" and "Burland" models of the compressibility of remolded clays." *C. R. Géoscience*. 340 (1) : 20-27.

Hattab, M. and Favre, J-L. (2009). "Experimental Compressibility analysis of the deepwater marine sediments from the gulf of guinea". Marine Petroleum Geology in press.

Leroueil, S., Tavenas, F., Brucy, F., La Rochelle, P. and Roy, M. (1979). "Behavior of destructuted natural clays." *Proc. Am. Soc. Civ. Engrs* 105, GT6. : 759-778.

Thomas, F., Rebours, B., Nauroy, J-F. and Meunier, J. (2005). "Minerological characteristics of Gulf of Guinea deepwater sediments." *Frontiers in offshore Geotechnics ISFOG 2005, proc. Int. Symp.*, Perth. Rotterdam, Balkema. : 19-21.

Strain Softening and Instability of Loose Sand in Plane-Strain Compression Tests

Dariusz Wanatowski[1], M. ASCE and Jian Chu[2]

[1]Lecturer, Nottingham Centre for Geomechanics, Faculty of Engineering, University of Nottingham, University Park, Nottingham NG7 2RD, United Kingdom; dariusz.wanatowski@nottingham.ac.uk
[2]Associate Professor, School of Civil and Environmental Engineering, Nanyang Technological University, Blk N1, 50 Nanyang Avenue, Singapore 639798; cjchu@ntu.edu.sg

ABSTRACT: Experimental data to study the strain softening and instability behavior of loose sand under plane-strain conditions are presented in this paper. K_0 consolidated drained and undrained tests under both deformation-controlled and load-controlled loading modes were carried out using a new plane-strain apparatus. The drained and undrained behaviors of very loose sand under plane-strain conditions were characterized. The test results show that the loading mode affects the post-peak behavior of sand and controls whether strain softening or instability will occur in the post-peak region. The failure line and critical state line are not affected by the loading mode.

INTRODUCTION

When the stress-strain behavior of soil is studied experimentally, laboratory tests can be conducted using either load controlled (LC) or deformation controlled (DC) loading mode. In tests conducted under the LC loading mode, loads are increased in either small load increments or at a constant rate. In tests conducted under the DC loading mode, specimens are sheared using a constant rate of vertical displacement. Chu and Leong (2001) has shown that when two tests are conducted under identical conditions except the loading mode, different post-peak behaviors can be obtained. For a test conducted under a DC mode, strain softening will occur, whereas for a test conducted under a LC mode, instability will take place, given the other conditions are the same. Here instability is defined as a behavior in which large plastic strains are generated rapidly due to the inability of a soil element to sustain a given load or stress.

In relation to the instability behavior, the so-called “instability line” has been defined by Lade and Pradel (1990) to specify the conditions under which static instability may occur. Lade (1992) proposed the instability line to be determined using undrained tests conducted under DC loading modes. As instability occurs under a LC loading condition, the instability line should logically be determined by undrained tests conducted under LC loading modes.

The objective of this paper is to study the strain softening and instability behavior of loose sand in drained and undrained tests under plane-strain conditions and to examine whether loading mode will affect the occurrence of strain softening and instability behavior of sand.

TEST ARRANGEMENT

The plane-strain apparatus (PSA) developed by Wanatowski and Chu (2006) was used in this study. The apparatus tested a prismatic soil specimen of 120 mm in height and 60 ×60 mm in cross-section. A plane-strain condition was imposed using two stainless steel vertical platens fixed in position by two pairs of horizontal tie rods. The lateral stress in this direction (σ_2) was measured by four submersible total pressure transducers.

The PSA used in this study is similar to that developed by Drescher et al. (1990). However, one major difference these two devices is that the lateral stress σ_2 in the PSA designed by Drescher et al. (1990) was not measured, whereas σ_2 in the PSA developed by Wanatowski and Chu (2006) was measured by the four pressure transducers. This enabled all three principal stress components σ_1, σ_2, and σ_3 to be measured directly. Furthermore, by comparing the σ_2 values at four different locations, the onset of shear bands could be identified as the point where the four σ_2 values start to diverge. It should be mentioned that some PSA's used by other researchers (e.g. Finno et al. 1996) also permit the measurement of σ_2 at different locations. However, the use of σ_2 measurements for the detection of shear bands has not been reported before.

For details of the plane-strain apparatus and testing system, see Wanatowski and Chu (2006).

MATERIALS AND METHODOLOGY

The soil tested was marine dredged silica sand, the so-called Changi sand, used for the Changi land reclamation project in Singapore. The sand grains were mainly sub-angular. The shell content of the sand was approximately 14%. The mean grain size of the sand was 0.30 mm. For the grain size distribution curve and detailed description of the physical and mechanical properties of the tested sand, see Leong et al. (2000) and Wanatowski and Chu (2006).

The specimens tested were prepared using the moist tamping (MT) method in which the sand was premixed to a moisture content of 5%. Due to the capillary suction between moist soil particles, the MT method could produce specimens looser than the maximum void ratio e_{max} measured for dry sand in accordance with ASTM D4254.

Shearing in deformation-controlled tests was carried out at a constant rate of 0.05 mm/min (drained) or 0.10 mm/min (undrained). The loading rate for load-controlled tests varied between 0.010 kN/min and 0.015 kN/min. These rates were chosen in accordance with previous experiments on Changi sand in a triaxial cell by Leong et al. (2000), and Chu and Leong (2001) so that the expected maximum deviatoric stress obtained from a LC test would be reached at similar axial strain as that in a DC test on an identical specimen. This was done to ensure that the effect of deformation rate on the stress-strain behavior of sand was negligible.

RESULTS

As discussed by Chu and Leong (2001) under axisymmetric conditions, the stress-strain behavior of sand manifested during pre-failure strain softening is different from that during pre-failure instability. However, the conditions that lead to strain softening and instability are the same, except that the former occurs when a specimen is sheared under a deformation-controlled loading mode and the latter under a load-controlled loading mode. Several pairs of parallel tests are compared to verify this assumption under plane-strain conditions. The term 'parallel tests' refers to two tests that are conducted on two duplicated specimens by following the same stress or strain paths, but with one under a LC loading mode and the other a DC loading mode (Chu and Leong 2001; Chu and Wanatowski 2009).

The results of a pair of parallel CK_0D tests, D09 and D09L, conducted on very loose sand under drained conditions are compared in Fig. 1. The specimens were K_0 consolidated to p'_c of 298 and 302 kPa respectively before shearing. Test D09 was conducted under a DC loading mode, while Test D09L under a LC loading mode. Fig. 1(a) shows that both tests reach the same failure line with a gradient $\eta_f = 1.16$. The stress-strain curves (Fig. 1(b)) and the volumetric strain versus axial strain curves (Fig. 1(c)) are almost identical up to the peak points. Since both the deviatoric stress and the volumetric strain have (or almost have) approached constant values at the end of each test, practically the critical state has been attained in both tests. Thus, the failure line obtained in Fig. 1(a) is also the CSL under plane-strain conditions. Nevertheless, the axial strain rate increases with time in the LC test (D09L) and becomes very large after the peak point as shown in Fig. 1(d). Thus the specimen in the LC test (D09L) has become unstable. Similar behavior was also observed in triaxial tests on loose sand by Chu and Leong (2001). The axial strain rate is constant throughout the whole DC test, as shown in Fig. 1(d).

The above comparison indicates that both strain softening and instability can occur in drained plane-strain tests in the post-peak region. Whether strain softening or instability will occur is affected by the loading mode adopted to conduct the test. Instability will not occur in a test conducted under a DC loading mode. The above findings pose a challenge to constitutive modeling, as the stress-strain relationships of soil in most existing models are not related to loading mode in which the soil is subjected.

The results of a pair of CK_0U tests conducted on very loose specimens under undrained conditions are presented in Fig. 2. Test U05 was conducted under a DC loading mode and Test U05L under a LC loading mode. The effective stress paths of the two tests and the CSL determined by drained tests on very loose sand (as shown in Fig. 1(a)) is shown in Fig. 2(a). It can be seen that the two effective stress paths were similar and both approached the CSL. It should be noted that the two tests ended at two different stress points on the CSL line. This implies that the post-liquefaction strength (i.e. the residual shear strength determined in the undrained shear tests) obtained from the DC and LC tests will be different.

In Fig. 2(a), a line can be drawn through the peak points of the undrained effective stress paths. This line has been called the instability line by Lade (1992). The gradient of the instability line obtained from the tests is $\eta_{IL} = 0.89$, as shown in Fig. 2(a). The zone bounded by the instability line and the CSL is called the zone of instability. Figure 2(a) appears to indicate that the same instability line was obtained for both the DC and the LC tests. The stress-strain curves are compared in Fig. 2(b). Similar pre-peak behavior was observed in both tests. Both peak deviatoric stresses occurred around an axial strain of 0.4%. However, the stress-strain curves in the post-peak region are different. In the DC test (U05), strain softening behavior was observed whereas in the LC test (U05L) instability took place. This can be seen more clearly from Figs. 2(c) and 2(d). In the LC test (U05L) the axial strain also increased suddenly at the peak (Fig. 2(d)). Thus, the specimen became unstable at the peak. Once the strain rate exceeded the maximum loading rate of the force actuator, the axial load could not be maintained and the deviatoric stress dropped suddenly at the peak (Fig. 2(c)). On the other hand, in the DC test (U05), the deviatoric stress reduced gradually with time (Fig. 2(c)) and the axial strain increased almost linearly with time (Fig. 2(d)) in the post-peak region. Therefore, strain softening occurred in Test U05. The excess pore water pressure versus time curves are also shown in Fig. 2(e). In Test U05, the pore water pressure increased gradually and reached a constant value at the end of shearing, whereas in Test U05L, the pore water pressure shot up after the specimen became unstable at the peak.

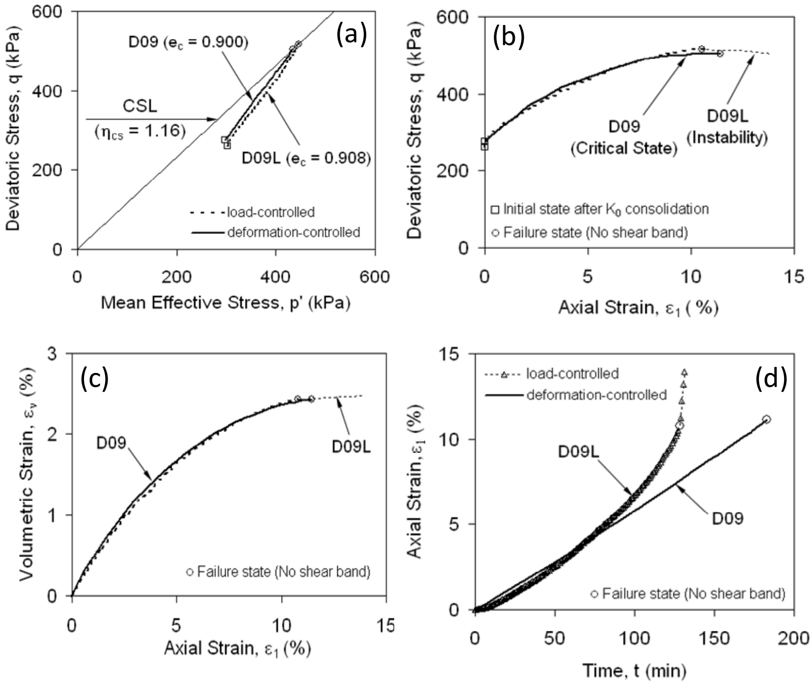

FIG. 1. Comparison of drained tests conducted on very loose sand under deformation-controlled and load-controlled loading modes.

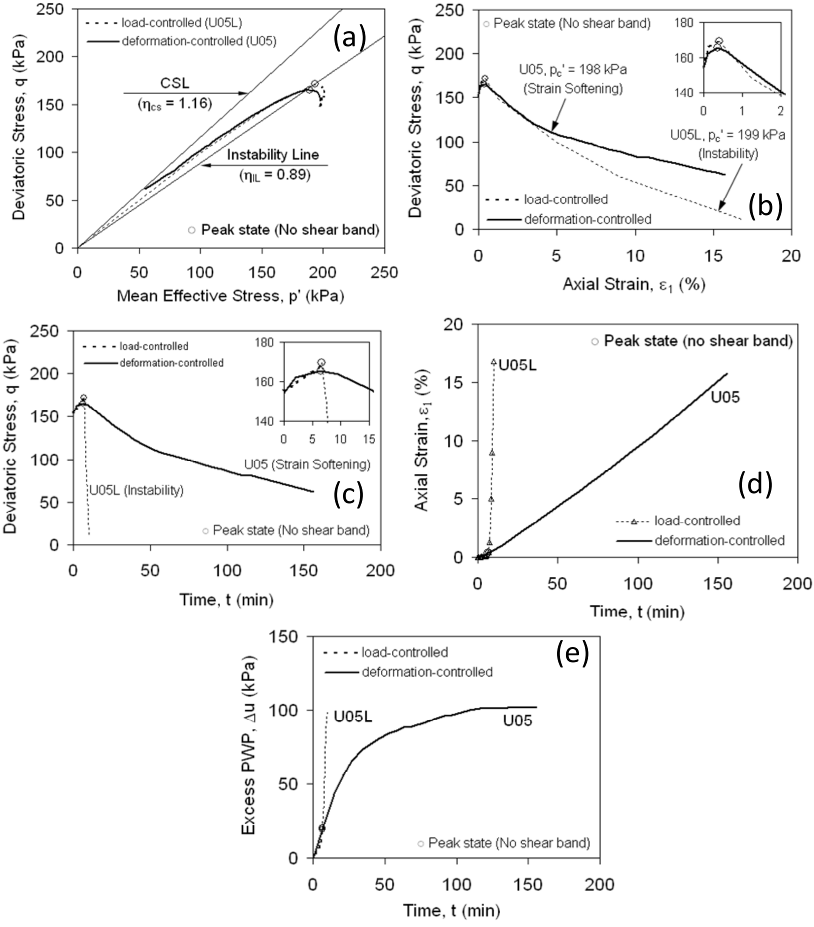

FIG. 2. Comparison of undrained tests conducted on very loose sand under deformation-controlled and load-controlled loading modes.

DISCUSSION

The CSL and instability line determined using data obtained from the DC tests carried out at different confining pressures (Wanatowski 2005) are plotted in Fig. 3 on both the q-p′ and the e-p′ planes. The data obtained from the LC tests are also plotted in Fig. 3 and these data are seen to be consistent with those from the DC tests. The instability line is not unique, but varies with the void ratio and stress level, as discussed in detail by Chu et al. (2003) and Wanatowski and Chu (2007). As the upper bound of the instability line is the CSL, only the data that form the lower bound of the instability lines, obtained from CK_0U tests on very loose specimens with a relative density of 0-2%, is presented in Fig. 3.

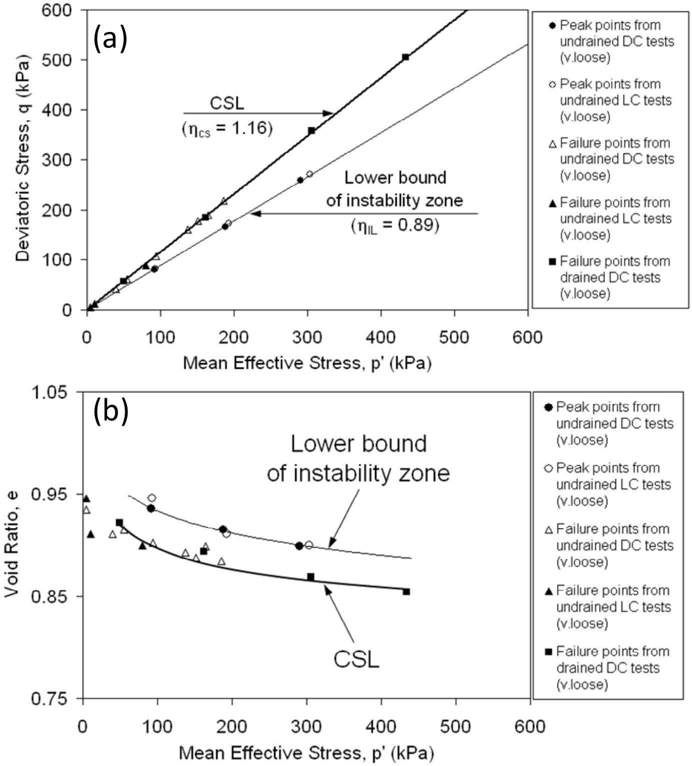

FIG. 3. CSL and instability line obtained from tests conducted under both deformation-controlled and load-controlled loading modes.

It can be seen that the lower bound of the instability line is not affected by the loading mode either. It should be pointed out that as the instability line is obtained using the peak points of the undrained stress paths (see Fig. 2), it specifies the onset condition for strain softening too. As the instability line represents the onset condition for both strain softening and instability, it implies that the mechanisms that govern strain softening and instability are the same, and instability or strain softening behavior may only be a different magnification of the same mechanisms under different loading conditions as pointed out by Chu and Leong (2001), Chu et al. (2003) and Chu and Wanatowski (2009). Whether strain softening or instability will occur depends on whether the loading condition is load or deformation controlled.

CONCLUSIONS

The strain softening and instability behaviors of loose sand under plane-strain conditions was studied by conducting K_0 consolidated drained and undrained tests using a new plane-strain apparatus. The test results have shown that the loading mode affects the post-peak stress-strain behavior of sand. Instability will occur when a test is conducted under a LC loading mode, whereas strain softening will take place when a test is conducted under a DC loading mode, given the other conditions the same.

It was also demonstrated that critical states were obtained from drained or undrained plane-strain tests on very loose sand. The data have shown that the CSL on both the q-p' and the e-p' planes is not affected by the loading mode. The instability line is not affected by the loading mode either. Therefore, the CSL and instability line determined using tests conducted under one type of loading mode will be applicable to tests conducted under another type.

REFERENCES

Chu. J. and Leong, W.K. (2001). "Pre-failure strain softening and pre-failure instability of sand: a comparative study." *Géotechnique,* Vol. 51 (4): 311-321.

Chu, J., Leroueil, S., and Leong, W. K. (2003). "Unstable behaviour of sand and its implication for slope stability." *Can. Geotech. J.*, 40, 873-885.

Chu, J. and Wanatowski, D. (2009). "Effect of loading mode on strain softening and instability behavior of sand in plane-strain tests." *J. Geotech. & Geoenv. Engrg.*, Vol. 135 (1): 108-120

Drescher, A., Vardoulakis, I. G., and Han, C. (1990). "A biaxial apparatus for testing soils." *Geotech. Test. J.,* 13(3), 226-234

Finno, R. J, Harris, W. W., and Viggiani, G. (1996). "Strain localization and undrained steady state of sand." *J. Geotech. Eng.,* 122(6), 462-473.

Lade, P. V. and Pradel, D. (1990). "Instability and flow of granular materials. I: Experimental observations." *J. Eng. Mech.,* 116(11), 2532-2550.

Lade, P. V. (1992). "Static instability and liquefaction of loose fine sandy slopes." *J. Geotech. Eng.*, 118(1), 51-71.

Leong, W. K., Chu, J., and Teh, C. I. (2000). "Liquefaction and instability of a granular fill material." *Geot. Testing J.*, 23(2), 178-192.

Wanatowski, D. (2005). "Strain softening and instability of sand under plane-strain conditions." *PhD thesis*, Nanyang Technological University, Singapore.

Wanatowski, D., and Chu, J. (2006). "Stress-strain behavior of a granular fill measured by a new plane-strain apparatus." *Geotech. Test. J.*, 29(2), 149-157.

Wanatowski, D. and Chu, J. (2007), Static liquefaction of sand in plane-strain, *Can. Geotech. J.*, 44(3): 299-313.

A Case Study of Undrained Shear Strength Evaluation from In-situ Tests in Soft Louisiana Soils

Lei Wei[1], Ph.D., P.E., M. ASCE, Rohit Pant[2], E.I.T., A.M. ASCE,
and Mehmet Tumay[3], Ph.D., P.E., F. ASCE

[1]Geotechnical Engineer, HNTB Corporation, 9100 Bluebonnet Centre Blvd, Suite 301, Baton Rouge, LA 70809; lwei@hntb.com
[2]Geotechnical Engineer, HNTB Corporation, 9100 Bluebonnet Centre Blvd, Suite 301, Baton Rouge, LA 70809; rpant@hntb.com
[3]Georgia Gulf Distinguished Professor Emeritus, Department of Civil & Environmental Engineering, CEBA 3505A, Louisiana State University, Baton Rouge, LA 70803; and Adjunct Professor, Bogazici University, Istanbul, Turkey. mtumay@eng.lsu.edu

ABSTRACT: The undrained strength is one of the governing soil properties when evaluating stability issues associated with clays. The undrained shear strength is not a unique measure of soil strength; it may be obtained by conducting laboratory tests or by in-situ tests, or a combination of both. This paper presents a case study using piezocone penetration test (PCPT or CPTu) and flat dilatometer test (DMT) to ascertain undrained shear strengths at a site in New Orleans where soft clay deposits are predominant. This paper attempted to correlate the undrained shear strengths obtained from PCPT and DMT to those obtained from laboratory unconfined compression and triaxial unconsolidated undrained tests. A calibration study was performed and a set of site-specific values were suggested to best suit the soils at the exploration site. The suggested parameters or correlations may be valuable to practitioners to evaluate undrained shear strengths in New Orleans area using popular in-situ test methods.

INTRODUCTION

In the current practice, the short-term stability of clayey soils is typically analyzed by total stress approach ($\varphi = 0$). The induced pore pressure is implicitly taken into consideration by utilizing the concept of "undrained shear strength". This is particularly the case when evaluating stability of saturated soft clays. However, there might be no such a unique value of undrained shear strength as different tests may conclude different undrained shear strength values. Traditionally field vane shear test (VT), laboratory triaxial unconsolidated undrained test (UU), laboratory unconfined compression test (UC) and laboratory direct simple shear test (DSS) are among those that are most widely used to determine the undrained shear strength. Sometimes the variation of undrained shear strength values from different tests may be relatively significant for some naturally deposited clays (Su and Liao, 2002). For example, Seed et al. (2008) suggested that a reduction factor of 0.82 may be applied to the undrained shear strength obtained from triaxial compression test in order to find the equivalent undrained shear strength obtained from DSS tests. Recently, more and more attention has been paid to evaluate soil properties using in-situ methods. Piezocone Penetration Test (PCPT or CPTu) (Tumay, et al., 1981; Zuidberg, et.al., 1982) and Flat Dilatometer Test (DMT) are robust, fast and relatively economical and therefore are being more and more widely used worldwide. Both PCPT and DMT measurements can be used to estimate soil undrained shear strengths through empirical correlations. In this paper, an attempt has been made to correlate PCPT and DMT based undrained shear strengths to those obtained by UU and UC tests based on limited data from a case study in the great New Orleans area. Therefore, the findings in this study may be considered local and more research efforts are needed in the future to gain further confidence towards evaluation of undrained shear strength using PCPT and DMT results.

Traditional cone penetration tests (CPT) or the piezocone penetration test with pore pressure measurements (PCPT) are becoming increasingly popular nowadays to assist subsurface investigations. One of the applications of CPT soundings is to estimate the undrained shear strength of clayey deposits. The CPT or PCPT based undrained shear strength is usually expressed in the following bearing capacity form:

$$s_u = \frac{q_t - \sigma_v}{N_{kt}} \tag{1}$$

where q_t is the tip resistance corrected for pore pressure effect (Campanella et al., 1983), σ_v is the total overburden and N_{kt} is the cone factor. Typically N_{kt} varies from 10 to 20, with 15 as an average (Robertson and Robertson, 2006).

Flat dilatometer test (DMT) is a relatively new in-situ test method, which was originally developed in the late 1970s in Italy by Silvano Marchetti. The use of DMT has been rapidly growing in past decades as one of the most popular in-situ tests available to researchers and practicing engineers (Lutenegger, 1988). Although DMT is good at assessing soil compressibility (Schmertmann, 1988), it can also be used to evaluate undrained shear strength by correlating with in-situ stresses. Marchetti (1980) suggested the undrained shear strength may be expressed as follows:

$$s_u = 0.22\sigma'_v(0.5K_D)^{1.25} \tag{2}$$

where σ'_v is the effective overburden while K_D is a DMT based horizontal stress index. The undrained shear strength is mainly governed by the effective stress state as well as the soil stress history. Equation (2) is believed to be based on the relationship proposed by Ladd et al. (1977):

$$(s_u/\sigma'_v)_{OC} = (s_u/\sigma'_v)_{NC}(OCR)^{\Lambda} \tag{3}$$

where OCR is the overconsolidation ratio while Λ is a constant. Mayne et al. (2001) suggested that Λ can generally be taken to be around 0.8 (Equation (4)). Mayne et al.

(2001) also suggested that, for intact soft clays and silts with OCR less than 2, the undrained shear strength and effective overburden ratio may be close to 0.22 (Equation (5)):

$\Lambda = 0.8$ (4)
$(s_u/\sigma'_v)_{NC} = 0.22$ (5)

Marchetti (1980) proposed a relationship between OCR and K_D as follows:

$\mathrm{OCR} = (0.5K_D)^{1.56}$ (6)

By combining Equations (3) through (6), one can easily get Equation (2). All the above equations are empirical relationships and hence site specific correlations would be ideal. This paper presents a case study to calibrate the relationships between the undrained shear strength and the PCPT and DMT measurements. The site is located in the New Orleans area and fine-grained materials were identified in the majority of the depths based on subsurface explorations.

SUBSURFACE CONDITIONS

A boring (14U2), a PCPT (92C2) and a DMT (DMT1) were drilled or pushed at the crown of existing levee adjacent to each other. Five-inch (diameter) Shelby tube was used to retrieve undisturbed samples continuously at the boring location and the undisturbed samples were later transported to the laboratory for index and strength tests. The top of the explorations is at approximate elevation 6 m and the bottom of the explorations is located at about elevation -18 m. The water table appears to be near elevation 2.4 m. The natural ground surface in the area is believed to be near elevation 0, above which fill materials (silty and sandy clay) were placed to raise the existing levees. The natural deposits are predominantly fat clays between El 0 to -18, except that an organic clay layer appeared to be present between approximate El -6 to -8 m and that a silt and sandy silt layer is located between approximate El -8 to -10 m.

The index property tests include moisture content, Atterberg limits and unit weight. The strength tests include unconfined compression (UC) and triaxial unconsolidated undrained compression tests (UU). The lab test results are shown in Figures 1a through 1c. The PCPT measurements (tip resistance, sleeve friction, pore water pressure (u_2) and friction ratio) are presented in Figures 2a through 2c while the measured DMT data, p_0 (corrected 1st pressure reading), p_1 (corrected 2nd pressure reading), K_D (horizontal stress index) and OCR (overconsolidation ratio) are presented in Figures 3a through 3c. It is noteworthy to point out that, except the upper levee fill materials, the predicted OCR in the majority depths of the natural deposits appears to be in the range of 0.7 to 0.8, indicating the soils may be underconsolidated. Although no Oedometer test results are available to confirm the OCR values, the authors tend to agree that the majority of the soils may be underconsolidated given the fact that the levees in the area have been raised in the past decade. Since this paper focuses the shear strength interpretations in native soils, all the in-situ measurements as well as laboratory test results in the next section are limited to El 0 to -18 m.

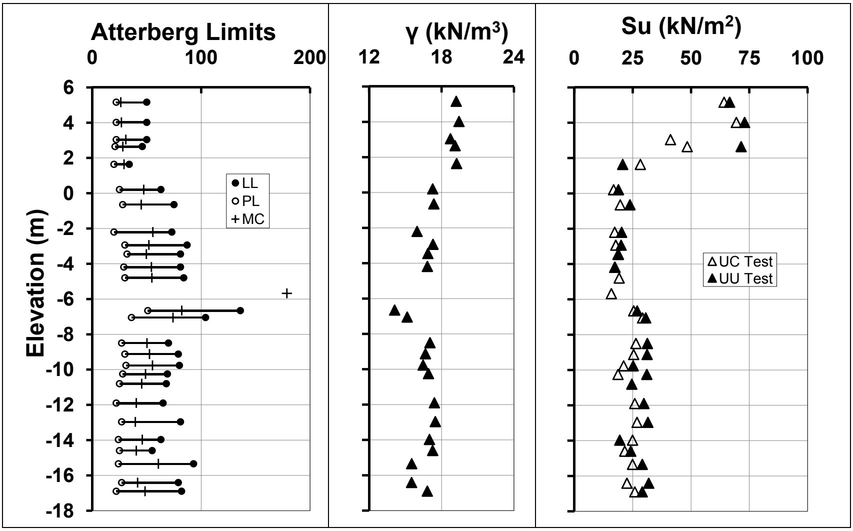

(2a) (2b) (2c)

Figure 1: (a) Atterberg Limits and Moisture Content; (b) Moist Unit Weight; (c) Undrained Shear Strength from Lab Tests

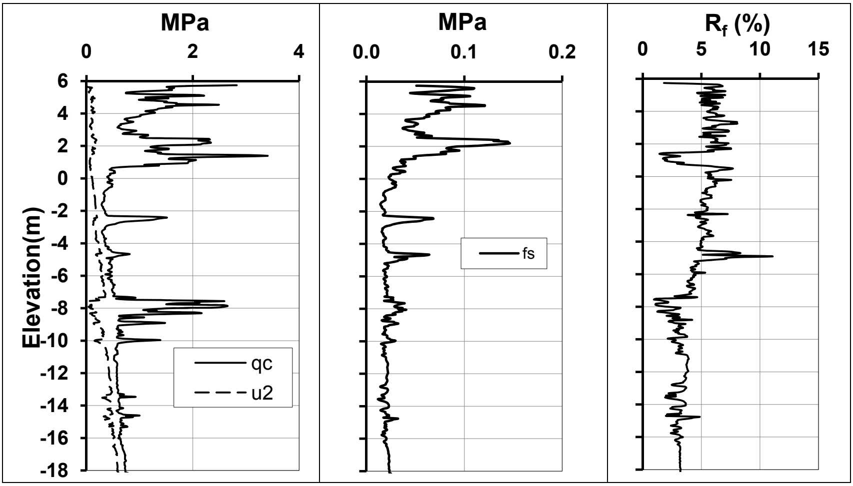

(3a) (3b) (3c)

Figure 2: (a) Tip Resistance and Pore Pressure; (b) Sleeve Friction; (c) Friction Ratio

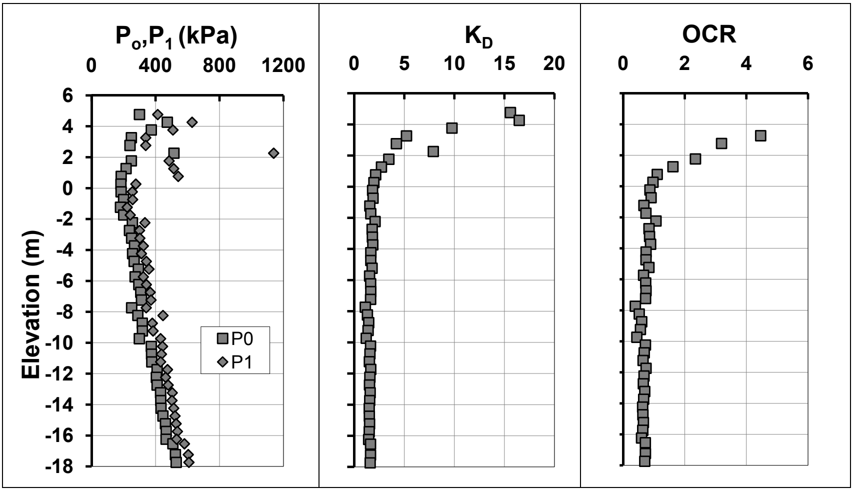

(4a) (4b) (4c)

Figure 3: (a) Corrected Pressure Readings; (b) Horizontal Stress Index; (c) Overconsolidation Ratio

DISCUSSIONS

PCPT Interpreted Shear Strength

Since Equation (1) is the most widely accepted format to estimate undrained shear strength from CPT or PCPT, this format is used to correlate the PCPT based undrained shear strength to the laboratory UU and UC test results. Typically N_{kt} varies from 10 to 20, with 15 as an average (Robertson and Robertson, 2006). Sunneset et al. (1989) further pointed out that N_{kt} may range from 10 to 15 for normally consolidated clay while in the range of 15 to 19 for overconsolidated clay. After hurricane Katrina, numerous subsurface explorations and associated studies have been conducted in the greater New Orleans area and reported N_{kt} values for normally consolidated clay are generally in agreement with Sunneset et al. (1989). Seed et al. (2008) reported a N_{kt} value of 12 near the 17th street drainage canal while Interagency Performance Evaluation Task Force (IPET, 2007) used an N_{kt} value of 15 in the same area.

In this case study, different N_{kt} values ranging from 10 to 15 were used and it was found that an N_{kt} value of 12 overall best fit the lab UU and UC data, as shown in Figure 4. This is particularly the case for the gray fat clay layer below El -10 as the PCPT based shear strengths were near the average value of the scattering UU and UC data points. Considering the fact that the soils may be lightly underconsolidated at the site, this may also suggest that an N_{kt} value towards the lower end of rang 10 to 15 may be also suitable to estimate undrained shear strength for underconsolidated clay by PCPT measurements.

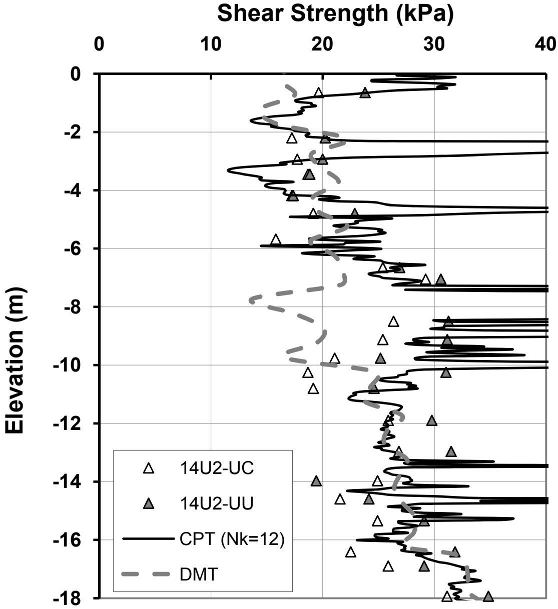

Figure 4: Comparison of in-situ vs laboratory shear strength

DMT Interpreted Shear Strength

DMT based shear undrained shear strength is correlated with two factors: 1. the undrained shear strength to effective overburden ratio (s_u/σ'_v) for normally consolidated clay; and 2. the stress history or the overconsolidation ratio (OCR), as indicated in Equation (3). One can either calibrate the s_u/σ'_v ratio or the Λ value or a combination of both to find a site specific empirical correlation. Since no laboratory Oedometer tests were performed, there is no solid foundation to calibrate the relationships between OCR and K_D. As a result, this paper tends to focus on the undrained shear strength with regard to effective overburden ratio (s_u/σ'_v).

The s_u/σ'_v ratio for normally consolidated clay is expected to vary with different soils. It may be as low as 0.16 for Northeastern US varved clay (Ladd and DeGroot, 2003) and it could be as high as 0.35 along some coastal area in Japan (Kamei and Iwasaki, 1995). Ladd and DeGroot (2003) suggested to simply use 0.22 for most homogeneous CL and CH sedimentary clays of low to moderate sensitivity, which is in agreement with Mayne et al. (2001) and Marchetti (1980). As for the soils in the New Orleans area, a value of 0.31 was reported by Seed et al. (2008) while a ratio of 0.24 was used by Interagency Performance Evaluation Task Force (IPET, 2007). In this study, the authors first attempted using a s_u/σ'_v ratio of 0.22 to estimate the undrained shear strength based on DMT data, which was exactly taken the format of

Equation (2). Then it was found that a s_u/σ'_v ratio of 0.21 may actually better to match the UU and UC points, as shown in Figure 4. As a matter of fact, a s_u/σ'_v ratio of 0.21 based interpretation makes the DMT predicted shear strengths in very close agreement with those predicted by PCPT. This is particularly the case for the gray fat clay layer below El -10 as illustrated in Figure 4. Again, this slightly reduction from 0.22 to 0.21 may reflect the fact that the majority of the soils under the levee may be lightly underconsolidated. However, the DMT interpreted undrained shear strengths appear to be significantly less than both the laboratory UU and UC results and the PCPT predicted shear strengths in the organic clay and silt layers (El -6 to -10 m) and the reason is unknown. It may imply that Equation (2) is not suitable for estimating undrained shear strength in organic clay or silt deposits, but significant more data and study will be needed to prove or disprove it.

CONCLUSIONS

Based on a case study in New Orleans area with limited testing data, an attempt was made to correlate the PCPT and DMT based undrained shear strengths with those measured in the laboratory by triaxial unconsolidated undrained compression (UU) and unconfined compression (UC) tests. It appears that both PCPT and DMT may be robust tools to predict soil undrained shear strengths with some work on site specific correlations. The widely accepted bearing capacity format (Equation (1)) works well at the test location with a cone factor N_{kt} value of 12. The PCPT predicted strengths fit well between the scattered UU and UC data, especially below El -10 in the natural gray fat clay layer. Marchetti's (1980) method (Equation (2)) is generally applicable at the site to predict undrained shear strength using DMT data. With an undrained shear strength to effective overburden ratio (s_u/σ'_v) of 0.21 instead of 0.22 in Equation (2) for normally consolidated soils, the DMT predicted strengths fit even better with both the UU and UC data and the PCPT predicted strengths, especially in the natural gray fat clay layer below El -10. Considering the fact that the soils may be lightly underconsolidated under the levee, the above reported site specific parameters (N_{kt} and s_u/σ'_v ratio) may need to be adjusted slightly to be applicable to adjacent normally consolidated clays. The DMT predicted undrained shear strength appears to be well below both the laboratory UU and UC results and the PCPT predicted shear strengths in the organic clay and silt layers (El -6 to -10 m), which may imply Equation (2) may not be suitable for estimating undrained shear strength in organic clay or silt deposits. However, more research efforts are needed to further look into it.

REFERENCES

Campanella, R.G., Robertson, P.K., and Gillespie, D. (1983). "Cone penetration testing in deltaic soils." *Can. Geotech. J.*, Vol. 20 (1): 23-35.

Interagency Performance Evaluation Task Force (IPET). (2007). "Performance evaluation of the New Orleans and southwest Louisiana hurricane protection system." Final Report, <https://ipet.wes.army.mil/> (November 2007).

Kamei, T. and Iwasaki, K. (1995). "Evaluation of undrained shear strength of cohesive soils using a flat dilatometer." *Soils and Foundations, Japanese Society of Soil*

Mechanics and Foundation Engineering, Vol. 35 (2): 111-116.

Ladd, C.C. and DeGroot, D.J. (2003). "Recommended Practice for Soft Ground Site Characterization." *The Arthur Casagrande Lecture, Proceedings of the 12th Panamerican Conference on Soil Mechanics and Geotechnical Engineering*, Boston, MA, Vol. 1: 3-57.

Lutenegger, A.J. (1988). "Current status of the Marchetti dilatometer test." *ISOPT-1*, De Ruiter (ed.), Rotterdam: 137-155.

Marchetti, S. (1980). "In-situ tests by flat dilatometer." *J. Geotechnical Engrg. Div., ASCE,* Vol. 106 (GT3): 299-321.

Mayne, P.W., Christopher, B.R., and DeJong, J. (2001). "Manual on subsurface investigations." FHWA NHI-01-031, Washington DC.

Robertson, P.K. and Robertson, K.L., (2006). "Guide to cone penetration testing and it's application to geotechnical engineering." Gregg Drilling and Testing Inc., www.greggdrilling.com.

Schmertmann, J.H. (1988). "Guidelines for using the CPT, CPTU and Marchetti DMT for geotechnical design, Vol. I-IV, FHWA, Washington DC.

Seed, R.B., Bea, R.G., et al., (2008). "New Orleans and Hurricane Katrina. III: The 17th Street Drainage Canal." *J. Geotechnical & Geoenv. Engrg.*, Vol. 134 (5): 740-761.

Senneset, K., Sandaven, R., and Janbu N. (1989). "Evaluation of soil parameters from piezocone tests." *Transportation Research Record 1235*, Washington DC: 24-37.

Su, S.F. and Liao, H.J. (2002). "Influence of strength anisotropy on piezocone resistance in clay." *J. Geotechnical & Geoenv. Engrg.*, Vol. 128 (2): 166-173.

Tumay, M.T., Acar, Y.B., Boggess, R. (1981). "Subsurface investigations with piezo-cone Penetrometer." *ASCE Special Publication on Cone Penetration Testing and Experience*, 1981: 325-342.

Zuidberg, H.M., Schaap, L.H.J., and Beringen, F.I. (1982). "A penetrometer for simultaneously measuring cone resistance, sleeve friction and dynamic pore pressure." *Proceedings, Second European Symposium on Penetration Testing, ESOPT II, Vol. 2, A.A.* Balkema, Rotterdam: 963-980.

Critical State Parameters of Kentucky Clay

Melanie R. Anderkin[1] and L. Sebastian Bryson[2], Ph.D., P.E.

[1]Research Assistant, Department of Civil Engineering, 161 Raymond Building, University of Kentucky, Lexington, KY 40506-0281; manderkin@uky.edu
[2]Assistant Professor, Department of Civil Engineering, 161 Raymond Building, University of Kentucky, Lexington, KY 40506-0281; bryson@engr.uky.edu

ABSTRACT: This paper examines the critical state parameters of clays typical to the physiographic regions of Kentucky, a state located in the southeastern United States. The critical state model is unique due to the fact that it links the soil consolidation characteristics with shear strength properties allowing prediction of soil behavior at various loading states. The critical state strength parameters for the clays are presented and well-established engineering material property correlations are translated into critical state representation, particularly those correlations that relate consolidation index and recompression index to liquid limit and specific gravity. The Kentucky clay soil parameters are then compared to these representations. Finally, new relationships correlating critical state parameters to consistency limits and particle size analysis are presented.

INTRODUCTION

The critical state concept is an idealization of the observed behavior of saturated remolded clays in triaxial compression tests. It is assumed that it applies to undisturbed soils and is therefore quite useful in interpreting soil behavior. The uniqueness of the critical state model lies in the fact that it links the soil consolidation characteristics with shear strength properties allowing prediction of soil behavior at various loading states.

This paper presents the critical state parameters of clays typical to the physiographic regions of Kentucky, which is located in the southeastern United States. Index and engineering properties were determined for clay soils obtained from several Kentucky regions. Utilizing these properties, critical state parameters were developed. Additionally, well-established material property correlations were expressed as critical state representations, particularly those correlations that relate consolidation index, C_c, and recompression index, C_r, to liquid limit, LL, and specific gravity, G_s.

REGIONAL GEOLOGY

Kentucky is split into six physiographic regions as shown in Figure 1. Soil data representing each region (with the exception of the Knobs) is presented herein. Each soil sample is identified based on a central county located in that region. The Lee County sample is from the Eastern Coal Fields region. This area is generally steep and mountainous with few flatlands. The soil is moist and medium to fine in texture. Colluvium is prevalent due to debris avalanche, landslide, creep, and sheet wash (Newell, 2001).

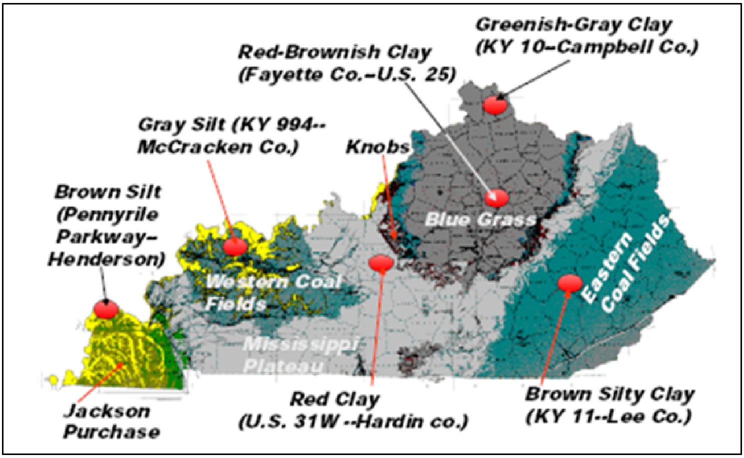

Figure 1. Physiographic Regions of Kentucky (Hopkins et al., 2006).

The Campbell and Fayette County samples are from the Bluegrass region, which is further subdivided into the Inner Bluegrass and Outer Bluegrass. Fayette County resides in the Inner Bluegrass, which is characterized as relatively flat with gently rolling hills. These soils are rich in minerals from phosphates. Campbell County is in the Outer Bluegrass. This area has more hills and valleys and is characterized by weathered limestone. The Hardin County sample is from the Mississippi Plateau region. The soil here is a residuum of limestone and dolomites, and the area was considered a grassland prairie prior to modern agriculture. The McCracken County sample is from the Western Coal Fields. This region is very similar to the Easter Coal Fields with the exception that the sandstone present here is more resistant to erosion producing a less mountainous terrain. Lastly, the Henderson County sample is from the Jackson Purchase region. Positioned at the head of the Mississippi River, this area is underlain with gravel, sand, silt and clay deposited 60-140 million years ago by the fluctuation of the Gulf of Mexico (Moore, 1994). Alluvium and Loess soils are also present.

LABORATORY TESTING

The soils analyzed represent those typical from six counties representing five physiographic regions within Kentucky. Index data such as moisture content, Atterberg limits, specific gravity, and particle size analysis were provided by Hopkins et al. (2006). The index data for the various soils are shown in Table 1. The data show that all of the soils fall within the silt and clay particle sizes. The fines contents range from 70.1 percent to 99.4 percent. Clay content ranges from 20 to 52.8 percent, and G_s ranges from 2.64 to 2.89. Plasticity properties were obtained, and the soils were classified according to the Unified Soil Classification System.

Table 1. Index Test Data.

Clay	G_s	Atterberg Data		% Passing		
		LL	PI	No. 10	No.200	0.002 mm
McCracken County	2.64	26.5	5.8	98.5	80.3	21.8
Henderson County	2.69	28.2	8.5	100.0	99.4	20.0
Hardin County	2.73	52.3	26.7	95.1	79.7	52.8
Lee County	2.76	34.4	7.6	90.6	70.1	21.2
Campbell County	2.76	41.1	18.9	95.9	91.4	40.8
Fayette County	2.89	47.7	19	96.4	83.7	50.5

Consolidation data such as C_c and C_r were obtained for the six clay samples from one-dimensional consolidation testing (i.e. oedometer testing). Effective strength data such as the effective critical state phi angle, ϕ'_{cs}, was obtained from standard isotropically consolidated undrained triaxial tests (CIU) with porewater measurements. The triaxial and consolidation data used for this research are presented in Table 2. A more detailed presentation of the experimental data is found in Hopkins et al. (2006).

Table 2. Triaxial and Consolidation Data.

Clay	M	ϕ'_{cs}	C_c	C_r	e_o
Hardin County	1.13	28.4	0.303	0.020	1.12
Lee County	1.28	31.8	0.132	0.037	0.613
Henderson County	1.35	33.4	0.060	0.008	0.766
McCracken County	1.30	32.4	0.101	0.037	0.505
Campbell County	1.13	28.4	0.210	0.108	0.852
Fayette County	1.24	30.9	0.228	0.081	1.066

CRITICAL STATE MODEL

In critical state soil mechanics, the state of a soil sample is described with three parameters; the effective mean stress, p', and the deviatoric (shear stress), q, and the void ratio, e. The failure state of soils in q - p' space is represented by the critical state line (CSL). The slope of the CSL is given by the parameter M, which defines the critical state stress ratio at failure. This ratio explicitly represents deviatoric stress at failure as $q_{cs} = Mp'_{cs}$. The relationship between M and the critical state phi angle, ϕ'_{cs}, for triaxial compression is

$$M = \frac{6\sin\phi'_{cs}}{3-\sin\phi'_{cs}} \tag{1}$$

Therefore, values of M can be determined from ϕ'_{cs} values obtained from triaxial tests. The M values used for this study are given in Table 2.

TRANSLATION OF ESTABLISHED RELATIONAL CORRELATIONS

A great deal of research has been devoted to providing practitioners with a means of estimating consolidation parameters using material properties. In order to extend this approach to critical state models, established empirical expressions correlating consolidation parameters C_c and C_r to LL and G_s were translated into critical state representations. The original empirical equations and critical state expressions are given in Table 3. Note, the critical state consolidation parameters are $\lambda = 0.434C_c$ and $\kappa = 0.434C_r$.

Table 3. Critical State Representation of Established Empirical Expressions.

Original Correlation	Reference	Critical State Representation
$C_c = 0.009(LL-10)$	Terzaghi and Peck (1967)	$\lambda = 0.004(LL-10)$
$C_c = 0.007(LL-7)$	Skempton (1944)	$\lambda = 0.003(LL-7)$
$C_c = 0.2343\left[\frac{LL(\%)}{100}\right]G_s$	Nagaraj and Murty (1985)	$\lambda = 0.1017\left[\frac{LL(\%)}{100}\right]G_s$
$C_r = 0.0463\left[\frac{LL(\%)}{100}\right]G_s$	Nagaraj and Murty (1985)	$\kappa = 0.020\left[\frac{LL(\%)}{100}\right]G_s$

Because many empirical expressions for consolidation parameters involve the liquid limit, LL and λ values from the Kentucky clays were plotted along with lines representing the critical state representations from some empirical expressions. This is shown in FIG 2. The result shown in FIG 2 indicate that the correlations of Skempton (1944), Terzaghi and Peck (1967) and Nagaraj and Murty (1985) overestimate $\lambda$by an average of 56, 47, and 50 percent, respectively. Linear regression of the Kentucky clay data provides a better match than is predicted from the aforementioned relations. The relation for the Kentucky clays is

$$\lambda = 0.0036[LL(\%) - 18] \tag{2}$$

The correlation coefficient, R^2, for the correlation is 0.9404.

CRITICAL STATE CORRELATIONS

Correlations were developed between critical state parameters and laboratory data. One of these correlations is presented in FIG 3. This figure shows critical state compression ratio, $\lambda/(1+e_o)$, plotted against *M*.

FIG 3 shows that as the compression ratio increases, *M* decreases. Thus, the data implies that as a soil becomes less compressible, it becomes stiffer in shear. A linear trend line through the data produces an expression for the Kentucky clays given as

$$M = -4.92(\lambda/1 + e_o) + 1.43 \tag{3}$$

The R^2 value for this correlation is 0.8561. Other empirical relationships among critical state parameters and material properties were investigated and the results are summarized in **Table 4**.

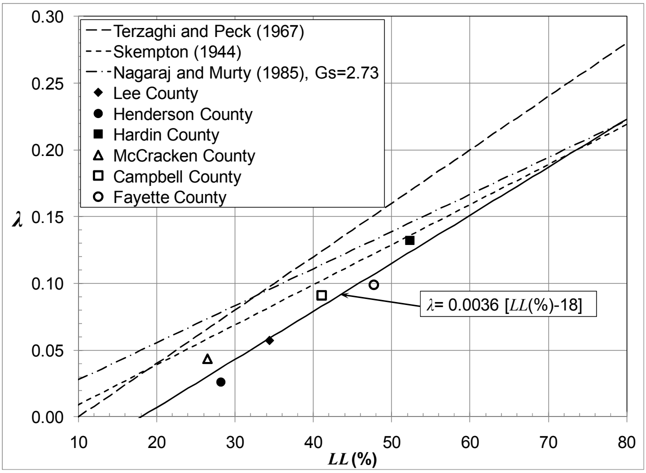

FIG 2. Slope of Normal Compression Line vs. Liquid Limit.

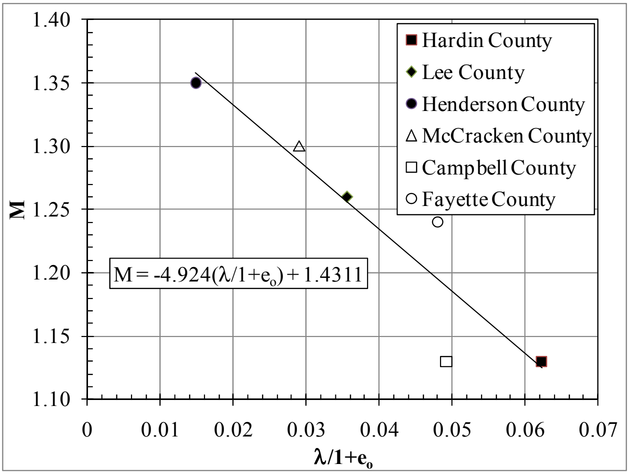

FIG 3. Slope of the Critical State Line vs. Critical State Compression Ratio.

Table 4. Summary of Empirical Equations.

Plot Variables	Equation	R^2 Value
$\lambda\ vs.\ LL(\%)$	$\lambda = 0.0036[LL(\%) - 18]$	0.9404
$\frac{\lambda}{G_s}\ vs.\ LL(\%)$	$\lambda = 0.0013[LL(\%) - 17]G_s$	0.9176
$\lambda\ vs.\ e_{LL}$	$\lambda = 0.1217e_{LL} - 0.0538$	0.9056
$\kappa\ vs.\ e_{LL}$	$\kappa = 0.0482e_{LL} - 0.024$	0.6029
$M\ vs.\ \frac{\lambda}{1+e_o}$	$M = -4.92\left(\frac{\lambda}{1+e_o}\right) + 1.43$	0.8561
$M\ vs.\ \frac{\lambda}{1+e_{LL}}$	$M = -5.86\left(\frac{\lambda}{1+e_{LL}}\right) + 1.44$	0.8557
$M\ vs.\ PI$	$M = -0.0091PI + 1.37$	0.7101

e_{LL} = void ratio at liquid limit = LL*G_s

CONCLUSIONS

The data presented herein was used to develop correlations between material properties and critical state parameters of clays typical to the state of Kentucky. The results of these efforts show that critical state parameters describing deformation behavior (i.e. λ and κ) are correlated to the liquid limit and the void ratio at liquid limit. For normally consolidated soils, the data shows the critical state parameter describing shear behavior (i.e. *M*) can be reliably inferred from the deformation behavior using the critical state compression ratio, $\lambda/(1+e_o)$. The data also shows *M* is correlated with Atterberg data. Thus, this work provides some simple relationships that can be used to obtain initial estimates of critical state parameter.

REFERENCES

Budhu, M. (2007). "A Critical State Model to Interpret Soil Behavior." *Soil Mechanics and Foundations,* Wiley, Hoboken, NJ, 284-336.

Hopkins, T. C., Beckham, T. L., and Sun, L. (2006). "Characteristics and Engineering Properties of the Soft Soil Layer in Highway Soil Subgrades." *Rep. No. KTC-06-13/SPR 270-03-1F,* Kentucky Transportation Center.

Moore, H. L. (1994). *A Geologic Trip across Tennessee by Interstate 40.* The University of Tennessee Press, Knoxville, TN.

Nagaraj, T., and Murty, B. R. S. (1985). "Prediction of the Preconsolidation Pressure and Recompression Index of Soils." *Geotechnical Testing Journal,* 8(4), 199-202.

Roscoe, K.H., and Burland, J.B. (1968). “On the Generalized Stress-Strain Behavior of Wet Clay.” *Engineering Plasticity*, J. Heyman and F. Leckie (eds.), Cambridge University Press, Cambridge, 535-609.

Scholfield, A., and Wroth, C.P. (1968). *Critical State Soil Mechanics*. McGraw-Hill, London.

Skempton, A.W. (1944). “Notes on Compressibility of Clays.” *Quarterly Journal of the Geological Society of London*, Vol.100, 119-135.

Terzaghi, K., and Peck, R.B. (1967). *Soil Mechanics in Engineering Practice,* 2nd ed., Wiley, New York.

Comparison in Mechanical Behavior between Undisturbed and Reconstituted Shanghai Soft Clay

Bo CHEN[1], De'an SUN[2] and Ke ZHOU[3]

[1]PhD candidate, Department of Civil Engineering, Shanghai University, 149 Yanchang Road, Shanghai, 200072, chenbo20020178@163.com
[2]Professor, Department of Civil Engineering, Shanghai University, 149 Yanchang Road, Shanghai, 200072, sundean@shu.edu.cn
[3]PhD candidate, Department of Civil and Environmental Engineering, University of South Carolina, 300 Main Stress, Columbia, SC, USA, 29208, hedou992@163.com

ABSTRACT: In order to study the effects of soil structure on compression and shear behavior, a number of isotropic compression and consolidated-drained triaxial shear tests on Shanghai soft clay in undisturbed and reconstituted samples have been carried out. Comparisons of measured compression curves indicate that undisturbed samples have larger void ratio than reconstituted samples at the same confining pressure. Comparisons of measured stress ratio-strain curves indicate that the confining pressure has no effect on the reconstituted samples but has an effect on the undisturbed samples. The strength of undisturbed samples is lower than that of reconstituted samples when sheared at the same confining pressure. This behavior is explained to be caused by the difference in void ratio between two type samples.

INTRODUCTION

Clay, a natural material distributed wildly all over the world, presents a lot of different physical properties and mechanical behavior. The mechanical behavior is also shapely affected by many factors, such as stress history, structure, degree of saturation, etc. Fortunately, there were many results from the study on clays, especially on remolded or reconstituted clay, such as the Cam-clay model, which is used widely in the practical engineering.

Now, much more attention is on the mechanical behavior of natural clay, which is more common in the filed. The study results show that there are many differences between undisturbed and reconstituted soils due to the structure in undisturbed soil, which was formed during the long-term deposit. Furthermore, there are many different attitudes to the mechanical behaviors of undisturbed soil after the post-yield stress state (Burland, 1990; Nagaraj, et al, 1990; Hong, et al, 2006).

With the objective of understanding the mechanical behavior and obtaining the corresponding parameters, such as compression index (C_c) and swelling index (C_s). A number of triaxial tests were performed on undisturbed and reconstituted Shanghai soft clay, including isotropic compression tests and triaxial consolidated-drained shear tests. The test results are useful to understanding the mechanical behavior of Shanghai soft clay and developing its constitutive model.

PHYSICAL PROPERTY

The tested undisturbed specimens were obtained from about 10-15 m below the ground surface at Pudong area of Shanghai by a fixed piston thick wall sampler. The specimen used for testing is a muddy silty clay, which is the most representative clay for Shanghai soils. The grain-size distribution and the Atterberg limits were measured by the hydrometer and the liquid-plastic combining device, respectively, and are shown in Table 1. It can be seen that most ingredient of Shanghai soft clay is silt, the liquid limit and plastic limit are 44.5% and 22.1%, respectively. Furthermore, the natural water content w_n ranges from 42.2% to 46.0%, and is almost the same as the liquid limit w_l. But the soil does not flow because of the soil structure.

ISOTROPIC COMPRESSION BEHAVIOR

To investigate the influence of soil structure on the compression behavior of Shanghai soft clay, seven isotropic compression tests were conducted, four tests for undisturbed specimens and three tests for reconstituted specimens. The reconstituted specimens were prepared as follows: slurry Shanghai soft clay was poured into a mold with diameter of 15cm and height of 16 cm, then applying different pressures for consolidation. The last pressures applied for consolidation was 70 kPa. Finally the pre-consolidation stress was released and the specimens were shaped for triaxial tests. The initial state, compression and swelling indices are summarized in Table 2.

Results of isotropic compression tests on undisturbed and reconstituted specimens are shown in FIG.1 in the e-log p plot, where e is void ratio and p is mean effective stress. It can be seen that the compression curves of undisturbed soil lie above those of corresponding reconstituted soils, which means that undisturbed specimens have larger void ratio at the same confining pressure due to soil structure. The difference in void ratio

Table 1. Physical Properties of Shanghai Soft Clay

Sand(%), 0.074~2mm	10.0	**Natural Water Content w_n (%)**	42.2~46.0
Silt(%), 0.005~0.074mm	63.4	**Liquid Limit, w_l(%)**	44.5
Clay(%),<0.005 mm	26.6	**Plastic Limit, w_p(%)**	22.4
Specific Gravity (g/cm^3)	2.70	**Plastic Index I_p**	22.1

Table 2. Initial State, Compression and Swelling Indices

No.	Specimen	Initial Water Content (%)	Void Ratio	Compression Index C_c	Swelling Index C_s
1	Undisturbed	42.2	1.138	0.322	0.054
2	Undisturbed	46.4	1.252	0.320	0.059
3	Undisturbed	45.6	1.231	0.310	No
4	Undisturbed	44.0	1.189	0.307	0.055
5	Reconstituted	37.4	1.010	0.255	0.052
6	Reconstituted	36.6	0.989	0.264	0.047
7	Reconstituted	36.0	0.973	0.261	No

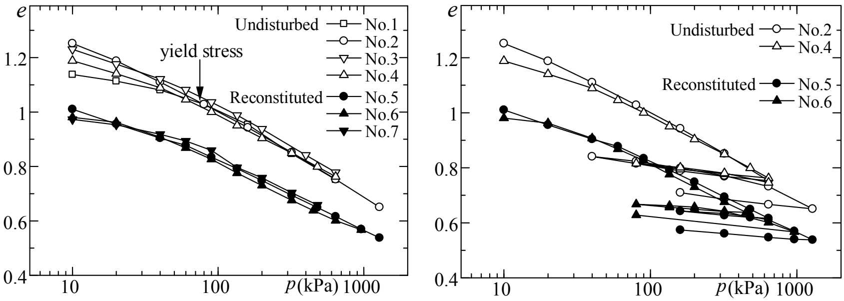

(a) Compression curves **(b) Compression and swelling curves**

FIG. 1. Isotropic compression and swelling curves.

of undisturbed and reconstituted states is about 0.2 at mean stress p= 10kPa. It can be imaged from FIG. 1 that the void ratio of two types of specimens is almost the same at a small enough mean stress. With increasing the stress, the void ratio difference between undisturbed and reconstituted specimens decreases gradually, which means that the soil structure of undisturbed soil destructed gradually and the effect of soil structure on the mechanical behavior is weakening. Also, it can be seen that the initial void ratio of reconstituted specimens is almost the same, but the initial void ratio of undisturbed specimens varies form 1.14 to 1.25, that's because undisturbed specimens were disturbed in different degree during the courses of sampling, transportation, storage and testing.

The compression curves of reconstituted Shanghai soft clay are straight lines, however, the compression curves of undisturbed specimens are constituted by two straight lines. The stress at the intersection point of two lines stands for the yield stress. The yield stress obtained from the tests data is about 80 kPa. The average values of compression index C_c and swelling index C_s are 0.320 and 0.056 for undisturbed specimens and those of reconstituted specimens are 0.260 and 0.049, respectively. Details of compression and swelling indices are shown in Table 2. Compared with undisturbed specimens, compression index C_c and swelling index C_s of reconstituted specimens are smaller about

23% and 14%, respectively.

It is noted that the yield point is not very obvious in FIG.2, which is due to disturbance during sampling with the fixed piston thick wall sampler and weathering, transporting, preparation of the specimen and testing, etc. The quality of used undisturbed samples is poor. If undisturbed samples with the high quality are obtained, the yield point becomes obviously and compression index will be larger.

SHEAR BEHAVIOR

To investigate the influence of soil structure on shear behavior of Shanghai soft clay, six triaxial consolidated-drained shear tests at constant confining pressure were performed, three for undisturbed specimens and three for reconstituted specimens. The initial states and confining pressure during shear are summarized in Table 3.

FIG.2 shows the results obtained from the shear tests on reconstituted specimens at different pressures in terms of σ_a / σ_r, ε_a, ε_v relations, where σ_a and σ_r are the axial and radial stresses, respectively; σ_a / σ_r is the principal stress ratio; ε_a and ε_v are the axial and volumetric strain, respectively. It can be seen from FIG.2 that the stress ratio-strain curves are the same at different confining pressures. It means that the stress ratio-strain curve is independent of the confining pressures, which is the same result predicted by the Cam-clay model. The critical state stress ratio M=1.36 can be obtained from the principal stress ratio σ_a / σ_r of 3.50 at critical state.

FIG.3 shows the comparison of the results obtained from the tests on undisturbed and reconstituted specimens. Because the stress ratio-strain curves of reconstituted specimens are the same, only the curve at confining pressure of 640 kPa is re-plotted in FIG.3. It can be seen that, at the same confining pressures, the stress ratio-strain and axial-volumetric strain curves of reconstituted specimens all lie above undisturbed specimens, which means that the reconstituted soil has higher strength and smaller volumetric strain, compared with those of undisturbed specimens. The stress ratio-strain curves of undisturbed specimens descend with increasing confining pressures, which means that the stress ratio-strain curves depend on the confining pressures. The stress ratio at failure is 3.25 for pressure 160 kPa but 2.85 for pressure 640 kPa, which is caused by the destruction of soil structure.

It is noted that the strength of undisturbed soil is lower than the reconstituted soil, which is similar with the results obtained by some researchers (Hong, et al., 2006; Graham & Li, 1985). However, there are some different results reported by other researchers. The different results from different researchers are not contradiction, for the strength of undisturbed soil not only depends on the structure, but also depends on void ratio during shear. The fact that the strength of undisturbed soils is lower than those of reconstituted soils is caused by the differences in void ratio, for the void ratio of undisturbed soils is much higher than the reconstituted soils.

Graham & Li (1985) plotted the test results in the plots of water content versus applied confining pressure and undrained shear strength. With the results, he reported that the

Table 3. Initial State of Specimens and Confining Pressure during Shear

No.	Specimen	Initial Water Content (%)	Void Ratio	Degree of Saturation (%)	Confining Pressure (kPa)
8	Undisturbed	44.40	1.199	96	160
9	Undisturbed	45.96	1.241	100	320
10	Undisturbed	44.00	1.188	100	640
11	Reconstituted	36.77	0.993	96	80
12	Reconstituted	36.37	0.982	100	200
13	Reconstituted	37.73	1.019	97	640

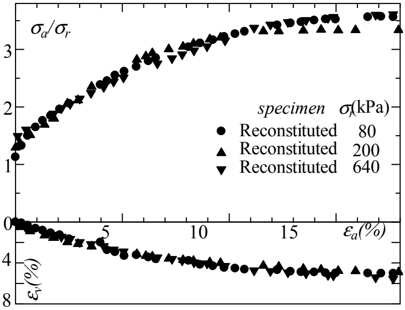

FIG. 2. Stress-strain curves of Reconstituted soils.

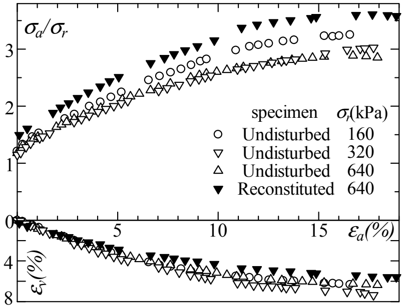

FIG. 3. Stress-strain curves of reconstituted and undisturbed soils.

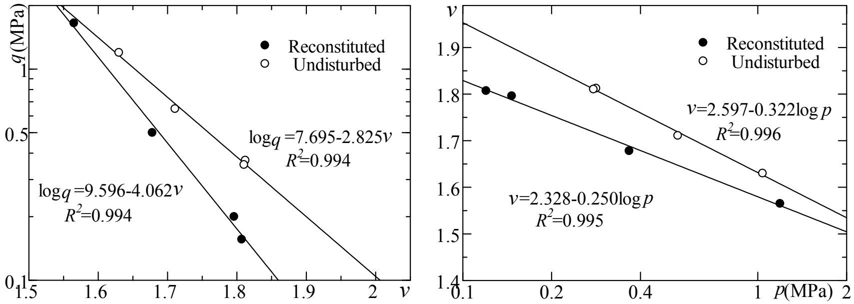

(a) *v* -log *q* curves **(b) *v*-log *p* curves**

FIG. 4. Critical state of reconstituted and undisturbed soils.

difference in strength between undisturbed and remolded states is caused by the difference in water content and remolded NCL(normal consolidation line) lies below the natural NCL is just in terms of specific volumes. In order to further investigate the strength behavior of undisturbed and reconstituted Shanghai soft clay. The test data is re-plotted in the plot of specific volume *v* (=1+*e*) versus corresponding drained deviator stress (*q*) and principal mean stress (*p*) at critical state, as shown in FIG.4 (a) and FIG.4(b), respectively.

The test data and fitting lines in Fig.4 show that the fitting lines correlate with the test data well. It can be imagined that, from FIG.4(a), with decreasing void ratio, two fitting lines will be intersect, which means that the strength of undisturbed and reconstituted soils is the same and the structure of undisturbed soils is completely damaged. It can be also seen that the strength line of reconstituted soils lies below the undisturbed soils, which means that at the same void ratio, the undisturbed soils have much higher strength than the reconstituted soils, which is caused by the structure. Hence, the strength of reconstituted soils is higher than undisturbed soils is due to difference in void ratio.

It can be imagined, from FIG.4(b), that two fitting lines will be intersect at enough large mean stress. It means that with the destruction of structure in undisturbed soils, the difference in void ratio between undisturbed and reconstituted soils decreases.

CONCLUSIONS

1. The compression curves of undisturbed soil lie above corresponding curve of reconstituted soils even the quality of undisturbed sample is poor. The void ratio of undisturbed specimens is about 0.2 larger than reconstituted specimens at mean effective stress *p*= 10kPa.
2. The stress ratio-strain curves of reconstituted samples are almost the same at different confining pressures, but it is not true for the undisturbed soil due to soil structure and the stress ratio is higher at low confining pressures.
3. The soil strength depends on both the structure and void ratio. It is possible that the strength of reconstituted soils is larger than that of undisturbed soils at the same confining pressure if the difference in void ratio between undisturbed and reconstituted soils is large enough. However, if they have the same void ratio, the strength of undisturbed specimens will be higher than reconstituted soils.

REFERENCES

Burland, J.B. (1990). "On the compressibility and shear strength of natural clay." *Geotechnique*, Vol. 40 (3): 329-378.

Graham, J. and Li, E.C.C. (1985). "Comparison of natural and remolded plastic clay." *J. of Geotechnical Engrg.,* Vol.111 (7): 865-881.

Hong, Z.S., Liu, S.Y., Shen, S.L., Negami T. (2006). "Comparison in undrained shear strength between undisturbed and remolded Ariake clays." *J. of Geotechnical & Geoenv. Engrg.,* Vol.132 (2): 272-275.

Nagaraj, T.S., Murthy, B.R.S., Vatsala, A., Joshi, R.C. (1990). "Analysis of compressibility of sensitive soils." *J. Geotechnical & Geoenv. Engrg.*, Vol. 116(1): 105-118.

Correlation Between Different Physical and Engineering Properties of Tropical Peat Soils from Sarawak

P.K. Kolay[1], M.R. Aminur[2], S.N.L. Taib[3], M.I.S. Mohd Zain[4]

[1]Assoc. Professor, [2]Master Student, [3]Senior Lecturer,[4]Assoc. Professor, Department of Civil Engg, University Malaysia Sarawak, 94300 Kota Samarahan, Sarawak, Malaysia; kkprabir@feng.unimas.my

ABSTRACT: The present paper describes the physical and engineering properties of tropical peat soils from Sarawak, Malaysia. Different physical properties such as organic content (OC), liquid limit (LL), fibre content (FC), specific gravity (G_s) and engineering properties (mainly the standard Proctor test) have been conducted on remoulded peat soil samples. The results show that, the value of LL, FC, Optimum Moisture Content (OMC) increases with an increase in OC. Also the results show that, G_s and MDD decrease with increasing values of OC. Furthermore, the plot of OC against G_s from the current study is compared with other researchers; whereby the correlation shows that R^2 values ranges from 0.71 to 0.95. This demonstrates that findings on local peat soils from Sarawak are in good agreement with other researchers as similar trends are observed. Consequently, geotechnical engineers can refer these correlations to comprehend the preliminary behavior of peat soil, where the geotechnical data are not readily available.

INTRODUCTION

Peat or highly organic soils are extreme soft and non-homogeneous. These soils are partly decomposed and fragmented remains of plants leaves, roots that have accumulated under water and fossilized. Normally the peat soils are formed in wetland bogs, moors, muskegs, mires, and peat swamp forests and they cover 5 to 8 % of the total land area of the Earths surfaces. Among them about 8 to 11 % are tropical peat soils which includes Indonesia, Malaysia, Brazil, Uganda, Zambia, Zambia, Venezuela, and Zaire (Mesri & Ajlouni, 2007). Malaysia covers approximately 2.7 million hectares of peat lands and out of that about 1.66 million hectares (i.e. 61%) are located in the deltas and coastal plains of Sarawak. Peat soils of Sarawak occupy 13% of the total land area and most of the year; these areas are waterlogged (Mutalib et al., 1991). Due to the high water level in this area, it is very difficult to determine the physical and geotechnical properties of peat soil. Edil (1994) emphasizes on characterizing peat and organic soils by certain index properties, to provide a basis for comparison of results of mechanical tests. Hobbs (1986) also suggested that it is convenient to relate the basic geotechnical properties of organic soils to some of the easily determined physical or index properties. Like the mineral soils, correlations between various index properties are also proved to be useful for peat soil.

Several researchers have tried to establish the relationship between index properties for different peat soils. Few researchers also evaluated the correlation between several parameters mainly physical and geotechnical properties for Netherland, USA, and Hungary peat soils (Skempton & Petley, 1970; Kakai & Farkas, 1988; Den Haan & El Amir, 1994). Very little data or correlations are available in Malaysia. Hence, the present study concentrates on the physical and geotechnical properties of peat soil from Sarawak and tries to establish the correlation between them, which will be useful for the geotechnical engineers. As a result, geotechnical engineers can refer to these correlations to comprehend the preliminary behavior of peat soil, where the geotechnical data are not readily available.

TEST MATERIALS AND METHODS

In this study, peat soil samples were collected from six different locations of Sarawak in Matang area (from 0.40-0.80 m depth) designated as M1 to M6. First the peat soil samples were sundried, grinded and passed through specific sieve and used for specific physical and engineering properties. The physical properties of peat soil samples were determined as per ASTM or BS as mentioned in Table 1. The organic content (OC) is calculated according to an equation proposed by Skempton & Petley (1970). The standard Proctor test has been conducted as per BS 1377: Part 4, 1990.

RESULTS AND DISCUSSION

Physical and Engineering properties

The results of different physical and engineering properties of the peat soil samples are presented in Table 1. From Table 1, it has been observed that sample M3 falls in the category with degree of humification H3 (Sapric), sample M4 can be categorized as H7 (Fibric) and other samples are H4 to H6 (Hemic) according to the Von Post (1922) scale. The OC of all the soil samples (except M1 and M4) are more than 75%, hence, it can be termed as peat soil according to ASTM D 2607-69 (1990). The result also shows that soil sample M3 has higher FC than the other soil samples except for sample M6. The G_s value for the sample M4 is higher as compared to the other samples. This may be attributed to the fact that sample M4 has a lower FC as compared to the other samples. The LL value is highest for sample M3 as this sample contains more FC and as a result it has high water absorption capacity as compared to the other samples. The standard Proctor tests were carried out for all peat soil samples to find out the compaction characteristics and the results are plotted in Fig.1. From Fig. 1, it can be noticed that soil sample M4 has Maximum Dry Density (MDD) of 8.67 kN/m^3 and the value of Optimum Moisture Content (OMC) is 54.90%. This may be attributed to the fact that sample M4 has lower FC, hence, the water absorption capacity is lower as compared to the other samples.

Table 1. Physical and Engineering properties of peat soil from Matang, Sarawak

Properties and methods		Sample					
		M1	M2	M3	M4	M5	M6
Natural Moisture Content (%), (BS1377: Part 2, 1990)		360.72	623.76	620.14	605.63	473.70	787.04
Degree of Decomposition (Von Post, 1922)		H6	H4	H3	H7	H5	H4
Loss on Ignition (N) (%), (ASTM D 2974, 2000)		67.88	81.59	85.67	44.74	79.70	83.08
Organic Content (OC) (%), (Skempton & Petley, 1970)		66.60	80.85	85.10	42.53	78.88	82.40
Specific Gravity, (G_s), (BS1377: Part 2, 1990)		1.64	1.56	1.45	1.82	1.62	1.48
Fiber Content (%), (ASTM D1997-91, 1996)		61.40	63.55	65	31.98	63.45	67.25
Liquid Limit (LL) (%), (BS1377: Part 2,1990)		73	77	78	69	79	75
Standard Proctor test, (BS1377: Part 4, 1990.)	MDD (kN/m^3)	8.11	7.20	7.06	8.67	7.26	7.17
	OMC (%)	56.10	60.64	65.36	54.95	62.84	60.25

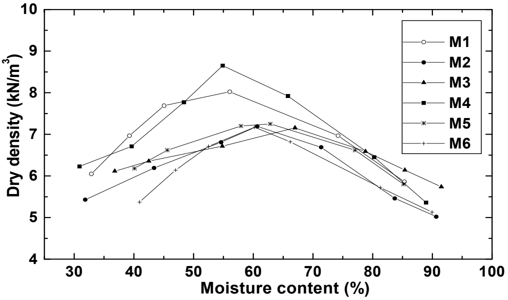

FIG. 1. Standard Proctor test for different peat soil samples.

Correlation between physical and engineering properties

The correlation between different physical and engineering properties were established and presented in this section. From Fig. 2 it can be observed that with an increase of LL and OMC, the value of MDD decreases. The correlations between them are presented in Equations 1 and 2 and the correlation shows that the R^2 values are 0.85 and 0.80, respectively. From Fig. 3 it can be observed that the value of LL, FC and OMC increase with an increase in OC.

$$LL = -50.737\ MDD + 114.38 \quad (1)$$

$$OMC = -52.53\ MDD + 100.62 \quad (2)$$

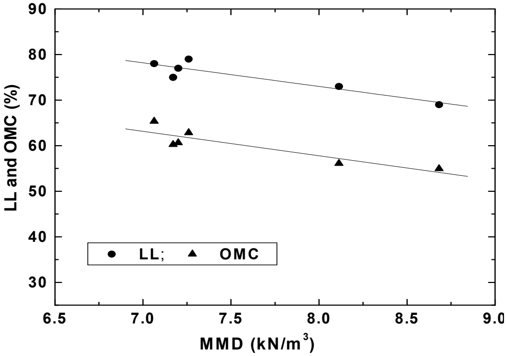

FIG. 2. Variation of LL and OMC versus MDD.

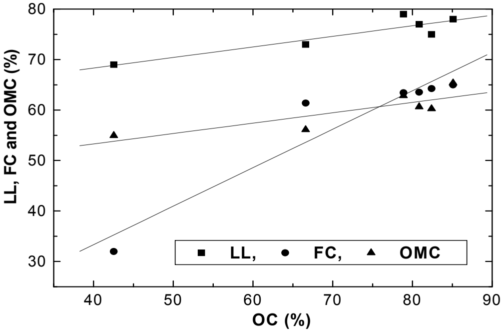

FIG. 3. Variation of LL, FC and OMC versus OC.

The correlations between them were established and represented in Equations 3, 4 and 5. Also the correlation shows that the R^2 values are 0.90, 0.82 and 0.71, respectively which are reasonably good.

$$FC = 0.762\ OC + 2.8509 \quad (3)$$
$$LL = 0.2088\ OC + 59.982 \quad (4)$$
$$OMC = 0.206\ OC + 45.04 \quad (5)$$

The relationship between MMD and OC is presented in Fig. 4 and the relationship between G_s and OC of previous studies and present study are shown in Fig. 5. Figs. 4 and 5 show that, with the increase of OC, there is a decrease of MDD and G_s. The correlation shows that the R^2 values (ranges between 0.95 and 0.89) are rather in good agreement for the peat soil and the trend is almost parallel with the previous studies (Skempton & Petley, 1970; Kaniraj & Joseph, 1996; Den Haan, 1997; Youventharan et al., 2007). The correlations among them are presented in Equations 6 and 7.

$$MDD = -0.0041\ OC + 1.0691 \quad (6)$$
$$G_s = -0.0078\ OC + 2.1605 \quad (7)$$

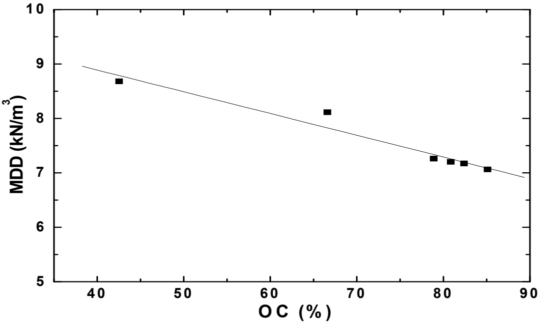

FIG. 4. Variation of MDD versus OC.

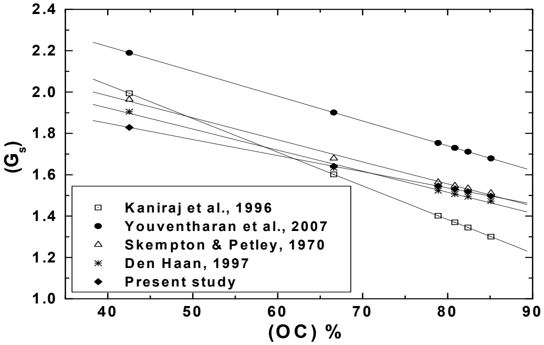

FIG. 5. Variation of G_s versus OC for present study and other researchers.

CONCLUSIONS

From the various laboratory test results obtained, the following generalized conclusions can be made:

- With an increase of FC, the value of G_s decreases while the values of G_s increase with a reduction in the loss on ignition (N).
- With an increase in the maximum dry density (MDD), the values of FC and OC decrease.
- From the correlation it can be concluded that, with the increase of LL and OMC, the value of MDD decreases. The correlation shows that the R^2 values are 0.85 and 0.80, respectively.
- With an increase in OC; the values of LL, FC and OMC also increase. Also the correlation shows that the R^2 values are 0.90, 0.82 and 0.71, which are also quite satisfactory.
- As the value of OC increases, values of MDD and G_s decrease. From the correlation, it can be observed that the R^2 values are 0.95 and 0.89 which are quite good and the trend is almost parallel with the previous studies.

The correlations between physical and engineering properties shows that the R^2 values (ranges from 0.71 to 0.95) are quite in good agreement for the peat soil and these correlations can be used by geotechnical engineers where the geotechnical data is not readily available.

REFERENCES

ASTM D 2607-69 (1990). “Classification of peats, mosses, humus, and related products”. *Annual Book of ASTM Standards,* Philadelphia, USA.

ASTM D 2974 (2000). “Standard test method for moisture, ash, and organic matter of peat and other organic soils”. *Book of ASTM Standards,* Philadelphia, USA.

ASTM D1997-91 (1996). “Standard test method for laboratory determination of the fiber content of peat samples by dry mass”. *Annual Book of ASTM Standards,* Philadelphia, USA.

BS 1377, Part 1–4 (1990). “Soils for civil engineering purposes”. *British Standards Institution.* London. UK.

Den Haan, E.J. (1997). “An overview of the mechanical behaviour of peat and organic soils and some appropriate construction techniques”. *In Proceedings on recent Advances in Soft Soil Engineering,* Kuching Sarawak, Ed. Huat et al., 17-45.

Den Haan, E.J. and El Amir, L.S.F. (1994). “A simple formula for final settlement of surface loads on peat”. *Proc. on Advances in Understanding and Modeling the Mechanical behaviour of peat*, Ed. Den Haan et al., Balkema. 35-48.

Edil, T.B. (1994). “Immediate issues in engineering practice”. *Proc. on Advances in Understanding and Modeling the Mechanical behaviour of peat*, Ed. Den Haan et al., Balkema, 403-444.

Hobbs, N.B. (1986). “Morphology and the properties and behaviour of some British and foreign peats”. *Quarterly J. of Engineering Geology.* Vol. 19: 7-80.

Kakai, J. and Farkas, J. (1988). “Strength and deformation tests of Hungarian peats. *Proc. 2nd Baltic CSMFE, Tallinn,* 48-54.

Kaniraj, S. R. and Joseph, R.R. (1996). “Geotechnical behavior of organic soils of North Sarawak”. *4th Int. Conference on Soft Soil Engineering,* Vancouver Canada.

Mesri, G., and Ajlouni, M., (2007). “Engineering properties of fibrous peats”. Journal of geotechnical and geoenvironmental engineering, *ASCE.* Vol. 133(7): 850-866.

Mutalib, A.A., Lim, J.S., Wong, M.H. and Koonvai, L. (1991). “Characterization, distribution and utilization of peat in malaysia, tropical peat”, *In Proceeding of the International symposium on Tropical Peatland,* Kuching, Malaysia, 7-16.

Skempton, A. W. and Petley, D. J. (1970). “Ignition loss and other properties of peats and clays from Avonmouth, King’s Lynn and Cranberry Moss”. *Geotechnique,* Vol. 20 (4): 343-356.

Von Post, L. (1922). “Sveriges Geologiska Undersøknings torvinventering och nogra av dess hittils vunna resultat (SGU peat inventory and some preliminary results”. *Svenska Mosskulturføreningens Tidsskrift, Jønkøping, Sweden 36.*

Youventharan, D., Huat, B. B.K. and Azlan, A. A. (2007). “Engineering properties and compressibility behavior of tropical peat soil”. *American Journal of Applied Sciences,* Vol. 4 (10): 768-773.

Comparison of Laboratory and Field Moduli of Compacted Geo-materials

Deren Yuan[1], Manuel Celaya[2] and Soheil Nazarian[3], M ASCE

[1]Research Specialist, the University of Texas at El Paso, dyuan@utep.edu
[2]Research Specialist, the University of Texas at El Paso, mcelaya@utep.edu
[3]Professor, the University of Texas at El Paso, nazarian@utep.edu

ABSTRACT: The moduli of compacted geo-materials are estimated in the laboratory or in the field. Laboratory tests are essential to obtain the parameters that affect the behavior of the materials. Field tests, especially nondestructive field tests, are more practical and desirable because they are rapid to perform, and because they test a volume of material in its natural state. Empirical relations between the resilient modulus and the modulus from in-situ test are sometimes used in the preliminary stages of design and planning. Unlike in situ methods, these relations do not take into account the site-dependent variation in material properties.

This paper represents an alternative process based on seismic nondestructive testing technology for relating the results from laboratory and field moduli from a number of chemically or mechanically stabilized geo-materials. Attention is also paid to understanding of the results from seismic tests and incorporating them in the existing design methods, specifications and common practices.

INTRODUCTION

Elastic modulus or modulus of elasticity (sometimes called Young's modulus) is one of the major parameters to qualify the elastic property of a stabilized and/or compacted material. Almost all materials are elastic to some degree as long as the applied loads do not cause them to deform permanently.

Resilient modulus test has been used for a long time to measure the representative moduli and to evaluate the nonlinear behaviors of bases and subgrades. In this test, repeated axial cyclic stresses of fixed magnitude and duration are applied to cylindrical test specimens while they are subjected to a series of confining pressures. The resilient (recoverable) axial deformations of the specimens are measured and used to calculate their resilient moduli. As a primary parameter, resilient modulus has been used by many highway agencies in their pavement design procedures.

There are disadvantages and limitations to the practical use of resilient modulus. The resilient modulus test is time consuming and requires skilled operators. More importantly, since the resilient moduli cannot be directly measured in the field, they are typically estimated using in-situ tests such as the Falling Weight Deflectometer

(FWD) or Dynamic Cone Penetrometer (DCP) tests. Many investigators have tried to develop relationships between the laboratory and these field moduli (Daleiden et al., 1994; Richter and Schwartz, 2003; Mohammad et al., 2007). In general, reasonably well-defined relationships cannot be developed between the laboratory and field moduli, especially for base materials.

Elastic wave or seismic-based nondestructive testing (NDT) methods for estimating the modulus of compacted base and subgrade materials in the laboratory and in the filed have been used for some time (Nazarian et al., 2002). Seismic methods are particularly attractive since they are the only methods that yield the same parameters (low-strain or seismic moduli) in the laboratory and field through simple analytical relationships.

This paper represents an alternative process for relating the results of laboratory and field modulus tests from a number of chemically or mechanically stabilized geo-materials. Attention is also paid to understanding of the results from seismic tests and incorporating them in the existing design methods, specifications and common practices.

METHODS, PRINCIPLES AND DEVICES

Laboratory Test

In the laboratory, the modulus of a compacted material is obtained from the free-free Resonant Column (FFRC) test on a cylindrical specimen. This method was originally introduced for estimating modulus of concrete (ASTM C-215). The principle of the FFRC method is based on the measurement of the fundamental resonant frequency of longitudinal vibration of a specimen when the specimen is subjected to an impulse load at its one end (see FIG 1). From the longitudinal resonant frequency, the laboratory modulus of a specimen can be calculated by:

$$E_{lab} = \rho \, (2 \, f_L \, L)^2 \qquad (1)$$

where f_L is the resonant frequency, and ρ and L is the mass density and length of the specimen, respectively. Since $2f_LL$ equals the P-wave velocity, E_{Lab} is formally called the P-wave or longitudinal modulus in linear elasticity (Mavko et al., 2003).

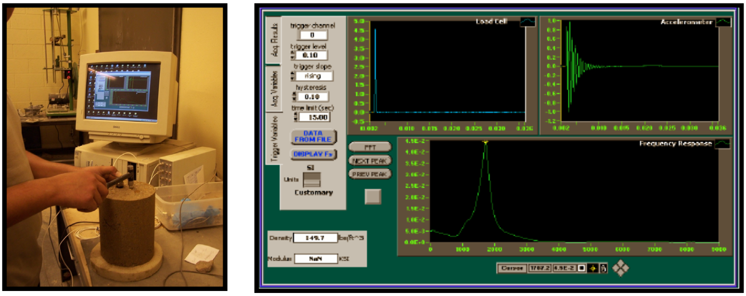

trigger channel 0
trigger level 0.10
trigger slope rising
hysteresis 0.10
time limit (sec) 15.00
Density 149.7 lbs/ft^3
Modulus NaN KSI
Cursor 1767.2 4.5E-2

a) FFRC Test Setup b) Records from a FFRC Test

FIG 1 - FFRC Test

Field Test

FIG 2 - PSPA

In the field, the modulus of a compacted geo-material is determined with a Portable Seismic Property Analyzer (PSPA). The PSPA consists of an impact source and two receivers packaged into a hand-portable unit that is operated by a computer (see FIG 2). The analysis of data collected with the PSPA is automatically conducted in the frequency-domain via the ultrasonic surface waves (USW) method. The USW method is based on the generation and detection of seismic surface (Rayleigh type) waves and is an offshoot of the spectral analysis of surface waves (SASW) method (Nazarian et al., 1993). In the USW method the average modulus of a compacted layer or to a specified depth, E_{Field}, can be directly calculated from:

$$E_{Field} = 2\,\rho\,[(1.13 - 0.16\nu)\,V_R]^2\,(1 + \nu). \tag{2}$$

where V_R is the measured average surface-wave velocity and $\nu$is the Poisson's ratio of the compacted material. For a giving material, Poisson's ratio can be assumed based on the documented values without introducing significant (a few percent) error.

Relationship of E_{Lab} and E_{Field}

For a given material with the same levels of moisture content, compaction and curing, the modulus, E_{Field}**,** can be related to the longitudinal modulus, E_{Lab}, as follows (Mavko et al., 2003):

$$E_{Field}/E_{Lab} = (1 + \nu)\,(1 - 2\nu)\,/\,(1 - \nu) \tag{3}$$

Unlike Equation 2, Poisson's ratio has a significant impact on the ratio, E_{Field}/E_{Lab}, in Equation 3. For instance, when Poisson's ratios are 0.2, 0.3 and 0.4, E_{Field}/E_{Lab} will be 0.90, 0.74 and 0.47, respectively.

REPRESENTATION OF RESULTS

The results from a number of projects are compared to demonstrate the relationship between the moduli obtained in the laboratory and in the field. The materials used in the laboratory were collected at several locations from each project. All field tests were performed on top of each layer during its construction.

Subgrade Materials

Two subgrade projects are introduced. One project consisted of an untreated section and a section of the same subgrade treated with 3% lime slurry. Another subgrade was constructed with 6% lime slurry to improve the plasticity index, strength and modulus of the original soil. The average laboratory and field moduli from these three sites are shown in FIG 3. For an assumed Poison's ratio of 0.35, E_{Field} /E_{Lab} of 0.62 is anticipated. . The ratios from actual tests are 0.67, 0.64 and 0.68 for different lime contents, which are close to the theoretical one, independent of the lime content.

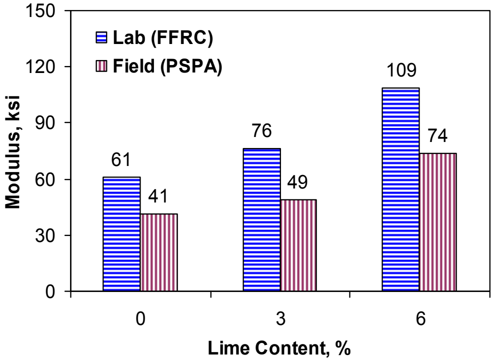

FIG 3 – Comparison of Subgrade Moduli Moduli

Base Materials

Four base materials from different full depth reclamation (FDR) projects were also studied. The mix designs for the four bases are summarized in Table 1. The results from the laboratory and field tests are shown in FIG 4. For simplicity, a Poison's ratio of 0.3 was assumed for all cases, which results in a theoretical E_{Field} /E_{Lab} of 0.74. In the order shown in Table 1, E_{Field} /E_{Lab} values from actual tests are 0.68, 0.66, 0.65 and 0.72. With an average of 0.68, these ratios are somewhat smaller than the theoretical one. The narrow range of ratios from the four mixes indicates that E_{Field} /E_{Lab} may be considered independent of mix portion, type of mix material and type and amount of additives.

Table 1 – Mix Designs of Chemical Treated Bases

Project	Material	Water Content	Additive
1	100% existing base	7.5%	2% cement
2	1/3 existing RAP, 1/3 existing base and 1/3 additional RAP	6.2%	1% cement + 4% asphalt emulsion
3	80% existing RAP and 20% existing base	5.2%	3% fly ash + 6% asphalt emulsion
4	30% existing RAP, 50% existing base and 20% add-rock	9.3%	7% fly ash

SEISMIC MODULUS AND RESILIENT MODULUS

Williams and Nazarian (2007) proposed a process to estimate the resilient moduli of unbound bases and subgrades from their laboratory seismic moduli. They indicated that since the resilient modulus test is a load-controlled test (i.e., at any confining pressure, a certain deviatoric stress is applied to the specimen irrespective of its stiffness), the strain experienced by a softer specimen at a given deviatoric stress is much higher than that of a stiffer specimen. The implication of this statement is that under current resilient modulus loading sequence, the softer material may always betested in the nonlinear range; whereas a very stiff (e. g., stabilized) material may always be tested in the linear range. To overcome this limitation, they modified the stress regimes applied to the specimen in the resilient modulus tests to obtain the unconfined low-strain resilient modulus (resilient modulus at zero confining pressure and at axial stresses corresponding to strains of less than 100 μstrain). Based on tests on about thirty specimens, they proposed that the unconfined low-strain resilient moduli are roughly half the seismic moduli. This relationship seemed to be independent of the type of the material used.

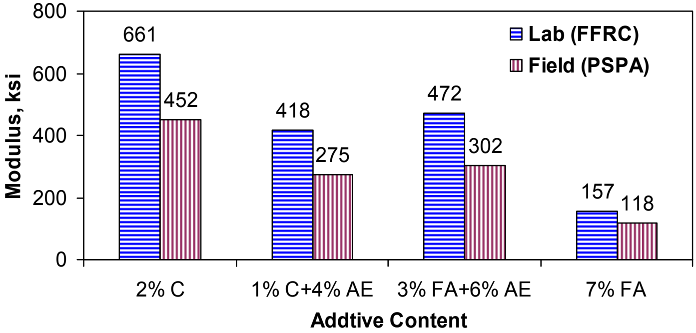

FIG. 4 – Comparison of Base Moduli

The ratios of lab seismic modulus (E_{Lab}) and low-strain unconfined resilient modulus (E_R) from laboratory tests on the stabilized base materials are shown in Table 2. The average resilient modulus to seismic modulus ratio of 0.5 obtained from this study is similar to that provided by Williams and Nazarian for untreated subgrades and bases.

Table 2 – Comparison of Seismic Modulus and Resilient Modulus

Mix	Seismic Modulus (FFRC), ksi	Resilient Modulus, ksi	E_R / E_{Seis}
1	595	345	0.58
2	546	242	0.44
3	656	375	0.57
4	418	175	0.42
Average			0.50

Since the stabilized materials generally experience stresses that are in the linear range, one can preliminarily conclude that the traditional resilient modulus of a stabilized material is about 70% of the field seismic modulus or 50% of the lab seismic modulus.

For unbound granular materials and subgrades, it is difficult to generalize the relationship between the field seismic modulus and lab resilient modulus because they often experience nonlinearity. The procedure recommended by Williams and Nazarian can be used to consider that nonlinearity.

CONCLUSIONS

Seismic NDT methods are a rapid, economic and relatively accurate means for characterization of pavement layers. Great potentials exist by using these methods in pavement design and quality control/quality assurance. To properly use the correlation between the moduli from laboratory and field tests, Poisson's ratio is a key factor.

ACKNOWLEDGMENTS

The work presented in this paper was supported by the Texas Department of Transportation.

REFERENCES

Daleiden, J. F., Killingsworth, B. M., Simpson, A. L. and Zamora, R. A. (1994). "Analysis of Procedures for Establishing In situ Subgrade Moduli." *Transportation Research Record*, 1462: 102-107, Washington, D.C.

Mavko, G., Mukerji, T., J. and Dvorkin, J. (2003). The Rock Physics Handbook, Cambridge University Press.

Mohammad, L. N., Gaspard, K., Herath, A. and Nazzal, M. (2007). "Comparative Evaluation of Subgrade Resilient Modulus from Non-destructive, In-situ, and Laboratory Methods", FHWA/LA.06/417, Louisiana Transportation Research Center, Baton Rouge, LA.

Nazarian, S., Baker, M. R. and Crain, K. (1993). "Fabrication and Testing of a Seismic Pavement Analyzer", Report H-375, Strategic Highway Research Program, Washington, D. C.

Nazarian, S., Yuan, D. and Arellano, M. (2002). "Quality Management of Base and Subgrade Materials with Seismic Methods", *Transportation Research Record*, 1786: 3-10, Washington, D. C.

Richter, C. A. and Schwartz, C. W. (2003). "Modeling Stress- and Moisture-induced Variations in Pavement Layer Moduli", *Transportation Research Record*, 1860: 33-40, Washington, D. C.

Williams, R, R, and Nazarian, S. (2007). "Correlation of Resilient and Seismic Modulus Test Results", *Journal of Materials in Civil Engineering*, Vol. 19 (12): 1026-1032.

Characterization of Compacted Loess by Electrical Resistivity Method

Fusheng Zha[1,2], Songyu Liu[3], Yanjun Du[4], Kerui Cui[5], Long Xu[6]

[1] PhD, School of resources and Environment Engineering, Hefei University of Technology, Hefei, 230009, P.R.China; Email: zhafusheng@163.com
[2] PhD, Institute of geotechnical engineering, southeast university, Nanjing, 210096, , P.R.China; Email: zhafusheng@163.com
[3] Professor, PhD, Institute of Geotechnical Engineering, Southeast University, 210096, P.R.China; Email: liusy@seu.edu.cn
[4] Professor, PhD, Institute of Geotechnical Engineering, Southeast University, 210096, P.R.China; Email: yanjundu@gmail.com
[5] Professor, PhD, School of resources and Environment Engineering, Hefei University of Technology, Hefei, 230009, P.R.China; Email: cuikerui001@163.com
[6] Graduate student, School of resources and Environment Engineering, Hefei University of Technology, Hefei, 230009, P.R.China; Email: xulong20051255@yahoo.com.cn

ABSTRACT: Loess, a wind-blown cemented silt deposit, covers extensive areas of northwest and northern central of China, and is used in most geotechnical constructions including embankments and liners. The purpose of this study is to evaluate the potential application of resistivity measurements for monitoring and assessing the quality of compacted loess soils. The relationships between soil resistivity, water content, pore fluid chemical components, degree of saturation and temperature have been studied based on the measurement of the resistivity of the compacted loess sample. Test results show that soil resistivity decreases with the increase in temperature, water content, degree of saturation and porosity. The higher conductivity of pore fluid, the lower soil resistivity.

INTRODUCTION

Loess, a wind-blown cemented silt deposit, covers extensive areas of northwest and north-central of China and is used in most geotechnical constructions, including embankments and liners in these areas (Li et al. 2001). In China, the application of static and dynamic compaction procedures to improve the shear strength, permeability, and deformation behavior of loess is a very common practice. Typical earthworks in geotechnical engineering that require the compaction of loess include: the construction of liners for solid waste disposal, embankments for roads and railroads, and the improvement of natural deposits for the emplacement of shallow foundations for light weight structures. Therefore, it is important to assess the geotechnical properties of the compacted loess.

The non-intrusive geophysical exploration methods have been applied to soil sciences for a considerable period. Among such methods, an electrical resistivity survey method seems particularly promising, which can be conducted sensitively, rapidly and nondestructively (Corwin and Lesch, 2005). Recent studies show that soil electrical resistivity depends on various factors, including porosity, pore fluid chemistry, water content, composition of solids, degree of saturation, particle shape and orientation and temperature(Zha, 2007). In practice, the geotechnical properties of compacted soils are determined on these same parameters. To assess a compacted soil with an electrical resistivity method, one must know how compaction conditions and compositional changes affect the electrical resistivity of the soil and how other factors, such as anomalies, lift interfaces, and the boundaries of the liner, affect the results of an electrical resistivity method (Abu-Hassanein et al. 1996).

The purpose of this study is to study on the electrical resistivity of compacted loessal soils, and to evaluate the potential application of resistivity method for assessing the geotechnical properties of compacted loessal soils. To achieve this, a series of laboratory test results are presented, the relationships between soil resistivity, water content, pore fluid chemical components, degree of saturation, porosity, pore structure, composition of the solids and temperature have been studied based on the measurement of the resistivity of the compacted loess samples. Factors controlling the soil electrical resistivity are discussed.

MATERIALS AND TEST METHODS

Electrical resistivity measurement: An apparatus named ESEU-1 soil electrical resistivity equipment is used for measuring vertical or horizontal electrical resistivity of the compacted loess samples. The validity of this apparatus in soil resistivity measurement has been examined (Liu et al. 2006). The circuit diagram of ESEU-1is shown in Fig.1.

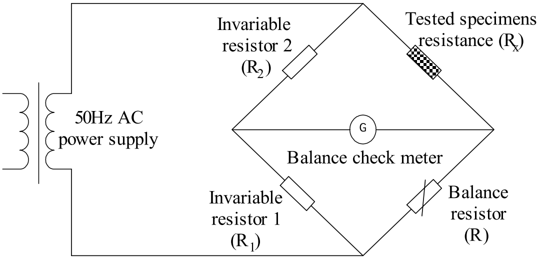

FIG. 1 The circuit diagram of ESEU-1

Compaction method: The compacted specimens were prepared according to the standard Proctor procedure, Chinese standard for soil testing in highway engineering (JTJ051-93). The procedure is almost the same with the ASTM (1993), with a compaction effort of 598.2kJ/m^3.

Loess: The loess tested in this study was sampled at a depth of 4.5-5 m from the village of Qianjing garden in Xi'an City, Shanxi Province of China. The soil is a sticky plastic soil with a yellow brown color. Physical properties of the tested loess are summarized in Table 1. The soil is classified as a ML-CL based on the plasticity chart (ASTM D2478).

Table 1 Physical properties of tested loess

Natural water content (%)	Density (g/cm3)	Liquid limit (%)	Plastic limit (%)	Optimum water content (%)
22.4	1.55	35.2	21.4	16.8
Maximum dry unit weight (g/cm3)	**Specific gravity**	**Porosity**	**Degree of saturation (%)**	**Soil classification**
1.80	2.72	0.53	53.1	ML-CL

Note: ML= silt with low liquid limit; and CL= clay with low liquid limit.

RESULTS AND ANALYSIS

Effects of temperature on soil electrical resistivity: Temperature affects the electrical resistivity of soil. Increasing the temperature, decreases the electrical resistivity of soil. Keller and Frischknecht (1966) report that the electrical resistivity of soil (ρ_T) at a temperature (T) can be related to a standard electrical resistivity measured at 18 $^{\circ}C$ (ρ_{18}) by

$$\rho_T = \frac{\rho_{18}}{1+\alpha(T-18)} \tag{1}$$

$$\text{or } \sigma_T = \sigma_{18} + \alpha \cdot \sigma_{18} \cdot (T-18) \tag{2}$$

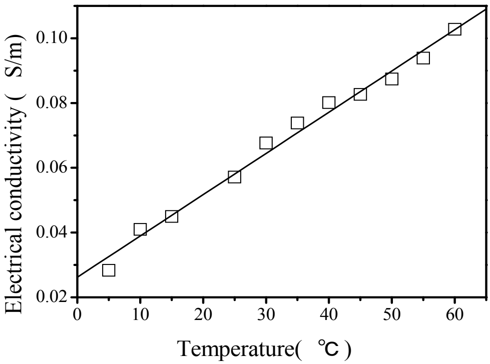

FIG. 2 Relationship between conductivity and temperature

where α = an experimental parameter that is approximately 0.025 $^{\circ}C^{-1}$, σ_T = the electrical conductivity of soil at temperature T, σ_{18} = the electrical conductivity of soil at temperature 18 $^{\circ}C$.

Fig.2 shows the variation of electrical conductivity of the tested loess with temperature. It is clear that soil electrical conductivity increased with the increase in temperature. The reason can be explained as follows: 1) the viscosity of the pore fluid in soil decreases with increasing temperature, and thereby soil electrical resistivity decreases; and 2) temperature rise increases the pore water polarization and pore water electrical conductivity, and thereby decreases soil electrical resistivity.

The experimental parameter α can be computed via Eq.(1), for the tested Xi'an undisturbed loess specimen, α=0.026 $^{\circ}C^{-1}$. In this study, all of the measured electrical resistivity are normalized based on the temperature of 18 $^{\circ}C$ using Eq.(1).

Effects of water content and pore fluid chemistry on soil electrical resistivity: Relationships between the soil electrical resistivity, water content, and pore fluid chemistry are shown in Fig.3. It is clear that at relatively low water content, the soil resistivity decreased rapidly with increasing the soil water content. However, when the water content exceeds the optimum water content, which is about 16.2%, the electrical resistivity decreased little although water content increased. The reason for this phenomenon can be explained as that at lower water content, the continuity of pore fluid channels improves with the increasing water content. Therefore, the electrical conduction of pore fluid was enhanced, resulting in the rapid decrease of the bulk electrical resistivity. This phenomenon, on the other hand, implies that the effect of soil microstructure on soil electrical resistivity. When water content exceeds the optimum water content, saturation degree of soils is relatively high, and the continuity of pore fluid channels already reached a satisfactory level. Hence the effect of water content on soil resistivity becomes insignificant.

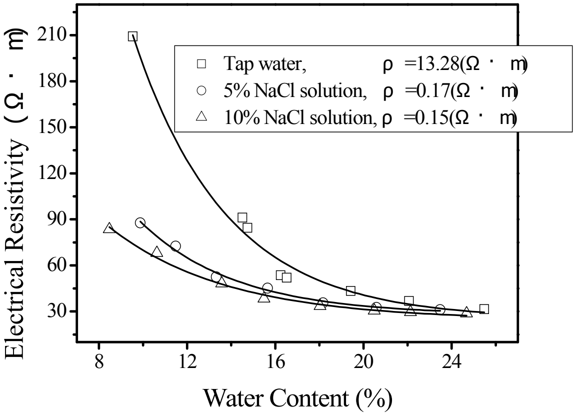

FIG.3 Effect of water content and pore water chemistry composition on electrical resistivity for compacted loess

The electrical resistivity of soil is also affected by the pore fluid chemistry (Abu-Hassanein et al. 1996). To investigate the effects of the pore fluid chemistry on the electrical resistivity of compacted loess, the mixed tap water, NaCl solution with the concentration of 5% and 10% were used. The test results are shown in Fig.3. It can be seen that the influence of the pore fluid chemistry on soil bulk resistivity is significant. The soil electrical resistivity decreased with decreasing resistivity of pore fluid. As soon as other conditions (e.g., water content, porosity, temperature) be equal, the lower electrical resistivity of pore fluid, the higher electrical conductance of pore fluid, the lower soil electrical resistivity.

Effects of degree of saturation on soil electrical resistivity: Soil electrical resistivity also depends on degree of saturation. There are three pathways of current flow contribute to the electrical conductivity of a soil: (i) a liquid phase pathway, (ii) a solid–liquid phase pathway primarily, and (iii) a solid pathway via soil particles that are in direct and continuous contact with one another. A compacted soil sample with higher degree of saturation generally results in more pronounced bridging between soil particle surfaces, and greater particle-to particle contact (Abu-Hassanein et al. 1996). Thus, a increase in degree of saturation not only reflects a increase in the volume of pores filled with water, but also increase particle-to-particle contact. The ultimate result is that increasing saturation degree results in a reduction in soil electrical resistivity.

The relationship between electrical resistivity of unsaturated soil and degree of saturation can be described as follows:

$$\rho = \rho_{sat} S_r^{-B} \tag{3}$$

where ρ =electrical resistivity of unsaturated soil; ρ_{sat} =electrical resistivity of the saturated soil; S_r =degree of saturation; B = an empirical parameter.

Fig.4 shows that the relationship between degree of saturation and electrical

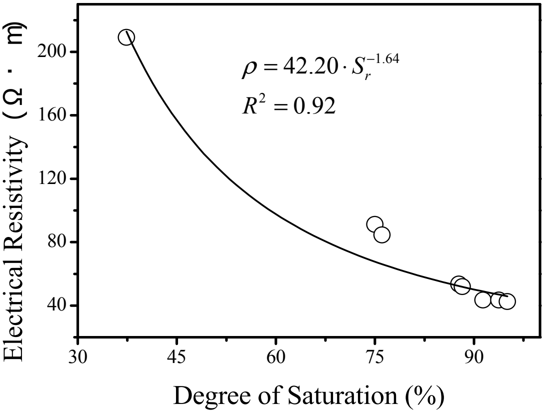

FIG.4 Relationship between resistivity and saturation for compacted soils

resistivity for the tested loess. It is clear that low resistivity occurs at higher degree of saturation. The model presented in Eq.(3) was fitted to experimental data. The results are shown in Fig.4. For the tested loess, ρ_{sat}=42.20 Ω • m，B=.64, and R^2=0.92 (describes how good is the fit).

CONCLUSIONS

The following conclusions can be drawn ρ_{sat} based on this experimental study.

1) Soil electrical resistivity decreases with the increase of water content. At lower water content, soil resistivity decreases rapidly with increasing water content. However, when the water content exceeds optimum water content, the effect of water content on the soil resistivity is insignificant.
2) Soil electrical resistivity decreases with the decrease in electrical resistivity of pore fluid.
3) Electrical conductivity increases with the increase in temperature. For the undisturbed Xi'an loess, the experimental parameter α=0.026 $^{\circ}C^{-1}$.
4) Soil electrical resistivity decreases with the increase in degree of saturation.

ACKNOWLEDGMENTS

Financial support of Natural Science Foundation of China (NSFC) (No. 40802079, 50478073, 50878052, 40972173) is gratefully acknowledged. The experimental study was performed in Southeast University, China. Special thanks are given to Prof. Liu Songyu and Prof. Du Yanjun, Institute of Geotechnical Engineering, Southeast University, for their supervised support.

REFERENCES

Abu-Hassanein, Z.C, Benson, C. H., and Blotz, L. R. (1996). "Electrical resistivity of compacted clays.". *J. Geotech. Engrg.,* ASCE, Vol. 122(5): 397-406.

Corwin, D.L., and Lesch, S.M. (2005). "Characterizing soil spatial variability with apparent soil electrical conductivity." . *Computers and Electronics in Agriculture*, Vol. 46:103-133.

Li Ning ,Cheng Guo-dong, and Xie Ding-yi. (2001). "Geomechanics development in civil construction in Western China.". *Chinese Journal of Geotechnical Engineering*, Vol. 23(3): 268-272 (in Chinese).

Liu, S.Y. Zha, F.S. and Yu, X.J. (2006). "Study on the laboratory measurement techniques of the electrical resistivity of soils.", *Journal of Engineering Geology*, Vol. 14(2):216-222 (in Chinese).

Keller, G.V, and Frischknecht, F.C. (1966). Electrical methods in geophysical prospecting. Pergamom Press, New York, N.Y.

JTJ051-93 (1993) Standard test methods of soils for highway engineering. China Communication Press, Beijing (in Chinese)

Zha Fu-sheng. (2007). Electrical resistivity of structured unsaturated soils and its application . Doctor Thesis, School of transportation, Southeast University.(in Chinese)

The Ultimate Uplift Capacity of Multi-Plate Anchors in Undrained Clay

Richard Merifield[1], A.M. ASCE and Colin Smith[2], M. ASCE, P.G.

[1]Senior Lecturer, Centre for Geotechnical & Materials Modelling, School of Engineering, The University of Newcastle, NSW 2308; richard.merifield@newcastle.edu.au.
[2] Senior Lecturer, Department of Civil and Structural Engineering, University of Sheffield, Sir Frederick Mappin Building, Mappin Street, Sheffield, S1 3JD; c.c.smith@sheffield.ac.uk.

ABSTRACT: Soil anchors are commonly used as foundation systems for structures requiring uplift resistance such as transmission towers, or for structures requiring lateral resistance, such as sheet pile walls. Anchors commonly have more than one plate or bearing element and therefore there is a complex interaction between adjacent plates due to overlapping stress zones. This interaction will affect the failure mode and ultimate capacity. However, no thorough numerical analyses have been performed to determine the ultimate pullout loads of multi–plate anchors. The primary aim of this research paper is to use numerical modelling techniques to better understand plane strain multi-plate anchor foundation behaviour in clay soils.

INTRODUCTION

Multi-plate anchors are geotechnical foundations that can be used as either tension or compression members and are composed of a number of plates welded along a central steel shaft, as illustrated in **FIG. 1**. The plates are typically constructed as a helix with a carefully controlled pitch. The anchors can have more than one plate located at appropriate spacing on the shaft. The central shaft is used to transfer axial loads to the anchor plates.

Unfortunately, current understanding regarding the behaviour of buried foundations, and multi-plate anchors in particular, is somewhat unsatisfactory and remains essentially unchanged for some 20 years. As a starting point, this paper will concentrate solely on the plane strain case of multi-plate anchors with the aim of better understanding the fundamental mechanics of the problem. The objective of the present paper are to gain a better fundamental understanding of multi–plate anchor behaviour and failure mechanisms.

There have been numerous theoretical studies that address the uplift of single horizontal anchors in clay as summarised by Merifield et al. (2001,2003). In contrast, there are very few publications that deal with the theoretical problem of multi–plate anchor foundations.

Anchor manufacturers have chosen to use one of three methods for predicting pullout capacity, namely, "cylindrical shear", "individual bearing", and an empirical method based on "installation torque". In general, manufacturers suggest that the cylindrical shear and individual bearing methods be used to determine capacity and the installation torque method be used as a field verification tool only.

PROBLEM OF ANCHOR CAPACITY

A general layout of the problem to be analysed is shown in **FIG. 1**. The anchor has a total of n individual plates of width B spaced evenly along the shaft at a distance of S. The anchor spacing ratio is defined as S/B and the anchor embedment depth is H/B. The soil has an undrained shear strength c_u and unit weight γ. Referring to **FIG. 1**, the total pullout-capacity for the anchor system can be expressed as a summation of the individual plate capacities, namely as;

$$Q_u = \sum_{i=1}^{n} Q_{ui} \qquad \leq Q_u^* \tag{1}$$

Where Q_{ui} is the ultimate pullout capacity of anchor i, n is the total number of anchor plates, and Q_u^* is the maximum/limiting capacity of a multi-plate anchor. The average ultimate bearing pressure q_{ui} for each anchor is

$$q_{ui} = \frac{Q_{ui}}{B} \tag{2}$$

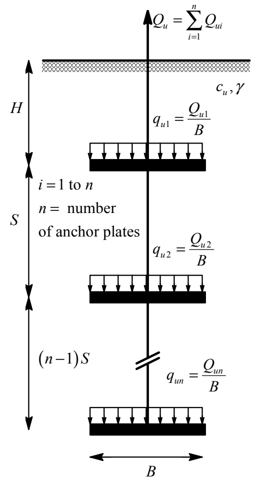

FIG. 1. Anchor Problem.

After allowing for immediate and no breakaway behaviour, anchors can be further classified as shallow or deep, depending on their mode of failure. An anchor is classified as shallow if, at ultimate collapse, the observed failure mechanism reaches the surface. In contrast, a deep anchor is one whose failure mode is characterised by localised shear around the anchor(s) and is not affected by the location of the soil surface.

For an individual anchor plate of width, B, and soil type, (γ, c_u), there exists a critical embedment depth, H_{cr} (**FIG. 2**(b)), at which the failure mechanism no longer extends to the soil surface and becomes fully localised around the anchor(s). This is true for both single and multi-plate anchors. When this type of behaviour occurs, the total ultimate capacity of the anchor will have reached a maximum limiting value Q_u^* (the asterisk on Q_u denotes deep failure).

In the context of a multi-plate anchor arrangement (**FIG. 1**), the type of deep failure mechanism will be a function of the anchor spacing ratio S/B. If the anchor spacing ratio S/B is large enough then each plate anchor will act independently from each other and produce a collapse mechanism like that shown in **FIG. 2**(c). This transition will occur at a critical value of $S/B=(S/B)_{cr}$. However, if the anchor spacing ratio S/B is small enough, such that each plate anchor is influenced by the location of adjacent anchors, then the collapse mechanism is likely to be global like that shown in **FIG. 2**(b). From a design perspective the maximum efficiency of a multi-plate anchor Q_u^* will be achieved if each of the anchor plates acts independently of each other (**FIG. 2**(c))

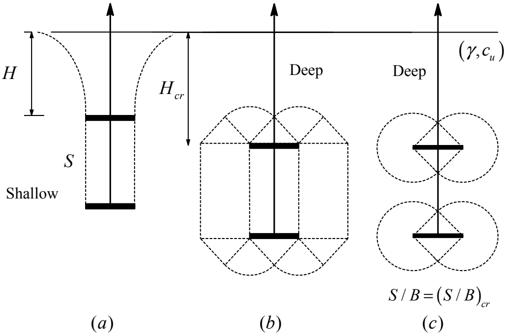

FIG. 2. Deep & Shallow Anchor Failure

The ultimate anchor bearing capacity in undrained clay for each anchor plate q_{ui} will be expressed as a function of the undrained shear strength in the following form

$$q_{ui}=\frac{Q_{ui}}{B}=c_u N_{ci} \tag{3}$$

where for a homogeneous soil profile

$$N_{ci}=\left(\frac{q_{ui}}{c_u}\right)_{\gamma\neq 0}=N_{coi}+\frac{\gamma H}{c_u} \tag{4}$$

and the term N_{coi} is an anchor break-out factor defined as

$$N_{coi}=\left(\frac{q_{ui}}{c_u}\right)_{\gamma=0} \tag{5}$$

The above equations reflect the complex nature of the pullout factor N_{cn} , as observed by Rowe and Davis (1982) and Merifield et al (2001), which is a function of both the embedment ratio and overburden pressure. The latter dependence is expressed in terms of the dimensionless quantity $\gamma H / c_u$.

When using equation (5) the inequality $Q_{ui}\leq Q_u^*$ must also be satisfied for each individual anchor plate. Therefore the value of N_{ci} has a limiting value of N_c^* that is easily obtained from equation (5) as

$$N_c^* = (2+3\pi) \tag{6}$$

NUMERICAL MODELLING

The displacement finite element software ABAQUS was used for solving this problem. The ABAQUS model consisted of two parts: the anchor (rigid body) and the soil (elasto-plastic). The soil was modelled as an isotropic elasto-perfectly plastic continuum with failure described by the Mohr–Coulomb yield criterion. The elastic behaviour was defined by a Poisson's ratio $\nu = 0.49$, and a ratio of Young's modulus to shear strength of $E/c_u = 400$. Although it is likely that shaft friction contributes to the capacity, the term is generally ignored in anchor design because of the uncertainties involved.

The strength of the anchor-soil interface was modelled using an interface roughness, α, where the maximum shear stress at the interface, $\tau_{max} = \alpha c_u$. For all analyses a smooth interface strength has been modelled, corresponding to $\alpha = 0$. A no-tension condition – allowing separation (or 'breakaway') of the anchor from the soil – has been imposed at the anchor-soil interface. Small strain analyses were performed on the pre-embedded anchor therefore neglecting the installation and large strain aspects of the problem. Such a 'wished in place' analysis is of course a simplification of what is actually a very complex problem.

To determine the collapse load of the anchor, displacement-defined analyses were performed in which the anchor was displaced vertically. A prescribed displacement was applied to the rigid anchor, resulting in uniform vertical motion of the entire anchor. The total nodal contact force along the anchor/soil interfaces in the vertical (V) direction was used to calculate the total ultimate load. In addition, the load carried by each individual anchor was obtained. A sample mesh is shown in FIG. 3.

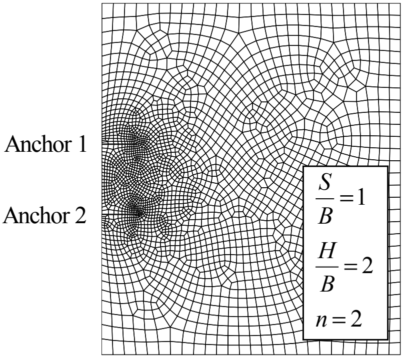

FIG. 3. Finite element mesh

In addition to the ABAQUS finite element modelling, a new numerical limit analysis procedure, Discontinuity Layout Optimization (DLO) (Smith and Gilbert (2007)) was used to solve the multi-plate anchor problem. The implementation of DLO in LimitState:GEO was utilised in this paper. The results are compared with the ABAQUS finite element solutions. Only a brief summary of the method is provided here. The reader is referred to Smith and Gilbert (2007) for a full description of the method.

PRELIMINARY RESULTS AND DISCUSSION

Finite element analyses were performed to obtain estimates of the anchor break-out factor N_{coi} in equation (5) for a range of embedment depths and anchor geometries. Analyses were conducted on two and three plate anchor geometries $(n = 2, 3)$ at anchor spacing ratios of $S/B = 1 \rightarrow 4$ and embedment depths of $H/B = 1 \rightarrow 10$. A range of DLO numerical upper bound analyses were also performed for the above.

The computed FE and DLO estimates of the anchor break–out factor N_{coi} are shown graphically in FIG. 4 for an anchor with two plates ($n = 2$). FIG. 4(a) plots the break-out factor for the anchor closest to the ground surface (Anchor 1). Results for anchor spacings of $S/B = 1 \rightarrow 4$ are also shown in this figure. The results indicate that there is only a small reduction in the capacity of the shallowest anchor plate (Anchor 1) due to the anchor plate below.

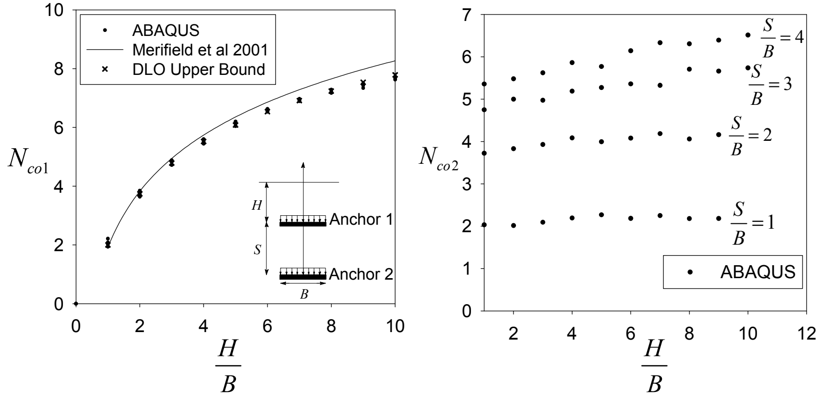

(a) (b)

FIG. 4. Break-out factors for multi-plate anchors

FIG. 4(b) plots the FE break-out factor for the anchor immediately below the shallowest anchor (Anchor 2, $i = 2$) as defined by equation (5), i.e. N_{co2}. The results show that the capacity of the anchor below the shallowest anchor is largely independent of the overall embedment ratio H/B, particularly for values of $S/B \leq 2$. The results indicate that, regardless of the number of plates along the shaft, the break-out factor for all anchor plates below the upper anchor can be conservatively estimated using equations for a single anchor (Merifield 2001) assuming they are embedded at an equivalent depth ratio of $H/B = S/B$.

The FE displacement patterns for a number of deep anchor problems are shown in FIG. 5. This figure illustrates the transition between the two types of deep anchor failure mechanism previously shown in FIG. 2. A global deep failure mechanism is visible in FIG. 5 (a),(b) while a local deep failure can be observed in FIG. 5 (c).

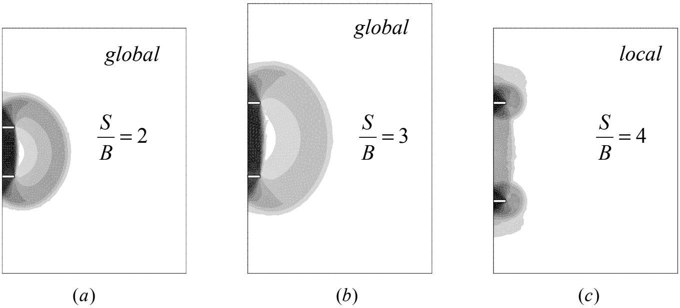

FIG. 5. Deep Anchor Failure

CONCLUSIONS

Preliminary analyses and results for multi-plate anchors have been presented. It is envisaged that further analyses will lead to the development of a practical design framework for multi-plate anchor foundations to replace existing semi–empirical design methods that are inadequate and have been found to be excessively under or over conservative. This framework can then be used by design engineers to more confidently estimate the pullout capacity of multi–plate anchors under tension loading.

REFERENCES

Merifield, R. S., Lyamin, A. V., Sloan, S. W. , and Yu, H. S. (2003). "Three-dimensional lower bound solutions for stability of plate anchors in clay." Journal of Geotechnical and Geoenvironmental Engineering **129**(3): 243-253.

Merifield, R. S., Sloan, S. W., Yu, H. S. (2001). "Stability of plate anchors in undrained clay." Geotechnique **51**(2): 141-153.

Rowe, R. K., Davis, E. H. (1982). "The behaviour of anchor plates in clay." Geotechnique **32**(1): 9-23.

Smith, C., Gilbert, M. (2007). "Application of discontinuity layout optimization to plane plasticity problems." Proceedings of the Royal Society -Mathematical Physical and Engineering Sciences **463**(2086): 2461-2484.

Vertical Stress under Point Load on Cross-Anisotropic Elastic Half-Space with Reduced Parameter Material Model

Amit Prashant[1], Abhishek Srivastava[2], and Gyan Vikash[3]

[1]Assistant Professor, Dept. of Civil Engineering, Indian Institute of Technology, Kanpur 208016, India; aprashan@iitk.ac.in
[2]Graduate student, Dept. of Civil Engineering, Indian Institute of Technology, Kanpur 208016, India
[3]PhD Research Scholar, Dept. of Civil Engineering, Indian Institute of Technology, Kanpur 208016, India; gvikash@iitk.ac.in

ABSTRACT: Natural soil deposits commonly exhibit cross-anisotropy about a vertical axis due to their depositional environment. This paper presents a study of the vertical stress distribution in a cross-anisotropic elastic soil deposit due to a point load. The study is based upon the exact solution derived by Liao and Wang (1998) that uses Fourier and Hankel transforms to solve the governing differential equations of the displacement functions. The solution has been first modified to consider a reduced parameter elastic model for cross-anisotropy as proposed by Graham and Houlsby (1983). The vertical stress distribution in the soil has been studied for a vertical point load with a varying degrees of anisotropy.

INTRODUCTION

Soil deposits exhibit considerably non-linear stress-strain response when subjected to external loading. The working loads taken for the design of foundations are generally low enough so as to allow only a small permissible settlement, and the resulting stress state does not exceed the initially linear stress-strain response. The depositional environment inevitably causes the soils to have different elastic parameters in horizontal direction than vertical. Therefore, modeling the soil as a cross-anisotropic linear elastic material may be the most pertinent choice for evaluating the stress distribution in soil mass for settlement calculations.

In a general formulation for stresses and strains (e.g. Liao and Wang, 1998) for a cross anisotropic material at least five independent elastic parameters are required. However the common laboratory tests during routine geotechnical investigations can determine at the most three parameters. Since a reduced parameter model does exist for such materials, it seems intuitive to apply those models to the existing stress formulations to make them easier to calibrate and hence make them practically more usable.

VERTICAL STRESSES IN CROSS ANISOTROPIC ELASTIC MEDIUM

Anisotropy in soil occurs mainly due to the mode of deposition and variation in consolidation stress level. The relationship between elastic strain increment $\delta\varepsilon_{ij}$ and effective stress increment $\delta\sigma_{ij}$ of a cross anisotropic material may be written using the generalized Hook's Law as follows (Love 1927; Kikgard and Lade 1991):

$$\begin{bmatrix} \delta\varepsilon_{11} \\ \delta\varepsilon_{22} \\ \delta\varepsilon_{33} \\ \delta\varepsilon_{44} \\ \delta\varepsilon_{55} \\ \delta\varepsilon_{66} \end{bmatrix} = \begin{bmatrix} \frac{1}{E} & \frac{-\nu'}{E'} & \frac{-\nu'}{E'} & & & \\ \frac{-\nu'}{E} & \frac{1}{E'} & \frac{-\nu}{E'} & & & \\ \frac{-\nu'}{E} & \frac{-\nu}{E'} & \frac{1}{E'} & & & \\ & & & \frac{1}{2G'} & & \\ & & & & \frac{(1+\nu)}{E'} & \\ & & & & & \frac{1}{2G'} \end{bmatrix} \begin{bmatrix} \delta\sigma'_{11} \\ \delta\sigma'_{22} \\ \delta\sigma'_{33} \\ \delta\sigma'_{44} \\ \delta\sigma'_{55} \\ \delta\sigma'_{66} \end{bmatrix} \tag{1}$$

where, E and E' are Young's Moduli in the plane of cross anisotropy and in a direction normal to it respectively. ν and ν' are Poisson's ratios characterizing the lateral strain response in the plane of cross anisotropy to a stress acting parallel or normal to it, respectively and G' is the shear modulus in the planes normal to the plane of cross anisotropy. The stresses and strains are referred to Cartesian system (x_1, x_2, x_3) where x_1 is the vertical axis of symmetry.

Liao and Wang (1998) derived the complete closed-form solutions of the displacements and stresses subjected to a point load in a cross anisotropic elastic half-space employing Fourier and Henkel transforms in a cylindrical co-ordinate system using the principal of superposition. According to the formulation vertical stress at a point below a vertical point load P_z in a cross anisotropic elastic medium is given by

$$\sigma_{zz} = \sigma'_{zz} + \frac{P_z}{4\pi}\left\{(A_{13} - u_1 m_1 A_{33})\left[T_1 m_1\left(\frac{z_a}{R^3_a}\right) - T_2 m_2\left(\frac{z_b}{R_b^3}\right)\right] - (A_{13} - u_2 m_2 A_{33})\left[T_3 m_1\left(\frac{z_c}{R_c^3}\right) - T_4 m_2\left(\frac{z_d}{R_d^3}\right)\right]\right\} \tag{2}$$

where

$$\sigma'_{zz} = \frac{P_z}{4\pi}k\left\{(A_{13} - u_1 m_1 A_{33})\left(\frac{z_1}{R^3_1}\right) - (A_{13} - u_2 m_2 A_{33})\left(\frac{z_2}{R_2^3}\right)\right\};\; k = \left(\frac{A_{13} + A_{44}}{A_{33} A_{44}(u_1^2 - u_2^2)}\right)$$

$$R_i = \sqrt{r^2 + z_i^2};\ (i = a, b, c, d, e);\ \ z_a = z_b = u_1 z;\ z_c = z_d = u_2 z;\ z_e = u_3 z$$

$$z_i = u_i\,|\,z\,|,\ R_i = \sqrt{r^2 + z_i^2} \quad (i = 1,2) \qquad m_i = \left(\frac{(A_{13} + A_{44})u_i}{A_{33}u_i^2 - A_{44}} \right) (i=1,2)$$

and where, r is the radial distance in plane of cross anisotropy and z is the vertical distance from point load to the point at which stress is to be calculated, respectively.

$$u_{1,2} = \pm\sqrt{0.5\left[s \pm \sqrt{s^2 - 4q} \right]}$$

$$s = \frac{A_{11}A_{33} - A_{13}(A_{13} + 2A_{44})}{A_{33}A_{44}} \qquad q = \frac{A_{11}}{A_{33}}$$

$$T_4 = \frac{k(u_1 + u_2)}{m_2(u_2 - u_1)} \quad T_3 = \frac{k}{m_1}\frac{2u_2(u_1 + m_1)}{(u_2 - u_1)(u_2 + m_2)} \quad T_2 = \frac{k}{m_2}\frac{2u_2(u_2 + m_2)}{(u_2 - u_1)(u_1 + m_1)} \quad T_1 = \frac{k(u_1 + u_2)}{m_1(u_2 - u_1)}$$

Here σ_{zz} and σ_{xx} are the vertical and horizontal stress at any point respectively. A_{ij} are the elements of the stiffness matrix which depend upon the soil parameters. These are defined as

$$A_{11} = \frac{E\left(1 - \frac{E}{E'}\nu'^2\right)}{(1+\nu)\left(1 - \nu - \frac{2E}{E'}\nu'^2\right)} \quad , \quad A_{13} = \frac{E\nu'}{1 - \nu - \frac{2E}{E'}\nu'^2} \quad , \quad A_{33} = \frac{E'(1-\nu)}{1 - \nu - \frac{2E}{E'}\nu'^2}$$

$$A_{44} = \frac{E}{2(1+\nu)} \quad , \quad A_{66} = G'$$

REDUCED PARAMETER MODEL

Graham and Houlsby (1983) presented a theoretical framework for describing the elastic anisotropy of soils as measured from triaxial tests. It involves only one parameter addition to the two required for describing isotropic elastic materials. In this study, the parameters chosen are E, ν and the additional parameter α (degree of anisotropy). Hence, the required 5 parameters are reduced to 3 to define the cross-anisotropic material. The parameters *E'*, ν', and *G'* are related to the other parameters as

$$E = \alpha^2 E'; \quad \nu = \alpha\nu'; \quad G' = E'/2(1+\nu') \tag{3}$$

There are three basic cases of cross anisotropy in elastic media: (i) vertically stiffer elastic media $\alpha < 1$, (ii) isotropic elastic media $\alpha = 1$, (iii) horizontally stiffer elastic media $\alpha > 1$. Adopting the reduced parameter model of anisotropy in the formulation, the stiffness matrix elements become:

$$A_{11}=\frac{E(1-v)}{(1+v)(1-2v)},A_{13}=\frac{Ev}{\alpha(1-2v)(1+v)},A_{33}=\frac{E(1-v)}{\alpha^2(1-2v)(1+v)},A_{44}=\frac{E}{2(1+v)},A_{66}=G'$$

The values of various parameters in Eq. 2 can be calculated using the new set of stiffness matrix elements.

$$D=s^2-4q=\frac{4(1-\alpha)(1+\alpha(1-2v))}{(1-v)^2} \tag{4}$$

$$s=\frac{2(1-\alpha v)}{(1-v)} \qquad q=\alpha^2$$

$$u_{1,2}=\pm\sqrt{\frac{1}{(1-v)}\left[(1-\alpha v)\pm\sqrt{(1-\alpha)(1+\alpha(1-2v))}\right]} \tag{5}$$

$$k=\frac{\alpha(1+v)(\alpha+2v(1-\alpha))}{2E\sqrt{(1-\alpha)(1+\alpha(1-2v))}} \tag{6}$$

It has already been shown by various researchers that Poisson's ratio for soils has a value less than 0.5 (Mavko et al. 1998). Considering the general case, it can be observed that for ν< 0.5 Eqs. (4) and (5) give real roots (i.e. D > 0) for $\alpha < 1$ (vertically stiffer elastic media) and complex values (i.e. D < 0) for $\alpha > 1$ (Horizontally stiffer elastic media). Since Eq. (6) becomes indeterminate for $u_1 = u_2$ i.e. $\alpha = 1$ (isotropic case), it can be solved by applying L'Hospital's rule by approaching $u_2 = u_1$. The solutions obtained for the isotropic case are

$$\sigma_{zz}=\sigma'_{zz}+\frac{P_z uz}{4\pi R^3}\frac{(A_{13}+A_{44})}{A_{33}*A_{44}}\left\{(A_{13}-umA_{33})\left(\frac{-\frac{d^2m}{du^2}}{2u^2(u+m)}-\frac{\frac{d^2m}{du^2}+\frac{dm}{du}+1}{2u^3(u+m)}\right)\right\} \tag{7}$$

$$\sigma'_{zz}=\frac{P_z}{8\pi}\frac{(A_{13}+A_{44})}{A_{33}*A_{44}}\left\{\frac{(A_{13}-A_{33}(u^2\frac{dm}{du}+2um))z}{R^3}-\frac{2(A_{13}-umA_{33})u^2z^3}{R^5}\right\} \tag{8}$$

Here $\frac{dm}{du}$ and $\frac{d^2m}{du^2}$ are the first and second derivatives of m with respect to u respectively. From Eq. (5), it can be observed that for α =1, $u_1 = u_2 = 1$. It is also known that when u = 1, m = 1.The equations. 7 and 8 reduce to

$$\sigma'_{zz}=\frac{P_z}{8\pi}\frac{(A_{13}+A_{44})}{A_{33}*A_{44}}\left\{\frac{1}{R^3}\left(A_{13}-A_{33}\left(\left(\frac{dm}{du}\right)_{u=1}+2\right)z\right)-\frac{2(A_{13}-A_{33})z^3}{R^5}\right\} \tag{9}$$

$$\sigma_{zz} = \sigma'_{zz} + \frac{P_z z}{4\pi R^3} \frac{(A_{13} + A_{44})}{A_{33} * A_{44}} \left\{ \frac{(A_{13} - A_{33})}{2} \left(-2 \left(\frac{d^2 m}{du^2} \right)_{u=1} - \left(\frac{dm}{du} \right)_{u=1} - 1 \right) \right\} \quad (10)$$

Hence by the above formulation all the parameters for a given cross anisotropic media (E, v, α) can be evaluated and the vertical stress at any point can be determined.

AN EXAMPLE

Considering a cross anisotropic elastic medium with E = 10^5 KN/m^2, ν= 0.3 and a downward vertical force of magnitude P = 100 KN acting at z = 0. The variation of vertical stress directly below the point of application of the force can be compared for various degree of anisotropy, as shown in FIG 1. The variation of vertical stresses at any fixed point, say, one meter right below to the vertical point load, for different values of degree of anisotropy (α) is shown in FIG 2. It can be observed in this figure that the value of vertical stress at $\alpha - 1^+$ and $\alpha - 1^-$ coincide with the value at $\alpha = 1$, and hence the curve is continuous and smooth at the isotropic condition. Similarly, isobars for various stress levels can be plotted for the given conditions and varying degrees of anisotropy. FIG 3 shows an example of such isobars, which indicates that the extent of stress distribution can change significantly depending on the degree of anisotropy.

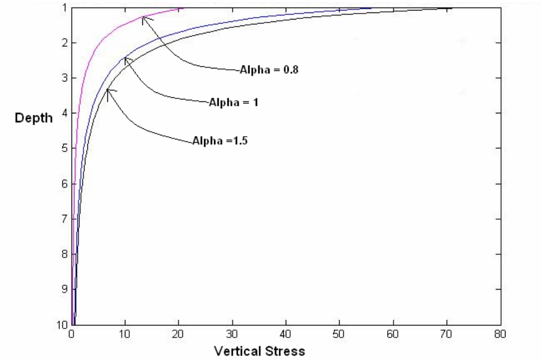

FIG. 1: Variation of vertical stress with depth for different α

CONCLUSIONS

The present study applies the reduced parameter model for cross anisotropic soils developed by Graham and Houlsby (1983) to the stress formulations for the elastic media developed by Liao and Wang (1998). The resulting formulations obtained are studied for various degrees of anisotropy. It is important to note that the complexities involved in calibration of a model dictate how extensively the model will be used in practice. Since the reduced parameter model is relatively easy to calibrate, the formulations based on this model are highly useful.

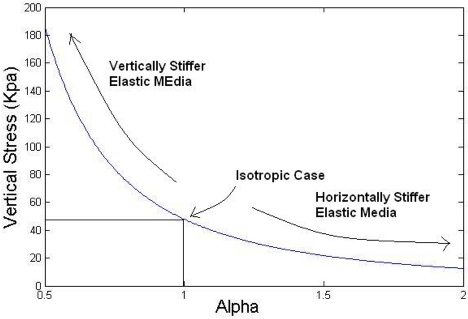

FIG. 2: Variation of vertical stress at a point with anisotropy.

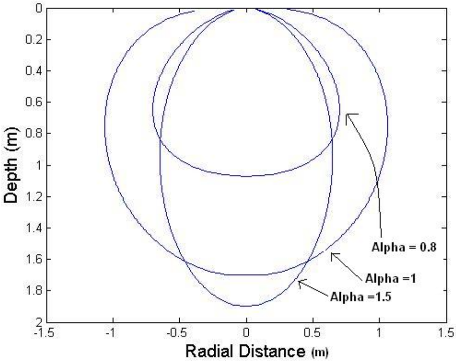

FIG. 3. 20 kPa Isobars for various degrees of anisotropy

REFERENCES

Graham, J., Houlsby, G.T. (1983). “Anisotropic elasticity of a natural clay.” *Geotechnique*, **33**(2): 165-180.

Kirkgard,M.M., and Lade,P.v. (1991). “Anisotropy of normally consolidated San Fransico Bay mud.” Geotech. Testing J., 14(3): 231-246.

Liao, J. J., and Wang, C. D. (1998). “Elastic solutions for a transversely isotropic half-space subjected to a point load.” *Int. J. Numer. Analyt.Meth. Geomech.*, **22**(6): 425-447.

Love, A.E.H. (1927). “A treatise on the mathematical theory of elasticity.” 4th edn. Cambridge University Press.

Mavko, G., Mukerji, T., Dvorkin, J., 1998. The Rock Physics Handbook. Cambridge University Press, Cambridge.

Calibration of 3-D Failure Criteria for Soils Using Plane Strain Shear Strength Data

Gyan Vikash[1], and Amit Prashant[2]

[1]PhD Research Scholar, Dept. of Civil Engineering, Indian Institute of Technology, Kanpur 208016,India; gvikash@iitk.ac.in
[2]Assistant Professor, Dept. of Civil Engineering, Indian Institute of Technology, Kanpur 208016,India; aprashan@iitk.ac.in

ABSTRACT: Design of many geotechnical problems, such as the stability of slopes and excavations, are strongly governed by the shear strength of soil represented in three dimensions. In literature, a number of failure criteria have been proposed using isotropic invariant of stress tensor in three dimensional stress spaces. For a linearly pressure-dependent material, there are four basic failure criteria which have been commonly used to describe the behavior; Mohr-coulomb, Drucker–Prager (1952), Lade and Duncan (1975), and Matsuoka and Nakai (1985). Mohr-Coulomb criterion is defined in a 2-D stress space and it follows plane strain condition. The other three which are 3-D failure criteria have been considered during this study for analysis. Calibration of such a model is relatively easy when the tests are performed in axisymmetric conditions and principal stresses are applied on the specimen, e.g. triaxial tests. This paper will present the solutions for calibrating such failure criteria assuming associative flow rule and using the shear strength parameter (ϕ_{ps}) obtained from the laboratory tests performed under plane strain conditions e.g. Direct Shear and Simple Shear Test.

INTRODUCTION

The classical approach of geotechnical design has been dependent on the Mohr-Coulomb failure criteria. It is well known that the intermediate principal stress (σ_2) can significantly influence the shear strength of soil and the Mohr-coulomb criterion does not capture the effect of σ_2. The geotechnical structures often involve complex stress states and the relative magnitude of $\sigma_2$varies from one location to the other. Over the years, the researchers have proposed several failure criteria which are applicable to general three dimensions stress conditions. These criteria have been also implemented in many of the commercially available software facilitating numerical simulation of geotechnical structures. Although the practitioners have shown their interest in employing these models during analysis, the calibration of such models has been still a challenge. Calibration of the 3-D failure criteria for soils can be done more accurately by performing a series of true triaxial tests; however, it is not preferred due to the cumbersome testing procedures and the lack of expertise available during common projects. It is often suggested to perform a series of traditional triaxial tests on solid cylindrical specimens of soil, which can provide the necessary data for calibration of model parameters. In the case of non-cohesive materials, it is relatively easy to perform the direct shear or simple shear tests under plane strain conditions in comparison to the traditional triaxial tests. As a result, it is not uncommon to see a geotechnical investigation report containing merely the shear strength data obtained from such plane strain tests. In this paper, the authors present the solution of calibrating the parameters of three most widely used 3-D failure criteria [1] Drucker–Prager (1952), [2] Lade and Duncan (1975), and [3] Matsuoka and Nakai (1985). Including the assumptions behind the analysis, the relationships have been presented here between the parameter of 3-D failure criteria and the effective friction angle ϕ'_{ps} under the plain strain conditions.

THREE-DIMENSIONAL FAILURE CRITERIA

The failure criteria presented herein are defined in the form of following stress invariants.

$$I_1 = \sigma'_1 + \sigma'_2 + \sigma'_3 \tag{1}$$

$$I_2 = \sigma'_1\sigma'_2 + \sigma'_2\sigma'_3 + \sigma'_1\sigma'_3 \tag{2}$$

$$I_3 = \sigma'_1\sigma'_2\sigma'_3 \tag{3}$$

$$J_2 = \frac{1}{6}\left[\left(\sigma'_1 - \sigma'_2\right)^2 + \left(\sigma'_2 - \sigma'_3\right)^2 + \left(\sigma'_1 - \sigma'_3\right)^2\right] \tag{4}$$

where I_1, I_2, I_3 are the first, second third invariants of the effective stress tensor respectively and J_2 is the second invariants of the deviatoric stress tensor. σ'_1, σ'_2 and σ'_3 are the major, intermediate, and minor principal effective stress respectively.

(1) Drucker-Prager Model

Drucker-Prager model is extended form of von Mises model. The von Mises failure criterion is not suitable for modeling the yielding of frictional material as it does not include the effect of hydrostatic stress on yielding. Experimentally, it is observed that the yielding of frictional material is dependent on hydrostatic stress. To overcome this limitation, Drucker and Prager (1952) proposed the following modified function for frictional soils.

$$f = \sqrt{J_2} - \alpha I_1 - K = 0 \tag{5}$$

where, $\alpha$is constant related to the internal friction angle of the material and Kis the cohesive strength of the material which is zero for non-cohesive or granular soil.

(2) Lade and Duncan's failure criterion

Lade and Duncan (1975) developed a relationship between the stresses at failure in terms of the first and third stress invariants, I_1 and I_3 .The failure criteria can be expressed as presented in equation (6) with K_l as a soil parameter.

$$\frac{I_1^3}{I_3} = K_l \tag{6}$$

(3) Matsuoka and Nakai's failure criterion

Matsuoka and Nakai (1985) proposed the following failure criteria which can be written in the form of the three stress invariants and a soil constant K_m.

$$\frac{I_1 I_2}{I_3} = K_m \tag{7}$$

CALIBRATION OF 3-D FAILURE CRITERIA

Calibration of each of the above mentioned 3-D failure criteria require at least three triaxial tests. If the friction angle through triaxial testing under axisymmetric conditions is known, it can be used to directly compute the parameters of 3-D models using the equations (8)-(10) below.

$$\alpha = \frac{2\sin\phi'}{\sqrt{3}\left(3-\sin\phi'\right)} \tag{8}$$

$$k_l = \frac{\left(3-\sin\phi\right)^3}{\cos^2\phi\left(1-\sin\phi\right)} \tag{9}$$

$$k_m = \frac{9-\sin^2\phi'}{\cos^2\phi'} \tag{10}$$

However, it is often difficult in routine projects to perform three triaxial tests to get the friction angle or 3-D model parameter. Generally, in the laboratory direct shear test or simple shear test is performed to determine the strength of the granular material. These tests are in plain strain condition. In the framework of the classical theory of plasticity, the parameters of above mentioned 3-D failure criteria can be directly related to plain strain shear strength parameter by assuming associative flow rule for which plastic potential surface and yield surface are same.

In the classical theory of plasticity, the flow rule defines the relationship between the next increment of the plastic strain $d\varepsilon_{ij}^{p}$, and the present state of stress σ_{ij} for a yielded element subjected to further loading. It states that in stress space, the plastic strain increment lies along the exterior normal to the plastic potential surface g and it can be can be expressed as

$$d\varepsilon_{ij}^{p} = d\lambda\left(\frac{\partial g}{\partial \sigma_{ij}}\right) \tag{11}$$

Here, dλis a positive scalar referred to as load factor. Since the models are assumed to be associative, the plastic potential can be represented by yield/failure criteria itself. Hence, the plastic potential function for the models in equations (5)-(7) can be given by equations (12)-(14) respectively.

$$g = \sqrt{J_2} - \alpha I_1 \tag{12}$$

$$g = I_1^3 - K_l I_3 \tag{13}$$

$$g = I_1 I_2 - K_m I_3 \tag{14}$$

It is fundamental assumption of the flow theory of plasticity that the total strain increment tensor in the plastic range may be decomposed in to the sum of elastic and plastic strain increment components. At failure, the magnitude of elastic strain is negligible in comparison to plastic strain component. Hence, it can be assumed that the total strain increment is equal to plastic strain increment.

$$d\varepsilon_{ij} = d\varepsilon_{ij}^{p} \tag{15}$$

Under the plain strain conditions, the normal strain in intermediate principal direction remains zero ($d\varepsilon_2 = d\varepsilon_2^p = 0$). Hence, equation (11) suggests the following.

$$\partial g / \partial \sigma_2 = 0 \tag{16}$$

After solving equation (16) for the plastic potentials given in equations (12)-(14), the value of α , K_l and, K_m are obtained as follows,

$$\alpha = \frac{(\sigma_1 - \sigma_3)}{2\sqrt{3}\left(\sigma_3^2 + \sigma_1\sigma_3 + \sigma_1^2\right)} \tag{17}$$

$$K_l = \frac{27\left(\sigma_3^2 + 2\sigma_1\sigma_3 + \sigma_1^2\right)}{(4\sigma_1\sigma_3)} \tag{18}$$

$$K_m = \frac{\sigma_1^2 + \sigma_3^2 + 3\sigma_1\sigma_3 + 2\sqrt{\left(\sigma_1^2\sigma_3^2 + \sigma_1^3\sigma_3 + \sigma_1\sigma_3^3\right)}}{\sigma_1\sigma_3} \tag{19}$$

The relationship between principal stress ratio and plain strain shear strength parameter $\phi_{ps}^{'}$ considering 2D stress state condition can be expressed as follows.

$$\left(\frac{\sigma_1}{\sigma_3}\right)_f = \frac{1+\sin\phi_{ps}^{'}}{1-\sin\phi_{ps}^{'}} \tag{20}$$

By substituting equation (20) into equations (17)-(19), the parameters of 3-D failure criteria can be expressed in terms of $\phi_{ps}^{'}$ as given in equations (21)-(23) respectively.

$$\alpha = \alpha\left(\phi_{ps}^{'}\right) = \frac{\sin\phi_{ps}^{'}}{\sqrt{3}\left(\sqrt{3}+\sin^2\phi_{ps}^{'}\right)} \tag{21}$$

$$K_l = K_l\left(\phi_{ps}^{'}\right) = \frac{27}{1-\sin^2\phi_{ps}^{'}} \tag{22}$$

$$K_m = K_m\left(\phi_{ps}^{'}\right) = \frac{5-\sin^2\phi_{ps}^{'}}{\cos^2\phi_{ps}^{'}} + 4\sec\phi_{ps}^{'} \tag{23}$$

Equations (21)-(23) represent the relationship between plain strain friction angle and the parameters of 3-D failure criteria. These relationships have been plotted in Figures 1 to 3, which can be used to directly obtain the parameters of 3-D failure criteria using the known value of angle of friction in plain strain conditions. From these figures, it is evident that as $\phi^{'}$ increases the value of α, K_l and K_m also increases.

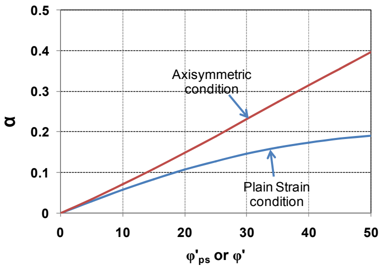

FIG. 1. Determination of α parameter for Drucker and Prager (1952) model

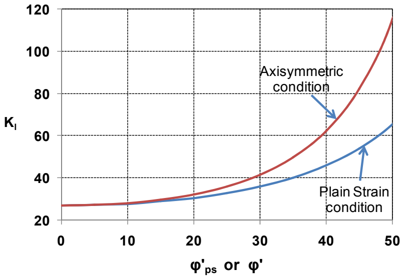

FIG. 2. Determination of K_l parameter for Lade and Duncan (1975) model

For axisymmetric condition, the value of failure parameters at a certain angle of friction is more than the plain strain condition. Since these parameters control the size of failure surface in 3-D stress space, soil with larger value of friction angle have larger size of failure surface in stress space i.e. the soil have larger failure strength.

The parameters have nonlinear relationships with the friction angles in all the cases. As a result, simplification of calibration by assuming the plane strain friction angle to be equal to or proportional to triaxial friction angle and use of conventionally available calibrations with respect to triaxial friction angle may lead to grossly erroneous interpretations. Hence, it is imperative to use the proposed relationships for directly calibrating the model in plane strain conditions.

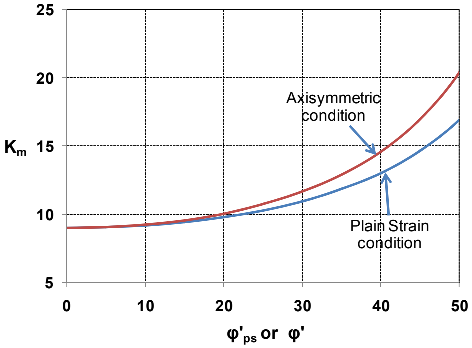

FIG. 3. Determination of "K_m" parameter for Matsuoka and Nakai (1985) model

CONCLUSIONS

This study explored calibration of three of the widely used 3-D failure criteria in geotechnical engineering being used to solve various boundary value problems. For granular material, these failure criteria were defined using one parameter which can be readily calibrated using the data from triaxial compression tests on soils. Based on the classical plasticity theory, a relationship between these parameters and plain strain shear strength data was established in this paper. Using these relationships one can calibrate the 3-D failure criteria using data obtained from Direct shear test or Simple shear test on soils under plane strain conditions. The plotted variations of 3-D failure parameters with the friction angle from triaxial compression and plane strain tests indicated significant difference with non-linear variability. It was suggested to use the new proposed relationships for calibration of models in pane strain conditions.

REFERENCES

Matsuoka, H., and Nakai, T. (1985). "Relationship among Tresca, Mises, Mohr-coulomb and Matsuoka-Nakai failure criteria." *Soils Found.,*25(4):123-128.

Matsuoka,H., Hoshikawa,T., and Ueno,K. (1990). "A general failure criterion and stress-strain relation for granular materials to metals" *Soils Found.*, 30(2): 119-127.

Lade, P. V. and Duncan, J. M. (1975). "Elastoplastic stress-strain Theory for cohesionless soil." *J. Geotech.Engg.Div.,*ASCE,101:1037-1053.

Improvement of Thermomechanical Model for Soil and Its FEM Analysis

Kong Liang[1], Li Xue-feng[2], Hua Li-kun[3]

[1] Professor, School of Sciences, Qingdao Technological University, Qingdao 266033, China; qdkongliang@163.com
[2] Doctor Candidate, Department of Geotechnical Engineering, Tongji University, Shanghai 200092, China; lixuefeng1928@163.com
[3] Associated Professor, School of Sciences, Qingdao Technological University, Qingdao 266033, China; hualikun@qtech.edu.cn

ABSTRACT: The thermomechanical approach to establishing elastic/plastic constitutive model for geomaterials not only has a tight mathematical structure, but also satisfies the laws of thermo-dynamics automatically and has a rigorous mathematic and physical basis. The isotropic thermomechanical model proposed by Collins (2002, 2005a) is introduced briefly and analyzed in detail. Aiming at its shortage of hardening law, the unified hardening parameter is incorporated into this model. And then, the model is extended to a unified thermomechanical model for soil which can be applied to both clay and sand. The FEM computer program of thermomechanical model and improved unified model are worked out. The adaptability and validity of improved model can be seen from the comparison and analysis of calculated results.

INTRODUCTION

The strength and constitutive relation is the core of modern soil mechanics, as well as the basis of computational soil mechanics. The traditional procedure for constructing elastic-plastic models for soils is to specify the elasticity law, yield condition, plastic potential and hardening laws independently of each other, which is inadequately rigorous in theory and there is no discussion of restrictions posed by the laws of thermo-dynamics, so it is irrational in some aspects (Zheng, Shen and Gong 2002). The thermomechanical approach to constitutive modeling for soils abandons these irrational aspects, and gets the whole of the constitutive structure (yield condition, flow rule, hardening law and elasticity law) just from two thermodynamic potentials (the free energy and the increment of dissipation function) by Legendre transformations (Collins and Houlsby 1997; Houlsby and Puzrin 2000). The major attraction of this approach is that it not only provides a tight mathematical structure, but also removes many factitious assumptions in traditional method and satisfies the laws of thermodynamics automatically. Professor I. F. Collins has done much work for the development and perfectness of this method (Collins and Houlsby 1997; Collins and Kelly 2002; Collins

2005a, 2005b; Collins and Muhunthan 2007), and proposed a thermomechanical constitutive model for soils (Collins and Hilder 2002, Collins 2005a). The model is flexible and adaptable, which can be amended with a different yield surface relatively easily (including the yield surface of modified Cam-clay model). But the model takes the plastic volume strain as hardening parameter, and uses the same hardening law as modified Cam-clay model, so it can't reflect dilatancy, and the deformation characteristic of over-consolidated clay and dense sand. Hardening and hardening law is the main ingredient of elastic-plastic model. Hardening and hardening parameters, determining its evolution, are closely related to the shape of yield surface. The stress-strain quantitative relation is deduced by the evolution law of hardening parameters corresponding to the yield surface. Yao et al (Yao, Luo and Sun 2002; Yao, Sun and Matsuoka 2008) proposed a unified hardening parameter, adapted for both clay and sand and independent in stress path, and developed the unified hardening model. In view of the solid mathematical foundation of thermomechanical model and the basic characteristic of unified parameter, the aim of this paper is to improve the isotropic thermomechanical model, proposed by Collins (2003, 2005a), to a unified model which adapt for both clay and sand by incorporating the unified hardening parameter. At first the introduction and analysis of Collins model is presented, and then an improved unified thermomechanical model is given. Finally, the corresponding FEM program is worked out, and the numerical examples are given.

ISOTROPIC THERMOMECHANICAL MODEL

Thermomechanical procedure and framework for constructing soil constitutive model can be seen in reference (Collins and Hilder 2002). The incremental dissipation function of the family of isotropic models proposed by Collins (2005a) is taken to be

$$\delta\Phi = \sqrt{(A\,\mathrm{d}\varepsilon_{\mathrm{v}}^{\mathrm{p}})^2 + (B\,\mathrm{d}\varepsilon_{\mathrm{s}}^{\mathrm{p}})^2} \tag{1}$$

where $\mathrm{d}\varepsilon_{\mathrm{v}}^{\mathrm{p}}$ is the volumetric plastic strain increment, and $\mathrm{d}\varepsilon_{\mathrm{s}}^{\mathrm{p}}$ is the shear plastic strain increment. The coefficient function *A* and *B* have the dimensions of stress and hence must be homogeneous functions of degree one in effective stress

$$\left.\begin{aligned} A &= (1-\gamma)p + \tfrac{1}{2}\gamma p_{\mathrm{c}} \\ B &= (1-\alpha)Mp + \tfrac{1}{2}\alpha\gamma Mp_{\mathrm{c}} \end{aligned}\right\} \tag{2}$$

where p is mean stress; p_{c} is consolidation pressure; α and γ is model coefficient; M is the slope of critical state line.

From the relation of dissipative stress σ_{ij}^{d} with the incremental dissipation function $\delta\Phi$, $\sigma_{ij}^{\mathrm{d}} = \partial(\delta\Phi)/\partial(\mathrm{d}\varepsilon_{ij}^{\mathrm{p}})$, the dissipative pressure and shear stress is

$$p_{\mathrm{D}} = \frac{A^2\mathrm{d}\varepsilon_{\mathrm{v}}^{\mathrm{p}}}{\delta\Phi},\quad q_{\mathrm{D}} = \frac{B^2\mathrm{d}\varepsilon_{\mathrm{s}}^{\mathrm{p}}}{\delta\Phi} \tag{3}$$

Eliminating the strain increments from Eq. (1) gives the yield condition in dissipative stress space

$$\frac{p_{\mathrm{D}}^2}{A^2}+\frac{q_{\mathrm{D}}^2}{B^2}=1 \qquad (4)$$

The dissipative yield loci are hence concentric ellipses. From Eq. (3), the flow rule in dissipative stress space can be obtained

$$\tan\psi=-\frac{\mathrm{d}\varepsilon_{\mathrm{v}}^{\mathrm{p}}}{\mathrm{d}\varepsilon_{\mathrm{s}}^{\mathrm{p}}}=-\frac{p_{\mathrm{D}}}{q_{\mathrm{D}}}\frac{B^2}{A^2} \qquad (5)$$

where ψ is dilation angle. The direction of the plastic strain increment is normal to the yield surface in dissipative stress space, in accord with the general theory. The critical state line (CSL) is defined to be the line on which $\mathrm{d}\varepsilon_{\mathrm{v}}^{\mathrm{p}}=0$, so $p_{\mathrm{D}}=0$ on the CSL from Eq. (3), and from the definition of shift stress, we have

$$p_{\mathrm{S}}=p_{\mathrm{CSL}} \qquad (6)$$

Where p_{CSL} is the effective pressure at the point where the yield locus meets the CSL. From the normal consolidation test, we can get $p_{\mathrm{S}}=\frac{1}{2}\gamma p_{\mathrm{c}}$, i.e. $p_{\mathrm{D}}=p-\frac{1}{2}\gamma p_{\mathrm{c}}$. For isotropic hardening, we assume that the plastic free energy function depends on $\varepsilon_{\mathrm{v}}^{\mathrm{p}}$, but not on $\varepsilon_{\mathrm{s}}^{\mathrm{p}}$, so $q_{\mathrm{S}}=0$, $q_{\mathrm{D}}=q$ (q is generalized shear stress). Eq. (4) can be rewritten in terms of true stress as

$$\frac{(p-\frac{1}{2}\gamma p_{\mathrm{c}})^2}{A^2}+\frac{q^2}{B^2}=1 \qquad (7)$$

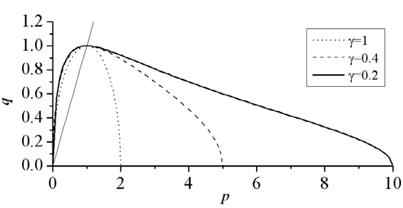

(a) α=1

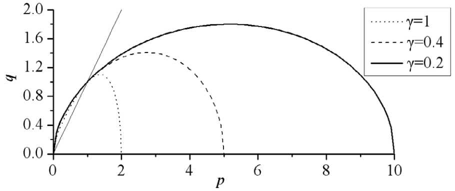

(b) α=0.5

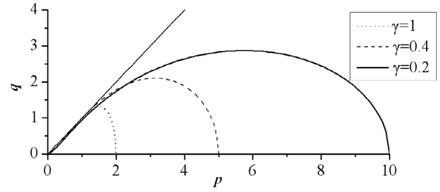

(c) α=1

FIG. 1. Yield loci at different value of α and γ(Collins and Hilder 2002)**.**

The flow rule in true stress space is

$$\tan\psi = -\frac{\mathrm{d}\varepsilon_{\mathrm{v}}^{\mathrm{p}}}{\mathrm{d}\varepsilon_{\mathrm{s}}^{\mathrm{p}}} = -\frac{p-\frac{1}{2}\gamma p_{\mathrm{c}}}{q}\frac{B^2}{A^2} \tag{8}$$

From Eq. (5) and (8), it can be seen that the plastic strain increment vector is normal to the elliptic yield locus in dissipative stress space, but if it is normal to the yield locus in true stress space lies on if the dissipation function depends explicitly on the current stress, i.e. the value of the coefficients in Eq. (2). Parameter α and γ have a well defined physical interpretation. α is a "tear drop" parameter, lie in the interval [0,1]. As α decreases from unity, the locus becomes less elliptical and more tear drop shaped as illustrated in Fig. 1. γ is a elongation parameter, also lie in the interval [0,1]. As γ decreases, the locus becomes more elongated as illustrated in Fig. 1. For example, $\alpha=\gamma=1$ for modified Cam-clay model, the dissipative function without current stress, and the flow rule is still normal in true stress space. When $\alpha\neq1$, $\gamma\neq1$, the dissipative function involves current stress, then the flow rule must be non-associated. For the former, the transform of yield locus from dissipative stress space to true stress space is just a simple translation; while for the latter, the yield locus not only translates, but also changes its shape, so the associated flow rule is no longer followed. The Coulomb model with an incompressible flow rule is recovered in the limit $\alpha=\gamma=0$.

For simple, assuming that the consolidation pressure p_c is just dependent on the plastic volumetric strain, the hardening law adopted in this model is (Collins and Hilder 2002)

$$\mathrm{d}p_{\mathrm{c}}=\frac{1}{\lambda-\kappa}p_{\mathrm{c}}\mathrm{d}\varepsilon_{\mathrm{v}}^{\mathrm{p}} \tag{9}$$

where λ is compression index and κ is expansion index.

IMPROVEMENT OF THE THERMOMECHANICAL MODEL

The isotropic thermomechanical constitutive model for soils proposed by Collins (2002, 2005a) has a rigorous mathematical and mechanical foundation, and can be amended with a different yield surface relatively easily (including the yield surface of modified Cam-clay model). Therefore it appears that the proposed model is flexible and adaptable. But the model still falls into single yield surface model. Choosing different hardening parameters results in different loading surfaces, and the uniqueness of boundary value problem can't be guaranteed. So the choice of hardening parameter and its corresponding hardening law is very important. From Eq. (9), it can be seen that Collins model takes the plastic volumetric strain as hardening parameter and ignore the influence of plastic shear strain on hardening. So the model can't reflect the hardening of geomaterials from all sides, as well as the dilatancy of soil (especially the dense sand and over-consolidated clay). It's necessary to improve the hardening law of the model.

Plastic strain is the fundamental reason of soil hardening. Many researcher takes the plastic volumetric strain $\varepsilon_{\mathrm{v}}^{\mathrm{p}}$, plastic shear strain $\varepsilon_{\mathrm{s}}^{\mathrm{p}}$ and the some combination of plastic strain, i.e. $f(\varepsilon_{\mathrm{v}}^{\mathrm{p}}, \varepsilon_{\mathrm{s}}^{\mathrm{p}})$, as hardening parameter respectively. Yao et al (Yao, Luo and Sun 2002; Yao, Sun and Matsuoka 2008) have been studied the stress-strain relation for a long time. They tried to explain and reason the rationality of hardening parameter from the basic mechanism and test results of sands and clay. They found the basic hardening parameter (such as ε_v^p, ε_s^p) is dependent on stress path, but the hardening parameter, as the key ingredient of elastic-plastic model, must be independent on stress path. Yao et al derived a simple and unified hardening parameter, which is independent on stress path, for both clay and sand

$$H = \int \mathrm{d}H = \int \frac{\mathrm{d}\varepsilon_v^p}{R(\eta)} \tag{10}$$

Where $R(\eta)$ is a factor dependent on stress path. It can remove the stress path dependent part of plastic volumetric strain increment $\mathrm{d}\varepsilon_v^p$ and make $\mathrm{d}\varepsilon_v^p/R(\eta)$ independent on stress path. The hardening parameter independent of stress path can be obtained by integrating along the stress path. The expression of $R(\eta)$ is

$$R(\eta) = \frac{M_f^4\left(M^4 - \eta^4\right)}{M^4\left(M_f^4 - \eta^4\right)} \tag{11}$$

Where M_f is the peak stress ratio $(q/p)_f$; M is the stress ratio at the critical state $(q/p)_{cs}$; η is the stress ratio q/p.

In order to avoid the disadvantage of Collins model due to taking the plastic volumetric strain as hardening parameter directly, the unified hardening parameter is incorporated into this model to improve the hardening law. The improved hardening law can be expressed as

$$\mathrm{d}p_c = \frac{p_c}{\lambda - K}\frac{\mathrm{d}\varepsilon_v^p}{R(\eta)} \tag{12}$$

The stress-strain curve of clay and sand is different, as well as the influencing extent of stress path. In general, shear makes the dense or medium-dense sand volume-contractive first and then volume-dilative, while shear makes the normally-consolidated clay or loose sand volume-contractive only. For this type soil of compressibility, the critical state stress ratio M is equal to the peak stress ratio M_f, $R(\eta) = 1$, and Eq. (12) is same as Eq. (9). For dilative materials, such as medium-dense sand, from Eq. (12), we have

① $\eta=0$ (isotropic compression), $\mathrm{d}\varepsilon_v^p = \left[(\lambda - \kappa)/p_c\right]\mathrm{d}p_c$, the deformation is compressive.

② $0 \le \eta \le M$ (stress contraction hardening phase), $\mathrm{d}\varepsilon_v^p > 0$, the deformation is stress contraction.

③ $\eta = M$ (phase transition state), $\mathrm{d}\varepsilon_v^p = 0$, it is the boundary between stress contraction and stress dilatancy.

④ $M < \eta < M_f$ (stress dilatancy hardening phase), $\mathrm{d}\varepsilon_v^p < 0$, the deformation is stress dilatancy.

It can be seen that the improved thermomechanical model can describe the special characteristic and dilatancy of dilative materials under different stress state,

FEM ANALYSIS OF THE MODEL

Numerical Example and Calculation Scheme

The numerical example is settlement of a foundation, which can be simplified to a plane strain problem. The element subdivision and boundary condition is shown in Fig. 2. The calculated model is 25m long and 20m deep, and the soil is Teton silt. The loads include three types: the soil gravity, unit weight is equal to 26.487kN/m^3; uniform load on top: q_0 = 200kPa; local load on the left side of top: q_1 = 600kPa. The used material parameters are listed in Tab. 1. Parameter α and γ is different from the calculation scheme.

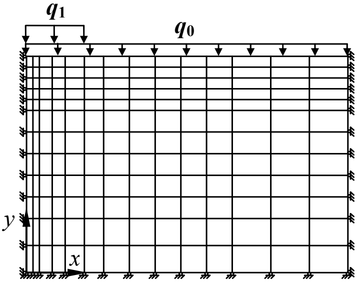

FIG. 2. FEM mesh and boundary conditions

TABLE 1. Model Parameters Used in Calculation

Hardening Parameters				**Test parameters**			
κ	λ	M	M_f	μ_0	E_0(kPa)	c(kPa)	φ(°)
0.00215	0.01004	1.4	1.55	0.3	19800	0.13	30

Four calculation schemes are adopted for comparatively analysis. Scheme 1: Collins model when $\alpha=\gamma=1$, i.e. modified Cam-clay model; scheme 2: the improved model when $\alpha=\gamma=1$; scheme 3: Collins model when $\alpha=0.5$, $\gamma=0.2$; scheme 4: the improved model when $\alpha=0.5$, $\gamma=0.2$. The yield loci of the model can be seen in Fig.1.

Calculated Results and Analysis

The isoline of stress σ_x, σ_y, τ_{xy}, calculated by scheme 4, is given in Fig.3 ~ Fig.5. The results calculated by other three schemes are similar to them. The stress distribution is the same, but the numerical value of stress is a little different. The regularities of stress distribution are consistent with the Boussinesq solution, the analytical solution based on elasticity.

The isoline of horizontal displacement, calculated by scheme 3 and scheme 4, is shown in Fig. 6 and Fig. 7 respectively. Fig. 8 is the isoline of vertical displacement calculated by scheme 4. Fig. 9 is the comparison of settlement on the top of foundation calculated by all four schemes. It can be seen from the comparison of calculated results that the movements and tendencies of displacement and deformation are similar, but the numerical value is different due to the different yield surface and hardening law. Scheme 1 and scheme 3 has the same hardening law but not the yield surface. In fact, the constitutive model in scheme 1 is modified Cam-clay model, which is suitable to normally-consolidated clay but not to dilative soil such as medium-dense sand. The yield surface used in scheme 3 is similar to Lade's teardrop yield surface, which is

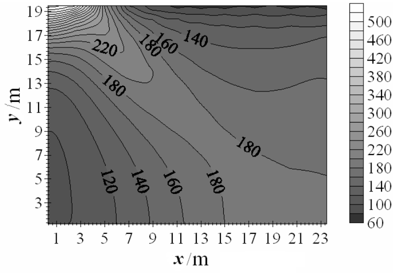

FIG. 3. Isoline of σ_x by scheme 4

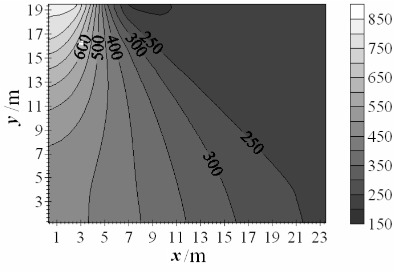

FIG. 4. Isoline of σ_y by scheme 4

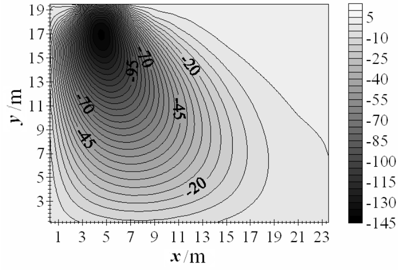

FIG. 5. Isoline of τ_{xy} by scheme 4

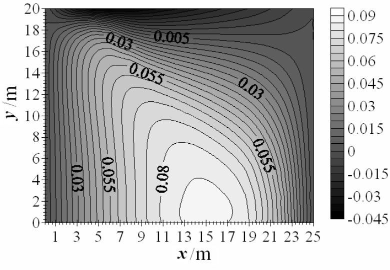

FIG. 6. Isoline of displacement in *x* direction by scheme 3

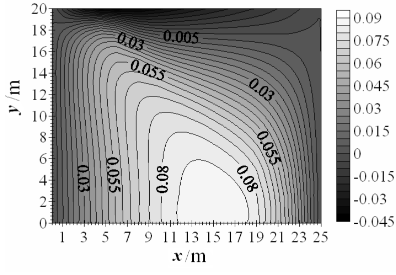

FIG. 7. Isoline of displacement in *x* direction by scheme 4

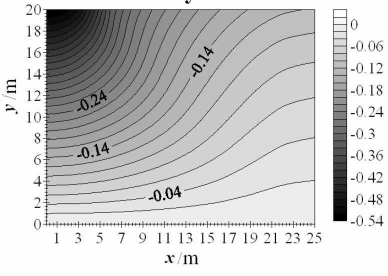

FIG. 8. Isoline of displacement in *y* direction by scheme 4

suitable to sand but it still has the limitation due to taking the plastic volumetric strain as hardening parameter. Scheme 2 and scheme 4 are corresponding to scheme 1 and scheme 3 respectively, while their constitutive model is improved by the unified hardening parameter to reflect the dilatancy of sand. As can be seen from Fig. 9, the settlement of foundation surface calculated by scheme 2 and 4 is less than before (that is, the settlement calculated by scheme 1 and 3), the overall small 5% ~ 15%, and the change is obviously big in where the stress is big. This is because the improved model can consider the dilatancy of sand, and the dilatancy is more obvious in high stress level.

It is concluded that the stress distribution calculated by four kinds of scheme is close, and the trend of displacement and deformation is similar but different numerical values. The calculated schemes include modified Cam-clay model, which is widely recognized in the world, so the rationality and validity of the improved model is verified indirectly. The improved thermomechanical model can reflect the soil dilatancy, embodying the characteristics of unified hardening parameter, and the purpose of improving is achieved.

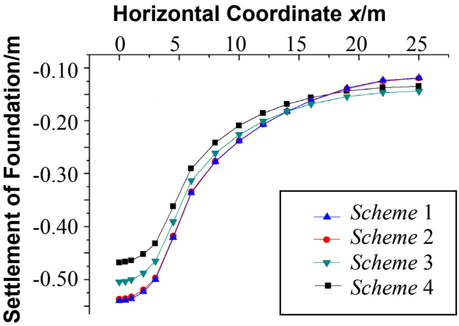

FIG. 9. Surface settlements

CONCLUSIONS

The thermomechanical approach to establishing elastic/plastic constitutive model for geomaterials gets the whole of the constitutive structure (yield condition, flow rule, hardening law and elasticity law) just from two thermodynamic potentials (the free energy and the increment of dissipation function). It not only has a tight mathematical structure, but also removes many factitious assumptions in traditional method and satisfies the laws of thermodynamics automatically. The thermomechanical constitutive model for soil proposed by Collins has the similar form with classic critical state theory. It has a simple structure and a good adaptability, and can be changed to different forms of yield surface through the different values of parameters. But the model still takes the plastic volume strain as hardening parameter, resulting in not fully reflect the degree of hardening of geotechnical materials, and also does not reflect the dilatancy of soil (especially sand and over-consolidated soil). The unified thermomechanical model improved by unified hardening parameter overcomes this shortcoming, and the parameters of model only increase one. The model can be applied to both compressive soil such as normally-consolidated clay and dilative soil such as medium-dense sand. The adaptability and validity of improved model is validated by FEM analysis for a foundation settlement problem.

ACKNOWLEDGMENTS

The authors appreciate the support of the National Natural Science Foundation of China (No. 50979037) and the Science Research Foundation of University in Ningxia.

REFERENCES

Collins, I.F. and Houlsby, G.T. (1997). " Application of thermomechanical principles to the modelling of geotechnical materials." *Proceeding of Royal Society of London*, Ser A 453:1975-2001.

Collins, I.F. and Kelly, P.A. (2002). "A thermomechanical analysis of a family of soil models." *Geotechnique*, Vol. 52 (7): 507-518.

Collins, I.F. and Hilder, T.A. (2002). "A theoretical framework for constructing elastic/plastic constitutive models of triaxial tests." *International Journal for Numerical and Analytical Methods in Geomechanics*, Vol. 26 (11): 1313-1347.

Collins, I.F. (2005a). "Elastic/plastic models for soils and sands." *International Journal of Mechanical Science*, Vol. 47: 493-508.

Collins, I.F. (2005b). "The concept of stored plastic work or frozen elastic energy in soil mechanics." *Geotechnique*, Vol. 55 (5): 373-382.

Collins, I.F., Muhunthan,B. and Tai A.T.T. (2007). "The concept of a “Reynolds-Taylor state” and the mechanics of sands." *Geotechnique*, Vol. 57 (5): 437-447.

Houlsby, G.T. and Puzrin, A.M. (2000). "A thermomechanical framework for constitutive models for rate-independent dissipative materials." *International Journal of Plasticity*, Vol. 16:1017-1047.

Yao, Y.P., Luo, T. and Sun, A.A. (2002). "A simple 3-D constitutive model for both clay and sand." *Chinese Journal of Geotechnical Engineering*, Vol. 24 (2): 240-246.

Yao, Y.P., Sun, D.A. and Matsuoka, T. (2008). "A unified constitutive model for both clay and sand with hardening parameter independent on stress path." *Computers and Geotechnics*, Vol. 35: 210-222.

Zheng, Y.R., Shen, Z.J. and Gong, X.N. (2002). " Principle of geotechnical plastic mechanics." China Architecture and Building Press.

A Three-Dimensional Unified Hardening Model for Anisotropic Soils

Yangping Yao[1],Yuxia Kong[2], Meng Li[3]

[1]Professor, Department of Civil Engineering, Beihang University, Beijing 100191, China; ypyao@buaa.edu.cn
[2]Ph.D candidate, ditto; kongyuxia@ce.buaa.edu.cn
[3]Master degree candidate, ditto; lemontree_0903@163.com

ABSTRACT: Based on the UH (unified hardening) model a new anisotropic constitutive model for anisotropic soils is presented in a new anisotropic transformed stress space. An anisotropic peak strength M_α is firstly introduced to represent the inherent anisotropy associated with particles' orientation distribution. An anisotropic transformed stress tensor $\tilde{\sigma}_{ij}^{a}$ is proposed by incorporating M_α with the original transformed stress tensor $\tilde{c}_{ij}$. The failure criterion and the stress-strain relationship for anisotropic soils are interpreted in the same constitutive framework. The capabilities of the proposed model are illustrated through comparisons of model simulations with experimental data. The basic soil parameters can be determined from the conventional triaxial compression tests on vertical specimens and horizontal specimens.

INTRODUCTION

Many geomaterials, such as sands and clays, display inherent anisotropy related to particles' orientation in the deposition process. Anisotropy can be separated into two major types in most granular materials-inherent and induced anisotropy. Soil anisotropy has obvious influences on strength and deformation response. A number of constitutive models have been proposed to probe the effects of anisotropy in granular materials. The fabric tensor F_{ij} for three-dimensional assemblies of granular soils was introduced to measure the inherent anisotropy due to the preferred orientation of constituent particles by Oda and Nakayama (Oda and Nakayama 1988). Based on the plastic potential surface proposed by Dafalias, many models were developed for anisotropic soils (Dafalias et al. 2002; Ling et al. 2002). A scaler-valued anisotropic state variable A was introduced into the hardening plastic modulus and the location of the critical state line to model the inherent fabric anisotropy (Li and Dafalias 2004; Dafalias et al. 2004). A rotation of the principal stress coordinate system was introduced to account for the effects of initial inherent anisotropy in the failure criterion of cross-anisotropic soils (Abelev and Lade 2004; Abelev et al. 2007).

The emphasis of this paper is to describe the behavior of anisotropic soils. An anisotropic transformed stress tensor $\tilde{\sigma}_{ij}^{a}$ is proposed, which is defined as a function of the original stress tensor σ_{ij} and an anisotropic peak strength M_{α}. In the anisotropic transformed stress space, the anisotropic soils can be taken as equivalent isotropic materials. The failure criterion and the stress-strain relationship for anisotropic soils are interpreted in the same constitutive framework. The capabilities of the proposed model are illustrated through comparisons of model simulations with experimental results.

ANISOTROPIC PEAK STRENGTH

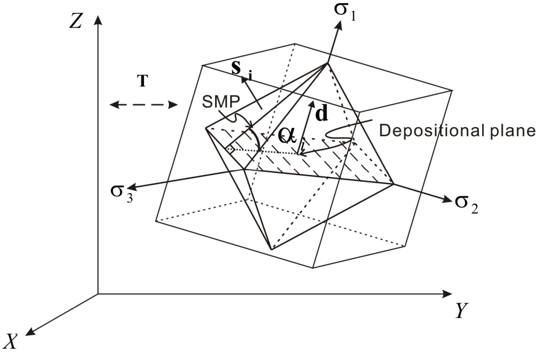

FIG. 1. Included angle between SMP and depositional plane.

SMP (Spatial Mobilized Plane) failure criterion was introduced by Matsuoka and Nakai for isotropic soils under three different principal stresses (Matsuoka and Nakai 1974). For anisotropic soils, both SMP and depositional plane have effects on deformation behavior. The included angle (α_i, FIG.1) made by SMP and depositional plane can be used to characterize inherent anisotropy of soils.

In FIG.1, X - Y - Z denotes the fixed physical space and σ_1 - σ_2 - σ_3 denotes the principal stress space. **T** is the transformation matrix from X - Y - Z space to σ_1 - σ_2 - σ_3 space. There are eight spatial mobilized planes which can be divided into four groups by every two parallel planes in the principal stress space. $\mathbf{s_i}$ ($i = 1,2,3,4$) is the normal vector of SMP, and **d** is the normal vector of depositional plane in the principal stress space. The included angle α_i between SMP and depositional plane can be deduced from their normal vectors

$$\alpha_i = \cos^{-1}(\mathbf{s_i}, \mathbf{d}). \tag{1}$$

Despite the depositional plane is perpendicular to the direction of any principal stress, all the spatial mobilized planes have the same included angle with the depositional plane. However, the depositional plane is not usually perpendicular to the direction of any principal stress, nor are the four included angles equal to each other.

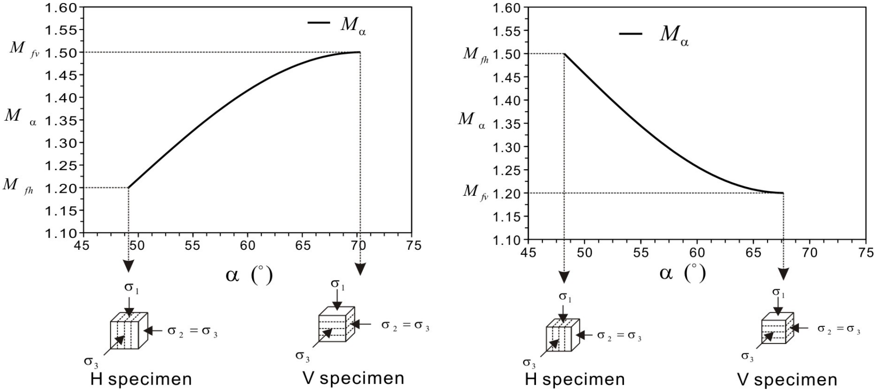

(a) $M_{fh} < M_{fv}$ (b) $M_{fh} > M_{fv}$

FIG. 2. Anisotropic peak strength M_α

With the minimum of the four included angles (α, Eq.(2)), we can link the stress state with the inherent anisotropy. The anisotropic peak strength M_α is defined as a function of α to take the particles' orientation distribution into account for describing inherent anisotropy.

$$\alpha = \min(\alpha_1, \alpha_2, \alpha_3, \alpha_4) \tag{2}$$

$$M_\alpha = M_{fh} + (M_{fv} - M_{fh}) \sin\left[\frac{\alpha - \alpha_{fh}}{\alpha_{fv} - \alpha_{fh}} \frac{\pi}{2}\right] \tag{3}$$

Construction of constitutive model describing soil anisotropy requires choosing anisotropic parameters correctly. For a given anisotropic soil, there are two basic parameters to be determined, ϕ_{fv} and ϕ_{fh}. ϕ_{fv} is obtained from triaxial compression tests on vertical specimens (V specimen) and ϕ_{fh} on horizontal specimens (H specimen) (FIG.2). All the parameters in Eq.(3) can be derived from ϕ_{fv} and ϕ_{fh} as following.

$$M_{fv} = \frac{6 \sin\phi_{fv}}{3 - \sin\phi_{fv}} \tag{4}$$

$$\alpha_{fv} = \cos^{-1}\sqrt{\frac{1 - \sin\phi_{fv}}{3 + \sin\phi_{fv}}} \tag{5}$$

$$M_{fh} = \frac{6 \sin\phi_{fh}}{3 - \sin\phi_{fh}} \tag{6}$$

$$\alpha_{fh} = \cos^{-1}\sqrt{\frac{1 + \sin\phi_{fh}}{3 + \sin\phi_{fh}}} \tag{7}$$

M_α can be used for both anisotropic and isotropic soils. When M_{fv} is unequal to M_{fh}, M_α changes with α and the soil is anisotropic (FIG.2). In FIG.2(a), when M_{fh} is less than M_{fv}, M_α is a increasing function of α. In FIG.2(b), when M_{fh} is greater than M_{fv}, M_α is a decreasing function of α. While M_{fv} is equal to M_{fh}, M_α becomes a constant and the soil is isotropic. M_α is helpful to construct the anisotropic transformed stress tensor, and to describe the stress-strain relationship for anisotropic soils.

ANISOTROPIC TRANSFORMED STRESS TENSOR

The transformed stress tensor $\tilde{\sigma}_{ij}$ provides a reasonable and simple approach for extending the models using stress parameters p and q to three-dimensional models (Matsuoka et al. 1999; Yao et al. 2008). To take the inherent anisotropy into account, it is necessary to specify the direction of the transformed stress tensor $\tilde{\sigma}_{ij}$ relative to the anisotropic peak strength M_α. A new transformed stress tensor is defined as

$$\tilde{\sigma}_{ij}^a = p\delta_{ij} + \frac{M_{max}}{M_\alpha}\frac{q^*}{q}(\sigma_{ij} - p\delta_{ij}) \tag{8}$$

in which $p = \sigma_{ii}/3$, $q = \sqrt{I_1^2 - 3I_2}$,

$$M_{max} = \max(M_{fv}, M_{fh}) \tag{9}$$

$$q^* = \frac{2I_1}{3\sqrt{(I_1 I_2 - I_3)/(I_1 I_2 - 9I_3)} - 1} \tag{10}$$

The stress direction of $\tilde{\sigma}_{ij}^a$ is always the same as the original σ_{ij}. The superscript a indicates that this variable is linked with anisotropy. In the new $\tilde{\sigma}_{ij}^a$ space, the anisotropic soil is equivalent to isotropic material with a peak stress ratio M_{max}. $\tilde{\sigma}_{ij}^a$ can be incorporated with the existed validated isotropic constitutive models.

ANISOTROPIC FAILURE CRITERION

A new failure criterion is defined by rendering the deviator stress $\tilde{q}^a$ a circle in the transformed stress space (FIG.3)

$$\tilde{q}^a = \tilde{p}^a M_{max} \tag{11}$$

where, $\tilde{p}^a = \tilde{\sigma}_{ii}^a/3$, $\tilde{q}^a = \sqrt{\frac{3}{2}(\tilde{\sigma}_{ij}^a - \tilde{p}^a\delta_{ij})(\tilde{\sigma}_{ij}^a - \tilde{p}^a\delta_{ij})}$.

Three sectors (I, II, III) are denoted in π-plane. FIG.4 illustrates the proposed criterion in π-plane in the physical stress space. When M_{fv} is equal to M_{fh}, the proposed criterion is the same as the original SMP. While M_{fv} unequal to M_{fh}, the failure criterion is just symmetrical about σ_z axis alone, which indicates that the proposed failure criterion can describe the anisotropy of soil strength.

For the anisotropic dense Santa Monica Bench sand, ϕ_{fv} is 39.4° and ϕ_{fh} is 37.5° (Lade 2008). The triaxial test results on this sand (Abelev and Lade 2004) is compared with the proposed anisotropic failure criterion and the SMP criterion (FIG.5). The proposed failure criterion fits the experimental results better in all three sectors than the the original SMP failure criterion.

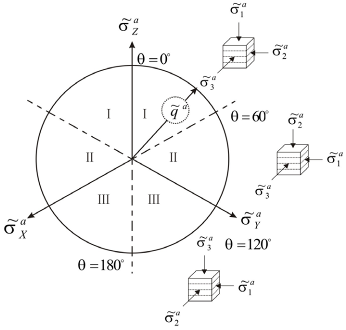

FIG. 3. Anisotropic failure criterion in anisotropic transformed stress space.

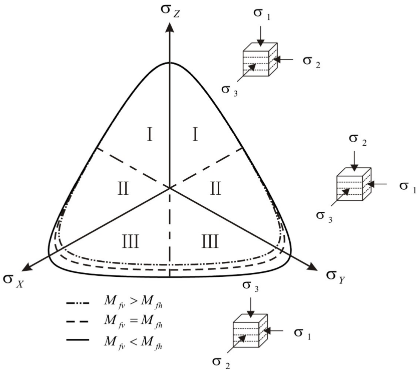

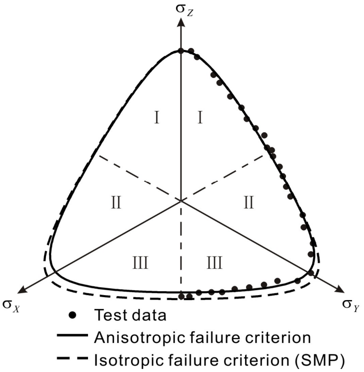

FIG. 4. Anisotropic failure criterion in physical stress space.

FIG. 5. Predicted and test results of dense Santa Monica Beach sand (Abelev and Lade 2004, ASCE).

ANISOTROPIC CONSTITUTIVE MODEL

The platform model is an isotropic three-dimensional unified hardening model (UH model) for over-consolidated clays. The key feature of the UH model is the adoption of a unified hardening parameter H. A new anisotropic constitutive model is proposed by incorporating $\tilde{\sigma}_{ij}^{a}$ with the UH model. This anisotropic model consists two yield surfaces (FIG.6) defined in the anisotropic transformed stress space.

Table 1. Equations for calculation of unified hardening parameter $\tilde{H}^{a}$

	Equations
$\tilde{\Omega}^{a}$	$\tilde{\Omega}^{a} = \left(M^{4} - \tilde{\eta}^{a^{4}}\right) / \left(\tilde{M}_{f}^{a4} - \tilde{\eta}^{a4}\right)$
M	$M = \max(M_{v}, M_{h})$
$\tilde{M}_{f}^{a}$	$\tilde{M}_{f}^{a} = 6\left[\sqrt{\frac{k}{\tilde{R}^{\beta}}\left(1+\frac{k}{\tilde{R}^{\beta}}\right)} - \frac{k}{\tilde{R}^{\beta}}\right]$
$\tilde{R}^{a}$	$\tilde{R}^{a} = \frac{\tilde{p}^{a}}{\tilde{\tilde{p}}_{x0}^{a}}\left(1+\frac{\tilde{\eta}^{a2}}{M^{2}}\right)\exp\left(-\frac{\varepsilon_{v}^{p}}{c_{p}}\right)$
$\tilde{\tilde{p}}_{x}^{a}$	$\tilde{\tilde{p}}_{x}^{a} = \tilde{p}^{a}[1+\tilde{q}^{a}/M^{2}\tilde{p}^{a2}]$
$\tilde{\eta}^{a}$	$\tilde{\eta}^{a} = \tilde{q}^{a}/\tilde{p}^{a}$
k	$k = M^{2}/12(3-M)$
c_{p}	$c_{p} = (\lambda - \kappa)/(1+e_{0})$

Adopting the unified hardening parameter $\tilde{H}^{a}$, the current yield surface is defined as:

$$f = g = \ln\frac{\tilde{p}^{a}}{\tilde{\tilde{p}}_{x0}^{a}} + \ln\left(1+\frac{\tilde{q}^{a2}}{M^{2}\tilde{p}^{a2}}\right) - \frac{1}{c_{p}}\tilde{H}^{a} = 0 \tag{12}$$

$$\tilde{H}^{a} = \int d\tilde{H}^{a} = \int \frac{\tilde{M}_{f}^{a4} - \tilde{\eta}^{a4}}{M^{4} - \tilde{\eta}^{a^{4}}} d\varepsilon_{v}^{p} = \int \frac{d\varepsilon_{v}^{p}}{\tilde{\Omega}^{a}} \tag{13}$$

The equations for calculating the anisotropic unified hardening parameter $\tilde{H}^{a}$ are listed in table 1.

The total strain increment is composed of elastic and plastic strain increments.

$$d\varepsilon_{ij} = d\varepsilon_{ij}^{e} + d\varepsilon_{ij}^{p} \tag{14}$$

The plastic strain increment is calculated as:

$$d\varepsilon_{ij}^{p} = \tilde{\Lambda}^{a}\frac{\partial f}{\partial\tilde{\sigma}_{ij}^{a}} \tag{15}$$

where the plastic factor $\tilde{\Lambda}^{a}$ for anisotropic soils is expressed as:

$$\tilde{\Lambda}^{a} = \tilde{\Omega}^{a} c_{p}\left(d\tilde{p}^{a} + \frac{2\tilde{p}^{a}\tilde{q}^{a}}{M^{2}\tilde{p}^{a2} - \tilde{q}^{a2}} d\tilde{q}^{a}\right) \tag{16}$$

Kirkgard and Lade (1991) had carried out series undrained tests of anisotropic San Francisco bay Mud to investigate the anisotropy effects on stress-strain relationship, pore pressure, and strength characteristics. These experimental results can be used to verify the proposed model. Material parameters in the predictions of anisotropic San Francisco bay Mud are listed in table 2. FIG.7-9 compare model predicted results with test data for anisotropic San Francisco bay Mud. These figures illustrated that the model predictions follow the trend of the experimental results well.

Table 2. Parameters for anisotropic San Francisco bay Mud

λ	κ	ν	M	$\phi_{fv}(^\circ)$	$\phi_{fh}(^\circ)$
0.3	0.06	0.15	1.12	23.0	28.2

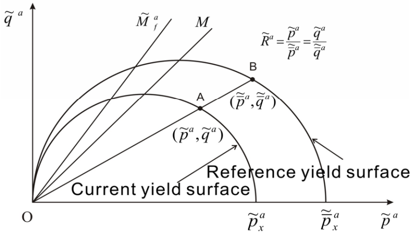

FIG. 6. Yield surfaces in anisotropic transformed stress space.

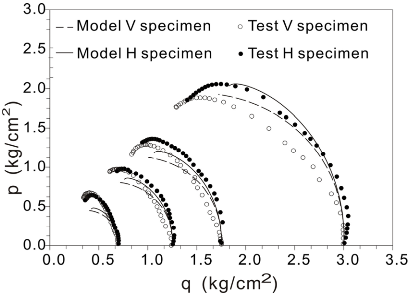

FIG. 7. Predicted results and test data of effective stress paths.

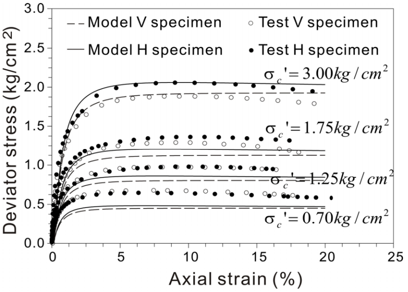

FIG. 8. Predicted results and test data (vertical deviator stress vs axial strain).

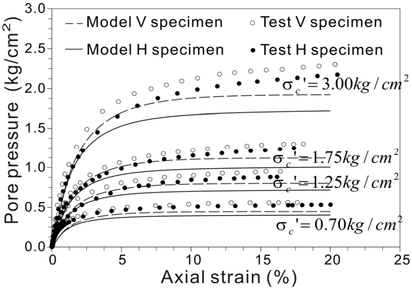

FIG. 9. Predicted results and test data (pore water pressure vs axial strain).

CONCLUSIONS

Based on the UH model a new anisotropic constitutive model for soils is presented in the anisotropic transformed stress space. The failure criterion and the stress-strain relationship for anisotropic soils are interpreted in the same constitutive framework. The proposed model has the following main features:

- The anisotropic peak strength M_α is introduced to take the particle orientation distribution into account for the description of inherent anisotropy.
- A new transformed stress tensor $\tilde{\sigma}_{ij}^{a}$ is established by incorporating M_α with the transformed stress tensor $\tilde{\sigma}_{ij}$.
- A new failure criterion is presented as a function of the included angle α between SMP and the depositional plane by incorporating α with the SMP failure criterion.
- An anisotropic constitutive model for soils is proposed in the new transformed stress space $\tilde{\sigma}_{ij}^{a}$, in which the soils can be taken as equivalent isotropic materials.

ACKNOWLEDGMENTS

This research was supported by the National Natural Science Foundation of China (Grant No's.10872016, 10672010, 50879001). This support is gratefully appreciated.

REFERENCES

Abelev,A.V., Gutta,S.K., Lade,P.V., and Yamamuro, J.A. (2007). "Modeling cross anisotropy in granular materials", *Journal of Engineering. Mechanics.*, ASCE, Vol. 33(8); 919-932.

Abelev, A. V. and Lade, P. V. (2004). "Characterization of failure in cross-anisotropic Soils." *Journal of Engineering Mechanics*, ASCE, Vol. 130(5); 599-606.

Dafalias, Y. F., Manzari, M. T., and Akaishi, M. (2002). "A simple anisotropic clay plasticity model." *Mechanics Research Communications*, Vol. 29(4); 241-245.

Dafalias, Y. F., Papadimitriou, a. G., and Li, X. S. (2004). "Sand plasticity model accounting for inherent fabric anisotropy." *Journal of Engineering Mechanics*, ASCE, Vol. 130(11); 1319-1333.

Kirkgard, M. M. and Lade, P. V. (1991). "Anisotropy of normally consolidated san francisco bay mud." *Geotechnical Testing Journal*, Vol. 14(3); 231-246.

Li, X. S. and Dafalias, Y. F. (2004). "A constitutive framework for anisotropic sand including non-proportional loading." *Geotechnique*, Vol. 54(1); 41-55.

Ling, H. I., Yue, D., Kaliakin, V. N., and Themelis, N. J. (2002). "Anisotropic elastoplastic bounding surface model for cohesive soils." *Journal of Engineering Mechanics*, ASCE, Vol. 128(7); 748-758.

Matsuoka, H. and Nakai, T. (1974). "Stress-deformation and strength characteristics of soil under three different principal stresses." *Proc. of JSCE*, 232, 59-70.

Matsuoka, H., Yao, Y., and Sun, D. (1999). "The Cam-clay models revised by the SMP criterion." *Soils and Foundations,* Vol. 39(1); 81-95.

Oda, M. and Nakayama, H. (1988). "Introduction of inherent anisotropy of soils in the yield function." *Micromechanics of Granular Materials. Proc. US/Japan Seminar, Sendai-Zao,* 1987, 81-90.

Yao, Y. P., Hou, W., and Zhou, a. N. (2009). "UH model: Three-dimensional unified hardening model for overconsolidated clays." *Geotechnique*, Vol. 59(5); 451-469.

Yao, Y. P., Sun, D. A., and Matsuoka, H. (2008). "A unified constitutive model for both clay and sand with hardening parameter independent on stress path." *Computers and Geotechnics*, Vol. 35(2); 210-222.

A Two Yielding Surface Elasto-Plastic Model with Consideration of Grain Breakage

Hu Wei, Dano Christophe, Pierre-Yves Hicher

Research Institute in Civil and Mechanical Engineering, UMR CNRS 6183, Ecole Centrale de Nantes, 44321 Nantes, France;wei.hu@ec-nantes.fr

ABSTRACT: An elasto-plastic model with two yield surfaces has been developed for the simulation of granular materials with consideration of grain ruptures. Grain breakage is induced by deviatoric as well as isotropic stresses. One yield function is based on a Mohr-Coulomb criterion with a hyperbolic hardening function of the plastic deviatoric strain. A second yield function is introduced to describe the plastic behaviour under compression, in which a hardening function of the plastic volumetric strain is introduced. The main assumption of this model is that, upon loading, the position of the critical state changes as a consequence of grain breakage. The effect of the grain size distribution is introduced in the relationship between the void ratio at critical state and the mean effective stress. Triaxial and oedometer tests have been performed on crushable granular materials. Comparison of experimental results and numerical simulations shows that the new model can reproduce with good accuracy the behaviour of granular materials subjected to grain ruptures during mechanical loading.

INTRODUCTION

Grain crushing is very common in granular materials. Some experimental results (Marsal 1967, Vesic & Clough1968, Hardin 1985, Kim 1995)have shown that grain crushing in a granular material occurs along deviatoric stress path as well as along isotropic stress path. Although it is agreed that deviatoric stresses induce more ruptures than isotropic stresses, the ruptures which are created by compression cannot be neglected. In order to consider the ruptures induced by isotropic and deviatoric stresses, an elasto-plastic model with two yield surfaces has been developed. Ruptures of particles are taken into account in the model by the evolution of the critical state. Indeed, ruptures of particles will produce a continuous evolution of the gradation and this change in the grain size distribution will provoke an evolution of the critical state of the material (Biarez and Hicher 1997). This evolution will be linked to the stress and strain amplitudes along a given loading path.

STRESS - STRAIN RELATIONSHIP

The constitutive model is an elasto-plastic model with two yield surfaces. The first yield surface is based on a Mohr-Coulomb criterion and a hyperbolic function is added into the model to be the hardening function. The second yield surface is a yield function for compression and a hardening function which includes the volumetric plastic strain is added. Critical state is also added into the model.

Non-linear elasticity

A non-linear hypo-elasticity has been selected. Young's modulus E and shear modulus G are power functions of the mean effective stress p'

$$G = G_0 \left(\frac{p'}{p_0'} \right)^n \tag{1}$$

$$E = E_0 \left(\frac{p'}{p_0'} \right)^n \tag{2}$$

G_0 and E_0 being the values of E and G for the reference mean effective stress p_0'. The parameters G_0, p_0' and n can be measured during a loading test by using, for example, bender elements technique.

The first yield function

The first yield function, noted as F_1, takes the following form

$$F_1(p',q,\theta,\kappa_1) = \frac{q}{M_p} \times m(\theta) - p' \times \kappa_1(\varepsilon_d^p) = 0 \tag{3}$$

where q is the deviator stress,

$$q = \sqrt{3 \times J_2} \tag{4}$$

J_2 is the second stress invariant:

$$J_2 = \frac{1}{2} s_{ij} : s_{ij} \tag{5}$$

s_{ij} is a component of the deviatoric stress tensor:

$$s_{ij} = \sigma_{ij} - \frac{1}{3} Tr(\sigma_{ij}) \times \delta_{ij} \tag{6}$$

p' is the effective mean stress:

$$p' = I_1 / 3 \tag{7}$$

and
$$\theta = -\frac{1}{3} Arc\sin\left(\frac{3\sqrt{3}}{2}\frac{J_3}{J_2^{3/2}}\right) \tag{8}$$

where
$$J_3 = \det(s_{ij}) \tag{9}$$

We have chosen a specific function of $m(\theta)$ in order to obtain the Mohr-Coulomb yield surface (Bardet,1980):

$$m(\theta) = \frac{6}{\sqrt{3}(3-\sin\varphi)}\left[\cos\theta - \frac{\sin\varphi}{\sqrt{3}}\sin\theta\right] \tag{10}$$

Hardening function for the Mohr-Coulomb yield surface

The equation of the hardening function for the first yield function takes the following form:

$$\kappa_1(\varepsilon_d^p) = r_{el} + \frac{\varepsilon_d^p(1-r_{el})}{a+\varepsilon_d^p} \tag{11}$$

Here r_{el} and a are two material parameters. r_{el} defines the size of the initial elastic domain and a controls the rate of the deviatoric plastic strain. $\kappa_1(\varepsilon_d^p)$ is an increasing function of ε_d^p. When $\varepsilon_d^p = 0$ (no plastic deformation), the function $\kappa_1(\varepsilon_d^p)$ is equals to r_{el} . When the perfect plastic state is reached ($\varepsilon_d^p \to \infty$), the value of the hardening function is equal to 1.

Plastic potential for the first yield surface

The plastic potential function is:

$$G_1(p',q) = \frac{q}{M_c(\theta)\times p'} + Ln(p') \tag{12}$$

G_1 is different from F_1 , therefore the model is non-associated. $M_c(\theta)$ has the following expression :

$$M_c(\theta) = M_c \times \frac{\sqrt{3}(3-\sin\varphi_c)}{6\left(\cos\theta - \frac{\sin\varphi_c}{\sqrt{3}}\sin\theta\right)} \tag{13}$$

φ_c is the characteristic angle which corresponds to the transition from the contracting domain to the dilating one:

$$\varphi_c = Arc\sin\left(\frac{3M_c}{6+M_c}\right) \tag{14}$$

The second yield function

In order to describe the behavior of granular materials along isotropic loading and to consider ruptures induced by compression, a second yield surface is added into the model. The second yield function is assumed to be as follows:

$$F_2(\sigma,\kappa_2) = p' - \kappa_2\left(\varepsilon^p\right) \quad \text{for } \sigma > P_p \tag{15}$$

κ_2 is another hardening function for the second yielding function which can be written as:

$$\kappa_2 = P_p 10^{\varepsilon^p / c^p} \tag{16}$$

where c^p is the compression coefficient in the ε^p - $\log\sigma'$ coordinate system. When compression σ is less than P_p, the plastic strain produced by the second yield function is null. P_p corresponds to the pre-consolidated stress. We assume that the isotropic compression and the critical state are parallel lines in the $e - \log p'$ plane by taking $c^p = \lambda$, where λ is the slope of critical state line.

The potential function we have chosen for the second yielding surface is very simple and is to only give a possible direction of plastic deformation, which is parallel to the axis of isotropic compression in the $p' - q$ plan.

$$G_2(p',q) = p' + k \tag{17}$$

where k is a constant.

Critical state

One of the most important concepts in soil mechanics is the critical state theory. At critical state, the material will remain at a constant volume while subjected to a continuous distortion. The void ratio corresponding to this state is e_c. The critical void ratio is a function of the mean effective stress p'. The relationship can be expressed as:

$$e_c = e_{ref} - \lambda Log(\frac{p'}{p_{ref}}) \tag{18}$$

The parameters (e_{ref}, p_{ref}) correspond to a reference point on the critical state line. The internal friction angle ϕ_u is a constant for the material. But the peak friction angle ϕ_p is dependent on the stress state and the void ratio:

$$\tan\phi_p = \left(\frac{e_c}{e}\right)^m \tan\phi_u \tag{19}$$

where m is a material constant (Biarez and Hicher 1994). In most conditions, the friction angle ϕ_u is assumed to be equal to the characteristic angle φ_c.

Taking into account grain rupture in the constitutive model

As shown in Figure 1, the critical state line in the $e - \log p'$ plane depends on the grain size distribution. If grain breakage occurs during loading, the grain size distribution evolves and the value of d_{60}/d_{10} increases. As a consequence, the critical state line is shifted towards the lower values of *e*, but the slope of the line remains almost constant. A simple way to describe the change of the critical state is to change the reference critical point ($e_{ref,} p_{ref}$).If one can assume that the slope remains constant, e_{ref} is the only variable necessary to control the evolution of the critical state line. For a given material the amount of grain breakage increases when increasing stresses and strains (Kim 1995). A simple way to consider the evolution of e_{ref} is therefore to make it a function of the two state variables. We chose the following quantity.

$$X^p = \int \sigma_{ij} d\left|\varepsilon_{ij}^p\right| \tag{20}$$

In order to describe the evolution of the critical state, the following expression is proposed:

$$1 - \frac{e_{ref}^{'}}{e_{ref}} = \frac{AX^p}{B + X^p} \tag{21}$$

In Eqation 21, two material parameters A and B are used to control the evolution of the critical state.

Parameter A controls the limit of the evolution of the critical state. Biarez and Hicher (1994) have proposed correlations between e_{max}, e_{min} and $C_u = d_{60}/d_{10}$. For values of C_u higher than 10, e_{max} and e_{min} remain almost constant. At the same time, the authors have suggested that the critical state line could be defined by two points (e_{max}, 0.1 MPa) and (e_{min}, 5 MPa). Therefore, when C_u reaches 10, the critical line will not evolve anymore. The parameter A can be defined from Figure 1.When $X^p \to \infty$, the following equations can be obtained.

$$1-\frac{e'_{ref}}{e_{ref}}=A \quad \text{and} \quad e'_{ref}=e_{ref}(Cu=10) \tag{22}$$

Parameter B accounts for the amount of grain ruptures, depending on the initial properties of the grains (mineralogy, shape, size, distribution). Poorly graded materials are more susceptible of grain ruptures than well graded ones (Kim 1995).Parameter B is used to control the speed of evolution of the critical state during loading.The smaller B is, the more easily the grain can be crushed and the critical state line will go down more rapidly.

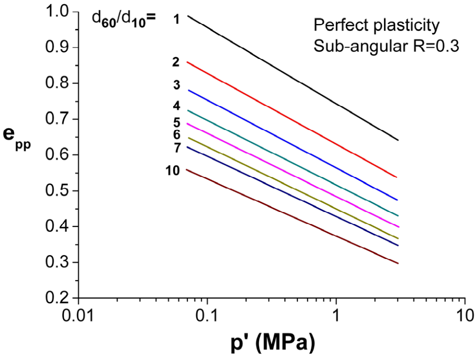

FIG. 1. Evolution of the critical state line with grain size distribution (after Biarez et Hicher, 1997).

MODEL CALIBRATION

In order to analyze the model's ability to reproduce the behaviors of granular materials when grain breakage occurs, we have simulated triaxial tests (Kim 1995) on crushed granite materials. The particle sizes vary from 6 mm to 12mm. The values of the constitutive parameters are given in Table 1. The results of the simulation are shown in Figure 2.

Table 1. Values of the parameters of the mode

E (MPa)	ν	e	Mc	r_{el}	a	e_{ref}	P_{ref} (kPa)	λ	m	A	B
325	0.2	0.80	1.76	0.001	0.003	1.24	100	0.206	0.05	0.31	500

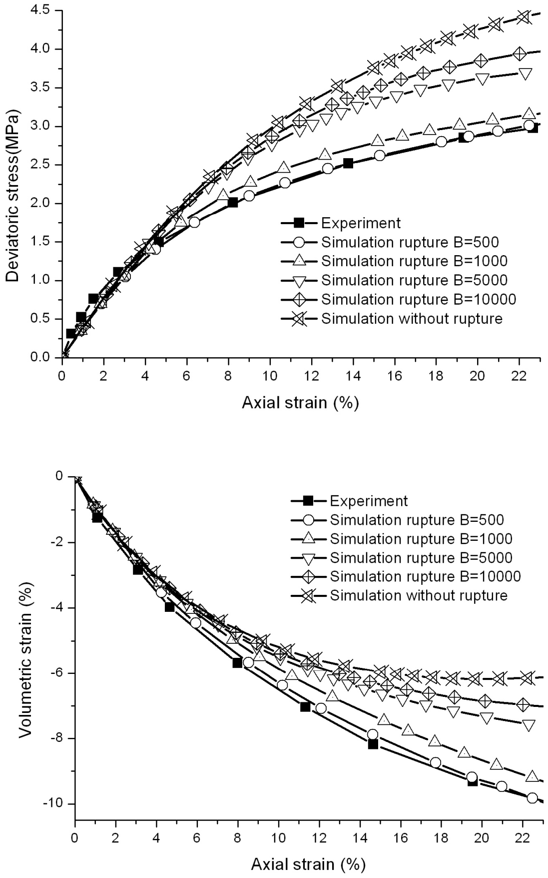

FIG.2. Numerical simulation and experimental results of the granite under a cell pressure of 1MPa with different B values.

Ruptures of particles can reduce the dilatancy of granular assemblies and increase the contractancy. Particle ruptures make specimens more likely to be compressed. The crushed granite material used here presents an important grading evolution. Particle breakage occurs rapidly, even at moderate confining stresses. The particle ruptures reduce the maximum strength of the specimen. The ruptures influence also the volume change: contractancy increases with the amount of grain ruptures. In the model, the rupture quantities of particles is controlled by parameter A and B. The simulation results change corresponding to different values of B. The ruptures increase as the parameter B decreases. When parameter B arrives at 500, the numerical results agree with the test results.

CONCLUSIONS

Due to grains ruptures during loading, the physical features of the materials, such as the grading, change. As a consequence, the critical state changes also and its evolution modifies the material behaviour by reducing its maximum strength, decreasing the tendency to dilate or increasing the tendency to contract. The constitutive model can take into account the evolution of the critical state line during the loading process as a function of the dissipation of the energy. A first validation of the model was performed using tests results on crushed granite. We demonstrated the ability of the model to take into account the effects of grain ruptures on the stress-strain relationship and on the volume change.

REFERENCES

Bardet, J.P. (1990). "Lode dependences for isotropic pressure-sensitive elastoplastic materials", *Journal of Applied Mechanics*, Vol 57:1131-1146.

Biarez, J. and Hicher, P-Y. (1994). "Elementary Mechanics of Soil Behaviour", Balkema.

Biarez, J. and Hicher, P-Y. (1997). "Influence de la granulométrie et de son évolution par ruptures de grains sur le comportement mécanique de matériaux granulaires", *Revue Française de Génie Civil*, Vol. 1 (4) :607-631.

Dano, C. (2001). "Comportement mécanique des sols injectes". PHD thesis, Ecole Centrale de Nantes,France.

Daouadji, A., Hicher, P-Y. and Rahma, A. (2000). "An elastoplastic model for granular materials taking into account grain breakage", *European Journal of Mechanics - A/Solids*, Vol. 20 (1):113-137.

Hardin, B.O. (1985). "Crushing of soil particles", *Journal of Geotechnical Engineering*, ASCE, Vol. 111 (10) :1177-1192.

Kim, M.S. (1995). "Etude Expérimentale du Comportement Mécanique des Matériaux Granulaires sous Fortes Contraintes ", PHD thesis, Ecole Centrale de Paris

Marsal, R.J. (1967). "Large scale testing of rockfill materials", *Journal of the Soil Mechanics and Foundation Division*, ASCE, Vol. 93 (SM2): 27-43.

Vesic, A.S. and Clough, G.W. (1968). "Behaviours of granular materials under high stresses", *Journal of the Soil Mechanics and Foundations Division*, ASCE, Vol. 94, (SM3): 661-668.

Modification of Subloading t_{ij} Model for Soft Rock

Maiko Iwata[1], Atsushi Yashima[2], Kazuhide Sawada[3], Masaya Hinokio[4]
and Ryota Otsu[5]

[1]Graduate Student, Department of Civil Engineering, Gifu University, Yanagido 1-1, Gifu, 501-1193; n3812101@edu.gifu-u.ac.jp
[2]Professor, Department of Civil Engineering, Gifu University, Yanagido 1-1, Gifu, 501-1193; yashima@gifu-u.ac.jp
[3]Associate Professor, River Basin Research Center, Gifu University, Yanagido 1-1, Gifu, 501-1193; sawada@gifu-u.ac.jp
[4]Associate Professor, Department of Civil Engineering, Gifu University, Yanagido 1-1, Gifu, 501-1193; hinokio@gifu-u.ac.jp
[5]Staff, Waterworks & Sewerage Bureau, Nagoya City Office, 2-45, Toyomae-cho, Higashi-ku, Nagoya, 461-0034;

ABSTRACT: Soft rock ground is widely distributed in Japan and slope failure of soft rock occurs frequently. It is necessary to understand the mechanical behavior of soft rock and to develop a constitutive model which can appropriately express the mechanical behavior of soft rock. In this research, a series of drained triaxial compression tests were carried out to modify the original constitutive model proposed by Nakai and Hinokio (2004). Based on the experimental results, the change of the yield surface during the shearing process was proposed. As the result, the stress-strain behaviors under different confining stresses were reproduced quantitatively by a modified constitutive model.

INTRODUCTION

Soft rock ground is widely distributed throughout Japan and slope failure of soft rock slope occurs frequently. In general, a numerical analysis is considered to be effective in predicting slope failure. In order to predict the slope failure by a numerical analysis, it is necessary to understand the mechanical behavior of soft rock and to develop a constitutive model which can appropriately express the mechanical behavior of soft rock. In a few decades, in order to understand the mechanical behavior of soft rock in detail, many experimental researches of soft rock were conducted, for example triaxial compression tests, triaxial creep tests (Aung, 2006) and plane strain compression tests (Ye et al., 2007) under several test conditions. Moreover, based on those results, a constitutive model for soft rock was proposed (Zhang et al., 2005).

In this study, in order to verify the constitutive model (Zhang et al., 2005), triaxial compression tests and numerical simulations were carried out. In the experiment, drained triaxial compression tests on soft rock were conducted under different confining stress. Based on the results of those triaxial tests the material parameters used in the numerical simulation were determined. From the results of the numerical simulation, it was found that the stress-strain behavior under low confining stress could not be reproduced well by the present constitutive model. Therefore, in order to overcome these shortcomings, in this research, the change of the shape of the yield surface was proposed.

TRIAXIAL COMPRESSION TEST

The rock sample used in this study was Ohya stone, a kind of sedimentary soft rock, which was mined by block sampling in Tochigi Prefecture, Japan. The size of the specimen used in triaxial test is 50mm in diameter and 100mm in height.

Before testing, the specimens were saturated and the B value of the samples was kept higher than 0.95. After being isotropically-consolidated for 6 hours under prescribed confining pressure, the specimen was subjected to constant-strain-rate compression test. Back pressure was 0.5 MPa during all process from consolidation to shearing in this study. The compression tests were conducted with a strain rate of 0.001%/min under different effective confining stresses of 0.1, 0.2, 0.3, 0.5, 1.0, 2.0, 3.0 and 4.0MPa.

FIG. 1 shows the results of the drained triaxial compression tests under different confining stresses. From the results, the strain softening behavior was clearly observed from all tests as shown in FIG. 1 (a). The results show a trend that the larger the confining stress, the larger the peak strength and the residual strength. The stress ratio at residual state was different in terms of the confining stress. From FIG. 1 (c), the results of volumetric strain also show the trend that the dilatancy behaviors depend on the confining stress.

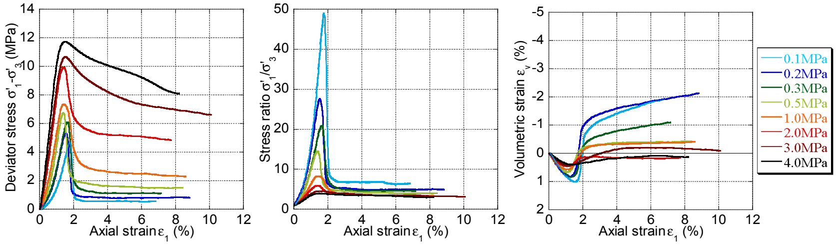

(a) deviator stress **(b) stress ratio** **(b) volumetric strain**

FIG. 1. Triaxial compression test results.

VERIFICATION OF CONSTITUTIVE MODEL FOR SOFT ROCK

Subloading tij model which is an elastoplastic model for normally and over consolidated soils was proposed by Nakai and Hinokio (2004). This model is based on the subloading surface concept (Hashiguchi, 1980) and tij concept (Nakai and Mihara, 1984). An elasto-viscoplastic model for soft rock which introduced time-dependent theory into the subloading tij model was proposed by Zhang et al. (2005). In this study, in order to verify the elasto-viscoplastic model, numerical simulations of triaxial compression test were conducted.

The material parameters used in the model were determined based on the experimental results of triaxial compression tests as shown in Table 1. Initial void ratio e_0 was determined in terms of the confining stress. Numerical simulations were conducted under same conditions as triaxial compression tests.

Table 1. Material parameters.

compression index	λ	0.020
swelling index	κ	0.005
void ratio at p'=98kPa	e_{NC}	0.553
stress ratio at critical state	R_{CS}	3.0
Poisson's ratio	ν	0.02
parameter of shape of yield surface	β	1.1
parameter of influence of density	a	850
time-dependency parameter	α	0.6
time-dependency parameter	C_n	0.02
initial void ratio	e_0	refer to the following table

σ'_{m0} (MPa)	0.1	0.2	0.3	0.5	1.0	2.0	3.0	4.0
e_0	0.476	0.471	0.467	0.462	0.456	0.449	0.444	0.441

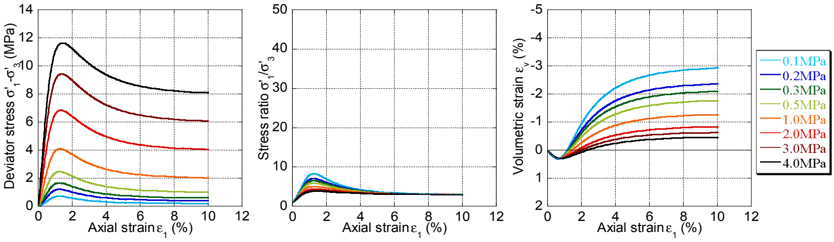

(a) deviator stress **(b) stress ratio** **(b) volumetric strain**

FIG. 2. Result of numerical simulation of triaxial compression test.

FIG. 2 shows the numerical results of triaxial compression test. From the comparison between the experiments and the numerical simulations, it was confirmed that the stress-strain behavior under high confining stress was reproduced by the constitutive model. However, the stress-strain behavior under low confining stress could not be reproduced well. The failure of soft rock slope occurs near the ground surface. Therefore, it is necessary to reproduce the mechanical behavior of soft rock under low confining stress.

In the original model, a parameter M^* which associated with shape of yield surface is represented by the principal stress ratio at the critical state in triaxial compression test $R_{CS}= (\sigma_1/\sigma_3)_{CS}$ as

$$M^* = \left(X_{CS}^{\beta} + X_{CS}^{\beta-1}\cdot Y_{CS}\right)^{\frac{1}{\beta}} \tag{1}$$

$$X_{CS} = \frac{\sqrt{2}}{3}\left(\sqrt{R_{CS}} - \frac{1}{\sqrt{R_{CS}}}\right), \quad Y_{CS} = \frac{1-\sqrt{R_{CS}}}{\sqrt{2}\left(\sqrt{R_{CS}}+0.5\right)} \tag{2}$$

Here, R_{CS} is constant. Therefore, the parameter M^* is constant and the shape of yield surface is also constant as shown in FIG. 3 (a) in the original model. However, the stress-strain behavior under low confining stress could not be reproduced well by the original model. In addition, it is found that the parameter M^* depends on confining stress from the stress-dilatancy relations obtained from the triaxial compression tests as shown in FIG. 4 (b). Therefore, in this study, a new parameter R is used instead of R_{CS} in Equation 2 and the change of R to reproduce the stress-strain behavior is assumed. The following points were considered in the assumption of the change of R.

- The lower the confining stress, the larger the value of R. This trend is based on the result of stress-dilatancy relations.
- R converges to R_{CS} at critical state. R_{CS} is constant and R_{CS} was determined as 3.0 from the result of the triaxial compression tests under higher confining stress in this study.
- An axial strain at the critical state is larger when the confining stress is low. Therefore, the state at axial strain of 10% is not critical state under low confining stress (0.1, 0.2, 0.3 and 0.5 MPa) in FIGS. 5 & 6.
- It is assumed that R is decreasing linearly during shear process.

FIG. 3(b) shows the shape of yield surface when R changes. FIG. 5 proposes the change of R. FIG. 6 shows the results of numerical simulation with the evolution rule of R.

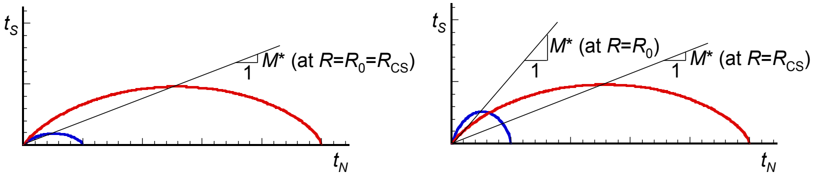

(a) *R* is constant **(b) *R* is not constant**

FIG. 3. Shape of yield surface.

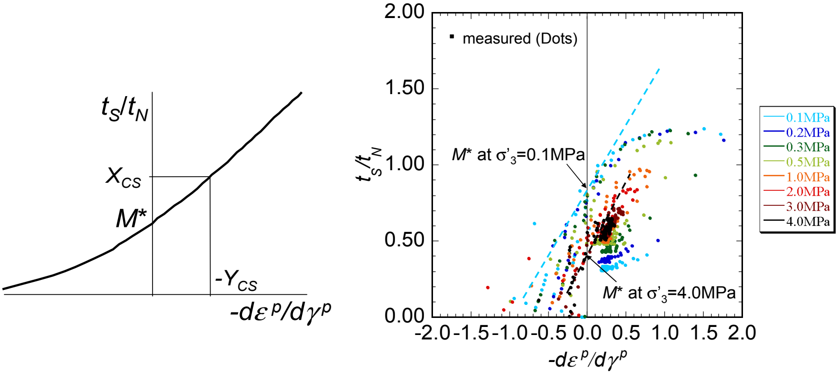

(a) theory **(b) triaxial compression test**

FIG. 4. Stress-dilatancy relations.

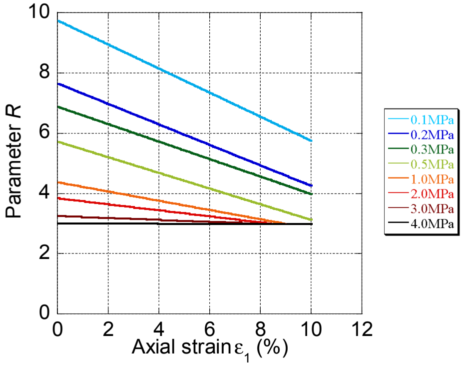

FIG. 5. Change of parameter *R*.

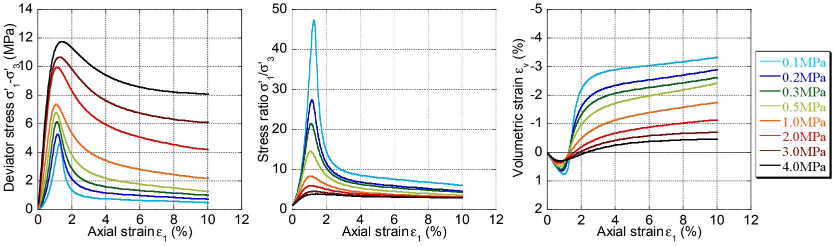

(a) deviator stress **(b) stress ratio** **(b) volumetric strain**

FIG. 6. Result of numerical simulation (*R* is not constant.).

CONCLUSIONS

- From the triaxial compression tests on soft rock, the strain softening behavior was clearly observed from all tests. It was confirmed that the peak strength, the residual strength and the dilatancy behaviors depend on the confining stress.
- From the numerical results by an original model, it was confirmed that the stress-strain behavior under high confining stress was reproduced by the present constitutive model. However, the stress-strain behavior under low confining stress could not be reproduced well.
- It was assumed that the shape of yield surface changes during shear process. It was assumed that new parameter R, which is associated with shape of yield surface, is decreasing linearly during the shear process. As the result, the stress-strain behaviors under different confining stresses were reproduced quantitatively.

In this study, it was assumed that R is decreasing linearly during shear process. As the result, the stress-strain behaviors under different confining stresses were reproduced quantitatively. However, the modification of the constitutive model for soft rock isn't complete at this stage. In the future, the change of R should be examined in detail.

REFERENCES

Aung H. (2006). "Modeling of time-dependent behavior of sedimentary soft rock and its application to progressive failure of slope." *Doctoral thesis*, Gifu University.

Hashiguchi, K. (1980). "Constitutive equation of elastplastic materials with elast-plastic transition, Jour. of Applied Mechanics, ASME, Vol. 102(2), 226-272."

Nakai, T. and Hinokio, M. (2004). "A simple elastoplastic model for normally and over consolidated soils with unified material parameters." *Soils and Foundations*, Vol. 44 (2), 53-70.

Nakai, T. and Mihara, Y. (1984). "A new mechanical quantity soils and its application to elastoplastic constitutive models." *Soils and Foundations*, Vol. 24 (2), 82-94.

Ye, G. L., Zhang, F., Naito, K., Aung, H. and Yashima, A. (2007). "Test on soft sedimentary rock under different loading paths and its interpretation." *Soils and Foundations*, Vol. 47 (5), 897-909.

Zhang, F., Yashima, A., Nakai, T., Ye, G. L. and Aung, H. (2005). "An elasto-viscoplastic model for soft sedimentary rock based on tij concept and subloading yield surface." *Soils and Foundations*, Vol. 45 (1), 65-73.

A Rate-dependent Constitutive Model for Sand and its FEM Application

Fulin Li[1], Fangle Peng[2], Ke Tan[3] and Warat Kongkikul[4]

[1]Department of Geotechnical Engineering, Tongji University, 1239 Siping Road, Shanghai 200092, P.R. China; lflmail@163.com
[2]Department of Geotechnical Engineering, Tongji University, 1239 Siping Road, Shanghai 200092, P.R. China; pengfangle@tongji.edu.cn
[3]Department of Geotechnical Engineering, Tongji University, 1239 Siping Road, Shanghai 200092, P.R. China; godisfair_tk@yahoo.com.cn
[4]Department of Civil Engineering, King Mongkut's University of Technology Thonburi, 126 Pracha-utid Road, Bangkok 10140, Thailand; waratk@gmail.com

ABSTRACT: It is well known that the deformation and strength characteristics of sand are very complicated, and time effects and strain localization are two of the most important aspects. A non-linear three-component rheology model consisting of a hypo-elastic component connected in series to a combination of non-linear inviscid and viscous components connected in parallel is proposed, which can take into account multi-factor influence on the deformation and strength characteristics of sandy soils. The inviscid component is described by an isotropic, energy-based hardening and softening, and non-associated energy model, while the viscous component is formulated based on the strain rate-dependent behavior of sandy soils. A finite element method (FEM) code incorporating the aforementioned model is validated by simulating the physical plane strain compression (PSC) tests on sand. It is shown that the proposed model can much better simulate the deformation and strength characteristics of sand, especially for the rate-dependent behaviors and strain localization into a shear band.

INTRODUCTION

The deformation and strength characteristics of sand are influenced by a lot of factors, such as void ratio, pressure, strength anisotropy, elastic anisotropy, stress dilatancy, volumetric hardening, time and strain localization induced by post-peak softening. In the present study, the time effects and strain localization are discussed. It is demonstrated that sand exhibits a complicated stress-strain-time behavior including instantaneous non-linearity and viscous effects. Loading rate effect, creep deformation and stress relaxation, which are the time-dependent response of material, should be attributed to the material viscous property. In the past, researchers have paid more attention to the study of creep and stress relaxation (Kuwano and Jardine 2002; Lade 2007). However, the effect of loading rate was not understood enough, especially under a change of loading rate. Matsushita et al. (1999) performed a set of plain strain compression (PSC) tests on Hostun sand to investigate the effects of constant rate of strain on the stress-stain behavior. It was found that the stress ratio and shear strain relationships for the constant axial strain rate, which are different by a factor of up to 500, are essentially independent of the axial stain rate. This trend was confirmed through drained triaxial compression tests performed on Antelope Valley sand (Lade 2007) and crushed coral sand (Lade et al. 2009). And it is different from the strain rate effects on clays, for which the stain rate corresponds to a unique stress-strain relation, exhibiting the isotach viscosity (Sorensen et al. 2007).

The most important aspect of loading rate effects is the trend in behavior observed in the tests under a change of loading rate (Matsushita et al. 1999; Tatsuoka et al. 2002; Peng et al. 2008; Li et al. 2009). In addition, the local strain fields in the specimen of Toyoura sand in drained PSC tests obtained by the photogrametric method (Tatsuoka et al. 1990) showed that the material strain-softening is associated with strain localization into a shear band(s) having a width independent of specimen size. In the present study, a non-linear three-component rheology model consisting of a hypo-elastic component connected in series to a combination of non-linear inviscid and viscous components connected in parallel was proposed, which can take into account both time effects and strain localization into a shear band for sand. By comparing the FEM simulated and measured results, it is shown that the rate-dependent behaviors and strain localization into a shear band can be well simulated.

FRAMEWORK OF CONSTITUTIVE MODEL

According to this non-linear three-component model (FIG. 1), the stress, σconsists of inviscid and viscous components, σ^f and σ^v, while the strain rate, $\dot{\varepsilon}$, consists of elastic and irreversible components, $\dot{\varepsilon}^{\mathrm{e}}$ and $\dot{\varepsilon}^{\mathrm{ir}}$, which can be expressed as:

$$\dot{\varepsilon} = \dot{\varepsilon}^e + \dot{\varepsilon}^{ir} \tag{1}$$

$$\sigma = \sigma^f + \sigma^v \tag{2}$$

E is the cross-anisotropic hypo-elastic component, P is the non-linear inviscid component, and V is the nonlinear viscous component, respectively.

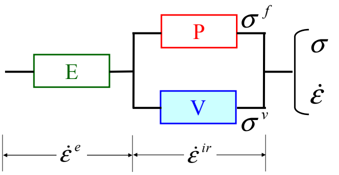

FIG. 1. Non-linear three-component elasto-viscoplastic model.

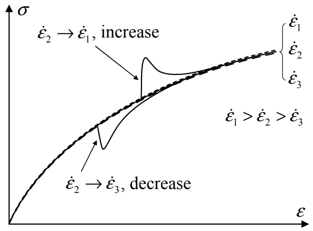

FIG. 2. Schematic diagram of loading rate effects on sand.

Cross-anisotropic hypo-elastic model

An inherent and stress system-induced cross-anisotropic compliance matrix for elastic strain increments was employed in the present study, which was obtained on the basis of the results from triaxial tests on large square prismatic specimens of sands measuring locally vertical and horizontal strains (Hoque and Tatsuoka 1998). According to the model, the elastic Young's modulus defined for the major principal strain increment taking place in a certain direction is a unique function of the normal stress acting in that direction, while the Poisson's ratios for elastic strain increments change with the changes in the stress ratio. More details about this model can be found in Hoque and Tatsuoka (1998).

Energy-based hardening and softening plastic model

The inviscid component P is formulated based on an isotropic, work-hardening and softening, and non-associated plastic model. The yield function, *F*, and the irreversible potential function, *G*, are assumed to be Mohr-Coulomb type and Drucker-Prager type, respectively. It was also assumed that strain localization into a shear band(s) starts suddenly at the peak stress state (Tatsuoka et al. 1993).

Yasin and Tatsuoka (2000) performed a series of drained PSC tests on the saturated dense Toyoura sand along various stress paths. It was found that all of the strain increments (i.e., axial, lateral, shear and volumetric) between two stress states noticeably depended on the intermediate stress paths. Then, the following modified irreversible strain energy was proposed as the work-hardening parameter (Peng et al. 2009):

$$W^{ir*} = \int \frac{\sigma_{ij}^{f}\,\mathrm{d}\varepsilon_{ij}^{ir}}{(p^{f}/p'_{a})^{n}} \approx \int \frac{t^{f}\cdot\mathrm{d}\gamma^{ir} + s^{f}\cdot\mathrm{d}\varepsilon_{vol}^{ir}}{(s^{f}/p'_{a})^{n}} \tag{3}$$

where $\sigma_{ij}^{f}\mathrm{d}\varepsilon_{ij}^{ir}$ is the irreversible strain energy increment; $t^{f} = (\sigma_{v}^{f} - \sigma_{h}^{f})/2$ and $s^{f} = (\sigma_{v}^{f} + \sigma_{h}^{f})/2$; $p'_{a} = 98.1\,\mathrm{kPa}$; $\mathrm{d}\gamma^{ir}$ and $\mathrm{d}\varepsilon_{vol}^{ir}$ are the irreversible shear and volumetric strains; *n* is a material constant (equal to 0.9 for Toyoura sand in PSC tests). σ_{v}^{f} and σ_{h}^{f} are the inviscid vertical and horizontal stresses activated in component P, while, σ_{v}^{v} and σ_{h}^{v} are the viscous stresses activated in component V.

According to Peng et al. (2009), the following hardening function for the pre-peak regime could be assumed:

$$X^{f}\left(W^{ir*}\right) = a \times \ln\left(\frac{W^{ir*}}{b\cdot p'_{a}} + h\right) \tag{4}$$

where X^{f} is a stress parameter which is a function of stress level, defined as:

$$X^{f} = \frac{t^{f}}{s^{f}} + r\cdot\ln\left(\frac{s^{f}}{p'_{a}}\right) \tag{5}$$

where *a*, *b*, *h* and *r* are the material constants, and *a* = 0.1288 , *b* = 3.4505×10^{-5}, *h* = 0.431, and *r* = 0.09 for Toyoura sand.

The irreversible strain energy hardening function at pre-peak is not flat at the peak state. Hence, it is necessary to introduce some modification to alleviate this drawback. Here, Eq. (6) is used to fit an arbitrarily chosen small range immediately before the peak stress state:

$$X^f\left(W^{ir*}\right) = X^f_{\max} \times \left(\frac{2\sqrt{W^{ir*}W_p}}{W^{ir*} + W_p} \right)^K \tag{6}$$

where $X^f_{\max}$ and W_p are the values of $X^f\left(W^{ir*}\right)$ and W^{ir*} at the peak stress state. The power K is a constant. Then, using the three-point fitting method, the parameter K is obtained as:

$$K = \log\left(\frac{X^f_1}{X^f_{\max}} \right) / \log\left(\frac{2\sqrt{W_1 \cdot W_p}}{W_1 + W_p} \right) \tag{7}$$

where W_1 is W^{ir*} obtained by substituting X^f_1 = 0.8 $\mathrm{X}^f_{\max}$ into the measured work-hardening function, Eq. (4).

To model the post-peak strain-softening property in a shear band, the following work-softening function was introduced:

$$X^f\left(W^{ir*}\right) = X^f_r + \left(X_{\max}{}^f - X_r{}^f\right)\exp\left[-\left(\frac{W^{ir*} - W_p}{W_r} \right)^2 \right] \tag{8}$$

where W_r is the irreversible work-softening parameter, which determines the rate of decrease in the inviscid stress parameter, $X^f\left(W^{ir*}\right)$, from the peak value, $\mathrm{X}^f_{\max}$, towards the residual value, X^f_r.

Following Tanaka and Sakai (1993), shear banding in a given finite element was introduced by using a strain localization parameter, S, in the additive decomposition of total strain increment as:

$$\mathrm{d}\varepsilon_{ij} = \mathrm{d}\varepsilon^e_{ij} + S \cdot \mathrm{d}\varepsilon^{ir}_{ij} \tag{9}$$

where $\mathrm{d}\varepsilon_{ij}$ and $\mathrm{d}\varepsilon^e_{ij}$ are the average total and elastic strain increments in a given finite element; $\mathrm{d}\varepsilon^{ir}_{ij}$ is the irreversible strain increment in a shear band; $S = F_b/F_e$, in which F_b is the area of the shear band in each finite element and F_e is the area of the finite element. By ignoring the effects of the orientation of shear band in each finite element, an approximated form of S can be expressed as:

$$S = w / \sqrt{F_e} \tag{10}$$

where w is the width of shear band, equal to 0.3 cm for Toyoura sand. No direction of shear banding is specified. It is implicitly assumed that the direction of shear band coincides in a broad sense with the direction of maximum shear strain. Therefore, the elasto-plastic stress-strain relation incorporating shear banding can be expressed as:

$$\mathrm{d}\sigma_{ij}^{f} = \left[D_{ijkl}^{e} - \frac{D_{ijkl}^{e} b_{kl} a_{ij}^{T} D_{ijkl}^{e}}{H' / S + a_{ij} D_{ijkl}^{e} b_{kl}} \right] \mathrm{d}\varepsilon_{ij} \tag{11}$$

where D_{ijkl}^{e} is the elastic matrix; $a_{ij} = \partial F / \partial \sigma_{ij}^{f}$; $b_{ij} = \partial G / \partial \sigma_{ij}^{f}$; and $H' = -(\partial F / \partial W^{ir*}) \cdot \sigma_{ij}^{f} \cdot b_{ij} / (s^{f} / p'_{a})^{n}$. More details about the energy-based model can be found in Peng et al. (2009).

Rate-dependent non-linear viscous model

Based on the results from the drained PSC, TC (triaxial compression), TE (triaxial extension) and DS (direct shear) tests on the unbound geomaterials, it was found that viscous properties of geomaterials can be characterized by σ^{v}, activated in component V in FIG. 1. σ^{v} is a function of ε^{ir}, $\dot{\varepsilon}^{ir}$ and the strain history parameter, h_{s}. Firstly, the isotach model was proposed to describe viscous properties of clay-like materials. In monotonic loading (ML) case, the isotach viscous stress, σ_{iso}^{v}, is a unique function of the instantaneous value of ε^{ir} and its rate $\dot{\varepsilon}^{ir}$, while it is always proportional to the instantaneous value of σ^{f}. Then, it can be expressed as:

$$\sigma^{v} = \sigma_{iso}^{v}(\varepsilon^{ir}, \dot{\varepsilon}^{ir}) = \sigma^{f}(\varepsilon^{ir}) \cdot g_{v}(\dot{\varepsilon}^{ir}) \tag{12}$$

where $g_{v}(\dot{\varepsilon}^{ir})$ is the viscosity function with $g_{v}(0) = 0$ and $g_{v}(\infty) = \alpha$(a positive constant) and given as follows for any strain history:

$$g_{v}(\dot{\varepsilon}^{ir}) = \alpha \cdot \{1 - \exp[1 - (|\dot{\varepsilon}^{ir}| / \dot{\varepsilon}_{r}^{ir} + 1)^{m}]\} \ (\geq 0) \tag{13}$$

On the other hand, for poorly-graded angular granular materials (i.e., Toyoura sand), the stress-strain relation exhibits a noticeable stress-overshooting and undershooting behavior (FIG. 2). Namely, upon a step increase in the strain rate, the stress value increased at a very high rate. After having exhibited clear yielding, the stress-strain curve tended to rejoin the original inferred one that would be obtained by continuous ML at constant strain rate. And a phenomenon of stress-undershooting took place immediately after a step decrease in the strain rate during otherwise ML. Di Benedetto et al. (2002) and Tatsuoka et al. (2002) indicated that the viscous properties of sands cannot be properly described by the isotach model. Hence, a new viscous model, called the TESRA (Temporary Effect of Strain Rate and Acceleration) model, had been proposed. This means even under the loading conditions, the effects of $\dot{\varepsilon}^{ir}$ and its rate (i.e., irreversible strain acceleration) on the σ^{v} value become temporary, therefore, the current σ^{v} value becomes a function of not only instantaneous values of ε^{ir} and $\dot{\varepsilon}^{ir}$ but also recent strain history. Then, the TESRA viscous stress, σ_{TESRA}^{v}, can be obtained as:

$$\sigma^{v} = \sigma_{TESRA}^{v}(\varepsilon^{ir}, \dot{\varepsilon}^{ir}, h_{s}) = \int_{\tau=\varepsilon_{1}^{ir}}^{\varepsilon^{ir}} [\mathrm{d}\sigma_{iso}^{v}]_{(\tau)} \cdot r_{d}^{(\varepsilon^{ir} - \tau)} \tag{14}$$

where ε_1^{ir} is the initial irreversible strain at $\sigma^v = 0$; $[\mathrm{d}\sigma^v_{iso}]_{(\tau)}$ is the developed viscous stress increment at $\varepsilon^{ir} = \tau$; r_d is the decay parameter that is positive less than unity. In this way, the current value of σ^v_{TESRA} (when $\varepsilon^{ir} = \varepsilon^{ir}$) depends on the history of ε^{ir}. When $r_d = 1.0$, σ^v_{TESRA} (Eq. (14)) is the same as σ^v_{iso} (Eq. (12)).

MODEL ASSESSMENT AND VALIDATION

A FEM code incorporating the aforementioned model for sand was developed. The Dynamic Relaxation technique was used to solve the non-linear equations caused by high friction angle materials such as the one analyzed in this study. The algorithm for updating the stress was developed by using the Return Mapping scheme, which is a first-order approximated Euler backward integration. The elasto-viscoplastic solution was incrementally obtained on the basis of the elasto-plastic solution.

The FEM mesh was divided into 20 and 16 in the vertical and horizontal directions with an element size of 6 mm × 6 mm (FIG. 3). The global initial width and height of mesh are 96 mm and 120 mm, respectively, which are the same as the dimensions of the sand specimen on σ_2-plane used in the drained PSC tests, which are used to validate the proposed model. The drained PSC tests were performed on saturated Toyoura sand under various loading histories. In the FEM analysis, the initial confining pressure was first applied to all the plane strain elements. The nodal velocities were equally applied at the top and bottom boundaries of the FEM mesh tracing the measured time history of vertical strain in the tests. The creep loading was simulated under stress-controlled conditions using the measured time histories of stress (i.e., $\dot{\sigma} = 0$).

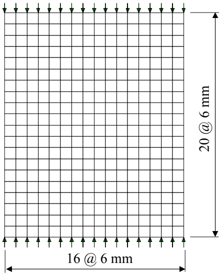

FIG. 3. FEM mesh.

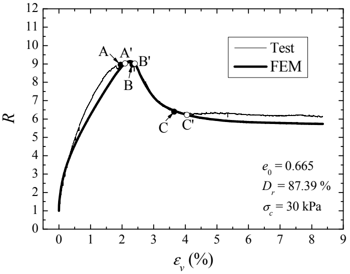

FIG. 4. FEM simulation of continuous monotonic loading test.

FIG. 4 compares the global R-ε_v relation of the measured result and the corresponding FEM simulation for the PSC test at a constant strain rate of 0.04 %/min. FIG. 5 compares the contours of the maximum shear strain, $\gamma_{\max}$, at the corresponding stages A, B and C from the test and stages A', B' and C' from the FEM simulation in FIG. 4. It can be seen that the overall pattern of stress-strain behavior is a good agreement between the test and the FEM simulation and the FEM analyses capture reasonably the strain localization into a V-shaped shear band.

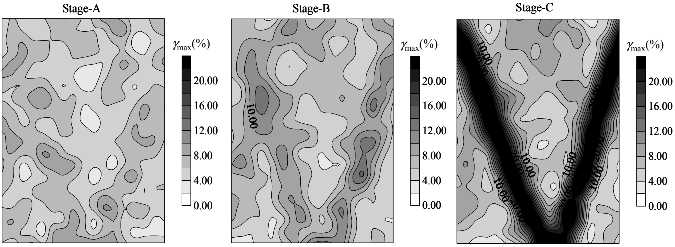

(a) physical test

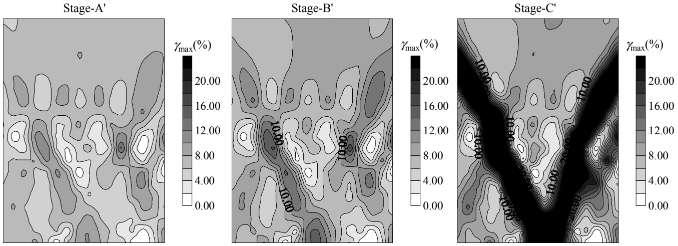

(b) FEM analyses

FIG. 5. Maximum shear strain fields for PSC test in FIG. 4: (a) physical test, and (b) FEM analyses.

FIG. 6 shows the FEM simulated results from the PSC test, where the strain rate was changed step-by-step several times with one stress relaxation stage and two creep loading stages. FIG. 7 shows the FEM simulated results from the PSC test at constant strain rate with multi-staged creep loading. The test results are also presented. By comparing the measured with the simulated R-ε_v relation, time histories of ε_v and R, it can be seen that the time effects on stress-strain relation are well simulated, such us the stress jump upon the step-change in the strain rate, creep deformation and stress relaxation.

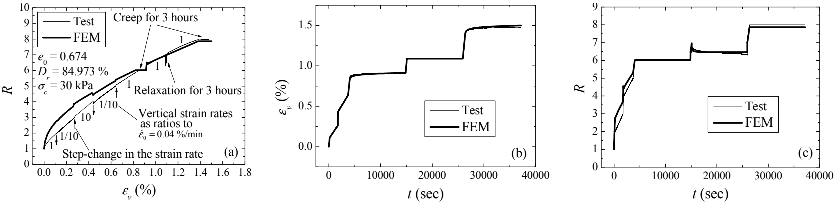

FIG. 6. FEM simulated and the measured results from PSC test under complex loading histories: (a) R-ε_v relation, (b) time history of ε_v, and (c) time history of R.

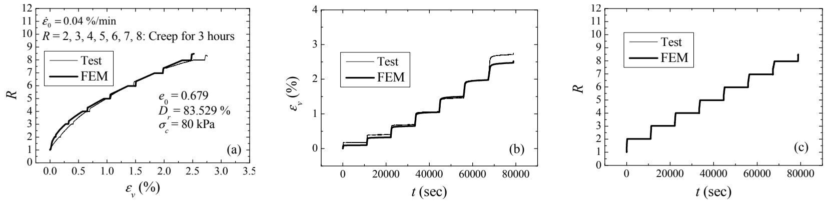

FIG. 7. FEM simulated and the measured results from PSC test with multi-stage creep loading: (a) R-ε_v relation, (b) time history of ε_v, and (c) time history of R.

CONCLUSIONS

(1) The proposed elasto-viscoplastic model is able to describe the features of non-linear pre-peak, pressure-sensitivity, non-associated flow characteristics, post-peak softening associated with strain localization into a shear band and time effects for sandy soils.
(2) The FEM analyses incorporating the proposed model can reasonably reflect the strain localization into a shear band as in the physical test and realistically simulate the viscous properties of sand, including loading rate effect, creep and stress relaxation.
(3) The whole process of simulation including the variable strain rate loadings, the creep loading and stress relaxation stages could be implemented in the FEM analyses.

ACKNOWLEDGMENTS

The authors would like to express their sincere thanks to Prof. Fumio Tatsuoka, Department of Civil Engineering, Tokyo University of Science, for his erudite guidance and discussions. The authors acknowledges gratefully the support provided by China National Key Technology R&D Program (2006BAJ27B02-02), SRF for ROCS (SEM), Shuguang Project (No. 05SG25), NSFC (No. 50679056 & 40972176), NCET (06-0378), and Shanghai Leading Academic Discipline Project (B308).

REFERENCES

Di Benedetto, H., Tatsuoka, F., and Ishihara, M. (2002). "Time-dependent shear deformation characteristics of sand and their constitutive modeling." *Soils Found.*, Vol. 42 (2): 1-22.

Hoque, E. and Tatsuoka, F. (1998). "Anisotropy in the elastic deformation of materials." *Soils Found.*, Vol. 38 (1): 163-179.

Kuwano, R. and Jardine, R.J. (2002). "On measuring creep behaviour in granular materials through triaxial testing." *Can. Geotech. J.*, Vol. 39 (5): 1061-1074.

Lade, P.V. (2007). "Experimental Study and analysis of creep and stress relaxation in granular materials." *Proc. of Sessions of Geo-Denver 2007: Advances in Measurement and Modeling of Soil Behavior* (GSP 173), ASCE, Reston/VA: 1-11.

Lade, P.V., Liggio Jr, C.D. and Nam, J. (2009). "Strain rate, creep, and stress drop-creep experiments on crushed coral sand." *J. Geotech. Geoenviron. Eng.*, Vol. 135 (7): 941-953.

Li, F.L., Peng, F.L., Li, J.Z. and Kongkitkul, W. (2009). "Strain rate effects on sand and its quantitative analysis." *J. Cent. South Univ. Technol.*, Vol. 16 (4): 658-662.

Matsushita, M., Tatsuoka, F., Koseki, J., Cazacliu, B., Di Benedetto, H. and Yasin, S.J.M. (1999). "Time effects on the pre-peak deformation properties of sands." *Proc. 2nd Int. Conf. on Pre-failure Deform. Charact. of Geomat.*, A. A. Balkema, Torino: 681-689.

Peng, F.L., Li, F.L., Li, J.Z., Kongkitkul, W. and Tatsuoka, F. (2008). "Viscoplastic behaviors and constitutive modeling of sands under change of loading rates." *Chin. J. Rock Mech. Eng.*, Vol. 27 (8): 1576-1585. (in Chinese)

Peng, F.L., Siddiquee, M.S.A., Tatsuoka, F., Yasin, S.J.M. and Tanaka, T. (2009). "Strain energy-based elasto-viscolastic constitutive modeling of sand for numerical simulation." *Soils Found.*, Vol. 49 (4): 611-629.

Sorensen, K.K., Baudet, B.A. and Simpson, B. (2007). "Influence of structure on the time-dependent behaviour of a stiff sedimentary clay." *Geotechnique*, Vol. 57 (1): 113-124.

Tanaka, T. and Sakai, T. (1993). "Progressive failure and scale effect of trap-door problem with granular materials." *Soils Found.*, Vol. 33 (1): 11-22.

Tatsuoka, F., Ishihara, M., Di Benedetto, H. and Kuwano, R. (2002). "Time-dependent shear deformation characteristics of geomaterials and their simulation." *Soils Found.*, Vol. 42 (2): 103-129.

Tatsuoka, F., Nakamura, S., Huang, C.C. and Tani, K. (1990). "Strength anisotropy and shear band direction in plane strain tests on sand." *Soils Found.,* Vol. 30 (1): 35-54.

Tatsuoka, F., Siddiquee, M.S.A., Park, C.S., Sakamoto, M., and Abe, F. (1993). "Modelling stress-strain relation of sand." *Soils Found.*, Vol. 33 (2): 60-81.

Yasin, S.J.M., and Tatsuoka, F. (2000). "Stress history-dependent deformation characteristics of dense sand in plane strain." *Soils Found.*, Vol. 40 (2): 77-98.

A Double Modified Plastic Work-Hardening Constitutive Model for Sand under Plane-Strain Conditions

Xiaoyu Bai [1], Fangle Peng[2], Ke Tan [3] and S.J.M.Yasin [4]

[1]Department of Geotechnical Engineering, Tongji University, 1239 Siping Road, Shanghai 200092, P.R. China & Shenzhen Metro Co. Ltd., 1016 Fuzhong No.1 Road, Shenzhen 518026, P. R. China; typhoon79@sohu.com
[2]Department of Geotechnical Engineering, Tongji University, 1239 Siping Road, Shanghai 200092, P.R. China; pengfangle@tongji.edu.cn
[3]Department of Geotechnical Engineering, Tongji University, 1239 Siping Road, Shanghai 200092, P.R. China; godisfair_tk@yahoo.com.cn
[4]Department of Civil Engineering, Bangladesh University of Science and Engineering, Dhaka 1000, Bangladesh; yasinsarwar@yahoo.com

ABSTRACT: Based on the results from the isotropic loading-unloading tests and a series of plane strain compression tests along different stress path on Toyoura sand, a couple of hardening functions respectively for shear and volumetric plastic strain for sand is introduced in the framework of double hardening elasto-plastic constitutive model. A modified form of plastic compressive strain energy, which is stress path-independent, and a volumetric yielding locus compose the compression hardening model. Another modified plastic shear strain energy, which is also stress path-independent, and a shear yielding locus compose the shear hardening model. Then, the plastic strains can be described as the sum of two independent parts. Based on the above, a double modified plastic work-hardening constitutive model for sandy soils is proposed. It is shown that, based on the direct comparisons between the results from the numerical calculation and corresponding drained plane strain compression tests on Toyoura sand, the above-proposed constitutive model could reasonably simulate the deformation and strength behavior of sand with different stress-path.

INTRODUCTION

The hardening rule is a necessary component in the plasticity theory. It is required that the hardening parameter has a unique relationship with stress state. But the deformation behavior of sand is deeply affected by stress paths. So it is difficult to find a hardening parameter or hardening function independent of stress path. The results from a series of high precision plane strain tests along different stress paths on Toyoura sand (FIG.1, Yasin and Tatsuoka 2000) show that the shear strain, volumetric strain, plastic shear strain, plastic volumetric strain and even plastic work are stress-path dependent. Therefore, they can not be taken as the appropriate hardening parameter. Based on the tests, a modified plastic work independent of stress path is proposed by Yasin and Tatsuoka (2000). Then an elastoplastic shear hardening constitutive model for sand is formulated based on the modified plastic work (Peng et al. 2009). In this model, the effects of stress path is properly considered. However, the single shear hardening constitutive model cannot simulate the plastic strain of sand during isotropic loading. So in constitutive modeling of sand, volumetric hardening reflects the phenomena of plastic deformation during isotropic loading should be included. Roscoe and Burland (1968) firstly introduced the conception of double-hardening, they suggested that the plastic strain occurred in soil should result from both the shear yielding and the volumetric yielding. Based on this, a great number of double-hardening (double-yielding) models (Lade 1977; Vermmer 1978; Yin 1988; Shen 1990) have been presented for geomaterials. In this paper, based on a series of high precision isotropic loading-unloading ($\sigma_1' = \sigma_3'$) triaxial tests (Hoque 1996; Hoque and Tatsuoka1998) and plane strain compression tests along different stress paths (Yasin and Tatsuoka 2000) on Toyoura sand, a modified plastic work double-hardening function independent of stress path is presented for sand. Based on the proposed hardening function, the shear-volumetric double hardening constitutive model for sand is formulated. Finally, the proposed model is validated by the comparisons between numerical calculation results and physical plane strain test results.

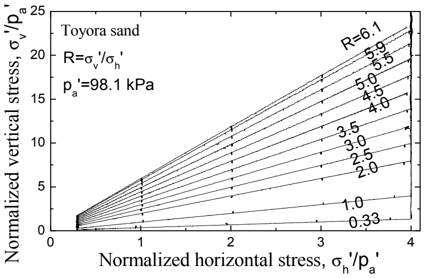

FIG.1. Stress paths for plane strain tests on Toyora sand (from Yasin and Tatsuoka 2000)

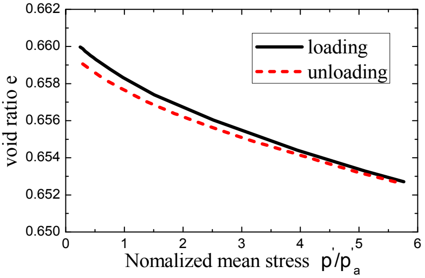

FIG.2. Isotropic loading- unloading experimental results for Toyora sand. (from Hoque 1996; Hoque and Tatsuoka 1998)

MODIFIED PLASTIC WORK VOLUMETRIC HARDENING FUNCTION

Different from metal, plastic deformation of sand occurs during isotropic loading-unloading. This comes to be known as volumetric hardening of sand. FIG.2 shows the isotropic loading-unloading experimental results for Toyora sand (Hoque 1996; Hoque and Tatsuoka 1998). The figure indicates the existence of plastic volumetric deformation under isotropic loading, and it is difficult to be explained by the single shear-hardening model.

The test results above show that the plastic deformation of sand composed of two parts, shear hardening and volumetric hardening. Based on isotropic loading-unloading experimental results for Toyoura sand, a modified plastic work volumetric hardening function for sand will be introduced. Unlike cohesive soil, the relation of sand between volumetric deformation and $\ln p'$ is always non-linear. Based on results from triaxial isotropic loading and unloading tests, Nakai (1989) proposed the following relation between plastic volumetric strain and mean effective stress for sand during isotropic loading:

$$\left(\varepsilon_{vol}^{p}\right)_{c} = \left(C_t - C_e\right)\left[\left(p'/p'_a\right)^{N} - \left(p'_0/p'_a\right)^{N}\right] \tag{1}$$

where C_t and C_e are constant related with isotropic loading-unloading curve, N is a material constant, p' is the mean effective stress, p'_0 is p' in the initial state, $p'_a = 98.1\text{kPa}$ is the atmospheric pressure. FIG.3 gives the relationship between $\left(p'/p'_a\right)^{N}$ and volumetric strain ε_{vol} during isotropic loading and unloading of Toyoura sand. For Toyoura sand, $C_t = 0.18$, $C_e = 0.16$, $N = 0.6$.

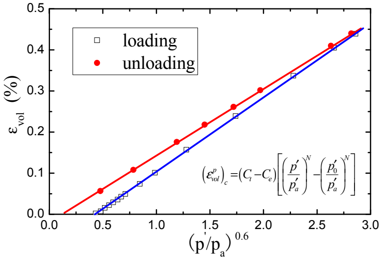

FIG.3 Fitting relationship between mean effective stress and volumetric strain during isotropic loading and unloading

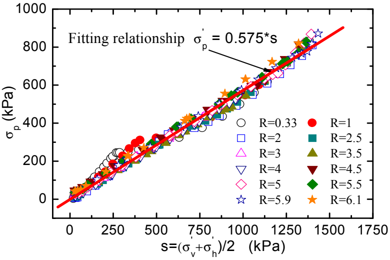

FIG.4 Fitting relationship between σ'_p and $s = \left(\sigma'_v + \sigma'_h\right)/2$

In plane strain conditions $p' = \left(\sigma'_1 + \sigma'_2 + \sigma'_3\right)/3 = \left(\sigma'_v + \sigma'_p + \sigma'_h\right)/3$. σ'_v, σ'_p and σ'_h are the principal stress in vertical, plane strain and horizontal direction respectively. So we need to know the value of σ'_p, the principal stress in plane strain direction, to calculate the plastic volumetric strain during isotropic loading. Stroud (1971) and Vermeer (1978) concluded the ratio of σ'_p to s ($s = \left(\sigma'_v + \sigma'_h\right)/2$) for sand is a constant under plane strain conditions, that is $\sigma'_p = Cs$. Before the proposal of plastic volumetric hardening function, the relation between σ'_p and principal stress in other two directions is discussed (FIG.4) based on results of plane strain tests along different R stress path on Toyoura sand from Yasin and Tatsuoka (2000).

FIG.4 validates the conclusion from Stroud (1971) and Vermeer (1978). For Toyoura sand, we could obtain the following fitting equation:

$$\sigma'_p = 0.575s \tag{2}$$

Substituting Eq.2 into Eq.1, we obtain the following equation:

$$\left(\varepsilon_{vol}^{p}\right)_{c}=\left(C_{t}-C_{e}\right)\left[\left(0.858s/p_{a}'\right)^{N}-\left(p_{0}'/p_{a}'\right)^{N}\right] \tag{3}$$

When double hardening is considered in the modeling, the total modified plastic work parameter $\mathrm{d}W_{t}^{p*}$ reach the following form:

$$\mathrm{d}W_{t}^{p*}=\mathrm{d}W_{s}^{p*}+\mathrm{d}W_{c}^{p*} \tag{4}$$

where $\mathrm{d}W_{s}^{p*}$ and $\mathrm{d}W_{c}^{p*}$ are increment of modified plastic work parameter induced by shear hardening and volumetric hardening, respectively. And $\mathrm{d}W_{c}^{p*}$ has following expression:

$$\mathrm{d}W_{c}^{p*}=\left[s\cdot\left(\mathrm{d}\varepsilon_{vol}^{p}\right)_{c}\right]/\left(s/p_{a}'\right)^{n} \tag{5}$$

where n is a material constant, and its determination can be given by the laboratory tests with different stress-path. According to Yasin and Tatsuoka (2000), $n=0.9$ for Toyoara sand. In the volumetric hardening function, a yield locus needs to be determined. Similar to Vermeer's double hardening model (Vermeer 1978), the line perpendicular to s axis in $s-t$ plane is chosen as the volumetric yield line. Here $t=\left(\sigma_{v}'-\sigma_{h}'\right)/2$. Thus the equation of volumetric yield locus could be given as:

$$X_{c}=s/p_{a}' \tag{6}$$

Substituting Eq.6 into Eq.3, the following equation is obtained:

$$\left(\mathrm{d}\varepsilon_{vol}^{p}\right)_{c}=0.858^{N}\cdot\left(C_{t}-C_{e}\right)\cdot N\cdot X_{c}^{N-1}\mathrm{d}X_{c} \tag{7}$$

Substituting Eq.7 into Eq.5 and integral it, the modified plastic work volumetric hardening function is obtained:

$$W_{c}^{p*}/p_{a}'=1.564\times10^{-4}\cdot\left(X_{c}^{0.7}-X_{c0}^{0.7}\right) \tag{8}$$

where X_{c0} is the X_{c} in the initial state.

MODIFIED PLASTIC WORK SHEAR HARDENING FUNCTION

When the effects of shear hardening and volumetric hardening are considered, the stress state function corresponding to shear hardening function has the same form with single shear hardening model (Yasin and Tatsuoka 2000; Peng et al. 2009):

$$X_s = \eta + r\ln(s/p'_{\mathrm{a}}) = t/s + r\ln(s/p'_{\mathrm{a}}) \tag{9}$$

where r is a material constant, and $t = (c'_v - c'_h)/2$.

Here the expression of shear hardening function is given as:

$$X_s = a\ln\left(Y_s/b + h\right) \tag{10}$$

where a, b, h are all Material constants, $Y_s = W_s^{p*}/p'_a = \left(W_t^{p*} - W_c^{p*}\right)/p'_a$, W_c^{p*} is given in Eq.8 . So the following equation is obtained:

$$W_s^{p*} = \int\left[t\cdot \mathrm{d}\gamma^p + s\cdot\left(\mathrm{d}\varepsilon_{vol}^p\right)_s\right]/\left(s/p'_a\right)^n \tag{11}$$

where n is same as the n in Eq.5. Based on results from plane strain compression tests for Toyoura sand, when $n = 0.9$ and $r = 0.09$, a unique relation between X_s and W_s^{p*}/p'_a with different stress path is achieved (FIG. 5), which is independent of stress path. Fitting the relation between X_s and W_s^{p*}/p'_a with Eq.10, the shear hardening function independent of stress path is obtained. For Tayoura sand, the value of parameters in the shear hardening function are $a = 0.1317$, $b = 4.0\times10^{-5}$, $h = -8.0$ (FIG. 6). More details about the modified plastic work-hardening model for plastic shear strain can be found in Peng et al. (2009).

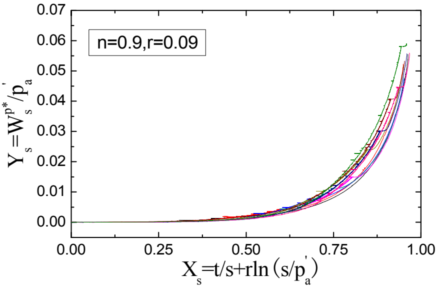

FIG.5. Relationship between X_s and W_s^{p*}/p'_a for different stress-path

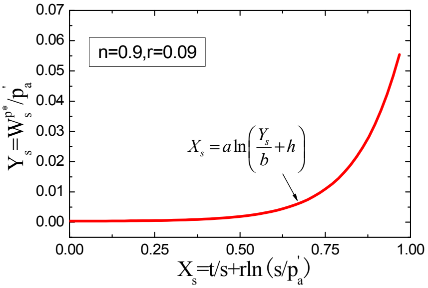

FIG.6. Shear hardening function of stress path-independent

SHEAR-VOLUMETRIC DOUBLE HARDENING CONSTITUTIVE MODEL

In the modified plastic work double-hardening constitutive model proposed for sand in this paper, Hoque's cross-anisotropy hypo-elastic model (Hoque 1996) is used. So the elastic section of the model considers the effects of anisotropy. The plastic section formulated based on the modified plastic work shear-volumetric double-hardening function mentioned above.

The yield function and plastic potential function for shear hardening are assumed to be Mohr — Coulomb and Drucker — Prager type respectively. Yield function F_s corresponding to shear hardening is defined as:

$$F_s = -\eta I_1 + \sqrt{J_2} / g(\theta) - k_1 = 0 \tag{12}$$

where I_1 is the first stress invariant, J_2 is the second stress deviator, $g(\theta)$ is the lode angle function, defined as:

$$g(\theta) = \frac{3 - \sin\varphi_{mob}}{2\sqrt{3}\cos\theta - 2\sin\theta\sin\varphi_{mob}} \tag{13}$$

η is the deviatoric stress in π plane when $\theta = 30°$, which controls the growth of shear yield surface with hardening parameter W_s^{p*} and is related to mobilized angle of internal friction, namely:

$$\eta = \frac{2\sin\varphi_{mob}}{\sqrt{3}(3 - \sin\varphi_{mob})} \tag{14}$$

φ_{mob} is mobilized angle of internal friction, and the expression of $\sin\varphi_{mob}$ is :

$$\sin\varphi_{mob} = \frac{\sigma_1' - \sigma_3'}{\sigma_1' + \sigma_3'} = \frac{\sigma_v' - \sigma_h'}{\sigma_v' + \sigma_h'} = t / s = X_s - r \cdot \ln(s / p_a') \tag{15}$$

Plastic potential function G_s corresponding to shear hardening is expressed as:

$$G_s = -\alpha' I_1 + \sqrt{J_2} - k_2 = 0 \tag{16}$$

For sand, k_2 and k_1 are all equal to zero. In plane stain conditions:

$$\alpha' = \frac{\tan\psi_{mob}}{\sqrt{9 + 12\tan^2\psi_{mob}}} \tag{17}$$

where ψ_{mob} is the mobilized dilatancy angle of sand, and could be given by dilatation relation. Considering the effect of both shear hardening and volumetric hardening, the mobilized dilatancy angle can be expressed as:

$$\psi_{mob} = \arcsin\left[-\left(\mathrm{d}\varepsilon_{vol}^{p}\right)_s / \mathrm{d}\gamma^p\right] \tag{18}$$

where $\left(\mathrm{d}\varepsilon_{vol}^{p}\right)_s$ is plastic volumetric strain increment caused by shear hardening (=total plastic volumetric strain increment- plastic volumetric strain increment caused by volumetric hardening). According to Yasin and Tatsuoka (2000), the average dilatancy relation can be expressed as:

$$t/s = m\left[-\left(\mathrm{d}\varepsilon_{vol}^{p}\right)_{s}/\mathrm{d}\gamma^{p}\right]+c \tag{19}$$

where m and c are material constants, and $m = 0.636$ and $c = 0.635$ for Toyoura sand.

For volumetric hardening, the yield functions and plastic potential function have the same form, that is $F_c = G_c$. The volumetric yield function is derived from volumetric hardening function:

$$F_c = \beta\left(\frac{\sigma_1' + \sigma_3'}{2p_a'}\right)^{\alpha} + k_1 - W_c^{p*}/p_a' = 0 = G_c \tag{20}$$

For Toyoura sand, $\alpha = 0.7$, $\beta = 1.564\times10^{-4}$, $k_1 = -\beta\left[s_0/p_a'\right]^{\alpha}$, s_0 is s in initial state.

MODEL VALIDATION

The proposed modified plastic work double-hardening constitutive model is applied into the numerical simulation of plane strain compression tests with different stress paths on Toyoura sand to validate the model. FIG. 7(a) and (b) show the comparisons between numerical simulation results and physical plane strain compression experimental results along different stress paths. It can be seen from FIG. 7(a) and (b) that results from numerical simulation are well accordance with those from physical tests. The double-hardening model proposed in this paper could not only simulate the effect of stress path properly, but also reflect the strength and deformation properties of sand reasonably.

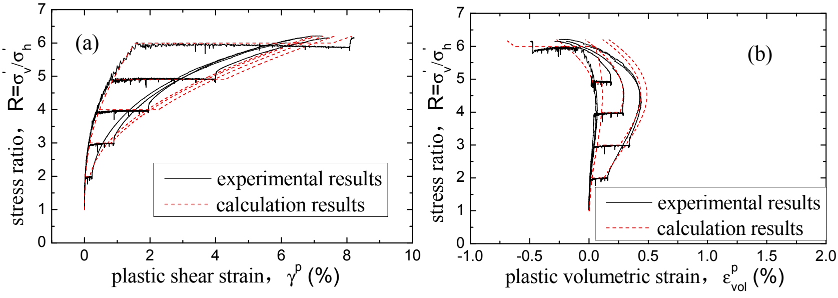

FIG.7 Comparisons between calculation results and physical experimental results: (a) Relation between plastic shear strain and principal stress ratio; (b) Relation between plastic volumetric strain and principal stress ratio.

CONCLUSIONS

(1) A couple of hardening parameter and function respectively for shear and volumetric plastic strain for sandy soils is proposed, which is stress path-independent.
(2) An elastoplastic double-hardening constitutive model incorporating the above hardening parameter and function is formulated. By the comparisons between results from numerical calculation and those from physical plane strain compression tests, the proposed constitutive model is validated. It is shown that the proposed model can reasonably reflect the strength and deformation characteristics of sand as well as the effect of stress path.

ACKNOWLEDGMENTS

The authors would like to express their sincere thanks to Prof. Fumio Tatsuoka, Department of Civil Engineering, Tokyo University of Science, for his erudite guidance and discussions. The authors acknowledge gratefully the support provided by China National Key Technology R&D Program (2006BAJ27B02-02), SRF for ROCS (SEM), Shuguang Project (No. 05SG25), NSFC (No. 50679056 & 40972176), NCET (06-0378), and Shanghai Leading Academic Discipline Project (B308).

REFERENCES

Hoque, E. (1996). "Elastic deformation of sands in triaxial test." *Ph. D. Thesis*, Tokyo: The University of Tokyo.

Hoque, E. and Tatsuoka, F. (1998). “Anisotropy in the elastic deformation of materials.” *Soils Found.*, Vol. 38 (1): 163-179.

Lade, P.V. (1977). "Elastoplastic stress-strain theory for cohesionless soil with curved yield surface." *International Journal of Solids and Structures*. Vol. 13: 1019-1035.

Nakai, T. (1989). "An isotropic hardening elastoplastic constitutive model for sand considering the stress path dependency in three-dimensional stresses." *Soils Found.*, Vol. 29 (1): 119-137.

Peng, F.L., Siddiquee, M.S.A., Tatsuoka, F., Yasin, S.J.M. and Tanaka, T. (2009). “Strain energy-based elasto-viscolastic constitutive modeling of sand for numerical simulation.” *Soils Found.*, Vol. 49 (4): 611-629.

Roscoe, K.H. and Burland, J.B. (1968). "On the generalized stress-strain behavior of ‘wet’ clay." *Engineering Plasticity*. Cambridge University Press, London: 535-609.

Shen, Z.J. (1990). "A new model for stress-strain relationship analysis of soil." *Proceeding of 5th Soil Mechanics and Foundation Engineering*, Chinese Architecture and Building Press, Beijing: 101-105. (in Chinese).

Stroud, M.A. (1971). "The behaviour of sand at low stress levels in the simple shear apparatus. " *Ph.D. Thesis*, Cambridge, UK: University of Cambridge.

Vermeer, P.A. (1978). "A double hardening model for sand." *Geotechnique*, Vol. 28 (4): 413-433.

Yasin, S.J.M. and Tatsuoka, F. (2000). "Stress history-dependent deformation characteristics of dense sand in plane strain." *Soils Found.*, Vol. 40 (2): 77-98.

Yin, Z. Z. (1988). "A double yielding surface stress-strain model for soil." *Chinese Journal of Geotechnical Engineering*, Vol. 10 (4): 64-71. (in Chinese).

Clay Subjected to Cyclic Loading: Constitutive Model and Time Homogenization Technique

Aurélie Papon[1], Zhen-Yu Yin[2], Yvon Riou[3], Pierre-Yves Hicher[4]

[1] PhD, Research Institute in Civil and Mechanical Engineering, UMR CNRS 6183, Ecole Centrale de Nantes, France; aurelie.papon@ec-nantes.fr
[2] Research fellow, Research Institute in Civil and Mechanical Engineering; zhenyu.yin@ec-nantes.fr
[3] Associate professor, Research Institute in Civil and Mechanical Engineering; yvon.riou@ec-nantes.fr
[4] Professor, Research Institute in Civil and Mechanical Engineering; pierre-yves.hicher@ec-nantes.fr

ABSTRACT: Numerical modeling of the behavior of geotechnical structures subjected to cyclic loading requires the consideration of two main aspects: the constitutive relationship and numerical strategy. The constitutive model has to be representative of the clay behavior, whereas the numerical strategy should be efficient in order to reduce the computation time. To simulate undrained triaxial cyclic tests on clay, a method of time homogenization is applied to a bounding surface plasticity model. This method of homogenization is based upon splitting time into two separate scales. The first scale relates to the period of cyclic loading and the second to the characteristic time of the material. Simulations of undrained triaxial cyclic tests on normally consolidated clay under one-way cyclic loading are carried out. The performance of time homogenization is numerically validated. The sensitivity of the time increment is also investigated.

INTRODUCTION

Structures such as wind power plants, offshore installations, embankments, railways and tunnels are subjected to a large number of loading cycles. The phenomenon of fatigue in soils is identified and characterized (Andersen 2009), but design tools for these geotechnical problems are missing. Two main problems have to be considered.

First, the constitutive model has to be able to reproduce with good accuracy the cyclic behavior of soil. During the last decades, multi-surface models have been developed. Most of them belong to kinematic hardening plasticity theory (Mroz 1967) or to bounding surface plasticity (Dafalias and Popov 1975). The latter receives significant attention because of its simplicity and efficiency. This type of model is selected for this study and described in the following section.

Second, the conventional simulation of a structure subjected to a large number of cycles is time consuming. Thus different strategies have to be developed which could require only the simulation of a few cycles, the other cycles being treated differently according to the strategies considered (e.g. Wichtmann 2005).

In this paper, one of these strategies, called time homogenization, is selected. Time homogenization, as spatial homogenization, is derived from mathematical perturbation theory. Bensoussan et al. (1978) followed by Sanchez-Palencia (1980) introduced these methods for periodic structures. This paper presents the principles upon which time homogenization is based and the conclusions are applied to the outlined model in order to simulate undrained triaxial cyclic tests.

CONSTITUTIVE MODEL

The constitutive model refers to the theory of bounding surface plasticity. The implementation of the model is based on the works of Dafalias and Herrmann (1986) and Manzari and Nour (1997). This model is a bounding surface version of the Modified Cam-Clay with Hooke's elasticity. It assumes two surfaces: the yield surface (called bounding surface) and the subyield surface (called loading surface). They are homothetic with the respect to a projection center. Figure 1a represents both surfaces and the projection center corresponds to the origin of the coordinates. The current stress point c defines the loading surface. When the current stress point is on the loading surface, an "image" stress $\bar{c}$ is defined as the projection of the current stress c on the bounding surface with respect to the projection center (see Fig. 1a).

The relation between image and current stresses is called the mapping rule. The flow rule is respected and the plasticity parameter is given by:

$$\lambda = \frac{1}{\overline{K}_P}\left(\frac{\partial F}{\partial \overline{\sigma}}\dot{\overline{\sigma}}\right) = \frac{1}{K_P}\left(\frac{\partial F}{\partial \overline{\sigma}}\dot{\sigma}\right) \tag{1}$$

where F is the potential surface. The plastic modulus at the current stress point K_P is a function of the plastic modulus at the image stress point $\overline{K}_P$ and of the distance between bounding and loading surfaces. Based on the relation proposed by Manzari and Nour (1997), the plastic modulus is given by:

$$K_P = \overline{K}_P + H_0 \cdot \frac{(1+e_0)}{\rho} \cdot p'^{\,3}_{c0} \cdot (\beta - 1) \tag{2}$$

where β is equal to the ratio $p'_{c0} / p'_{c\sigma}$ (see Fig. 1a). When the current stress point c is on the bounding surface ($\beta = 1$), Eq. (2) is reduced to the same form as the conventional Modified Cam-Clay model.

The constitutive model has the parameters of the Modified Cam-Clay model (Young's modulus E, Poisson's ratio ν, critical state slope M, consolidation pressure p'_{c0}, $\rho = \lambda - \kappa$ with λ slope of the normal consolidation line and κ slope of the swelling line, and initial void ratio e_0), and one additional parameter, namely the hardening parameter H_0. Figure 1b represents the simulation of an undrained triaxial test on a normally consolidated clay under one-way cyclic loading in (p',q) plan. The values of the model parameters are given in Table 1 and H_0 is taken equal to 1000.

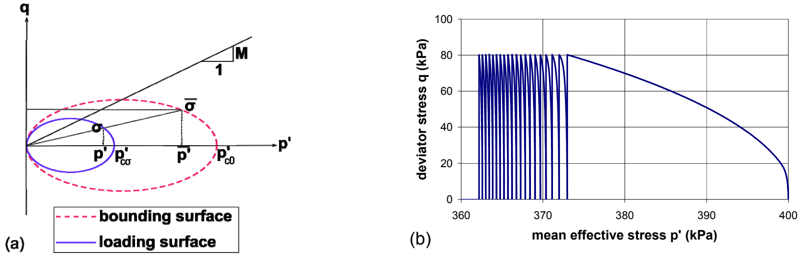

FIG. 1. (a) Representation of bounding and loading surfaces in (p', q) plan. (b) Simulation of an undrained triaxial test on a normally consolidated clay under one-way cyclic loading in (p',q) plan.

TIME HOMOGENIZATION

Fatigue of a material subjected to cyclic loading evolves slowly in comparison to the duration of one single loading cycle. It cannot be detected by considering only few cycles, but by considering a large number of cycles. Therefore the evolution during one single load cycle needs to be described by an accurate time scale, whereas a coarser one is enough for the fatigue evolution.

The aim of time homogenization is to separate the effects that take place at the two time scales in order to use small time increments only when it is necessary and so reduce time computation. To do so, we define the time characteristic of the cycles τ_0 (the period) and the time characteristic of the fatigue phenomenon t_r which depends on material properties. On a graph representing the evolution of a variable related to fatigue (e.g. permanent strain or pore pressure) as a function of the time, t_r can be defined as the time corresponding to the intersection of the line of the asymptotic behavior and the tangent at the origin. τ_0 and t_r can be characterized by two different units. The ratio of these units is noted ζ From this small positive ratio and the natural time scale describing the long-term fatigue, a second time scale describing the loading can be derived: $\tau = t/\zeta$ The time homogenization method, as it is explained further, consists in approximating displacements and stresses by using asymptotic expansions with respect to the ratio ζ Since we consider the first order of the asymptotic expansions, the smaller the ratio ζ the better the results.

Although the selected constitutive model is a time-independent model which does not involve any notions of time, we can still apply this method by considering a fictitious time related to the number of cycles. Mathematical proof is given by Guennouni (1988), who considers an elastoplastic problem as the limit of a series of elastoviscoplastic problems. As shown by Guennouni (1988) and Yu (2002), the homogenization method makes possible the separation of the two time scales so that the original initial-boundary value problem (Pb) can be divided into two problems (Pb*) and (Pb**).

$$
\text{(Pb)} \quad \begin{cases} \sigma_{ij,j} + b_i(x) = 0 \\ \sigma_{ij} = C_{ijkl} : (\varepsilon_{kl} - \varepsilon_{kl}^{p}) \\ \dot{\varepsilon}_{kl}^{p} = \lambda \dfrac{\partial F}{\partial \sigma_{kl}} \\ \dot{p}'_c = p'_c \dfrac{1+e}{\lambda - \kappa} \dot{\varepsilon}_v^{P} \end{cases} \quad \text{and} \quad \begin{cases} \varepsilon_{ij} = \dfrac{(u_{i,j} + u_{j,i})}{2} \\ u_i(x, t=0) = \tilde{u}_i(x) \\ u_i = \bar{u}_i(x,t) \\ \sigma_{ij} n_j = f_i(x,t) \end{cases} \qquad (3)
$$

where b_i corresponds to volumetric forces; σ_{ij}, ε_{ij} and ε^P_{ij} are respectively the components of stress, strain and plastic strain tensors; C_{ijkl} the components of elastic tensor; u_i the component of displacement vector. The displacement, stress, plastic strain and hardening variable are approximated by asymptotic expansions in the form of:

$$
\alpha^{\varsigma}(x,t) = \sum_{M=0,1,..} \varsigma^{M} \alpha_M(x,t,\tau) \qquad (4)
$$

where α_M τ-periodic. Using Eq. (3) and (4) and considering the first-order term of the asymptotic expansions, it appears that the plastic strains and the hardening variable are τ-independent, so that their evolution is noticed only in the long term. Moreover, the global behavior of the material can be divided into the non-oscillatory long-term behavior and the oscillatory short-term behavior. The first part is defined as the average over a cycle of the first-order term of the asymptotic expansions; the second part as the remaining term.

$$
\begin{aligned} u_0(x,t,\tau) &= \langle u_0(x,t,\tau)\rangle + \chi_0(x,t,\tau) \\ \sigma_0(x,t,\tau) &= \langle \sigma_0(x,t,\tau)\rangle + \phi_0(x,t,\tau) \\ \varepsilon_0(x,t,\tau) &= \langle \varepsilon_0(x,t,\tau)\rangle + \psi_0(x,t,\tau) \end{aligned} \qquad \text{where } \langle \bullet \rangle = \frac{1}{\tau_0}\int_0^{\tau_0} \bullet \, d\tau \qquad (5)
$$

The non-oscillatory and oscillatory terms are respectively the response fields of the problems (Pb*), called the macro-chronological problem, and (Pb**), called the micro-chronological problem. It is worth noting that (Pb**) is a linear elastic problem, which can be solved at the beginning of the calculation. The constitutive relation of (Pb*) is called the homogenized constitutive relation and depends on the behavior of the material. Eq. (6) and (7) give both problems (Pb*) and (Pb**) as follows:

$$
\text{(Pb*)} \quad \begin{cases} \langle \sigma_{0ij} \rangle_{,j} + b_i(x) = 0 \\ \langle \sigma_{0ij} \rangle_{,t} = C_{ijkl} : (\langle \varepsilon_{0kl} \rangle_{,t} - \varepsilon_{0kl,t}^{p}) \\ \varepsilon_{0kl,t}^{p} = \langle \lambda \dfrac{\partial F}{\partial \sigma_{0kl}} \rangle \\ p'_{c0,t} = p'_{c0} \dfrac{1+e}{\lambda - \kappa} \varepsilon_{0v,t}^{P} \end{cases} \quad \text{and} \quad \begin{cases} \langle u_{0i} \rangle (x, t=0) = \tilde{u}_i(x) \\ \langle u_{0i} \rangle = \langle \bar{u}_i(x,t,\tau) \rangle \\ \langle \sigma_{0ij} \rangle n_j = \langle f_i(x,t,\tau) \rangle \end{cases} \qquad (6)
$$

$$
\text{(Pb**)} \quad \begin{cases} \phi_{0ij,j}(x,t,\tau) = 0 \\ \phi_{0ij,\tau}(x,t,\tau) = C_{ijkl} : \psi_{0kl,\tau}(x,t,\tau) \end{cases} \quad \text{and} \quad \begin{cases} \chi_{0i}(x, t=\tau=0) = 0 \\ \chi_{0i}(x,t,\tau) = \bar{u}_i(x,t,\tau) - \langle \bar{u}_i(x,t,\tau) \rangle \\ \phi_{0ij} n_j = f_i(x,t,\tau) - \langle f_i(x,t,\tau) \rangle \end{cases} \qquad (7)
$$

NUMERICAL VALIDATION

The model with homogenization is implemented in a FORTRAN routine which is used to simulate undrained triaxial tests and to estimate the reduction of time computation. An undrained triaxial test on a normally consolidated clay under one-way cyclic loading (q = 80 kPa) is assumed for the numerical validation. The permanent strain is defined as the strain remaining after a cycle. The values of the model parameters corresponding to a kaolinite clay are summarized in Table 1. The first ten cycles are simulated conventionally because of the important rate of permanent strains at the beginning of the calculation (see Fig. 1b).

Table 1. Model parameters.

E (kPa)	ν	M	p'_{c0} (kPa)	κ	λ	e_0	H_0
30000	0.3	0.7	400	0.04	0.19	1.5	1000; 3000;10000

The time increment corresponds to N_c cycles. Simulations are carried out for three values of N_c: 50, 100 and 200. The homogenized calculation is about N_c times faster than the conventional one. Figures 2(a-b) show the influence of N_c over 2000 cycles. The maximal error for permanent strain (83%) due to homogenization appears for N_c = 200 at the 210th cycle. However, the error is reduced to 14% after 2000 cycles and becomes less than 1.2% after 30000 cycles (see Fig. 2c).

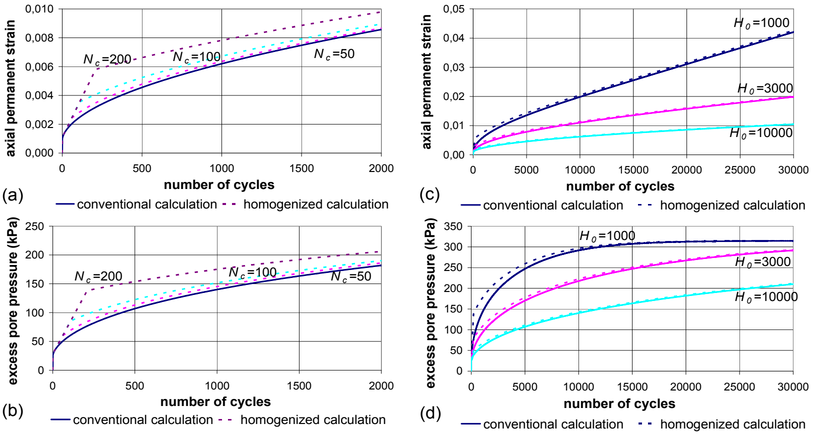

FIG. 2. Comparison of conventional and homogenized calculations: (a) permanent strain / (b) excess pore pressure for H_0 = 1000 and N_c = 50, 100, 200; (c) permanent strain / (d) excess pore pressure for H_0 = 1000, 3000, 10000 and N_c = 200.

Figures 2(c-d) compare the conventional and homogenized calculations with different values of the hardening parameter. The characteristic time t_r depends on this parameter, as shown by the different curvature of the curves, and it explains why the calculation with $H_0 = 1000$ is at first the most affected by the homogenization strategy.

CONCLUSIONS

The example of cyclic modeling outlined in this paper shows to what extent time homogenization can be used to efficiently and accurately model cyclic behavior of soils. When applied to a bounding surface plasticity model, this strategy can significantly improve computational efficiency and guarantees over a large number of cycles that the same results will be obtained as by conventional calculations. Particular attention should be paid to the choice of the time increment. The paper presents the numerical validation for the time homogenization technique applied to a bounding surface model. For further studies, it will be interesting to validate the approach by using real experimental testing results on soil samples as well as boundary value problems.

REFERENCES

Andersen, K. H. (2009) "Bearing capacity under cyclic loading – offshore, along the coast, and on land." *Can. Geotech. J.*, Vol. 46: 513-535.

Bensoussan, A., Lions, J.L. and Papanicolaou G. (1978). "Asymptotic analysis for periodic structures." *Studies in mathematics and its applications.*, North-Holland.

Dafalias, Y.F. and Herrmann, L.R. (1986) "Bounding surface plasticity II: application to isotropic cohesive soils." *J. Eng. Mech. Div.,* Vol. 112 (12): 1263-1291.

Dafalias, Y.F. and Popov E.P. (1975) "A model of nonlinearly hardening materials for complex loading." *Acta. Mech.*, Vol. 23 : 173-192.

Guennouni, T. (1988). "Sur une méthode de calcul de structures soumises à des chargements cycliques : l'homogénéisation en temps." *Mathematical modelling and numerical analysis.*, Vol. 22 (3): 417-455.

Manzari, M.T. and Nour, M.A. (1997). "On implicit integration of bounding surface plasticity models." *Comput. Struct.*, Vol. 63 (3): 385-395.

Mroz, Z. (1967) "On the description of anisotropic hardening." *J. Mech. Phys. Solids*, Vol. 15: 163-175.

Sanchez-Palencia, E. (1980). "Non-homogeneous media and vibration theory." *Lectures Note in Physics.*, Vol. 127.

Wichtmann, T. (2005) "Strain accumulation in sand due to cyclic loading: drained triaxial tests." *Soil Dyn. Earthq. Engng.*, Vol. 25: 967-979.

Yu, Q. and Fish J. (2002) "Temporal homogenization of viscoelastic and viscoplastic solids subjected to locally periodic loading." *Comput. Mech.*, Vol. 29: 199-211.

Modeling Anisotropic, Debonding and Viscous Behaviors of Natural Soft Clays

Zhen-Yu Yin[1]

[1]Research fellow, Research Institute in Civil and Mechanical Engineering, Ecole Centrale de Nantes, 44300 France; zhenyu.yin@gmail.com

ABSTRACT: A new viscoplastic model is developed extended from overstress theory of Perzyna. A scaling function based on the experimental results of constant strain-rate oedometer tests is adopted, which allows viscoplastic strain-rate occurring wherever the stress state is inside or outside of the reference surface. The inherent and induced anisotropy is incorporated using the formulations of yield surface and its rotation of S-CLAY1. The bonds are progressively destroyed by plastic straining by incorporating the concept of an intrinsic yield surface. No additional test is needed for determining all model parameters compared to the Modified Cam Clay model, and the parameters determination is straightforward. The experimental verification is carried out with reference to the constant strain-rate and creep tests on two natural clays.

INTRODUCTION

The soft and sensitive clay deposits formed after the Pleistocene period cover most of the densely populated low-lying coastal areas in the world. The construction on soft soil deposits has become increasingly important in last decades. A safe and economical design and construction on soft soils becomes an important issue.

The behavior of soft sensitive clay is very complicated. It exhibits several features: (a) a significant degree of anisotropy developed during their deposition, sedimentation, consolidation history and any subsequent straining; (b) some apparent bonding which will be progressively lost during straining; (c) time-dependent stress-strain relationship which has a significant influence on the shear strength and the preconsolidation pressure.

In order to describe all these features, Yin & Karstunen (2008) proposed an elasto-viscoplastic model based on overstress theory of Perzyna (1966) with an elastic region assumed. This hypothesis leads the present model to a less effort in parameter determination.

In this paper, we propose a new model extended from overstress theory of Perzyna (1966) with no elastic region exist in the stress space. The proposed model is based on the strain-rate effect on preconsolidation pressure. It is different from creep models (i.e., Leoni et al. 2008) based on the concept of instant and delayed compression of

Bjerrum. Since the proposed model is directly extended from overstress model, the same flow rule is kept. The model is validated by simulating tests on two natural soft clays.

CONSTITUTIVE MODEL

According to Perzyna's overstress theory, the total strain-rate is additively composed of the elastic strain-rates and viscoplastic strain-rates. The viscoplastic strain-rate $\dot{\varepsilon}_{ij}^{vp}$ is assumed to obey an associated flow rule with respect to the dynamic loading surface f_d (Perzyna, 1966):

$$\dot{\varepsilon}_{ij}^{vp} = \mu \left\langle \Phi(F) \right\rangle \frac{\partial f_d}{\partial \sigma'_{ij}} \tag{1}$$

where μ is referred to as the fluidity parameter; the dynamic loading surface f_d is treated as a viscoplastic potential function; $\Phi(F)$ is the overstress function representing the distance between the dynamic loading surface and the static yield surface.

Based on the strain-rate effect on the preconsolidation pressure from oedometer tests, a power-type scaling function was adopted for the viscoplastic strain-rate:

$$\Phi(F) = \left(\frac{p_m^d}{p_m^r} \right)^{\beta} \tag{2}$$

where β is the strain-rate coefficient; $p_m{}^d$ is the size of dynamic loading surface and $p_m{}^r$ is the size of reference surface. In this equation, the rate of viscoplastic volumetric strain always exists whatever the value of ratio p_m^d / p_m^r .

Based on experimental investigation by Wheeler et al. (2003), an elliptical surface is adopted to describe the dynamic loading surface and the reference surface:

$$f_d = \frac{\frac{3}{2}\left(s_{ij} - p'\alpha_{ij}\right):\left(s_{ij} - p'\alpha_{ij}\right)}{\left(M^2 - \frac{3}{2}\alpha_{ij} : \alpha_{ij}\right)p'} + p' - p_m^d = 0 \tag{3}$$

where s_{ij} is the deviatoric stress tensor; α_{ij} is the deviatoric fabric tensor (see Wheeler et al. 2003); M is the slope of the critical state line; p' is the means effective stress; and $p_m{}^d$ is the size of dynamic loading surface corresponding to the current stress state. The reference surface has an elliptical shape identical to the dynamic loading surface, but has a different size $p_m{}^r$.

The rotational hardening law proposed by Wheeler et al. (2003) was adopted:

$$d\alpha_d = \omega \left[\left(\frac{3\sigma_d}{4p'} - \alpha_d \right) \left\langle d\varepsilon_v^{vp} \right\rangle + \omega_d \left(\frac{\sigma_d}{3p'} - \alpha_d \right) d\varepsilon_d^{vp} \right] \tag{4}$$

where the function of MacCauley. The soil constant ω controls the rate at which the deviatoric fabric tensor heads toward their current target values, and ω_d controls the relative effect of viscoplastic deviatoric strains on the rotation of the elliptical surface.

The amount of particle bonding is described with a scalar state variable χ. The size of reference yield surface p_m^r can be expressed by the size of intrinsic surface p_{mi} and the bonding ratio χ as follows:

$$p_m^r = (1+\chi)\, p_{mi} \tag{5}$$

The expansion of the intrinsic surface, which represents the intrinsic hardening of the material, is assumed to be due to the inelastic volumetric strain ε_v^{vp}, similarly to the critical state models:

$$dp_{mi} = p_{mi}\left(\frac{1+e_0}{\lambda_i-\kappa}\right)d\varepsilon_v^{vp} \tag{6}$$

The bonding ratio (amount of particle bonding) χ is changing due to bond degradation ultimately to zero. The degradation law proposed by Gens & Nova (1993) was adopted:

$$d\chi = -\chi\xi\left(\left|d\varepsilon_v^{vp}\right| + \xi_d d\varepsilon_d^{vp}\right) \tag{7}$$

where the soil constant ξ controls the absolute rate of destructuration and ξ_d controls the relative effect of viscoplastic deviatoric strains in destroying the bonds.

Overall, additional to the different flow rules used from creep models, the proposed model accounts for destructuration.

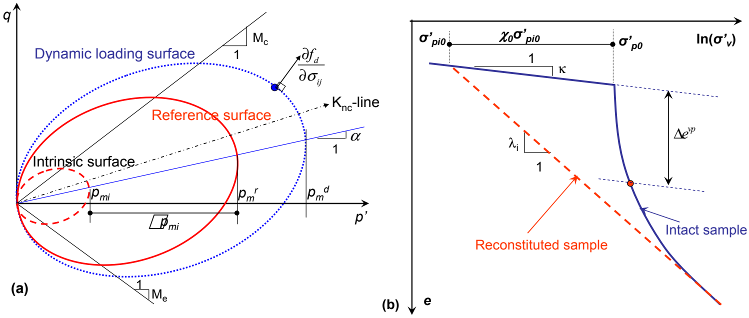

FIG. 1. Definitions for the model in (a) triaxial space, (b) one-dimensional space

MODEL PARAMETERS

The initial reference preconsolidation pressure σ'^r_{p0} obtained from oedometer test is used as an input to calculate the initial size p_{m0} by the following equation (derived from Eq.3 of reference surface)

$$p_{m0} = \left\{\frac{\left[3-3K_0-\alpha_0\left(1+2K_0\right)\right]^2}{3\left(M_c^2-\alpha_0^2\right)\left(1+2K_0\right)} + \frac{\left(1+2K_0\right)}{3}\right\}\sigma'^r_{p0} \tag{8}$$

where $K_0 = \dfrac{6-2M}{6+M}$, $\alpha_0 = \eta_{K0} - \dfrac{M^2-\eta_{K0}^2}{3}$, $\eta_{K0} = \dfrac{3M}{6-M}$

Based on Wheeler et al. (2003) and Leoni et al. (2008), other two anisotropy parameters can be obtained by,

$$\omega_d = \frac{3\left(4M^2-4\eta_{K0}^2-3\eta_{K0}\right)}{8\left(\eta_{K0}^2+2\eta_{K0}-M^2\right)}, \omega = \frac{1+e_0}{\left(\lambda_i-\kappa\right)} \ln\frac{10M^2-2\alpha_0\omega_d}{M^2-2\alpha_0\omega_d} \tag{9}$$

Derived from Equations of destructuration law, destructuration parameters can be obtained by,

$$\chi_0 = S_t - 1 \tag{10}$$

$$\xi + \xi\cdot\xi_d \frac{2(\eta-\alpha)}{\left(M^2-\eta^2\right)} = \frac{-(1+e_0)}{e^{vp}} \ln\left[\frac{\sigma'_f}{\chi_0 \exp\left(\dfrac{e^{vp}}{\lambda_i-\kappa}\right)\sigma'_{vi0}} - \frac{1}{\chi_0}\right] \tag{11}$$

where S_t is soil sensitivity. The ξ and ξ_d can be obtained from one oedometer test combined with one isotropic compression test by selecting several points in post-yield e-logp' curves, and then taking the average values.

The parameters μ and β can be very easily determined from oedometer tests at constant strain-rate by selecting a reference strain-rate (where σ'^{r}_{p0} corresponding to the selected strain-rate). The β can be obtained from the slope of $\log\dot{\varepsilon}_v - \log\sigma'_{p0}$ curve.

$$\mu = \dot{\varepsilon}_v^r \frac{\lambda-\kappa}{\lambda} \frac{M^2-\alpha_0^2}{M^2-\eta_{K0}^2} \tag{12}$$

Alternatively, the viscosity parameters can also be obtained from conventional oedometer test as follows:

$$\mu = \frac{C_{\alpha ei}\left(M^2-\alpha_0^2\right)}{\tau\left(1+e_0\right)\left(M^2-\eta_{K0}^2\right)} \text{ and } \beta = \frac{\lambda_i-\kappa}{C_{\alpha ei}} \tag{13}$$

The $C_{\alpha ei}$ is the creep index when all bonds are destroyed (e.g. from data under very high stress level). The reference time τ depends on the duration of load increment used in the conventional oedometer test (normally τ = 1 day), from which the initial reference preconsolidation pressure σ'^{r}_{p0} is obtained.

Overall, no additional test is needed when using the proposed model, compared to the Modified Cam Clay model. Since some parameters can be calculated from others, the parameters we need as input are summarized in Table 1.

TEST SIMULATIONS

Tests on Berthierville clay by Leroueil et al. (1988) were selected to validate the model performance on one-dimensional behavior. The viscosity parameters from two methods (one from conventional test: first line in Table 1, the other from CRS test: second line in Table 1) were also examined. Figure 2(a) shows simulations based on both sets of parameters compared to the experimental results. The comparisons demonstrate that both methods of calibrating parameters are suitable for modeling the stress-strain-strain rate behavior of soft sensitive clay. Figure 2(b) presents the comparison between predictions and experimental results for creep tests. Both predictions by using parameters from conventional test and CRS test are suitable compared to experimental results, although there is a slight difference between two predictions. This slight difference on the predicted creep deformation is due to the slight difference on β

Table 1. Selected values of model parameters for tested clays

Parameters	ν'	λ_i	κ	e_0	M	σ'^{r}_{p0}	χ_0	ξ	ξ_d	μ(s^{-1})	β
Bethierville clay	0.25	0.29	0.032	1.73	1.5	49	2.7	11	0.3	8.8E-8	18.7
	0.25	0.29	0.032	1.73	1.5	63	2.7	11	0.3	1.7E-5	18
Haney clay	0.25	0.32	0.05	2	1.28	340	8	11	0.3	1.5E-7	26

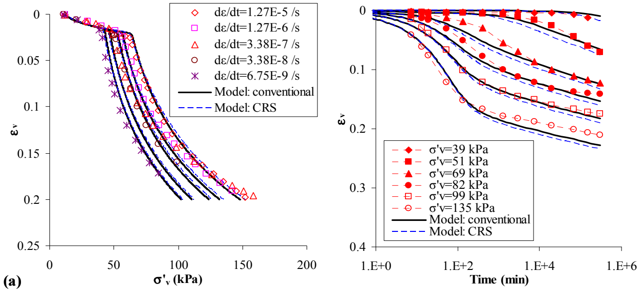

FIG. 2. Test simulations for oedometer tests on Berthierville clay.

Vaid and Campanella (1977) conducted undrained triaxial tests at constant strain rate varying from 0.0001 to 10 %/min and undrained creep triaxial tests under applied constant deviatoric stress varying from 193 to 329 kPa on undisturbed Haney clay. The parameters based on text data were selected (Table 1). Figure 3(a) shows a good fit between the simulations and experimental data. The proposed model well captured the strain-rate effect on the undrained shear strength with strain softening process due to destructuration. Figure 3(b) shows that the model can reproduce the undrained creep behaviour of soft clay in terms of strain evolution versus time under different applied stress levels.

CONCLUSIONS

A new constitutive model accounting for soil anisotropy, destructuration and viscosity has been developed. The model was extended from overstress approach using the concept of reference surface instead of the static yield surface. A scaling function based on the strain-rate effect on the preconsolidation pressure of oedometer tests was adopted for the convenience of parameters determination. The new model adopted the formulations of a yield surface with rotational kinematic hardening (Wheeler et al., 2003) and of destructuration (Gens & Nova 1993) so that it is capable of describing the viscosity, anisotropy and destructuration coupled phenomena. The proposed model can capture three coupled phenomena without any additional test, compared to the Modified Cam Clay model, required for parameter determination. The experimental validation was carried out with reference to the one-dimensional tests (constant strain-rate tests, long-term creep tests) on Berthierville clay and triaxial tests (constant strain-rate tests, undrained creep tests) on Haney clay. All comparisons between predicted and measured results demonstrate that the proposed model can successfully reproduce the time-dependent behavior of natural soft clays under different loading conditions.

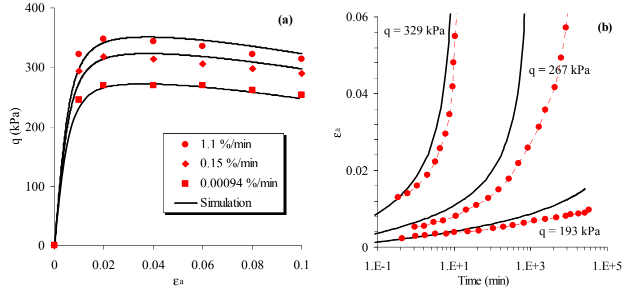

FIG. 3. Test simulations for undrained triaxial tests on Haney clay.

REFERENCES

Gens, A. and Nova, R. (1993). “Conceptual bases for a constitutive model for bonded soils and weak rocks.” *Proceedings of International Symposium on Hard Soils - Soft Rocks*, Athens, 485–494.

Leoni, M., Karstunen, M. and Vermeer, P.A. (2008). ”Anisotropic creep model for soft soils.” *Géotechnique*, Vol. 58 (3): 215-226.

Leroueil, S., Kabbaj, M. and Tavenas, F. (1988). “Study of the validity of a σ′v-εv-dεv/dt model in site conditions.” *Soils and Foundations*, Vol. 28 (3): 13-25.

Perzyna, P. (1966). “Fundamental problems in viscoplasticity.” *Advances in Applied Mechanics*, Vol. 9: 243-377.

Vaid, Y.P. and Campanella, R.G. (1977). “Time-dependent behaviour of undisturbed clay.” *ASCE Journal of the Geotechnical Engineering*, Vol. 103 (7): 693-709.

Wheeler, S.J., Näätänen, A., Karstunen, M. and Lojander, M. (2003). ”An anisotropic elasto-plastic model for soft clays.” *Can. Geotech. J.*, Vol. 40(2): 403–418.

Yin, Z.-Y. and Karstunen, M. (2008). “Influence of anisotropy, destructuration and viscosity on the behavior of an embankment on soft clay.” *Proc. IACMAG08*, Goa, India, 2008, 4728-4735.

On the Modeling of Anisotropy and Destructuration of Shanghai Soft Clay

Yanhua Liu [1], Maosong Huang [2]

[1] PhD student, Department of Geotechnical Engineering, Tongji University, Shanghai 200092, China; yanhua3537@126.com
[2] Professor, Department of Geotechnical Engineering, Tongji University, Shanghai 200092, China; mshuang@tongji.edu.cn

ABSTRACT: The aim of this paper is to constitute a simple anisotropic elasto-plastic model that can predict the mechanical behavior of saturated structured soils. Undrained triaxial tests and drained stress probe tests under isotropic and anisotropic consolidation modes were performed on natural undisturbed samples of Shanghai soft clay to study the yielding characteristic. The effect of damage to structure caused by accumulated plastic strain is modeled with an inner variable that allows the size of the bounding surface to decay with plastic deformations. An anisotropic tensor and rotational hardening law were introduced to reflect the initial anisotropy and the evolution of anisotropy. Combined with the isotropic hardening rule, rotational hardening rule and degradation law of structure were incorporated into the bounding surface formulation with an associated flow rule. Validity of the model was verified by the undrained isotropic and anisotropic triaxial test results for Shanghai soft clay. The effects of stress anisotropy and loss of structure were well captured by the model.

INTRODUCTION

Structure and plastic anisotropy are the essential nature of naturally deposited soft clay, which have considerable influence on the strength and stress-strain response of natural clays. Sometimes loading causes a destructuration of the initial structure, and this is particularly true in soft clays (Bothkennar clay, Smith et al., 1992). Neglecting the anisotropy of soil behavior may lead to highly inaccurate predictions of soil response under loading (Zdravkovic et al., 2002). From an engineering point of view, the need for a natural clay model which can accurately predict the behavior of soft clay with the increased construction activity in recent years has become more urgent.

There are various approaches to developing the constitutive models which are capable of describing the mechanical behavior of natural clay. To model the destructuration of structural clays, it is logical to start from a model that appears to have met with some success in matching the behavior of remoulded material and add to it some measure of structure (Rouainia & Muir Wood, 2000). At the same time, numerous constitutive models that account for plastic anisotropy of natural clays have been proposed, in which S-CLAY1 model proposed by Wheeler et al. (2003) is a relatively simple elastoplastic anisotropic model. Most existing models in the literature account for either structure or anisotropy, only few models consider both properties of natural clays. Several researchers (e.g. Kavvadas & Amorosi, 2000; Rouainia & Muir Wood, 2000) developed numerical models for natural soils within the framework of kinematic hardening, which consider simultaneously the anisotropic and structural effect on the mechanical behavior of soils. Those models can in general achieve good results but often at a price of complexity.

The main aim of this paper is to demonstrate that a simplified bounding surface model is sufficient to simulate both the anisotropic and structural properties of natural clays. Experimental data from undrained triaxial tests and drained stress probe tests on Shanghai soft clay are presented to support the proposed model.

MODEL DESCRIPTION

Bounding Surface

Based on the experimental observations, an anisotropic reference surface, which is an inclined ellipse on the *p*-*q* plane, is used to model the intrinsic behavior of the reconstituted soils. And then a structure surface or bounding surface which has the same elliptical shape as the reference surface is adopted to describe the effect of initial structure and control the process of destructuration. For simplicity, the loss of structure is assumed to affect merely the size of yielding surface. A Scalar variable *r* called structural parameter is defined:

$$r = \overline{p}_c / p_c \tag{1}$$

where $\overline{p}_c$ is structural yielding stress; p_c is initial consolidation stress. Namely, *r* defines the ratio between the sizes of the structure surface and reference surface. The curves of the reference surface and structure surface are shown in Fig.1. The value of *r* has $r \geq 1.0$ due to its physical meaning. For $r = 1.0$, the soil is completely destructured.

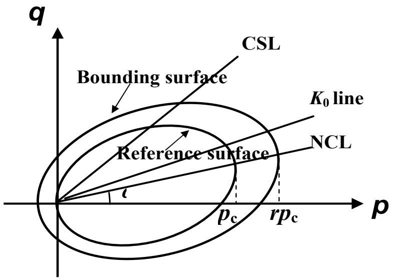

FIG.1. Reference surface and bounding surface of anisotropic model for structured clays

We consider that the reference surface for describing the behavior of the destructured soil is an anisotropic elliptical form. The mathematical equation of the reference surface is defined by

$$f = (p - p_c)(p + \frac{R-2}{R} \cdot p_c) + (R-1)^2 \frac{q_a^2}{\chi} = 0 \tag{2}$$

For simplicity, we consider that the structure surface has the same elliptical shape as the reference surface. The mathematical equation of structure surface is given by

$$F = (p - \overline{p}_c)(p + \frac{R-2}{R} \cdot \overline{p}_c) + (R-1)^2 \frac{q_a^2}{\chi} = 0 \tag{3}$$

where

$$\alpha = \sqrt{3\alpha_{\mathrm{ij}}\alpha_{\mathrm{ij}}/2} \tag{4}$$

$$q_{\alpha} = \sqrt{3J_{2\alpha}} \quad , \quad J_{2\alpha} = \frac{1}{2}s_{\mathrm{ij}}^{\alpha}s_{\mathrm{ij}}^{\alpha} \tag{5}$$

$$s_{\mathrm{ij}}^{\alpha} = s_{\mathrm{ij}} - \sigma_{\mathrm{kk}}\alpha_{\mathrm{ij}}/3 \tag{6}$$

$$\chi = (M-\alpha)[2\alpha(R-1)^2 + M - \alpha + \sqrt{4\alpha(R-1)^2 M + (M-\alpha)^2}\,]/2 \tag{7}$$

where α_{ij} is the anisotropic tensor defining the anisotropy of clays; α defines the inclination of yield surface in *p-q* stress space, which is the second invariant of anisotropic tensor; σ_{ij} is stress tensor; s_{ij} is deviatoric stress tensor; s_{ij}^{α} is the reduced deviatoric stress tensor; q_{α} is the reduced equivalent shear stress; $J_{2\alpha}$ is the reduced second stress invariant; *R* is the shape parameter, which controls the ratio of the two major axes of the yield surface; *M* is the slope of critical state line in triaxial space, which is defined by the reduced Lode angle θ_a as follows:

$$\theta_{\alpha} = \frac{1}{3}\sin^{-1}\left[\frac{3\sqrt{3}}{2}\left(\frac{J_{3\alpha}}{J_{2\alpha}^{3/2}}\right)\right] \tag{8}$$

$$J_{3\alpha} = s_{\mathrm{ij}}^{\alpha}s_{\mathrm{jk}}^{\alpha}s_{\mathrm{ik}}^{\alpha}/3 \tag{9}$$

$$M = \frac{2mM_{\mathrm{c}}}{(1+m)-(1-m)\sin 3\theta_{\alpha}} \tag{10}$$

where $J_{3\alpha}$ is the reduced third stress invariant; *m* is a material parameter defined as $m = M_{\mathrm{e}}/M_{\mathrm{c}}$ in which M_{c} and M_{e} are the critical state stress ratios for triaxial compression and triaxial extension in *p-q* stress space.

As defined in Liang & Ma(1992) and Ling & Yue (2002), the initial anisotropic tensor α_{ij}^{0} are expressed through a constant A_0 with the initial stress states

$$a_{ij}^{0} = \frac{s_{ij}^{0}}{p_c} \quad , \quad s_{ij}^{0} = \sigma_{ij}^{0} - p_c\delta_{ij} \tag{11}$$

For the initial stress ratio $K_0 = \sigma_3^0/\sigma_1^0$, the components of the tensor are given as follows:

$$\alpha_{11}^{0} = 2k^{0}\,,\ \alpha_{22}^{0} = \alpha_{33}^{0} = -k^{0}\,,\ \alpha_{12}^{0} = \alpha_{23}^{0} = \alpha_{13}^{0} = 0 \tag{12}$$

Where

$$k^{0} = A_0\frac{1-K_0}{1+2K_0} \tag{13}$$

For isotropic consolidated specimens K_0=1.0, thus $k^0 = 0$. For the K_0-consolidated specimen, A_0=0.65-1.0 (Liang & Ma.1992).

Hardening Rules

Isotropic hardening. In line with the Cam-Clay model, a volumetric hardening rule is adopted. p_c is controlled only by the plastic volumetric strain rate $\dot{\varepsilon}_v^p$, given by

$$\dot{p}_c = p_c \dot{\varepsilon}_v^p / (\lambda^* - \kappa^*) \tag{14}$$

where $\lambda^* = \lambda/(1+e_0)$ and $\kappa^* = \kappa/(1+e_0)$ with λ and κ being the slopes of the normal compression line and swelling line in the e-ln$p$ space; e_0 is initial void ratio.

Rotational/anisotropic hardening: The rotational rate of the bounding surface is controlled by the evolution of the anisotropic tensor α_{ij}. We adopt a similar form to the anisotropic/rotational law proposed by Wheeler et al. (2003).

The proposed form of modified hardening law is

$$\dot{\alpha}_{ij} = \mu\rho\left[\left(\frac{3s_{ij}}{4p} - \alpha_{ij}\right)\cdot\langle\dot{\varepsilon}_v^p\rangle + \beta\left(\frac{s_{ij}}{3p} - \alpha_{ij}\right)\cdot\left|\dot{\varepsilon}_s^p\right|\right] \tag{15}$$

where the parameter β controls the relative effectiveness of plastic shear strains and plastic volumetric strains in determining the overall current target value for α_{ij}; and the soil constant μ controls the absolute rate at which α_{ij} approaches its current target value (Wheeler et al.2003) . An extra parameter ρ is introduced in order to control the change rate of α_{ij} as the stress ratio $\eta = q/p$ approaches the critical state value M. This suggests the following expression for ρ

$$\rho = \left\langle 1 - \left|\frac{\eta}{M}\right|\right\rangle \tag{16}$$

Destructuration law: The scalar variable r represents the progressive degradation of soils, which controls the ratio between the sizes of structure surface and reference surface. According to Rouainia & Muir Wood (2000), the scalar variable r is assumed to be a monotonically decreasing function of the plastic strain. The following exponential destructuration law is adopted

$$r = 1 + (r_0 - 1)\exp\left(\frac{-k_d \varepsilon_d^p}{\lambda^* - \kappa^*}\right) \tag{17}$$

where r_0 denotes the initial structure and k_d is a parameter which describes the rate of destructuration with strain. This equation takes the main effect of damage by both plastic volumetric and plastic deviatoric strains into account through the plastic destructuration strain ε_d^p, which has the following form

$$\varepsilon_d^p = \int\sqrt{(1-B)\cdot(d\varepsilon_v^p)^2 + B\cdot(d\varepsilon_s^p)^2} \tag{18}$$

where $d\varepsilon_v^p$ is plastic volumetric strain increment; $d\varepsilon_s^p$ is plastic shear strain increment; B is a non-dimensional scaling parameter which controls the relative contributions to damage of the plastic strain increments $d\varepsilon_v^p$ and $d\varepsilon_s^p$.

Mapping Rule: In the proposed model, the projection center is fixed at the origin of p-q stress space. And following the linear radial mapping rule (Dafalias & Herrmann.

1982), for any actual stress point σ_{ij}, there is a unique image stress point $\bar{\sigma}_{ij}$ on the bounding surface corresponding to the current stress point. The following relationships are used in relating current stress states to those at the bounding surface:

$$\bar{\sigma}_{ij} = b\sigma_{ij}\,,\ b = \frac{\delta_0}{\delta_0 - \delta} \tag{19}$$

where δ and δ_0 denote respectively, the distance and the ultimate distance between current stress point and image stress point.

Bounding Plastic Modulus: Associated flow is assumed, thus the bounding surface function also serves as the plastic function. The plastic strain rate is determined as

$$\dot{\varepsilon}^{\mathrm{p}}_{\mathrm{ij}} = \langle \dot{\phi} \rangle \frac{\partial F}{\partial \bar{\sigma}_{ij}} \tag{20}$$

where $\dot{\phi}$ is the plastic loading index, is defined as follows

$$\dot{\phi} = \frac{1}{H_{\mathrm{p}}} \frac{\partial F}{\partial \bar{\sigma}_{\mathrm{ij}}} \dot{\sigma}_{\mathrm{ij}} = \frac{1}{\bar{H}_{\mathrm{p}}} \frac{\partial F}{\partial \bar{\sigma}_{\mathrm{ij}}} \dot{\bar{\sigma}}_{\mathrm{ij}} \tag{21}$$

The plastic modulus is related to the bounding plastic modulus through the followi ng relationships

$$H_{\mathrm{p}} = \bar{H}_{\mathrm{p}} + \varsigma \mathrm{P_a} [(\frac{\partial F}{\partial p})^2 + (\frac{\partial F}{\partial q})^2][(\frac{\delta_0}{\delta_0 - \delta})^{\psi} - 1] \tag{22}$$

$$\psi = \psi_0 \exp(-\xi \varepsilon^{\mathrm{p}}_{\mathrm{s}}) \tag{23}$$

where $\varepsilon^{\mathrm{p}}_{\mathrm{s}} = \int \dot{\varepsilon}^{\mathrm{p}}_{\mathrm{s}}$, which denotes the cumulative plastic strain. P_{a} is the atmosphere pressure, ς and ψ_0 and ξ are the model parameters.

Model Parameters: Most of the traditional parameters can be obtained from conventional laboratory tests. Undrained stress path of the normal consolidated soil may be used to obtain the value of shape parameter R as mentioned by Ling & Yue (2002). The structural parameters k_d and B can be determined by comparing triaxial compression and one-dimensional compression tests. As to the anisotropic hardening parameters, Zentar et al. (2002) suggested that the value of μ for a particular soil will normally lie in the range $10/\lambda$ to $15/\lambda$. And Wheeler et al. (2003) suggested the value of β/M between 0.5 and 1.0. The parameters for stiffness interpolation ψ_0, ξ and ς are obtained by best fitting the experimental results.

SIMULATIONS OF EXPERIMENTS ON SHANGHAI SOFT CLAY

Summary of Experiments

A program of tests on samples of Shanghai soft clay was undertaken to investigate the validity of the proposed model. For the present study, undisturbed samples were taken at depths of 10 m, with in-situ horizontal consolidation stress σ'_{hc}=41kPa and vertical consolidation stress σ'_{vc}=68.6kPa. Thus, the initial mean effective stress p_c was determined to be 50.3 kPa. Some physical properties of Shanghai soft clay at the depth of interest are presented in Table 1.

Table 1. Index Properties of Shanghai Soft Clay

w(%)	w_L(%)	w_P(%)	I_P	I_L	G_s	S_t	e_0	OCR	K_0
51.8	44.17	22.4	21.77	1.35	2.74	4.86	1.402	1.0	0.6

Figure 3 shows the results of the oedometer tests on undisturbed samples. Based on the results, the consolidation yield stress (σ'_y) was determined to be 110.5 kPa. The initial structural parameter, r_0 =1.61, is determined approximately from σ'_y / σ'_{vc}. The compression index and swelling index (C_c and C_s) of one- dimensional consolidation tests are 0.489 and 0.107 respectively. λ and κ are obtained from C_c and C_s where $\lambda = C_c/2.303$ and $\kappa = C_s/2.303$.

Undrained triaxial tests under isotropic and anisotropic (K_0=0.6) consolidation modes were performed, with the initial effective reconsolidation stress p'=50, 100, 150, 200, 300 kPa.

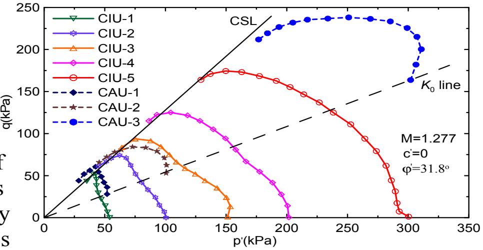

FIG.2. Stress paths in undrained triaxial tests

Figure 2 shows the stress paths of the CIU (isotropically consolidated undrained) and CAU (anisotropically consolidated undrained) tests with a constant axial strain rate. With the progress of strain, it is observed that stress paths reach their peak strength and finally approach a narrow zone in the stress space. This phenomenon shows that the critical state concept could be applied to natural clay at large strains. The slope of critical state line, M , was determined to be 1.277, which corresponds to effective angle of internal friction $\varphi' = 31.8^\circ$.

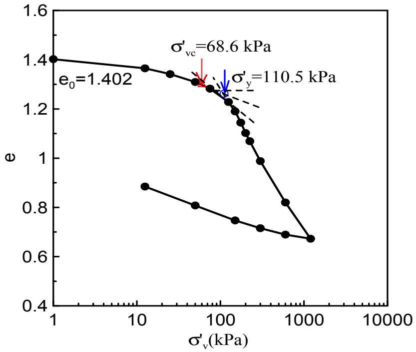

FIG.3. e-logσ'_v curve in oedometer tests

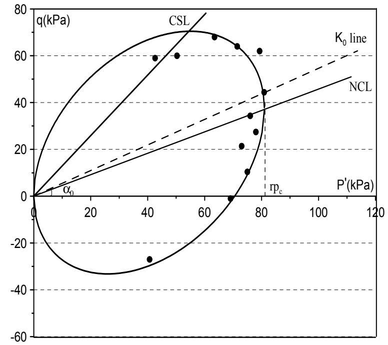

FIG.4. Structure surface

In addition, several stress- controlled drained triaxial tests were carried out in order to obtain the yield points in the stress space. The yield points, which were determined by plots of the deviator stress q against the shear strain ε_s and the mean effective stress p' against the volumetric strain ε_v, are shown in Fig.4. The predicted structure surface from eq. [3] is also shown in Fig.4. The parameter A_0=0.844 was determined from the experimental yield points, which corresponds to α =0.46, giving the inclination of the yield curve. Inspection of Fig.4 shows that the yield curve expression of eq. [3] is a reasonable fit to the experimental data.

Model Simulations

Two groups of triaxial loading tests performed both on isotropically and anisotropically (K_0=0.6) compressed samples of Shanghai soft clay are used to illustrate the capabilities of the proposed model. Table 2 shows the value of model parameters for Shanghai soft clay. These values e_0=1.402, p_c=50.3 kPa, r_0=1.61, A_0=0.844 for the initial stress state have been used for all simulations.

Table 2. Model Parameters for Shanghai Soft Clay

Traditional						Structural		Anisotropic		Stiffness interpolation		
λ	κ	M_c	M_e	ν	R	k_d	B	μ	β	ψ_0	ξ	ς
0.212	0.046	1.277	0.9	0.2	2.0	0.65	0.5	50.0	0.7	10.0	1.5	3.0

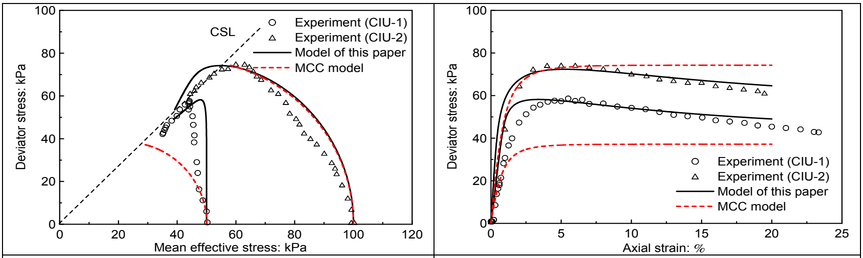

(a) Stress path curve

(b) stress-strain curve

FIG.5. Simulation of undrained tests on isotropically consolidated clay

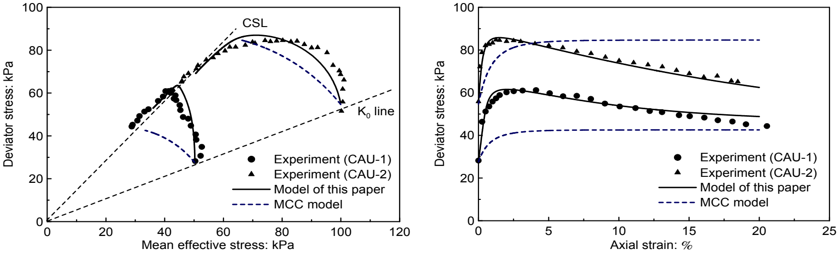

(a) Stress path curve

(b) stress-strain curve

FIG.6. Simulation of undrained tests on anisotropically consolidated clay

Figure 5 presents the undrained compression behavior of Shanghai soft clay with two different isotropic consolidation pressures of 50 and 100 kPa. The model of this paper simulations are in good agreement with the experimental data. The predicted effective stress paths converge towards ultimate remoulded undrained strengths on the critical state line. Figure 6 shows the comparison between the results of two models and the experimental data for two undrained compression tests on anisotropically reconsolidated specimens. The prediction for anisotropic compression tests by the proposed model was fairly satisfactory, illustrating that the proposed model is capable of capturing both structural and anisotropic properties of natural clays. In general, the proposed model gives much better prediction than that of the MCC model.

CONCLUSIONS

A simple model, based on the critical state concept and bounding surface plasticity, has been formulated to describe structure and plastic anisotropy of natural soft clay. The comparisons with triaxial test results of Shanghai soft clay under isotropic and anisotropic consolidation modes, revealed the predictive capability of the proposed model.

ACKNOWLEDGEMENTS

This research is supported by two grants from the National Natural Science Foundation of China (Grant No. 50778132 and Grant No. 50825803).

REFERENCES

Dafalias, Y.F. and Herrmann, L.R. (1982). “Bounding surface formulation of soil plasticity.” *Soil mechanics—Transient and cyclic loads*, G. N. Pande, and O. C. Zienkiewicz, eds., John Wiley & Sons, New York: 253-282.

Kavvadas, M. and Amorosi, A. (2000). “A constitutive model for structured soils.” *Geotechnique*, 50(3): 263-273.

Liang, R.Y. and Ma, F.G. (1992). “Anisotropic plasticity model for undrained cyclic behavior of clays. I: Theory.” *Journal of Geotechnical Engineering*, ASCE, 118(2): 246-265.

Ling, H.I. and Yue, D. (2002). “anisotropic elastoplastic bounding surface model for cohesive soils.” *Journal of Engineering Mechanics*, ASCE, 129(7): 748-758.

Rouainia, M. and Muir Wood D. (2000). “A kinematic hardening constitutive model for natural clays with loss of structure.” *Geotechnique*, 50(2):153-164.

Smith, P.R., Jardine, R.J. and Hight, D.W. (1992). “The yielding of Bothkennar clay.” *Geotechnique,* 42(2): 257-274.

Wheeler, S. J., Naatanen, A., Karstunen, M., and Lojander, M. (2003). “An anisotropic elasto-plastic model for soft clays.” *Canadian Geotechnical Journal*, 40(2): 403-418.

Zentar, R., Karstunen, M. , Wiltafsky, C., Schweiger, H.F., Koskinen, M. (2002b). “Comparison of two approaches for modeling anisotropy of soft clays.” *In*: Proceedings of the 8th International Symposium on Numerical Models in Geomechanics (NUMOG VIII), Rome. 115-121.

Zdravkovic, L., Potts, D.M. and Hight, D.W. (2002). “The effect of strength anisotropy on the behavior of embankments on soft clay.” *Geotechnique*, 52(6): 447-457.

Hypoplastic Model for Simulation of Deformation Characteristics of Bangkok Soft Clay with Different Stress Paths

Sompote Youwai[1], Piyachat Chattanjai[2], Pornkasem Jongpradist[1]
and Warat Kongkitkul[3]

[1]Assistant Professor, Department of Civil Engineering, King Mongkut's University of Technology Thonburi, Bangmod, Thung-kru, Bangkok Thailand; sompote.you@kmutt.ac.th
[2]Doctoral Student, College of Civil Engineering, Tongji University, Shanghai, China.
[3]Lecturer, Department of Civil Engineering, King Mongkut's University of Technology Thonburi, Bangmod, Thung-kru, Bangkok Thailand

ABSTRACT: This paper presents the development of hypoplastic model for simulating deformation characteristics of Bangkok Soft Clay. The results from drained triaxial tests of Bangkok Soft Clay were simulated by the new hypoplastic model with applied stress path of 0-180 degrees in p-q stress space. The proposed hypoplastic model has satisfy performance to predict the deformation characteristics of Soft Bangkok Clay. The stiffness of proposed model varied according to load and unloading condition and different applied stress path.

INTRODUCTION

To design a geotechnical engineering project, generally, stability and serviceability of such design project have to be considered. To predict the unforeseen deformation by numerical analysis, the appropriate constitutive model of each material is essentially needed. For continuum problems, the incremental stress path of soil element would be in different directions. Therefore, soil model should be able to support different applied stress and strain paths. Currently, a number of constitutive models were developed based on elastic-plastic framework for predicting such non-linear behavior. The elastoplastic model was characterized by a series of additional notion which hide the mathematical structure of constitutive equation. Then, the elastoplasticity model was further developed for simulating the hardening behavior of soil. The yield surface can be changed with increment of plastic strain. The Modified Cam-Clay Model (Roscoe and Burland, 1968) was one of the successful elastic-plastic hardening models. For hypoplastic model, several hypoplastic equations were developed for simulation stress-strain behaviors of clay (Here and Kolymbas, 2004: Masin, 2005). For Bangkok Soft Clay, Tanseng (2005) used hypoplasticity of Wu (1990) to simulate the behaviour of Bangkok Clay. With the concept of Structural tensor Weifner and Kolymbas (2007) proposed the hypoplastic model to predict the behavior of clay in overconsolidated state. However, these aforementioned hypoplastic models cannot not predict of Bangkok Clay behavior under isotropic consolidation with unloading condition and the deformation characteristics of soft clay with different applied stress path. Thus, the main objective of this paper is to propose the constitutive model based on the concept of hypoplastic for predicting stress-strain behavior of Bangkok Clays with different applied stress path. The applied stress path was varied from 0 degree to 180 degree in p-q stress space.

THE HYPOPLASTIC SIMULATION OF SOFT BANGKOK CLAY

The hypoplastic model was developed based on the model proposed by Weifner and Kolymbas (2007) as shown as follows:

$$\begin{aligned}\overset{o}{T} &= C_1 \mathrm{tr}(T + f_b S)D + C_2 \frac{\mathrm{tr}((T + f_b S)D)}{\mathrm{tr}(T + f_b S)}(T + f_b S) \\ &+ C_3 \frac{(T - f_b S)^2}{\mathrm{tr}(T + f_b S)}\sqrt{\mathrm{tr}D^2} + C_4 \frac{(T^* - f_b S^*)^2}{\mathrm{tr}(T + f_b S)}\sqrt{\mathrm{tr}D^2}\end{aligned} \tag{1}$$

$$\overset{o}{S} = \mathrm{tr}D\ (\mu 1 + \lambda \frac{T^*}{trT}) \tag{2}$$

$$S^* = S - \frac{1}{3}(\mathrm{tr}S)1 \tag{3}$$

$$f_b = (P'/P_{ref})^{\beta} \tag{4}$$

The revised version of hypoplastic model was done by adding Equation (5) for description the isotropic condition at various applied stress path as follows:

$$\overset{o}{C}_1 = \log\left(\frac{P_{max}}{P}\right) \times \Delta P \times C_5 + C_6 \times (1 + a_a) \times \sqrt{\left(\Delta q^2\right)} \times a_b \tag{5}$$

$$a_a = \sin\left[\tan^{-1}\left(\frac{\Delta q}{\Delta p}\right)\right] \tag{6}$$

$$a_b = (a_a - \alpha_c) \tag{7}$$

$$\alpha_c \approx \sin\left[\tan^{-1}(M_c)\right] \tag{8}$$

where T is the stress tensor; T^* is the deviatoric part of stress tensor; D is the stretching tensor; $\overset{o}{T}$ is the objective stress rate; S is the structure tensor; p is the mean stress; q is the deviatoric stress. According to Equation (5), the first term of this equation was represented to the loading and unloading effect. The maximum past pressure (Pmax) was recorded and normalized Pmax with the current stress state (P). With increasing of the magnitude of over consolidation ratio (OCR), the logarithm term was increasing. The logarithm term was multiplied by incremental of mean stress (ΔP) for defining the direction of stress increment. The second term was represented to the effect of the various applied stress path. For the concept of this term, if the applying stress path angle was lower than the slope of critical state line (Mc), the magnitude of ΔC1/Δt (Eq. 5) decreased caused increasing overall stiffness of constitutive model. The absolute incremental deviatoric stress (Δq) (Eq. 5) affected to the decreasing of the stiffness under the increasing of stress path angle. C5 and C6 coefficients were used for varying the influence of the characteristic of two portion (Eq. 5). For isotropic consolidation in normally consolidated state case, the magnitude of Δq equals to zero caused Equation 5 having only first portion.

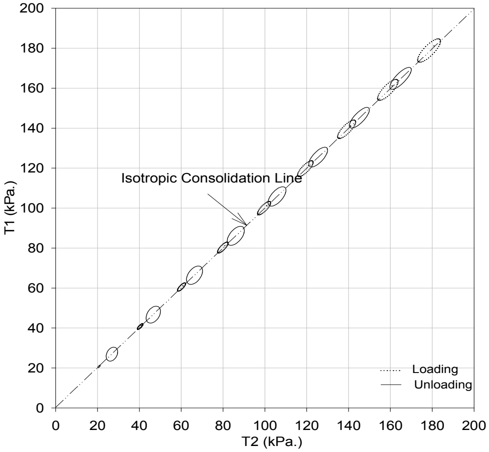

FIG. 1. Stress response envelop of proposed hypoplastic model under isotropic stress condition

The series of stress respond envelop represented to the performance of new constitutive equation with under isotropic consolidation behavior were shown in FIG 1. The circular shape represents the increment of stress with increment of a unit of strain applied from 0 to 360 degree (stress response envelop) all around the stress point. The model parameters were tabulated in table 1. In loading condition for normally consolidated state, the magnitude of $\overset{\circ}{C}_1$ was equal to 0. Therefore, the sizes of stress respond envelop and shape of the new constitutive equations was the similar to those predicted by of Weifner and Kolymbas (2007) model in the normally consolidated behavior. With consideration of the size of stress respond envelop after unloading passing the maximum confining stress, the magnitude of $\overset{\circ}{C}_1$ was changed caused the size of the stress respond envelop being increased under the isotropic consolidation unloading behavior. The stress respond envelop changed its shape form elliptic shape to elliptic-circular shape. These characteristics proposed model were suitable for prediction of the clay behavior under unloading condition.

Table 1. Model parameters for proposed hypoplastic model

C_1	C_2	C_3	C_4	C_5	C_6	Q	μ	λ	α_c
-1.00	-32.00	-50.00	20.00	110.00	100.00	-1.00	70.00	100.00	0.90

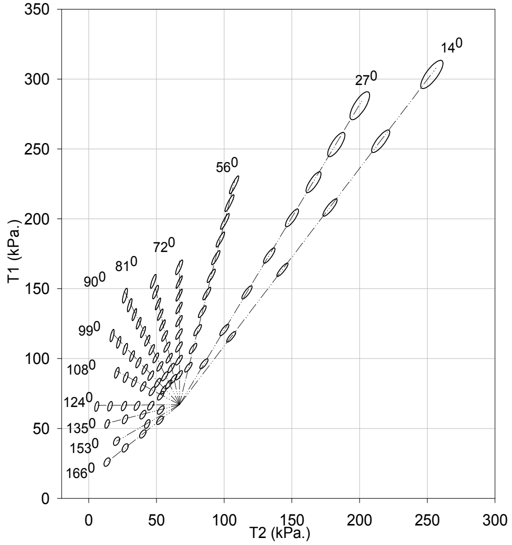

FIG. 2. Stress response envelop of proposed hypoplastic model with different applied stress p

To investigate of the performance of new constitutive equation, the stress respond envelop under the different applied stress path in compression loading and unloading zone was shown as FIG 2. The series of the stress respond envelop was simulated by the parameters in Table 1 at the OCR equal to 2.75 and maximum past pressure at 184 kPa. For simulation of stress respond envelop on the applying stress path of 14^0, 27^0, 153^0 and 166^0, the size stress respond envelop increased the stiffness during the simulating of drained triaxial tests and decreasing the stiffness in the other applying stress path. The new series of stress respond was different form those of the Weifner and Kolymbas (2007) model. The size of stress respond envelop of Weifner and Kolymbas (2007) model model was decreased when increasing of the applying stress path angle.

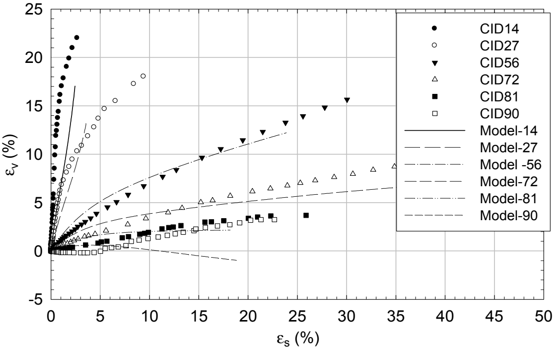

FIG. 3. Relationship between volumetric strain and distortional strain

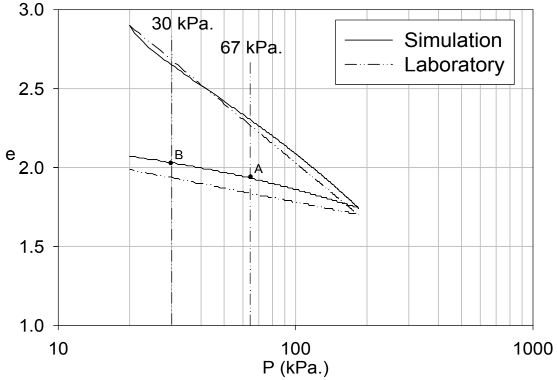

FIG. 4. Simulation of isotropic compression

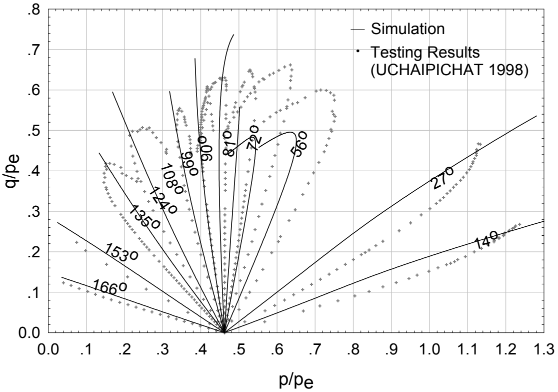

FIG. 5. Normalize stress path with equivalent stress

The performance of this constitutive equation was presented by the comparison of the numerical simulation and the series of experimental testing results of drained triaxial tests and isotropic consolidation as shown in FIGS 3-5. The predicted volumetric strain was reasonably agree well with testing results as shown in Fig. 3. The simulation of isotropic compression test was demonstrated the successful simulation with loading and unloading stress condition with different overconsolidated ratio (OCR). However , for unloading stress state, model simulation for void ratio of isotropic compression test was slightly under-predicted as shown in Fig. 4. The drained triaxial testing results was used the applying stress paths of 0^0-180^0 in q - p' spaces at the OCR equal to 2.75 and maximum past pressure at 184 kPa (Asavadorndeja, 2001). The stress path normalization with the equivalent mean stress (P_e) was shown as FIG 5. The simulation results by using new hypoplastic model were reasonably agree well with the testing results. However, with the angle of stress path being more than 90 degress (p-q stress space), the predicted normalized deviatoric stress (q/p_e) was higher than experimental results.

CONCLUSIONS

This paper presented the hypoplastic model for simulating the deformation characteristics of Soft Bangkok Clay with different stress path of 0 -180 in p-q stress space. The stiffness of proposed hypoplastic model was increased with unloading condition and decreasing of the angle of applied stress path in p-q stress space. The proposed hypoplastic model can reasonably simulate the deformation characteristics of Soft Bangkok Clay with different applied stress path with single set of model parameters.

REFERENCES

Roscoe, K.H. and Burland, J.B., (1968). “On the generalised stress-strain behaviour or 'wet' clay”, In Heyman, J. and Leckie F., editors, Engineering Plasticity, Cambridge University: 535-609.

Herle, I. and Kolymbas, D., (2004) “Hypoplasticity for soils with low friction angles”, *Computers and Geotechnics*, Vol. 31, pp. 365–373.

Mašín, D., (2005) “A hypoplastic constitutive model for sand”, *International Journal for Numerical and Analytical Method in Geomechanics*, Vol. 29: 311-336

Tanseng, P. (2005). “Implementations of Hypoplasticity and Simulations of Geotechnical Problems”, *Ph.D. dissertation*, University of Innsbruck, Institute of Geotechnics and Tunnelling.

Wu, W. and Kolymbas, D., (1990). “Numerical testing of the stability criterion for hypoplastic constitutive equations”, *Mechanics of Materials*, Vol. 9: 245-253.

Weifner, T. and Kolymbas, D. (2007). “A hypoplastic model for clay and sand”, *Acta Geotechnica*, Vol 2: 103-112.

Asavadorndeja, P. (2001). “Modelling The Behavior of Overconsolidated Clay”, *M.Eng. Thesis,* AIT Bangkok.

Role of Microstructure in the Mechanical Behaviour of Clay

N. Kochmanová[1] and H. Tanaka[2]

[1]Ph. D. candidate, Laboratory of Soil Mechanics, Hokkaido University, Sapporo-Shi Kita-Ku, Kita 13 Jo Nishi 8 Chome 060-8628, Japan; kochman@eng.hokudai.ac.jp
[2]Professor, Laboratory of Soil Mechanics, Hokkaido University, Sapporo-Shi Kita-Ku, Kita 13 Jo Nishi 8 Chome 060-8628, Japan; tanaka@eng.hokudai.ac.jp

ABSTRACT: Bentonite, a smectite clay, is widely used in geotechnical engineering as drilling mud, liner material, and has been proposed as buffer material for high-level nuclear waste disposal. This study focuses on the microstructure formation of unsaturated Kunigel-V1, a bentonite clay, and the effect that the microstructure formation has on its mechanical behaviour. The microstructure was studied with Mercury Intrusion Porosimetry (MIP) and a Scanning Electron Microscope (SEM), while the mechanical behaviour was studied using Constant Rate of Strain (CRS) consolidation testing and Constant Volume Direct Shear (CVDS) testing. Test results indicated that aggregates increased in number and size with the addition of water. However, an increase in applied pressure resulted in the dissipation of air, and a decrease in size of the intra and inter-aggregate spaces. The clay's microstructure had little influence on the friction angle (φ), but did affect the dilatancy of the soil.

INTRODUCTION

Bentonite is a widely used material in geotechnical engineering due to its low permeability and swelling behaviour. Bentonite is composed of both swelling minerals, such as smectite, and non-swelling minerals. Smectite minerals are 2:1 clays (two tetrahedral sheets and one octahedral sheet). The space between the layers is occupied by water molecules and exchangeable cations, creating a weak bond between the combined sheets (Mitchell and Soga, 2005). Swelling of bentonite is caused by the adsorption of water into this space. The microstructure of bentonite thus changes depending on the amount of water, which in turn affects the mechanical behaviour of the clay. Although the swelling behaviour of bentonite has been studied extensively, its effect on the mechanical behaviour is limited thus far. Thus the aim of this ongoing study is to gain an understanding of the microstructure of bentonite, and to determine the effect on its mechanical behaviour. The microstructure was studied with Mercury Intrusion Porosimetry (MIP) and a Scanning Electron Microscope (SEM), while the mechanical behaviour was studied by running a series of Constant Rate of Strain (CRS) consolidation and Constant Volume Direct Shear (CVDS) tests.

EXPERIMENTAL STUDY

Kunigel-V1 is a commercial sodium type bentonite, containing 48 % to 57 % montmorillonite (smectite mineral) and non-swelling minerals such as quartz, feldspar, and zeolite, from Yamagata Prefecture, Japan (Komine 2004; Komine et al. 2009). The material properties are presented in Table 1. Samples were prepared at gravimetric water contents ranging from the natural water content to a water content of 70 %. Distilled water was sprayed onto the soil 24 hours prior to testing to create natural aggregates, resulting in non-homogenous samples. The objective of using distilled water in this study was to maintain consistent water chemistry conditions.

CRS testing assesses the compression behaviour of clay, and the effect the water content has on its behaviour. The compression behaviour is in turn affected by the microstructure, thus the difference in compression indicates a difference in the microstructure. CRS testing was carried out on samples with an approximate thickness of 20 mm. The samples were loaded under a constant strain ranging from 0.02 to 0.1 mm per minute, and pressures ranging from 200 kPa to 10 MPa. Additional water was introduced into the loading cell following CRS testing in selected samples, resulting in sample submergence. MIP and SEM samples were compressed using the CRS testing apparatus, and were freeze-dried and placed in a vacuum for 24 hours prior to testing. MIP was used to determine the pore size distribution of a sample, while SEM allowed viewing of the sample’s microstructure. CVDS testing was undertaken to show the influence of the microstructure on the strength and stress paths of the samples.

RESULTS AND DISCUSSION

Constant Rate of Strain (CRS) Consolidation

Figure 1 shows the effects of water on the compression behaviour of Kunigel-V1 through selected CRS test results. Initial void ratio differences between samples of the same water content (0.5 at lower water contents and 2.5 at 70% water content) are attributed to sample preparation methods, namely whether or not the sample was manually compressed prior to testing. The addition of water to dry Kunigel-V1 resulted in the formation of microstructures. Eventually macrostructures formed as the clay particles began to bond. Aggregates formed and surrounded the water molecules, resulting in the introduction of air into the system due to the limited quantity of water. The formation of aggregates also resulted in the creation of micro and macropores. Aggregate size increased with an increase in water content, as seen by the increase in initial void ratio. An increase in pressure resulted in the collapse of the macrofabric, and in some cases a collapse of the microfabric, as seen by the decrease in void ratio with an increase in pressure, with collapse occurring more readily at higher water contents. Also, compression of the clay resulted in the dissipation of air from both the macro- and micro-pores; however, the water did not dissipate, but rather moved from the macro- to the micro-pores. At approximately 150 kPa, it is believed that the macro

Table 1: Material Properties

Property	Kunigel-V1
G_s (g/cm3)	2.799
Natural Water Content	5.0 - 6.2 %
Liquid Limit (LL)	499 %
Plastic Limit (PL)	39 %
Percentage smaller than 2 μm	~65%

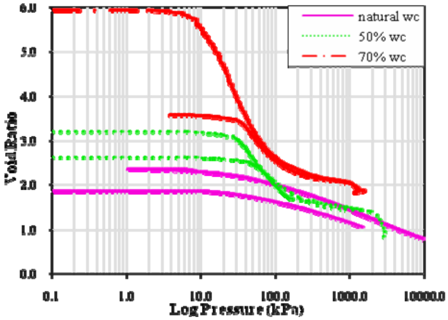

Figure 1: CRS test results

aggregate samples with water contents of 50% and 70 % collapsed. However, the water present in the micro-pores limited the amount of allowable compression, shown by a decrease in the consolidation rate. Thus an S-shaped curve was characteristic for all samples, with the compression index increasing with an increase in water content.

Mercury Intrusion Testing (MIP)

Figure 2 shows the MIP results. Figure 2a shows the pore distribution curves for natural water content samples. A unimodal curve, with a pore entrance diameter of 2 μm, was observed at a pressure of 200 kPa. This indicates that a large volume of similarly sized voids exists at this pressure. A decrease in the pore entrance diameter was observed with an increase in pressure to 3 MPa (1.8 μm) and 10 MPa (1.0 μm). Figure 2b shows the pore distribution curves for Kunigel-V1 samples at higher water contents. At a pressure of 200 kPa and a water content of 30 % and 50 %, a higher volume of larger sized pores was observed compared with samples at their natural water content; increasing the pressure results in bimodal curves centred at 0.5 μm and 0.8 μm for 30 % water content samples and 0.3 μm and 0.5 μm for 50 % water content samples. Delage et al. (2006) stated that for compacted soils, a bimodal curve indicates the presence of an aggregate microstructure, with the modes showing the intra and inter-aggregate pore spaces. The presence of the semi-bimodal curves suggested that the difference between the intra and inter-aggregate pore spaces was not as large as expected or could not be observed for the specimens in this study. Submergence of the samples caused a rearrangement of the particles, resulting in a smaller quantity of smaller sized pores, as seen by the shift in the MIP curves for both the 30 % and 50 %

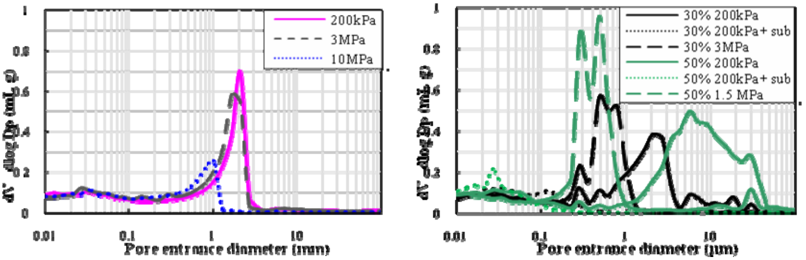

a) **b)**

Figure 2: MIP results a) natural water content b) higher water contents

water content samples at a pressure of 200 kPa. It is believed that once in contact with the water molecules, the particles rearrange themselves, resulting in smaller pores, contributing to the difference between the unsaturated and submerged samples.

Scanning Electron Microscope (SEM)

Figure 3 shows the SEM results for Kunigel-V1. All samples have the same magnification, where the white bar represents 5 μm. Figures 3a and b show Kunigel-V1 samples at a natural water content and at large compression pressures of 3 MPa and 10 MPa. The particles were already in an aggregated state, and an increase in water content resulted in the formation of larger aggregates as a result of both increased aggregation, and an increase in the swelling of existing aggregates, as seen by the particle alignment and presence of voids in Figure 3c and e. An increase in pressure resulted in a realignment of the particles and a collapse of the microstructure, as seen in Figure 3d and f for the 30 % and 50 % water content samples, respectively.

Constant Volume Direct Shear (CVDS) Test

Table 2 and Figure 4 show the results of the CVDS testing. Samples were tested at three different vertical confining pressures: 50 kPa, 100 kPa, and 200 kPa. Once the vertical displacement was fixed, samples were sheared at a rate of 0.2 mm/min under constant volume conditions. Due to the low permeability of Kunigel-V1 ($\sim 10^{-11}$ – 10^{-12} cm/s) drainage did not occur, thus a total stress analysis was used in this study. The results presented in Figure 4a show that an increase in water content to 30 % resulted in an increase in shear strength, whereas an increase to 50 % resulted in a decrease in shear strength. No structures were observed at the clay's natural water content, and the aggregates that formed at 30 % water content were smaller in size than those formed at 50 % water content, resulting in smaller pore entrance diameters, which could cause an increase in matric suction, and thus an increase in strength (Rao & Revanasiddappa 2005). Figure 4b shows the stress paths and failure envelopes for the samples tested, including a saturated sample from Namikawa & Shirai (1998). The average angle of friction (φ) (total stress) for the samples tested in this study was 41.6°, and the angle of friction for the saturated sample was 15.3°. A change in water content had little effect on the friction angle of unsaturated Kunigel-V1 at the water contents

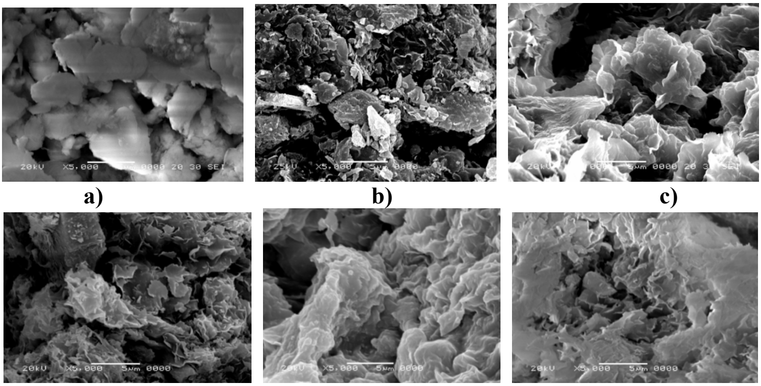

a) b) c)

d) e) f)

Figure 3: SEM results. a) dry, 3MPa b) dry, 10MPa c) 30%, 0.2MPa d) 30%, 3MPa e) 50%, 0.2MPa f) 50%, 3MPa

Table 2: CVDS Summary

Water Content	Pressure (kPa)	τ_{max} (kPa)	τ_{max} /P
Natural	50	13.4	0.268
	100	24.92	0.2492
	200	51.42	0.2571
30%	50	38.63	0.7726
	100	61.26	0.6126
	200	103.36	0.5168
50%	50	35.77	0.7154
	100	45.14	0.4514
	200	67.56	0.3378

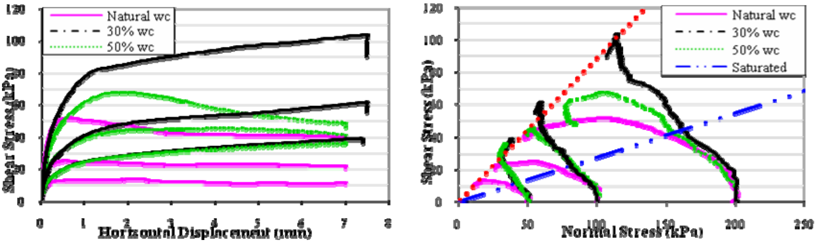

a) b)

Figure 4: CVDS results a) shear and b) stress paths

tested. However, at a water content of 50 % and a confining pressure of 200 kPa it is apparent that the angle of friction is moving towards the failure envelope of the saturated sample. The increase in friction angle with a decrease in water content may be due to matric suction. In this case the friction angle would remain constant, and the apparent cohesion would increase with an increase in matric suction. The decrease in friction angle with saturation is due to the lubricating effect of the water on the particles. The effects of the microstructure are clearly seen in the stress paths of the samples tested, which show apparent dilatancy of the clay. The 30 % and 50 % water content samples at 50 kPa confining pressure showed dilative behaviour. At 30 % water content, aggregate sizes are large enough to act as granular particles, but do not contain enough water to be easily remoulded, as is the case with the 50 % water content samples. At a confining pressure of 50 kPa, the aggregates of the 50 % water content sample remain intact, as not enough pressure is applied to cause the aggregates to collapse and thus be remoulded.

SUMMARY AND CONCLUSIONS

Kunigel-V1 microstructure was observed in this study through a series of laboratory tests. In dry conditions Kunigel-V1 was slightly aggregated; the addition of water increased aggregation, and resulted in an increase in the number and size of voids, seen by the CRS, MIP, and SEM results. An increase in pressure at higher water contents resulted not only in the collapse of aggregates, but in some cases also a collapse of the microstructures, seen by the CRS, MIP, and SEM results. The changes in soil structure had little effect on the strength of the soil, though it did influenced the dilative behaviour, as seen in the CVDS results. Saturation of Kunigel-V1 results in a lubricating effect on the particles, indicated by the decrease in friction angle.

ACKNOWLEDGMENTS

The authors would like to thank the Port and Airport Research Institute and their staff for their assistance and use of the Mercury Porosimeter and the Scanning Electron Microscope used in this study.

REFERENCES

Delage, P. Marcial, D. Cui, Y.J. & Ruiz, X. (2006). "Ageing effects in a compacted bentonite: a microstructure approach." Géotechnique 56(5): 291-304.

Komine, H. (2004). "Simplified evaluation for swelling characteristics of bentonites." *Engineering Geology* 71: 265-279.

Komine, H., Yasuhara, K., & Murakami, S. (2009). "Swelling characteristics of bentonites in artificial seawater." *Canadian Geotechnical Journal* 46: 177-189.

Mitchell, J.K. and Soga, K. (2005). Fundamentals of Soil Behaviour, Third edition, John Wiley & Sons, Inc.

Namikawa, T. & Shirai, K. (1998). "Consolidated Undrained Triaxial Compression Test for Compacted Bentonite. (In Japanese)." *Proceedings of the thirty-third Japan National Conference on Geotechnical Engineering*. Yamaguchi, Japan.

Rao, S.M., & Revanasiddappa, K. (2005). "Role of microfabric in matrix suction of residual soils." *Engineering Geology*. 80(1-2): 60-70.

A Microstructural Approach for Modeling the Mechanical Behavior of Structured Clays

Zhen-Yu Yin[1], Ching S. Chang[2] and Pierre-Yves Hicher[3]

[1] Research fellow, Research Institute in Civil and Mechanical Engineering, Ecole Centrale de Nantes, 44321, France; zhenyu.yin@gmail.com
[2] Professor, Department of Civil and Environmental Engineering, University of Massachusetts, Amherst, MA 01002, USA. E-mail: chang@ecs.umass.edu
[3] Professor, Research Institute in Civil and Mechanical Engineering, Ecole Centrale de Nantes, 44321, France. E-mail: pierre-yves.hicher@ec-nantes.fr

ABSTRACT: This paper presents a stress-strain model for the behavior of structured clays using a microstructural approach. Clay material is considered as a collection of clusters, which interact with each other mainly through mechanical forces. The bonds of structured clays are considered as the bonded forces between clusters in contact. The bonds can also be reduced due to a damage mechanism at a cluster contact during loading. The elasto-plastic stress-strain relationship for structured clays is derived by using the granular mechanics approach which takes into account the behavior at grain level. The model is used to simulate one-dimensional test and undrained triaxial tests. Typical trend of the behavior of structured clay is captured by the proposed model.

INTRODUCTION

Experimental work has highlighted the role of microstructural features in the compressibility and shear strength of natural clays, comparing such properties with those observed on the corresponding reconstituted material (e.g. Clayton et al. 1992, Burland et al. 1996, Graham 2006). The observed differences between natural and reconstituted clays were attributed to structure, defined as the combination of cluster arrangement (fabric) and inter-cluster bonding. This inter-cluster bonding can be related to several different processes that might occur in a clayey deposit on a geological timescale, such as percolation of calcium carbonate, or weak lithification. During loading, the stresses at certain inter-cluster contacts can be thought to reach the bond strength, and a mechanical bond degradation (de-bonding) process is initiated. Bond degradation is an irreversible phenomenon that, experimentally, appears to be controlled by plastic strain accumulation (e.g. Gens & Nova 1993).

The inter-cluster bonding can be directly considered in micro-mechanics approach, such as the stress-strain model developed by Yin et al. (2009) for clay. In this model, the stress-strain relationship for an assembly can be determined by integrating the behavior of the inter-cluster contacts in all orientations using a static hypothesis, which relates the average stress of the cluster assembly to a mean field of cluster contact forces. Since some properties (e.g., elastic stiffness, plastic hardening) are stress-dependent, the results also exhibit naturally the stress-induced anisotropy. This is the advantage of the micromechanical approach compared to conventional plasticity models, i.e., the stress-induced anisotropy is physically characterized in a more direct way than the conventional method of specifying the position of initial yield surface.

In this paper, a new micromechanics based model is developed for structured clays considering inter-cluster bonding and introducing debonding process. The model is examined by simulating one-dimensional compression test and undrained triaxial tests.

MICROMECHANICAL MODEL

Inter-cluster Behavior

Elastic stiffness**:**

On each contact plane, an auxiliary local coordinate can be established as shown in Fig. 1 where *n*, *s*, *t* are three orthogonal unit vectors that form the local coordinate system. The contact stiffness of a contact plane includes normal stiffness, k_n^α, and shear stiffness, k_r^α. The elastic stiffness tensor is defined by

$$f_i^\alpha = k_{ij}^{\alpha e} \delta_j^{\alpha e} \tag{1}$$

which can be related to the contact normal and shear stiffness

$$k_{ij}^{\alpha e} = k_n^\alpha n_i^\alpha n_j^\alpha + k_r^\alpha \left(s_i^\alpha s_j^\alpha + t_i^\alpha t_j^\alpha \right) \tag{2}$$

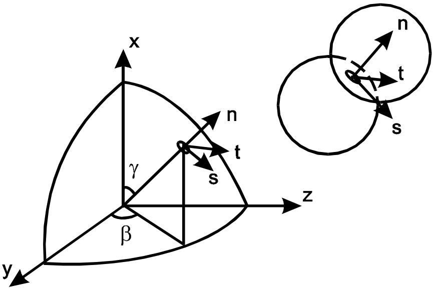

FIG. 1. Local coordinate at inter-cluster contact.

The value of the stiffness for two elastic spheres can be estimated from Hertz-Mindlin's formulation. For sand grains, a revised form was adopted, given by

$$k_n = k_{n0} \left(\frac{f_n}{f_{ref}} \right)^n ; \quad k_r = k_{rR} k_{n0} \left(\frac{f_n}{f_{ref}} \right)^n \tag{3}$$

where f_{ref} is the reference value by $f_{ref} = \frac{3V}{Nl} p_{at}$ (p_{at} is atmosphere pressure equal to

101.3 kPa, *V*/*N* is the total number of contacts per unit volume), f_n is the contact force in normal direction. l is the branch length between the two clusters. k_{no}, k_{rR} and *n* are material constants.

Plastic yield and hardening functions for shear sliding:

Based on experimental observations on global behavior (i.e., Burland et al. 1996, Graham 2006), the yield function for shear sliding is assumed to be of Mohr-Coulomb type, defined in a contact-force space (e.g. f_n, f_s, f_t).

$$F\ (f_n, f_r, H_1) = \frac{f_r}{f_n + f_b} - H_1\left(\delta_r^p\right) \tag{4}$$

where f_b is the force by inter-cluster bonds, $H_1(\delta_r^P)$ is a hardening/softening function. Note that the shear force f_r and the rate of plastic sliding δ_r^P can be defined as

$$f_r = \sqrt{f_s^2 + f_t^2} \quad \text{and} \quad \delta_r^p = \sqrt{\left(\delta_s^p\right)^2 + \left(\delta_t^p\right)^2} \tag{5}$$

The hardening function is defined by a hyperbolic curve in $H_1 - \delta_r^p$ plane, which involves two material constants: ϕ_p and k_{p0}.

$$H_1 = \frac{k_{p0} \tan\phi_p\, \delta_r^p}{\tan\phi_p + k_{p0}\delta_r^p} \tag{6}$$

The value of H_1 asymptotically approaches the apparent inter-cluster friction angle $\tan\phi_p$. The initial slope of the hyperbolic curve, k_{p0}, is assumed to relate k_n by a constant k_{pR}:

$$k_{p0} = k_{pR} k_n = k_{pR} k_{n0} \left(\frac{f_n}{f_{ref}}\right)^n \tag{7}$$

The plastic sliding often occurs along the tangential direction of the contact plane with an upward or downward movement, thus the shear-induced dilation/contraction takes place. The dilatancy equation used here is similar to that proposed by Taylor (1948), given by

$$\frac{d\delta_n^p}{d\delta_r^p} = D\left(\tan\phi_0 - \frac{f_r}{f_n + f_b}\right) \tag{8}$$

where *D* is material constants for stress dilatancy.

Plastic yield and hardening functions for normal compression:

In order to describe the compressible behaviour between two clay clusters, a second yield surface is added. The second yield function is assumed to be as follows:

$$F_2\left(f_n, \kappa_2\right) = f_n - H_2\left(\delta_n^p\right) \quad for\ f_n > \left(f_{pc} + \omega f_b\right) \tag{9}$$

The hardening function $H_2(\delta_n^p)$ is defined as:

$$H_2 = \left(f_{pc} + \omega f_b\right)\exp\left(\frac{\delta_n^p}{c_p}\right) \tag{10}$$

where c_p is the compression index for the compression curve plotted on $\delta_n^p - \log f_n$ plane.

Inter-cluster bonds degradation:

Based on experimental observation that the shear strength decreases during straining, the inter-cluster bonds degradation was analysed as a damage of the bonded contacts. Therefore, a damage law was introduced in the expression of the bonding force amplitude, expressed a follows:

$$f_b = f_{b0} \exp\left(-\xi \sqrt{\left(\delta_n^p\right)^2 + \xi_r \left(\delta_r^p\right)^2} \right) \tag{11}$$

where f_{b0} being the initial bonding force, and ξ ξ_r the factors of damage.

Elasto-plastic relationship:

With the elastic and plastic behavior described above, the final incremental force-displacement relationship of the inter-cluster contact can be derived, given by

$$\dot{f}_i^{\alpha} = k_{ij}^{\alpha p} \dot{\delta}_j^{\alpha} \quad \text{or} \quad \mathbf{f} = \mathbf{K}\boldsymbol{\delta} \tag{12}$$

Detailed expression of the elasto-plastic stiffness tensor can be derived from yield function and flow rule (see Yin et al. 2009).

Influence of density state:

In this model, a static hypothesis is used. Due to the assumption of static constraints, the interactions among clusters have been neglected and the system tends to be softer than true behavior. To account for the interactions among neighboring clusters, a density state $\varphi = e_c / e$ is introduced in reference to the void ratio at critical state which can be obtained by:

$$e_c = e_{ref} - \lambda \ln\left(\frac{p'}{p_c} \right) \tag{13}$$

where $\xi$and λare two material constants, *p'* is the global mean effective stress of the packing.

The resistance can be related to the state of packing void ratio *e* by:

$$\tan\phi_p = \left(\frac{e_c}{e} \right)^{m_1} \tan\phi_\mu \tag{14}$$

where m_1 is a material constant.

The local phase transformation line $\tan\phi_0$ depends not only on the internal friction angle ϕ_μ, but also on the density state, by:

$$\tan\phi_0 = \left(\frac{e_c}{e} \right)^{-m_2} \tan\phi_\mu \tag{15}$$

This relationship allows a dense packing to dilate at earlier stage of shear loading.

Overall stress-strain relationship

The stress-strain relationship for an assembly can be determined from integrating the behavior of inter-cluster contacts in all orientations. In the integration process, a micro-macro relationship is required. Using the static hypothesis, we obtain the relation between the global strain and inter-cluster displacement. The stress increment can be obtained by the contact forces and branch vectors for all contacts. Details can be found in Yin et al. (2009).

MODEL PERFORMANCE

In this section, we examine the model performance on typical one-dimensional and triaxial behaviors of structured clays. For this purpose, values of some basic parameters for Otaniemi clay in Yin et al. (2009) were selected (see Table 1). Using these parameters, one-dimensional compression test and undrained triaxial tests with different levels of initial confining pressure were simulated.

Figure 2 shows simulated results for an assumed one-dimensional compression test. In this test, the global initial intrinsic yield stress is assumed as 50 kPa, the global initial bonding stress for compression (corresponds to ωf_b) is assumed as 100 kPa. The simulations were carried out with different values of ξ The model well captured the trend of one-dimensional compression behavior of structured clays.

Figure 3 shows simulated results for an assumed undrained triaxial compression test. The global initial intrinsic yield stress of 50 kPa and the global initial bonding stress for shear (corresponds to f_b) of 20 kPa are taken for all simulations. The simulations were carried out with different initial isotropic compression pressure: 20, 80, 300 kPa. The model well captured the trend of undrained triaxial compression behavior of structured clays.

Table 1. Values of model parameters for simulations

k_{n0}	k_{rR}	k_{pR}	D	m_1	m_2	e_0	e_{ref}	p_{ref}	λ	c_p
30	0.75	1	1	1	2	2.8	1.5	300	0.46	0.038

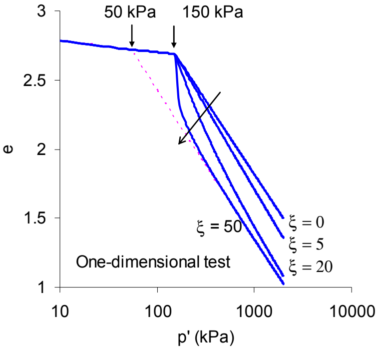

FIG. 2. Simulated results for one-dimensional compression test ($\xi_d = 0.4$).

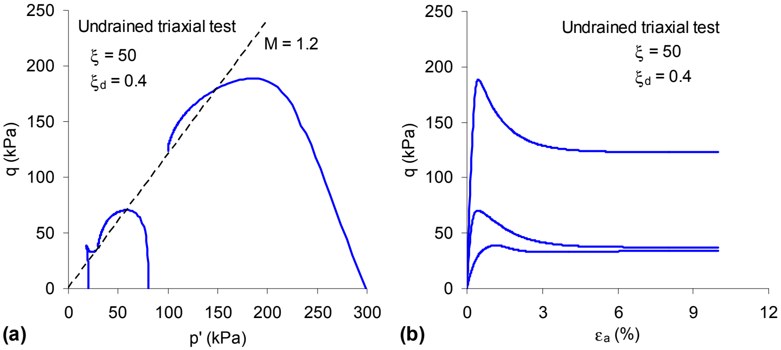

FIG. 3. Simulated results for undrained triaxial compression test.

CONCLUSIONS

A stress-strain model for the behavior of structured clays using a microstructural approach has been developed. Clay material is considered as a collection of clusters, which interact with each other mainly through mechanical forces. The bonds of structured clays are considered as the bonded forces between clusters in contact. A damage mechanism for bonding force at a cluster contact was introduced. The elasto-plastic stress-strain relationship for structured clays is derived by using the granular mechanics approach which takes into account the behavior at grain level. One-dimensional test and undrained triaxial tests were simulated. All simulations demonstrate that the model can well capture the trend of typical behaviors of structured clays.

REFERENCES

Burland, J.B.; Rampello, S.; Georgiannou, V.N. and Calabresi, G. (1996). “A laboratory study of the strength of four stiff clays.” *Geotechnique*, Vol. 46(3): 491-514.

Clayton, C.R.I.; Hight, D.W. and Hopper, R.J. (1992). “Progressive destructuring of Bothkennar clay: Implications for sampling and reconsolidation procedures.” *Geotechnique*, Vol. 42(2): 219-239.

Gens, A. and Nova, R. (1993). “Conceptual bases for a constitutive model for bonded soils and weak rocks.” *Proceedings of International Symposium on Hard Soils - Soft Rocks,* Athens, 485–494.

Graham, J. (2006). “The 2003 R.M. Hardy lecture: Soil parameters for numerical analysis in clay.” *Canadian Geotechnical Journal*, Vol. 43(2): 187-209.

Yin, Z.-Y.; Chang, C.S.; Hicher, P.-Y. and Karstunen, M. (2009). “Micromechanical analysis of kinematic hardening in natural clay.” *International Journal of Plasticity*, Vol. 25(8): 1413-1435.

Engineering Properties and Micro-structural Characteristics of Cohesive Soil in the Interactive Marine & Terrestrial Deposit

Yan-hua Liu[1], Hong Zhang[2], Ming-lei Shi[3]

[1] Department of Geotechnical Engineering of College of Civil Engineering, Tongji University, Shanghai 200092, China; yanhua3537@126.com
[2] Key Laboratory of Road and Traffic Engineering of the Ministry of Education, Tongji University, Shanghai 201804, China; zhanghong3537@126.com
[3] Transportation College Southeast University, Nanjing 210096, China; mingleish@163.com

ABSTRACT: Cohesive soil of the interactive marine & terrestrial sediment is deposited along the north side of the Yangtze River estuary of China. The natural deposit has poor physical properties, whose natural moisture content is close to or greater than the liquid limit and the void ratio is close to or greater than one, which is similar to that of the natural soft marine clay, while the former have much higher in-situ strength and sensitivity than the latter. Oedometer tests and corresponding micro-structural tests under different consolidation stresses are performed on both the undisturbed and the remolded interactive deposit soil to investigate the reason which causes the abnormal combination between the poor physical properties and good mechanic characteristic indexes. It is found that the natural interactive deposit soil, which belongs to strong structural soil, shows good uniformity between micro-structural change and macro- mechanical properties.

INTRODUCTION

There is several dozen meters cohesive soil deposited along Nantong-Qidong expressway of the north side of the Yangtze River estuary of China. Such cohesive soil has poor physical properties, in which are embodied that the natural moisture content is close to or greater than the liquid limit and the void ratio is close to or greater than 1. The physical properties are similar to that of the soft natural marine clay, but the compressibility and strength indexes are different from the latter.

According to the original survey data, most of deposits along Nantong-Qidong expressway belong to soft clay. However, engineering practices proved that it is unreasonable to some extent, adopting the thought of soft clay to design the embankment of testing sections. It needs to be investigated that what reason has led the unreasonable design method and whether the natural interactive deposits could be treated as soft clay or not.

Cohesive soils in the different regions manifested kinds of structural characteristics, to some different degree, its geotechnical properties were impacted by the occurrence environment and deposition conditions. Many researchers have made great efforts to understand the behavior of cohesive soils in different regions. The geotechnical characteristics of structural clays deposited in Shanghai and Zhanjiang of China were researched by Zhang (1983). Mesri et al. (1975) researched on the composition and compressibility of typical clay of Mexico City. Gong et al. (2000) studied on the formation of clay structure and its influence on mechanical characteristics of clay in Hangzhou. And other researchers have carried out substantial investigation on structural characteristics of cohesive soils in the different areas (e.g. Grand Baleine clay, Locat, 1985; Huaiyin clay, Shi, 1997).

To investigate deeply the mismatched behavior between the poor physical properties and good mechanical characteristics of cohesive soil deposited in Yangtze River estuary, some new samples are taken by free piston thin wall sampler technique along Nantong-Qidong expressway. One-dimensional consolidation tests and corresponding micro-structural tests under different consolidation stresses are performed on both the undisturbed and the remolded samples. The vacuum freeze drying method was adopted to prepare the micro-structural samples, in which decreases effectively the sample disturbance.

BASIC ENGINEERING PROPERTIES

The physical characteristics of the natural interactive cohesive soil are shown in Fig.1 and Table 1. It can be seen that the wet density are normal, ranging from 1.6~2.0g/cm^3, while the dry density which varies within 1.2~1.5g/cm^3 are relative low. Most of the void ratio is close to or greater than 1. So the soil belongs to cohesive soil with low density (Jiang, 1986). The natural water contents (40% or so) is excessive or close to liquid limit which below generally to 50, however, plasticity indexes range from 6~15, and grain size composition is mainly silt. According to engineering classification of soils, the natural interactive deposit soil belongs to soft clay, of which the properties are low plasticity and low liquid limit.

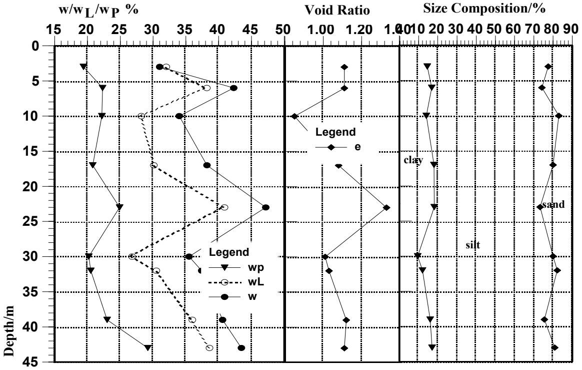

Fig. 1 Physical Index of Cohesive Soil

Table 1. Physical Property and Compression Characteristic of Cohesive Clay

sample	thin wall	thick wall	depth (m)	ρ_0 (g/cm^3)	ρ_d (g/cm^3)	I_P	$a_{100\text{-}200}$ (Mpa^{-1})	undist q_u(kPa)	remold q_u(kPa)	S_t
No.1	◆		3.0	1.68	1.28	12.60	0.74	46.4	4.64	10.0
No.2		◆	6.0	1.83	1.29	15.90	0.65	26.0	5.20	5.0
No.3		◆	10.0	1.98	1.48	6.00	0.72	25.3	5.50	4.6
No.4	◆		17.0	1.82	1.32	9.30	0.08	65.0	5.28	12.3
No.5		◆	23.0	1.74	1.18	16.00	0.76	21.3	5.92	3.6
No.6		◆	30.0	1.83	1.35	6.60	0.54	29.2	6.21	4.7
No.7		◆	32.0	1.85	1.35	10.00	0.66	19.5	5.57	3.5

In this study, two kinds of sampling methods were used to obtain the undisturbed specimens. As shown in Table1, the thin-walled samples which are less disturbed and are considered to keep perfectly the original structural characters of soil, have higher unconfined compressive strength and sensitivity than that of the thick-walled samples. The comparison of test results between thin wall sample and thick wall sample has effectively proved that the interactive cohesive soil deposited along the north side of the Yangtze River estuary, is some kind of strong structural soil. Sampling quality is vital to evaluate correctly engineering properties of soil, in particular strong structural soil which is sensitive to mechanical disturbance and stress release in the process of sampling (Nagaraj et al. 1990). It should be noted that bad sampling quality can lead to distortion of laboratory test results and wrong conclusion.

Fig.2 and Fig.3 show the uniaxial compression curve of thin-walled undisturbed samples (No.1 and No.4) and corresponding remolded samples. It can be seen that the compressive curve of undisturbed sample lies above that of remolded sample, and they gradually converge with the increase in stress level. On the compression curve of undisturbed sample, there is an obvious inflection point, in which the compressive behavior of soil indicates significant differences. According to the results of previous studies and field investigations, the natural interactive deposit soil has never been subjected to a maximum stress history being larger than the current overburden pressure (Huang et al. 1996), i.e. the soil of sampling sites is normally-consolidated soil. The pre-consolidated pressure should be equal to effective self-weight stress, which are determined to be $\sigma_{sz(NO.1)} = 23kPa$ and $\sigma_{sz(NO.4)} = 140kPa$ respectively. While the consolidation pressures corresponding to inflection points are 60kPa and 400kPa for No.1 and No.4 respectively, which are greater than their effective self-weight stress. It has been well documented that many natural sedimentary soils have a consolidation yield stress larger than the overburden pressure (Schmertmann, 1991). This is attributed to the resistance of soil structure developed during the depositional and the post-depositional processes (Nagaraj et al. 1990). According to Burland (1990), the ratio of consolidation yield stress to pre-consolidation pressure, is named as yield stress ratio. For No.1 and No.4, the yield stress ratios are 2.61 and 2.86 respectively, indicating that the natural interactive deposit is normally-consolidated strong structured soil.

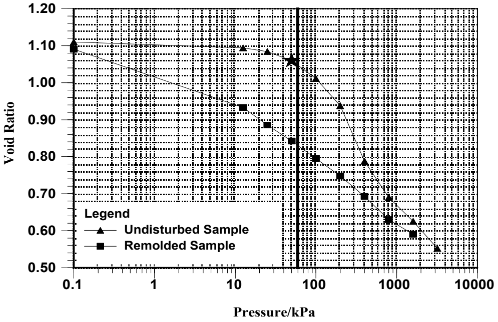

Fig. 2. e-log(p) Curve of Sample No.1

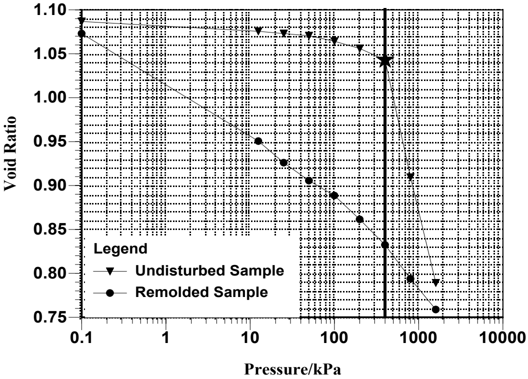

Fig. 3. e-log(p) Curve of Sample No. 4

As shown in Fig.2 and Fig.3, the compression curve of undisturbed sample can be well interpreted by two parts in the *e*-lg*p* plot, i.e. pre-yield state and post-yield state. In the pre-yield state which refers to that the applied stress level is less than the consolidation yield stress, the mechanical behavior of soil is hardly unchanged because of the resistance of initial structure. When the applied load is beyond the consolidation yield stress, the compressive behavior of soil enters into post-yield state, in which a small increment of force can lead to greater change of void ratio in that the original structure of soil is mostly destroyed. It can be known that it is unreasonable to evaluate the compressibility of soil with the compressive coefficient $a_{100-200}$, seeing that the compressive behavior comes into being turn on the point of consolidation yield stress (Feng, 1992). As to No.1 sample, which the consolidation yield stress (60kPa) is lower than 100 kPa, the compressive coefficient ($a_{100-200(No.1)}$=0.74Mpa^{-1}) is distorted heavily. Thus, in the course of evaluating engineering characteristic, the wrong conclusion on high compressibility was given. In engineering practice, we have to emphasize the influence of structure on compressibility of soil, and assess the compressibility of soil according to practical loading interval.

MICRO-STRUCTURAL CHARACTERISTICS

To investigate the micro-mechanism of macro-mechanical behavior of the interactive deposited soil, a series of micro-structural tests were carried out. Fig.4 shows the typical micrograph of undisturbed cohesive soil sample. In this micrograph, structural elements of soil present the aggregate-flocculation structure. And the most of flaky elements affix to the surfaces of granular particles, which play an important role in cementation of inter-particle. Meanwhile, it can be seen that there is fewer big trellis pores in view of numerous contact points among granular particles.

A certain amount of diatom debris deposits are observed in SEM sample, as shown in Fig.5. Diatom is a eucaryotic microorganism with single cell, of which the cell wall is filled with silica ($SiO_2 \cdot nH_2O$). It had been researched by Tateishi(1997) on a kind of soil in Japan involving plentiful natural diatom debris, which indicates strong structural characteristic with high moisture and high strength and stiffness. The engineering properties of interactive cohesive soil deposited along the north side of the Yangtze River estuary, are similar to that of above researched deposit, associating poor physical characters with good mechanical behaviors.

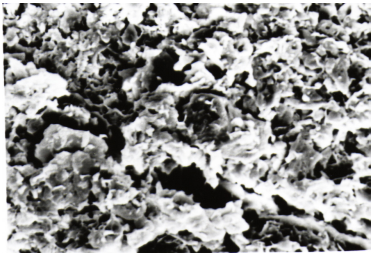

Fig.4. SEM Image of Undisturbed Sample

Fig.5. Diatom Debris

Considering that the deformation and failure of soil are caused essentially by the existence of voids in soil, micro-structural parameters related to void are drawn in the process of micrographs. To get the micro-structural parameters of soils, the image processing system of German LeicaQwin5000 is used. Pore size distributions of No.1 and No.4 under different consolidation pressure are shown in Table 2. Fig.6 and Fig.7 show the comparison relation curves of Area Fraction of Void versus consolidation pressure between undisturbed samples and remolded samples. The Area Fraction of void refers to the ratio of the measured pore areas and the total image areas, which represents the content of voids in soils. As shown in Table 2, pore size of less than 5 micrometer takes major proportion in undisturbed sample, and there is not macro pore whose pore size exceeds 10 micrometer. This conclusion is coincident with that of observed micrograph. When the applied stress is under structural yield stress, the change of pore distribution in both of undisturbed samples is slight. And the pore percentage of several intervals of 5～10μm and 2～5μm and 1～2μm, are decreased substantially with the increase in stress level when the applied stress is larger than the consolidation yield stress. Meanwhile, the content of pore in the group of (<1μm) is increased obviously, on the condition that the load exceeds structural yield stress. It is noted that the resistance of soil structure gradually disappears under the higher stress than consolidation yield stress.

Table 2. Pore Size Distribution of Undisturbed Sample under Different Pressure

Sample	Consolidation pressure(kPa)	<1μm	1~2μm	2~5μm	5~10μm	>10μm
No.1	0	29	41	23	7	0
	12.5	32	40	22	6	0
	50	58	29	12	1	0
	100	67	24	6	3	0
	400	74	15	6	5	0
Sample	**Consolidation pressure(kPa)**	**<1μm**	**1~2μm**	**2~5μm**	**5~10μm**	**>10μm**
No.4	0	37	33	24	6	0
	12.5	40	34	21	5	0
	50	43	30	22	5	0
	200	60	28	10	2	0
	800	74	17	2	7	0

Fig.6 and Fig.7 present the comparison in curves of Area fraction of void versus consolidation pressure between undisturbed and remolded interactive cohesive soil. The Area Fraction of Void decreases with the increasing consolidation pressure, as to both undisturbed and remolded sample. On the relationship curve for undisturbed sample, there is an obvious inflection point, at which the Area Fraction of Void takes on clear change. While the curve between Area Fraction of Void and consolidation pressure corresponding to remolded sample, is almost linear. Comparing the curves between void ratio versus consolidation pressure and Area Fraction of Void versus consolidation pressure, the varying tendency of Area Fraction of Void is similar to that of void ratio with the increase of applied stress. But the consolidation pressure corresponding to inflection point on the latter curve is less than that of the former, which is attributed to disturbance once again in the process of sample preparation for micro-structural tests. Under the premise of indeed undisturbed specimen, i.e., the sample is not disturbed at all, there is no doubt that the consolidation yield stress corresponding to inflection point of two curves should be uniform absolutely.

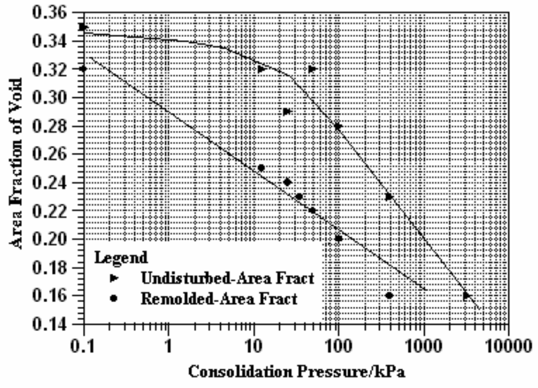

Fig. 6. Curve of Area Fraction of Void vs. Consolidation Pressure of Sample No.1

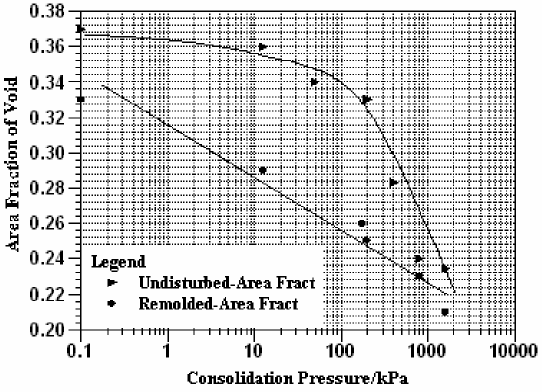

Fig. 7. Curve of Area Fraction of Void vs. Consolidation Pressure of Sample No.4

CONCLUSIONS

Based on the analysis of physical indexes and consolidation test and micro-structural test, several conclusions are summarized as follows.

(1) The natural interactive cohesive soil in the north side of the Yangtze River estuary belongs to strong structural soil, according to the research results of

consolidation test and microstructure test.

(2) The existence of structure in interactive cohesive soil is an essential factor, of which causes to the abnormal combination of poor physical indexes and good mechanical properties. The neglect of structure results in unreasonable design in practical engineering.

(3) Emphasizing the influence of soil structure on physical and mechanical properties, the different change laws are presented in pre-yield and post-yield stages.

(4) The unanimous tendencies of micro-structural parameters and macro-structural parameters under consolidation pressure, indicates macroscopic properties of soil are the external behaviors of micro-mechanism.

(5) Paying attention to influence of soil disturbance on engineering characteristics, the test results received from undisturbed soil could reflect relatively of the true engineering properties of soil.

REFERENCES

Burland, J.B. (1990). “On the compressibility and shear strength of natural clays.” *Géotechnique*, 40:329－378.

Feng, M.Z. (1992). “Compression curve of soft cohesive soil.” *Chinese Journal of Geotechnical Engineering*, 14(9): 95－100.

Gong, X.N., et al. (2000). “The formation of clay structure and its influence on mechanical characteristics of clay.” *Journal of Hydraulic Engineering*, (10):43-47.

Huang, H.Z., Tang, B.G., Yang, W.D. (1996). “Sedimentary geology of the Yangtze River Delta.” Beijing: China Geological Press.

Jiang, G.C. (1986). “Structure stability of cohesive soil and behavior of some special soil.” *Chinese Journal of Geotechnical Engineering*, 8(4):71-73.

Locat, J., Lefebvre, G. (1985). “The compressibility and sensitivity of an artificially sediment clay soil: the Grande –Baleine marine clay.” Quebec. *Marine Geotechnical*, 6 (1): 1－27.

Mesri, G. Roskhsar, A., Bohor, B.F. (1975). “Composition and compressibility of typical samples of Mexico City clay.” *Géotechnique*, 25 (3): 527－554.

Nagaraj, T.S., Srinivasa Murthy, B. R., Vatsala, A. et al. (1990). “Analysis of compressibility of sensitive soil.” *Proc*. ASCE.J. GEO. 116(1):105-118.

Schmertmann, J. H. (1991). “The mechanical aging of soils.” *Journal of the Geotechnical Engineering Division*, American Society of Civil Engineers, 117(9): 1288 - 1330.

Shi, B. (1997). “Quantitative research on the orientation of microstructures of clayey soil.” *Acta Geologica Sinica*,71(1): 36-43.

Tateishi, Y. “Geotechnical properties of diatom earth and stability of surface layer for the cut slope.” Doctoral Thesis, Saga University.

Zhang, C.H. (1983). “Geotechnical characteristics of two structure clays.” *Journal of Nanjing Hydraulic Research Institute*, (4): 65－71.

Investigating the Microstructure of Compacted Crushed Callovo-Oxfordian Argillite

Chao-Sheng Tang[1], Anh-Minh Tang[2], Yu-Jun Cui[2],
Pierre Delage[2], Bin Shi[1], Christian Schroeder[3]

[1]School of Earth Sciences and Engineering, Nanjing University, China;
tangchaosheng@nju.edu.cn; shibin@nju.edu.cn
[2]Ecole des ponts - ParisTech, U.R. Navier/CERMES, France ;
tang@cermes.enpc.fr; cui@cermes.enpc.fr; delage@cermes.enpc.fr
[3]ANDRA (French Radioactive Waste Management Agency), France;
Christian.Schroeder@andra.fr

ABSTRACT: Some aspects of the macroscopic geotechnical behavior of compacted soils are highly related to their microstructure. This paper presents a qualitative and quantitative microstructure investigation of compacted samples made up of crushed Callovo-Oxfordian argillite. This material is considered as being possibly used as backfill material in radioactive waste disposal at great depth. Scanning electron microscopy and mercury intrusion porosimetry technique were employed to determine the fabric and pore size distribution properties of the samples. The results show that an increase of the compaction effort only results in the reduction of the inter-aggregates porosity. After wetting, the sample displays a relative homogenous microstructure with a decrease in the macropores population.

INTRODUCTION

Compacted soil is widely used in geotechnical, hydraulic and geoenvironmental engineering in embankments, earth-dams, waste repositories, as structure foundation, etc. The engineering properties of compacted soils (including compressibility, shrinkage, swelling, collapse and permeability) are controlled by the microstructure. In this context, a large number of investigations have been carried out about the microstructure of compacted soils (Lambe, 1958; Diamond, 1970; Sridharan et al., 1971; Ahmed et al., 1974; Delage et al., 1996, Romero et al. 1999).

In France, compacted crushed Callovo-Oxfordian (COx) argillite has been considered as a possible sealing/backfilling material in geological high-level radioactive waste repository at great depth. Considering the important role of sealing/backfilling material in the long term safety of the repository, the microstructure changes of compacted crushed COx argillite samples after undergoing complex hydro-mechanical changes corresponding to the in-situ changes after placement should be well understood. In the present investigation, mercury intrusion porosimetry (MIP) and scanning electron microscopy (SEM) tests were performed on compacted crushed COx argillite samples. The microstructure changes of samples that were submitted to different compaction and wetting conditions were investigated.

Material

Compacted samples were prepared from pieces of intact Callovo-Oxfordian (COx) argillite taken from the site of ANDRA URL of Bure (North-eastern France) at a depth of about 490 m. COx argillite contains 40–45% clay minerals (mainly illite–smectite interstratified minerals and illite), 20–30% carbonates and 20–30% quartz and feldspar (Fouché *et al.*, 2004). The argillite was air-dried and crushed to powder, the grain size distribution of which is presented in Fig. 1, from dry sieving.

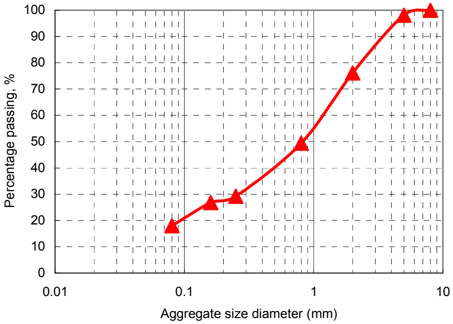

FIG. 1. Grain size distribution of the crushed COx argillite powder

SAMPLE PREPARATION

Freeze-drying is widely accepted as the most appropriate dehydration technique. In this technique, small sized samples are quickly frozen by plunging them into liquid nitrogen submitted to vacuum so as to cool it down to its freezing point (-210°C). Being nitrogen at its freezing temperature, no bubbling occurs when plunging the small samples, resulting in an extremely quick freezing process that occurs with no expansion due to the cryptocrystalline state of the ice (Delage and Pellerin, 1984; Delage et al. 1996; Romero and Simms, 2008). Once frozen, samples are placed under vacuum (10^{-2} mm Hg) and water is sublimated with no shrinkage, in the absence of air-water capillary menisci.

EXPERIMENTAL METHODS

Compaction and wetting

To investigate the effect of the compaction stress on soil microstructure, a mass of air-dried crushed COx powder was statically compacted in an oedometer cell to dry unit masses of 1.8 and 2.0 Mg/m^3. For some samples, once a dry density of 2.0 Mg/m^3 was reached, the sample was unloaded to 7.0 (a value close to the in-situ effective stress) or 0.5 MPa (a low value to allow comparison). Distilled water was then infiltrated so as to saturate the samples under a constant volume condition. Samples were subsequently freeze-dried so as to perform MIP tests and SEM observation.

Microstructure investigations

Mercury penetration in a porous medium is characterized by the interfacial mercury-solid tension (σ=0.484 N/m) and the contact mercury-solid angle (θ=141.3°). Based on Laplace's law (Eq. 1), a mercury pressure p range of 0.1–200 MPa corresponds to an entrance pore diameter d range of 15 - 0.008 μm respectively. The pore size distribution (PSD) curve obtained is characterized by both the pore size density function and the cumulative curve of intruded mercury that also defines the total mercury intruded void ratio e_m (mercury intrusion volume / solid volume).

$$d = \frac{4\sigma\cos\theta}{p} \tag{1}$$

SEM observations were carried out by using an ISI-ABT-55 scanning electron microscope.

RESULTS AND DISCUSSION

In Fig. 2a, the cumulative PSD curves of compacted and intact COx argillite samples are presented. As expected, the total intruded mercury volume characterized by e_m strongly depends on the soil dry density. As the dry density increases from 1.8 to 2.0 Mg/m^3 the final e_m decreases from 0.44 to 0.38. Unsurprisingly, the total intruded volume of the intact sample is much lower than that of compacted samples due to significantly higher dry density (2.25 Mg/m^3) at natural state. After wetting under constant volume condition, the intruded mercury volume appears not to be significantly influenced by the applied initial axial stress σ_{vi} (7 or 0.5 MPa). However, the wetting process results in a clear increase of mercury intrusion at pore diameter range of 0.4-0.6μm.

In Fig.2b, a typical bimodal porosity of aggregate microstructure is observed in compacted samples (Ahmed et al., 1974) compared to the unimodal porosity of the intact sample that characterizes a matrix microstructure. The curve defines the average dimensions of the intra-aggregate and inter-aggregates pores. The modal size of intra-aggregates pores remains in the range of 0.03-0.04 μm and is slightly affected by the hydromechanical path followed (increased mechanical load or applied wetting path). However a significant decrease in the modal size of inter-aggregates pores is observed when the dry density increases under loading from 1.8 to 2.0 Mg/m^3. The modal size of the inter-aggregates pores shifts from 4.25 to 2.13 μm respectively. This behavior is compatible with the results obtained by Delage et al. (1996) on a compacted silt soil that showed that the distribution of intra-aggregate pores was the same for samples with different water contents and dry densities. Therefore, it can be concluded that the volumetric deformation of compacted soil under mechanical load only results from the changes in inter-aggregates porosity.

The subsequent wetting path applied on the samples compacted at 2.0 Mg/m^3 induces a significant reduction in the average entrance diameter of the inter-aggregates pores

(Fig. 2b). Similar behavior was reported by Cui et al. (2002) who observed that macroscopic void ratio decreased with decreasing suction. This is due to the expansion and exfoliation of the aggregates that result in the filling of macropores.

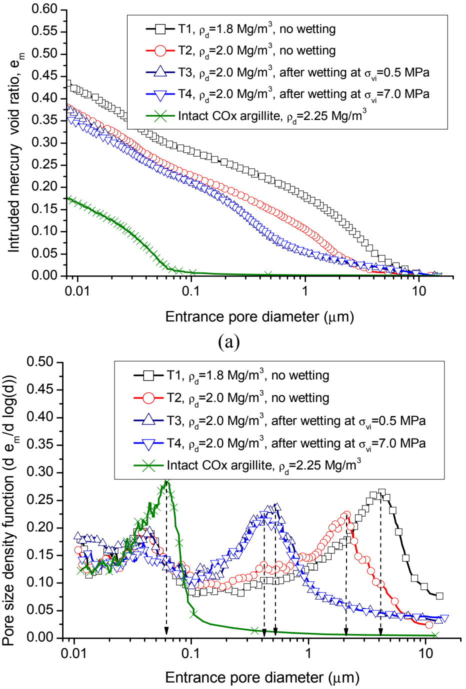

(a)

(b)

FIG. 2. MIP test results of compacted and intact samples: (a) cumulative intruded mercury void ratio; (b) pore size density function

By using the Environmental Scanning Electron Microscope (ESEM), Montes et al. (2004) evidenced the swelling and the destructuration of clay aggregates when wetting the COx argillite. In Fig. 2b, when samples were wetted under constant volume, a slight difference in the PSD curves was observed in spite of the difference in applied axial stress (0.5 and 7.0 MPa*)*. But it cannot be concluded that the applied axial stress level has no influence on soil microstructure, whereas depends on test conditions. If the sample is wetted under constant volume condition as described in this investigation, the effect of initial applied axial stress on the PSD evolution may be slight. If the sample is wetted under constant axial stress condition, the increase of stress would also results in reducing the size of macropores (Cuisinier and Laloui, 2004).

Fig. 3 presents respectively the SEM pictures of compacted samples with dry density of 2.0 Mg/m^3 before and after wetting. Before wetting (Figs. 3a), aggregates made up of clay particles are evident with diameter of several microns to a hundred microns.

Aggregates are separated by inter-aggregate pores with dominant diameter of 1-2μm. This microstructure is compatible with the aggregate size distribution shown in Fig. 1 and with the pore size distribution measurements of Fig. 2.

Fig. 3b presents the SEM picture of the compacted sample after wetting under σ_{vi}=0.5 MPa. It can be seen that the wetted sample shows a quite different overall image in spite of having the same dry density (2.0 Mg/m^3). Aggregates are no longer evident with apparent coating of hydrated larger clayey platelets. The large pores found before wetting the samples are no longer evident, and some large inter-aggregate pores seem to have been filled with the clay fraction. Most of the inter-aggregates are smaller than 0.5 μm. In addition, one can also identify smaller pores, particularly within the particles stacked by clayey platelets, where very small sizes probably exist within the coatings or inter-aggregate links. These microstructure changes of compacted soil after wetting are consistent with the observation made by Komine and Ogata (1999) and Cui et al. (2002). For the sample wetted at initial axial stress of 7.0 MPa, no significant difference was observed with the sample wetted at σ_{vi}= 0.5 MPa.

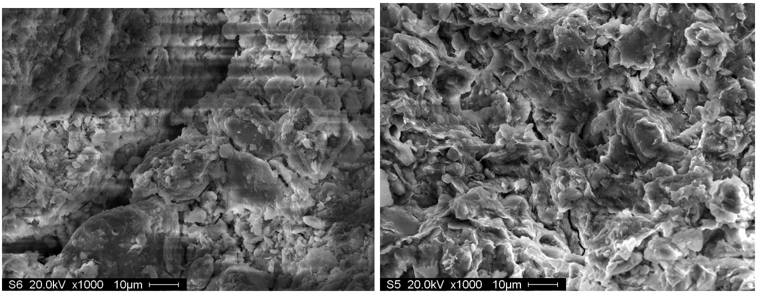

(a) (b)

FIG. 3. SEM pictures of the compacted samples: (a) ρ_d = 2.0 Mg/m^3, before wetting; (b) ρ_d = 2.0 Mg/m^3, after wetting under σ_{vi} = 0.5 MPa.

CONCLUSION

An investigation of the microstructure of compacted crushed COx was carried out by means of scanning electron microscopy (SEM) and mercury intrusion porosimetry (MIP) techniques. Some general conclusions are drawn as follows:

Unlike the intact COx argillite, which exhibits unimodal porosity, the compacted crushed COx argillite exhibits a typical bimodal porosity. During compaction, the increase in load only results in the decrease in the inter-aggregate porosity with a reduction of the average entrance inter-aggregate pore size. At the same time, the intra-aggregate porosity remained unchanged after undergoing different compaction efforts.

Under constant-volume conditions, water wetting also induces a decrease of the size of macro-pores. The initial stress condition slightly influences the pore size distribution. After wetting, many large inter-aggregate pores are filled by exfoliation and subdivision of the hydrated clay aggregates. The initially observed aggregates are no longer evident. The microstructure of sample becomes more homogeneous.

The findings of this investigation are very significant for better understanding the macroscopic behavior of soil during compaction and wetting, especially for the design of some practical engineering, such as foundation compression, stability of building constructed on swelling soil.

ACKNOWLEDGEMENTS

The authors wish to acknowledge ANDRA (the French Radioactive Waste Management Agency) for its financial support. The views expressed in this paper are that of the authors and do not engage ANDRA in any matter.

REFERENCES

Ahmed S., Lovell C.W. & Diamond S. 1974. "Pore sizes and strength of compacted clay." *ASCE J. Geotech. Eng. Div.,* Vol. 100, 407-425.

Cui, Y.J. Loiseau, C. and Delage, P. (2002). "Microstructure changes of a confined swelling soil due to suction controlled hydration." *Proceedings of 3rd International Conference on Unsaturated Soils*, Recife, Brazil. In: Juca´, de Campos, Marinho (eds) Unsaturated Soils, vol.2. A.A. Balkema Publishers, Lisse, pp 593-598, 10-13.

Cuisinier, O. and Laloui, L. (2004). "Fabric evolution during hydro-mecanical loading of a compacted silt." *International Journal for Numerical and Analytical Methods in Geomechanics*, Vol. 28 (6): 483-499.

Delage, P. Audiguier, M. Cui, Y.J. and Howatt, M.D. (1996). "Microstructure of a compacted silt." *Can. Geotech. J.,* Vol. 33:150-158.

Delage P, Lefebvre G. (1984). "Study of the structure of a sensitive Champlain clay and of its evolution during consolidation." *Can. Geotech. J.*, 21:21-35.

Diamond S. (1970). "Pore size distribution in clays. "*Clays and Clay Minerals,* Vol. 18, 7-23.

Fouché, O. Wright, H. Le Cléac'h, J.M. and Pellenard, P. (2004). "Fabric control on strain and rupture of heterogeneous shale samples by using a non-conventional mechanical test." *Applied Clay Science,* Vol. 26 (1-4): 367-387.

Komine, H. and Ogata, N. (1999). "Experimental study on swelling characteristics of sand-bentonite mixture for nuclear waste disposal." *Soils and Foundations*, Vol. 39 (2): 83-97.

Lambe, T.W. (1958). "The structure of compacted clays." *J. Soil Mech. Found. Div.,* ASCE, Vol. 84 (2):1-34.

Montes, H.G. Duplay, J., Martinez, L., Escoffier, S. & Rousset, D. (2004). "Structural modifications of Callovo-Oxfordian argillite under hydration.dehydration conditions. *Applied Clay Science* 25, No. 3-4, 187-194.

Romero E., Gens A. & Lloret A. 1999. "Water permeability, water retention and microstructure of unsaturated compacted Boom clay." *Engineering Geology*, Vol. 54, 117-127.

Romero E., Simms, P.H. (2008). "Microstructure investigation in unsaturated soils: A review with special attention to contribution of mercury intrusion porosimetry and environmental scanning electron microscopy." *Geotech Geol. Eng.,* Vol. 26 (6): 705-727.

Sridharan A., Altschaeffl A.G. and Diamond S (1971). "Pore size distribution studies." *ASCE Journal of the Soil Mechanics and Foundations Division*, Vol. 97, 771-787.

Analytical Solution and Numerical Simulation of Shear Bands along Different Stress Paths in Three-dimensional Stress State

Wenzhan Zhen, De'an Sun and Yaoyao Chen

Department of Civil Engineering, Shanghai University, Shanghai 200072, China; 357737863@qq.com; sundean@shu.edu.cn; bingoyy11@yahoo.com.cn

ABSTRACT: This paper presents an analytical solution and numerical simulation of a failure mode in over-consolidated clays based on the elasto-plastic description of the material. First, a bifurcation analysis is performed to study the failure mode of the over-consolidated clay specimen along different stress paths. It is shown that the occurrence of either homogeneous failure or localized failure depends on the Lode angle. The bifurcation does not occur in tests along the stress paths at the Lode angle in the ranges of -30° ~ -26.5° and 7.5° ~ 30°. However, bifurcation points are detected in tests along stress paths with the Lode angle varying from -26.5° to 7.5°. Second, the elastoplastic model is integrated into the software ABAQUS. Three-dimensional (3D) finite element simulations along stress paths of the triaxial compression, triaxial extension, and plane strain are performed. The results have validated the capacity of the model to simulate the instability and strain localization phenomena.

INTRODUCTION

Strain localization, in the form of narrow shear zones known as a shear band, is a well-known phenomenon in geomaterials when a certain limit state is approached. The limit state is induced when material goes to softening or geometrical nonlinearity, and the bifurcation of deformation is reached. The bifurcation modes of deformation are widely observed when deformation becomes large, and a failure state is approached. Even in element tests, the occurrence of bifurcation modes is unavoidable, no matter how much effort is made to prevent inhomogeneity of deformation.

The phenomenon of shear banding has been studied extensively over the last three decades by different researchers in experimental, theoretical and numerical methods. Various theoretical interpretations for bifurcation modes of deformation (Hill and Hutchinson, 1975; Rudnicki and Rice, 1975; Vardoulakis, 1980; Ottosen et al., 1991; Peric et al., 1993) have been made up to the present. The theoretical analysis shows that bifurcation and instability conditions in geomechanics are closely related to the elasto-plastic model, and thus the bifurcation study can give some insight into the failure mechanism of geomaterials and may provide further understanding for elasto-plastic constitutive behavior. Besides analytical study, numerical simulations of strain localization have been made by several investigators (Yatomi and Yashima, 1989) and shear bands have been observed.

This paper presents analytical and numerical solutions of the occurrence of bifurcation of deformation and shear strain localization in over-consolidated clays along different stress paths. A unified hardening (UH) model for over-consolidated clays (Yao et al., 2009), which embodies many vital soil behaviors, is employed in this study.

OUTLINE OF THE UNIFIED HARDENING (UH) MODEL

Theoretical analysis shows that bifurcation of deformation in geomechanics is closely related to the used model. In order to investigate strain localization of over-consolidated clays, a UH model is employed, which can capture characteristics of stress-strain relationships, shear dilatancy, strain hardening and softening, and stress-path based behavior of over-consolidated clays in 3D stress states, using the SMP criterion and the corresponding transformed stress. The yield function can be written as

$$f=\frac{\lambda-\kappa}{1+e_0}\left[\ln\frac{\tilde{p}}{\tilde{p}_0}+\ln\left(1+\frac{\tilde{q}^2}{M^2\tilde{p}^2}\right)\right]-\tilde{H}=0 \tag{1}$$

where

$$\tilde{H}=\int dH=\int\frac{M_f^4-\tilde{\eta}^4}{M^4-\tilde{\eta}^4}d\varepsilon_v^p \tag{2}$$

$$M_f=6\left[\sqrt{\frac{k}{R}\left(1+\frac{k}{R}\right)}-\frac{k}{R}\right] \tag{3}$$

$$R=\frac{\tilde{p}}{\tilde{\bar{p}}_0}\left(1+\frac{\tilde{\eta}^2}{M^2}\right)\exp\left(-\frac{1+e_0}{\lambda-\kappa}\varepsilon_v^p\right)\qquad 0<\mathrm{R}\le 1 \tag{4}$$

$$k=\frac{M^2}{12(3-M)} \tag{5}$$

where, the superscript ~ denotes the transformed stress space, H is a hardening parameter, ε_v^p denotes the plastic volumetric strain. λ and κ are the slopes of normal compression line and unloading line, respectively, e_0 is the initial void ratio, M and M_f are the stress ratios at the critical state and potential failure, respectively. R is over-consolidation parameter, $\bar{p}_0$ is constant and corresponds to the length of p-axes of the reference yield ellipses at initial condition when $\varepsilon_v^p=0$, p is the mean stress, q is the deviatoric stress, and $\eta=p/q$.

BIFURCATION ANALYSIS FOR THE UH MODEL

The localized failure mode is characterized by a shear band formation, due to strain localization which has been well described by Rudnicki and Rice (1975). It is assumed that the velocity and the stress fields are continuous up to a state at which planar weak discontinuities may develop in a homogeneous specimen under uniform deformation. Across a weak discontinuity plane *S* in Fig.1, the velocity and stress fields are initially continuous, but the gradient of velocity will experience a jump. The bifurcation criterion corresponds to the vanishing of determinant of acoustic tensor Γ_{ij} as follows:

$$\det(\Gamma_{ij}) = \det(n_i D^{ep}_{ijkl} n_j) = 0 \quad \text{with } i,j,k,l = 1,2,3 \tag{6}$$

where n_i is the unit vector normal to a shear band, and D^{ep}_{ijkl} is the elasto-plastic tensor.

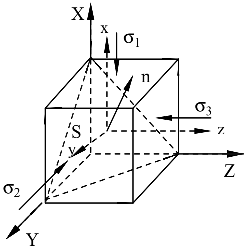

FIG. 1. Sketch of weak discontinuity plane in principal stress space.

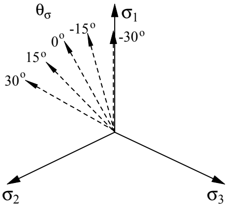

FIG. 2. The Lode angles in the deviatoric stress plane.

PREDICTION OF FAILURE MODES IN OVER-CONSOLIDATED CLAYS

Experimental observations have shown that a weak discontinuity plane *S* occurs in two-dimensional plane in Fig.1 under true triaxial stress condition. Substituting $n_2 = 0$ in Eq. (6), the bifurcation condition is given as follows:

$$A\tan^4\theta + B\tan^2\theta + C = 0 \tag{7}$$

where

$$A = D^{ep}_{1313} D^{ep}_{1111} \tag{8}$$

$$B = D^{ep}_{1111} D^{ep}_{3333} - D^{ep}_{1133} D^{ep}_{1313} - D^{ep}_{3311} D^{ep}_{1313} - D^{ep}_{1133} D^{ep}_{3311} \tag{9}$$

$$C = D^{ep}_{1313} D^{ep}_{3333} \tag{10}$$

$$\tan\theta = -n_1 / n_3 \tag{11}$$

Here, the elasto-plastic tensor D^{ep}_{ijkl} of the UH model can be written as

$$D^{ep}_{ijkl} = D^{e}_{ijkl} - D^{e}_{ijmn} \frac{\partial f}{\partial \tilde{\sigma}_{mn}} \frac{\partial f}{\partial \sigma_{st}} D^{e}_{stkl} / X \tag{12}$$

where

$$X = \frac{M_f^4 - \tilde{\eta}^4}{M^4 - \tilde{\eta}^4} \frac{\partial f}{\partial \tilde{\sigma}_{ii}} + L \frac{\partial f}{\partial \sigma_{ii}} \frac{\partial f}{\partial \tilde{\sigma}_{jj}} + 2G \frac{\partial f}{\partial \sigma_{ij}} \frac{\partial f}{\partial \tilde{\sigma}_{ij}} \tag{13}$$

in which *L* and *G* are Lame's constants, δ_{ij} is the Kronecker delta, and D^{e}_{ijkl} is the elastic constitutive tensor.

Bifurcation condition Eq. (7) is capable of predicting the failure modes of the UH model along different stress paths, which are specified by different Lode angles in Fig. 2. This solution conducted using $\lambda/(1+e_0)=0.0508$, $\kappa/(1+e_0)=0.0112$, $M=1.36$, $\nu=0.3$. The bifurcation solution of the model is achieved under a constant mean stress (p=196kPa) and a constant over-consolidation ratio (OCR=8). The closed-form solutions are listed in

Table 1, which presents the bifurcation strain and stress ratios at bifurcation and peak. Table 1 shows that the bifurcation is detected if the Lode angle is equal to -22.5°, -15°, 0° and 7.5°. But bifurcation does not occur along the stress paths at the other Lade angle.

The bifurcation and peak stress points are identified by solving Eq. (7), and are illustrated in Fig. 3. The figure presents the bifurcation points in the hardening regime before the peak for Lode's angles of -22.5°, -15°, 0° and 7.5°.

Bifurcation stress points are presented and compared with the peak stress points in Fig. 4. For stress paths at the Lode angle in the ranges of -30° ~ -26.5° and 7.5° ~ 30°, bifurcation does not occur at all and uniform deformation at the peak state may be achieved in the test if there is no initial imperfection in the specimen. There are bifurcation points detected in the hardening regime with Lode's angle varying from -26.5° to 7.5°, which indicates that the failure occurs as banded shear strain localization.

Table 1. Theoretical Solutions of Bifurcation by the UH Model

Lode's Angle	Bifurcation Strain Points (%)	Bifurcation Stress Ratio	Peak Stress Ratio Point
-22.5°	3.50	6.46	6.90
-15°	2.55	5.87	7.18
0°	2.60	5.68	6.81
7.5°	3.30	6.51	6.53

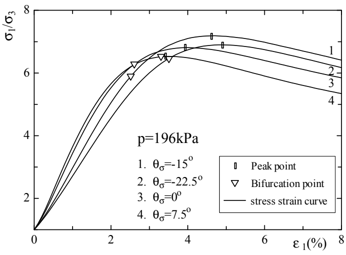

FIG. 3. Bifurcation and peak points.

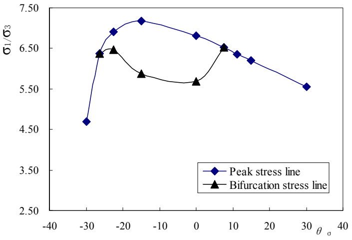

FIG. 4. Dependence of bifurcation and peak points on the Lode angle.

NUMERICAL SIMULATION OF SHEAR BANDS

Shear localization response is now studied by simulating the laboratory tests using the 3D nonlinear finite element program ABAQUS. The UH model described earlier in the paper is implemented through the user material subroutine interface (UMAT). A cubical specimen with the dimensions of 10cm×10cm×10cm is assumed and triaxial compression, triaxial extension and plane strain tests are simulated. In the simulations of the triaxial compression test, the pressure is applied to both lateral surfaces. Under the plane strain test, the normal displacements on one of the lateral faces are prescribed to zero. In both cases, load is applied with the axial displacement (strain) control on the top surface. In the triaxial extension tests, the specimen is loaded by controlling lateral displacement on both lateral surfaces. In all these tests, the mean pressure p and OCR stay constantly with p equal to 196 kPa, and OCR equal to 8). The parameters as described previously are employed for all numerical simulations. The effects of initial imperfection from a homogeneous state are taken into account by introducing weak elements with OCR=1. This permits the softening behavior and shear localization in specimens to be analyzed for different degrees of initial heterogeneity.

Although there is no bifurcation for the stress paths for the triaxial compression and extension tests with the Lode angles of -30° and 30°, as described previously in Fig. 4, the simulation results show that two planar shear zones are clearly visible in the contour plot of deviatoric strain in Fig. 5(a) and Fig. 6(a). This is because that the weak elements, which are embedded into the specimens, can induce the occurrence of the shear bands. Fig. 5(b) and Fig. 6(b) present the stress-strain relationships of the ideal and real specimens. These results show that shear bands leads to a sharp drop in the average stress in the softening regime after the peak stress points.

For the plane strain test, the stress path has a varying Lode's angle, starting from about -18° at isotropic state to about the theoretical value of 0° near the bifurcation point. The closed-form solutions agree well the shear bifurcation that occurs in the hardening regime. The numerical simulations do not display any visible shear bands in Fig. 7(a). The reason is that numerical difficulties of severe mesh-dependency were encountered in the finite element computations, due to the specimens with a low degree of initial heterogeneity (reflected by the number of weak elements). These difficulties were characterized by the solution that fails to converge in a reasonable number of equilibrium

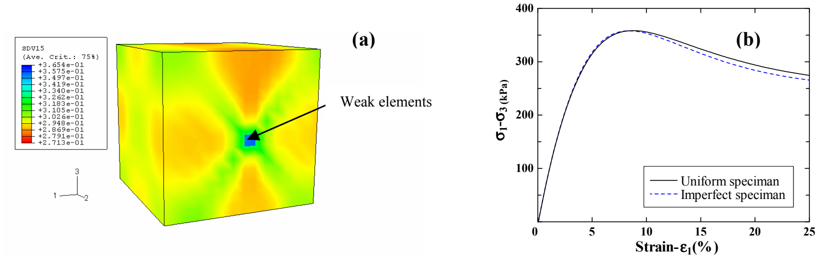

FIG. 5. Numerical simulation of the triaxial compression tests: (a) contour plots of the deviatoric strain (b) The stress-strain curves.

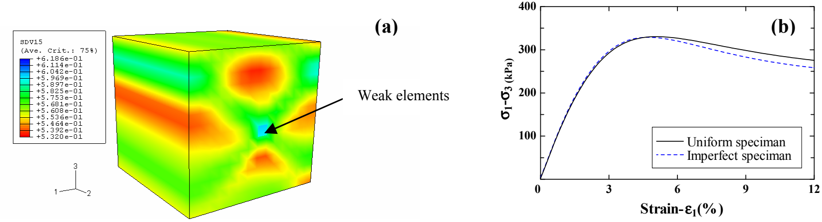

FIG. 6. Numerical simulation of the triaxial extension tests: (a) contour plots of the deviatoric strain, and (b) The stress-strain curves.

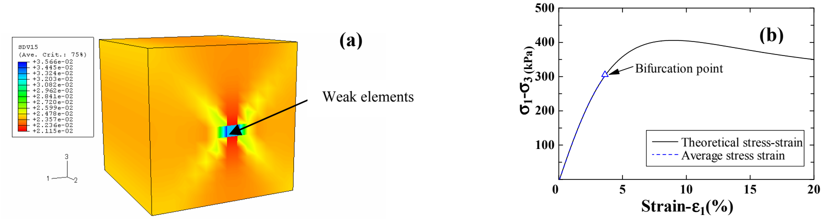

FIG. 7. Numerical simulation of the plane strain tests: (a) contour plots of the deviatoric strain, and (b) The stress-strain curves.

iterations. The analytically predicted bifurcation point was reached as shown in Fig. 7(b).As a result, numerical simulation cannot get the post-bifurcation behavior. The micro-polar theory, non-local theory and higher-gradient theory introduce a characteristic length, which can regularize the failure process.

CONCLUSIONS

The closed-form analysis and the numerical simulation of bifurcation along different stress paths in 3D stress were performed. The bifurcation of the UH model depends on Lode's angle. Bifurcation does not occur at the Lode angle in the ranges of $-30^o \sim -26.5^o$ and $7.5^o \sim 30^o$. However, bifurcation points in the hardening regime are detected with Lode's angle varying form -26.5^o to 7.5^o. The structural responses of specimens along different stress paths have been studied numerically. The numerical simulations show that the initial imperfections do not change the failure mode in the plane strain test, but affect the occurrence of shear bands in the triaxial compression and extension tests.

REFERENCES

Hill, R. and Hutchinson, J.W. (1975). "Bifurcation phenomena in the plane tension test." *J. Mech. Phys. Solids*. Vol.23: 239-264.

Rudnicki, J.W. and Rice, J.R. (1975). "Conditions for localization of deformation in pressure-sensitive dilatant materials." *J. Mech. Phys. Solids*. Vol.23: 371-394.

Ottosen, N.S., Runesson, K., and Peric, D.(1991). "Discontinuous bifurcations of elastic-plastic solids at plane stress and plane strain." *Int. J. Plasticity*, Vol. 7(1): 99-121.

Peric, D., Runesson, K. and Sture, S. (2009). "Prediction of plastic localization using the MRS-Lade model." *J. Geotechnical & Geoenv. Engrg.*, 1993, Vol. 119(4): 639-661.

Vardoulakis, I. (1980). "Shear band inclination and shear modulus of sand in biaxial tests." *J. Numer. Anal. Meth. Geomech.*, Vol.4: 103-119.

Yatomi, C., Yashima, A., Iizuka, A. and Sano, I. (1989). "Shear bands formation numerically simulated by a non-coaxial Cam-clay model." *Solis & Foundations*. Vol. 29(4): 1-13.

Yao, Y.P., Hou, W. and Zhou, A.N. (2009). "UH model: three-dimensional unified hardening model for overconsolidated clays." *Geotechnique*. Vol. 59(5):451-469.

Comparative Modeling of Shear Localization in Granular Bodies with FEM and DEM

Lukasz Widulinski[1], Jan Kozicki[1], Jacek Tejchman[1]

[1]Department of Civil and Environmental Engineering, Gdansk University of Technology, Gdansk 80-952, Poland, tejchmk@pg.gda.pl

ABSTRACT: The intention of the paper is to compare the calculations of shear zones in granular bodies using two different approaches: a continuum and a discrete one. In the first case, the FEM based on a micro-polar hypoplastic constitutive law was used. In the second case, the DEM was taken advantage of, where contact moments were taken into account to model grain roughness. The comparative calculations were performed for a passive case of a translating and rotating retaining wall.

INTRODUCTION

The earth pressure on retaining walls belongs to a classical problem of soil mechanics. In spite of intense theoretical and experimental research on this problem over more than 200 years, there are still large discrepancies between theoretical solutions and experimental results due to the complexity of the deformation field in granular bodies near the wall caused by localization of deformations. The localization can appear as single, multiple or pattern of shear zones depending upon initial and boundary conditions. The shear zones can be plane or curved. The multiple patterns of shear zones are not usually taken into account in engineering calculations.

The realistic earth pressures can be only calculated with continuum models which are able to describe the formation of shear zones with a certain thickness and spacing, i.e. the constitutive model has to be endowed with a characteristic length of micro-structure (Tejchman et al. 2007).

In this paper, the geometry of shear zones in initially dense sand during passive earth pressure tests of a retaining wall was calculated for a plane strain case using two different approaches.

First, the finite element method was used on the basis of a micro-polar hypoplastic constitutive model (Tejchman and Gorski 2008, Tejchman 2008). Second, a discrete element method YADE developed at University of Grenoble was applied (Kozicki and Donze 2009, Belheine et al. 2008). The continuum and discrete calculations were carried with same initial void ratio of cohesionless sand. The calculated geometry of shear zones was compared with model tests (Leśniewska 2000).

MICRO-POLAR HYPOPLASTIC MODEL

Non-polar hypoplastic constitutive models (Gudehus 1996) are capable of describing the salient properties of granular materials, e.g. non-linear stress-strain relationship, dilatant and contractant behaviour, pressure. dependence, density dependence and material softening. A further feature of hypoplastic models is the inclusion of critical states, in which deformation may occur continuously at constant stress and volume. The hallmark of these models is their simple formulation and procedure for determining the parameters with standard laboratory experiments. The material parameters are related to granulometric properties, viz. size distribution, shape, angularity and hardness of grain (the calibration procedure was given in detail by Herle and Gudehus (1999)).

Hypoplastic constitutive models without a characteristic length can describe realistically the onset of shear localization, but not its further evolution. In order to account for the post bifurcation behavior, a characteristic length was introduced into the hypoplastic model by means of a micro-polar theory (Tejchman and Gorski 2008), which makes use of rotations and couple stresses (having clear physical meaning for granular materials). The characteristic length is equal to the mean grain diameter. The constitutive relationship requires ten material parameters, which are determined with one single oedometric compression test with an initially loose specimen, one single triaxial test with a dense specimen, from the angle of repose and with conventional index tests (Tejchman and Gorski 2008).

DISCRETE ELEMENT METHOD

The discrete element method (DEM) is a numerical approach where a solid material can be represented by a collection of particles interacting among themselves in the normal and tangential direction. In spite their simplicity, the method is able to reproduce a complex incremental stress-strain response of granular materials (Iwashita and Oda 1998). The limitations of the method is: necessity of long computational time and difficulty to validate it experimentally. Discrete elements can have different geometries, but to keep a low calculation cost, usually the simplest spherical geometry was chosen. However, the spherical geometry is too idealized to accurately model phenomena exhibited by real granular materials. In the paper, the so-called soft-particle approach was used, i.e. the model allows for particle deformation modeled as an overlap of spheres. To approximately simulate grain roughness, contact moments were introduced to spheres which were transferred through contact surfaces (Iwashita and Oda 1998, Kozicki and Donze 2008).

NUMERICAL RESULTS

The continuum and discrete calculations were performed with a sand body of a height of 200 mm and length of 400-480 mm. The height of the retaining wall located at the right side of the sand body was assumed to be h = 170 mm. Two sides and the bottom of the sand specimen were assumed to be very rough. The retaining wall was assumed to be stiff and very rough. Three different wall modes were assumed in passive tests: horizontal translation, rotation around the wall bottom and rotation around the wall top.

In plane strain FE calculations, 3200 triangular elements were used. The calculations were carried out with large deformations and curvatures (updated Lagrange formulation). The initial stresses were generated using a K_o-state without polar quantities. The calculations were carried out with nine material parameters assumed for so-called Karlsruhe sand on the basis of a single oedometric compression test, a single triaxial test (Tejchman 2008) and conventional index tests. The mean grain diameter was $d_{50} = 0.5$ mm. To enhance and promote the whole process of the shear zone formation, the initial void ratio e_o was distributed non-uniformly in the sand body, i.e. it was equal in each finite element to $e_o = 0.60 + 0.05r$, where r is a random number within the range of (0.01, 0.99).

In DEM calculations, 4000 spheres with different radii from the 0.4-1.2 cm ($d_{50} = 5$ mm) were assumed (the assumption of the real mean grain diameter $d_{50} = 0.5$ mm was not possible due to the time limit). The material was initially dense, the mean initial void ratio of the entire granular specimen was ($e_o = 0.60$). The specimen depth was equal to the grain size. The discrete material parameters were assumed on the basis of a homogeneous triaxial test for Karlsruhe sand (Widuliński et al. 2009): $E_c = 30$ GPa (modulus of elasticity of contact), $\upsilon_c = 0.3$ (Poisson's ratio of contact), $\mu = 30^o$ (inter-particle friction coefficient), $\eta = 1.0$ (parameter controlling the elastic limit of the rolling behaviour), $\beta = 0.15$ (parameter describing the rolling stiffness). Thus, the results of a homogeneous triaxial test (without shear localization) were similar for the FEM and DEM.

Figures 1 and 2 present the FE results (normalized load-displacement diagram and deformed meshes with a distribution of the micro-polar rotation) and Figs.3 and 4 demonstrate the corresponding DEM results (normalized load-displacement diagram and deformed body with the grain rotations).

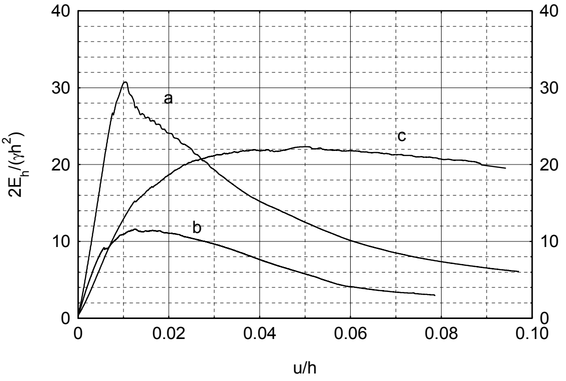

FIG. 1 Resultant normalized earth pressure force $2E_h/(\gamma h^2)$ versus normalized wall displacement *u/h* for initially dense sand (passive case): a) translating wall, b) wall rotating around top, c) wall rotating around bottom (γ - initial density of sand, h – wall height) (FEM)

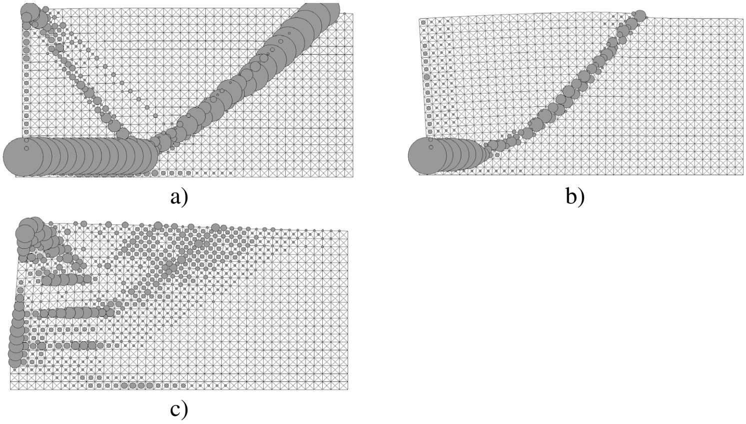

FIG. 2 Deformed FE-meshes with distribution of Cosserat rotation for initially dense sand during passive earth pressure with a) translating wall, b) wall rotating around top, c) wall rotating around bottom

The evolution of the horizontal earth wall pressures is similar in all cases within the FEM and DEM (Figs. 1 and 3). The earth pressure forces increase, reach a maximum (*u/h* = 1-5%), next show softening and tend to asymptotic values (at about *u/h* = 7-9%). The maximum horizontal wall force is the highest for the wall translation, and the lowest for the wall rotation about the top. The maximum normalized horizontal earth pressure forces are high, 12-31, due to the high initial void ratio of sand, large wall roughness, high relationship between the mean grain diameter and wall height and low initial stress level.

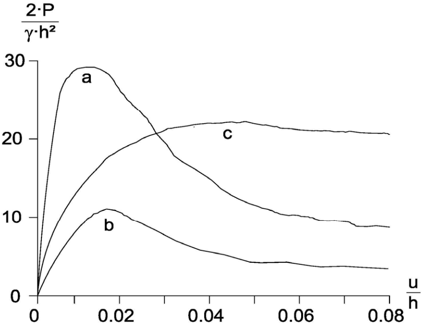

FIG. 3 Resultant normalized earth pressure force *2P/(γh²)* versus normalized wall displacement *u/h* (passive case) for initially dense sand: a) translating wall, b) wall rotating around top, c) wall rotating around bottom (DEM)

For the wall translation (FEM), five shear zones are obtained: one vertical along the very rough retaining wall, one zone projecting horizontally from the wall base, one inclined (slightly curved) zone spreading between the wall bottom and free boundary, and two radial oriented shear zones starting to form at the wall top (Fig.2a). The inclined shear zone becomes dominant in the course of deformation. The horizontal shear zone develops only at the beginning of the wall translation. The thickness of the dominant shear zone is about $30 \times d_{50}$ (on the basis of the Cosserat rotation) and its inclination from the bottom is about 40°.

In the case of the wall rotation around the top (FEM), only one shear zone occurs which is more curved than the shear zone during the wall translation (Fig.2b). When the retaining wall rotates around the bottom (FEM), a pattern of curved parallel shear is obtained (Fig.2c).

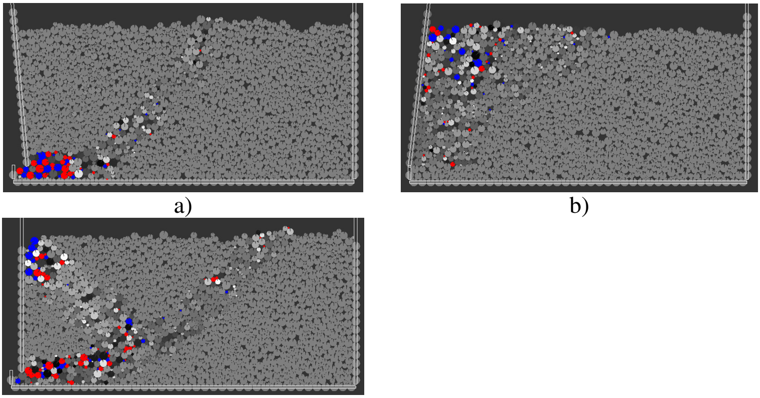
a) b)

c)

FIG. 4 Deformed granular body with grain rotations for initially dense sand during passive earth pressure with a) translating wall, b) wall rotating around top, c) wall rotating around bottom (DEM)

In the case of DEM simulations, the geometry of shear localization is similar (on the basis of grain rotations) except of the case with the wall translation where only one radial shear zone was obtained. The calculated geometry of shear zones with FEM and DEM is in accordance with experiments (Le niewska 2000).

CONCLUSIONS

The following conclusions can be drawn on the basis of the performed numerical continuum and discrete studies on shear localization during a plane strain passive earth pressure problem:

A micro-polar hypoplastic approach and a discrete element method are capable to capture a complex patterning of shear zones in the interior of the granular material. However, a continuum model is more advantageous due to a possibility to simulate larger specimens with smaller grain sizes. The discrete model is still limited by computation time.

The geometry of shear zones depends strongly on the type of the wall movement (translation, rotation around the bottom or around the top). The experimental deformation field including shear zones is realistically reproduced.

The largest passive earth pressure occurs with the horizontal translation of the wall, it is smaller with the wall rotation around the bottom and again smaller with the wall rotation around the top.

Conventional earth pressure mechanisms with slip surfaces are roughly reproduced. Realistic earth pressure coefficients can be obtained with actual values of internal friction angles.

REFERENCES

Belheine N, Plassiard, JP, Donze FV, Darve F, Seridi A (2009) Numerical simulations of drained triaxial test using 3D discrete element modeling. Computers and Geotechnics, 11, 5

Gudehus G (1996) Comprehensive equation of state of granular materials. Soils and Foundations, 36(1): 1-12

Herle I, Gudehus G (1999) Determination of parameters of a hypoplastic constitutive model from properties of grain assemblies. Mechanics of Cohesive-Frictional Materials, 4(5): 461-486

Iwashita K, Oda M (1998) Rolling resistance at contacts in simulation of shear band development by DEM. ASCE J Eng Mech, 124(3):285–92

Kozicki J, Donze FV (2008) A new open-source software developed for numerical simulations using discrete modelling methods. Computer Methods in Applied Mechanics and Engineering, 197: 4429-4443

Leśniewska D (2000) Analysis of shear band pattern formation in soil. Habilitation Monography, Institute of Hydroengineering of the Polish Academy of Sciences, Gdansk

Tejchman J, Bauer E, Tantono SF (2007) Influence of initial density of cohesionless soil on evolution of passive earth pressure. Acta Geotechnica, 2 (1): 53-63

Tejchman J, Gorski J (2008) Computations of size effects in granular bodies within micro-polar hypoplasticity. Int. J. Solids and Structures, 45 (6): 1546-1569

Tejchman J (2008) FE modeling of shear localization in granular bodies with micro-polar hypoplasticity. Springer Series in Geomechanics and Geoengineering (eds. W. Wu and R. Borja)

Widuliński L, Kozicki J, Tejchman J (2009) Numerical simulations of a triaxial test with sand using DEM. Archives of Hydro- and Mechanical Engineering, 56, 3-4:3-26

A Micro-Mechanical Simulation of Sand Liquefaction Behavior by DEM

Danda Shi[1], Jian Zhou[2], Jianfeng Xue[3] and Jiao Zhang[4]

[1] Lecturer, College of Ocean Environment and Engineering, Shanghai Maritime University, Shanghai 200135, China; shidanda@163.com
[2] Professor, Department of Geotechnical Engineering, Tongji University, Shanghai 200092, China; tjuzj@vip.163.com
[3] Lecturer, School of Applied Science and Engineering, Monash University, Churchill, 3842, VIC, Australia; jianfeng.xue@sci.monash.edu.au
[4] Lecturer, Department of Civil Engineering, Shanghai Technical College of Urban Management, Shanghai 200432, China; ggglg@163.com

ABSTRACT: A two-dimensional Particle Flow Code (PFC2D) was applied to simulate sand liquefaction behavior induced by cyclic loading. The numerical sample was prepared with 4061 discs with its particle size distribution similar to Fujian Standard sand. Based on the theory of strain-controlled undrained cyclic triaxial test, a constant volume numerical test was carried out under cyclic loading with uniform strain amplitude. The macroscopic responses of the sample were obtained and the variation of average coordination number under cyclic loading was analyzed. The effects of cyclic strain amplitude and confining pressure on liquefaction resistance were further analyzed in numerical simulations. It was found that the numerical tests reproduced the general characteristics of liquefaction behavior of saturated sand under cyclic loading. The effects of cyclic strain amplitude and confining pressure on the liquefaction resistance of the numerical sample were comparable with reported experimental results.

INTRODUCTION

Liquefaction is an important phenomenon associated with the undrained response of loose granular materials. Various types of laboratory tests have been conducted to study the development of liquefaction under cyclic loading, such as the cyclic triaxial test, cyclic simple shear test and cyclic torsional test (e.g. Seed and Lee, 1966; Ishihara et al, 1975; Koseki et al, 2005). The studies have focused on the stress-strain relationships and the generation of cumulative excess pore water pressure under undrained cyclic loading conditions. Ishihara et al (1975) presented typical results of strain-controlled undrained cyclic triaxial tests. They observed that during a strain-controlled cyclic loading test, the progressively buildup of pore water pressure causes the migration of effective stress path towards the origin and the increase of stress ratio of shear stress to mean effective principal stress. Nevertheless, the responses of materials in laboratory tests are very sensitive to the methods of sample preparation and the rate of loading etc.

Hence quantitative evaluation of dynamic behavior of soil with physical modeling remains difficult.

Analytical treatments on liquefaction behavior of granular materials generally assume continuum behavior even while soil is a multiphase particulate medium. Problems arise with this assumption due to soil's inherent granular nature and the consequent deformation and failure modes. The continuum models are phenomenological, and primarily concerned with mathematical modeling of the observed phenomena without detailed attention to their fundamental physical significance. Discrete Element Method (DEM) pioneered by Cundall (1971) is a useful tool for an in-depth understanding of the fundamentals of liquefaction behavior. The method models the assemblies as discrete particles interacting through contact forces. The macro behavior of soils can be obtained by keeping track of micro behavior of soil particles.

In this paper, a strain-controlled undrained cyclic triaxial test was firstly conducted on Fujian standard sand with relative density of 30%. Based on experimental results, a two-dimensional discrete element method computer code PFC2D was then used to investigate the liquefaction behavior of an assembly of 4061 discs subjected to undrained (constant volume) cyclic loading. Both macro- and micro-scale response of numerical samples were comprehensively studied. The effects of cyclic strain amplitude and confining pressure on liquefaction resistance were also analyzed.

EXPERIMENTAL TEST

Fujian standard sand, a standard sand often used by researchers in China, was used for the strain-controlled cyclic triaxial test in the lab. The physical properties and particle size distribution of the material are presented respectively in Table.1 and Fig.1. A specimem of 38mm in diameter and 76mm in height was created by air pluviation method to a void ratio of 0.749. The specimen was saturated with de-aired water flowing from the bottom to the top and thereafter a back pressure of 200kPa was applied to improve the degree of saturation. The measured value of pore water pressure coefficient (B) was above 0.98. After the process of saturation, the specimen was isotropically consolidated under a confining pressure of 200kPa. Deviatoric strain ($\varepsilon_1-\varepsilon_3$) amplitude ($\varepsilon_{\mathrm{sm}}$) of 0.45% was cyclically applied under a frequency of 1Hz. The "initial liquefaction" criterion suggested by Seed and Lee (1966) was used to define the liquefaction of sand.

Table 1. Physical properties of tested sand

Properties	Values
specific gravity (G_s)	2.643
maximum void ratio ($e_{\max}$)	0.848
minimum void ratio ($e_{\min}$)	0.519
mean particle size (D_{50}) /mm	0.34
coefficient of uniformity (U_c)	1.542
coefficient of curvature (C_c)	1.104

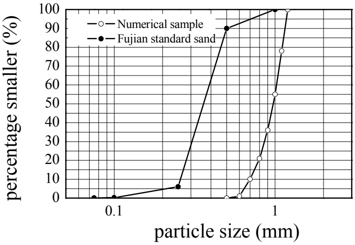

Fig.1. Particle size distribution

Fig.2 shows the results of the laboratory test. In the Figures and the following, q is defined as shear stress $((\sigma'_1-\sigma'_3)/2)$, p' is defined as mean effective principal stress $((\sigma'_1+\sigma'_3)/2)$, ε_s is defined as deviatoric strain $(\varepsilon_1-\varepsilon_3)$ and excess pore water pressure ratio (r_u) is defined by the ratio of pore water pressure (u) to the initial confining pressure (σ'_{30}).

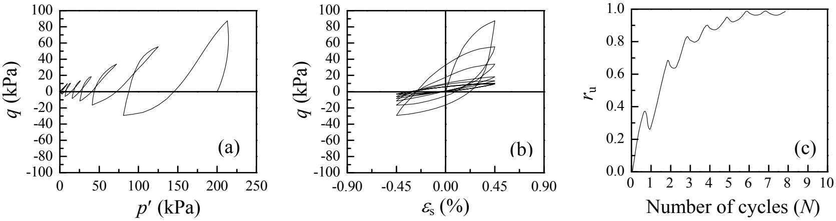

Fig.2. Results of the laboratory test

From Fig.2, some typical liquefaction characteristics of saturated loose sand under strain-controlled cyclic loading condition can be concluded:

(1) The mean effective principal stress decreases gradually and steadily, and the effective stress path gradually migrates to origin due to the cumulative buildup of pore water pressure as shown in Fig.2(a). It is noted that the magnitude of shear stress during compression is larger than that during tension.

(2) The sample attains a peak shear stress of 87.2kPa in the first cycle. Thereafter shear stress reduces gradually in successive cycles and finally reaches zero (Fig.2(b)). It is clearly denoted that both strength and stiffness of the sample experience significant loss with successive cyclic loading.

(3) Fig.2(c) displays a sharp increase of pore water pressure in the first and second cycles, and the sample reaches the initial liquefaction state after about 7 cycles.

NUMERICAL SIMULATION

Sample preparation

A biaxial numerical sample was created using PFC2D program with 85mm in height and 40mm in width. The particle diameter ranges from 0.6mm to 1.2mm. The sample composed of 4061 particles with the particle size distribution plotted in Fig.1. The two-dimensional void ratio of the sample is 0.316. The U_c and C_c values of numerical sample are 1.529 and 1.095, which are very close to those of the sand sample (indicated in Table1). The value of D_{50} of numerical sample is 0.9mm, which is about three times of that of the sand. The objective of enlarging particle size is to reduce the particle number generated in the simulation. It is concluded by Jensen et al (2001) that enlarging particle size will not significantly affect the macro response of numerical sample, provided that the ratio of the mean particle sizes (D_{50}) less than 30.

In PFC2D, a linear or a non-linear Hertz-Mindlin contact model can be used for the description of contact behavior between particles. The parameter calibration for the simulation of Fujian standard sand with linear or non-linear Hertz-Mindlin model has already been done in authors' previous research (Zhou and Shi, 2007). In the present study, a non-linear Hertz-Mindlin model was used to describe the particle contact behavior with the values of micro parameters of shear modulus G_u=5×10^{11}Pa and poisson's ratio ν_u=0.35. Coulomb friction law was adapted for the relative slipping between particles with friction coefficient f_c=0.8. The particle density is 2.643×10^3kg/m^3, which is the same value as Fujian standard sand.

An isotropic confining pressure of 200kPa was applied on the sample by a numerical servo-control procedure. Constant volume cyclic shear test was performed with four boundary walls moving in two-way prescribed velocities. By doing this, an undrained strain-controlled cyclic test taken in experimental test can be numerically simulated (Ng and Dobry, 1994; Sitharam, 2003). It was assumed that the all-round total stress is constant and equal to σ'_{30} during this constant volume cyclic part of the test, as in cyclic triaxial test. Thus, the excess pore water pressure in numerical simulation was defined as the difference between the calculated horizontal stress and the initial confining stress.

Results of numerical simulation

The results of numerical simulation are shown in Fig.3. Fig3(a) shows the plot of shear stress (q) versus mean effective principal stress (p'). The effective stress path move progressively towards origin and the rate of movement is more remarkable in the first two cycles than in the subsequent cycles. The sample reaches the initial liquefaction state after 4 cycles. The effective stress path does not rest on the origin when the sample is in the post-liquefaction stage, but moves up and down companied with the loading and unloading cycles. This special feature is called as "phase transformation" behavior in laboratory tests (Ishihara et al, 1975), and can be well reproduced in the simulation.

Fig.3(b) shows the plot of shear stress (q) versus deviatoric strain (ε_s). It can be obviously seen that the calculated hysteresis loops gradually declined with the number of cycles increases. The shear stress decreases faster in the first cycle. The decrease of shear stress and the degradation of cyclic modulus are quite comparable to the experimental results in Fig.2(b).

Fig.3(c) shows the plot of excess pore water pressure ratio (r_u) versus the number of cycles (N). Compared with experimental results (Fig.2(c)), although the number of cycles to initial liquefaction are not equal, the increase regularity of excess pore water pressure is similar to that observed in the laboratory test.

Fig.3(d) shows the plot of stress ratio (q/p') versus deviatoric strain (ε_s). It is clearly shown that there is a progressive increase in stress ratio on both compression and extension sides as the number of cycles increases. The maximum value of stress ratio will not exceed ±1.0 in the process of cyclic loading. This response reflected in the numerical test is in good agreement with experimental results reported by Wang (2003), whose research illustrated the distinction and interrelation between liquefaction, state of limit equilibrium and failure of soil mass.

Fig.3(e) shows the plot of average coordination number (C_n) versus the number of cycles (N). C_n is calculated as the total number of contacts divided by the number of particles. The decreasing tendency of average coordination number with increasing N is clearly displayed. The results showed that, the coordination number decreases a little before initial liquefaction occurs, which means that, the reduction of the number of contacts between particles start to reduce dramatically after initial liquefaction. This results in a decrease of effective stress in the macro scale.

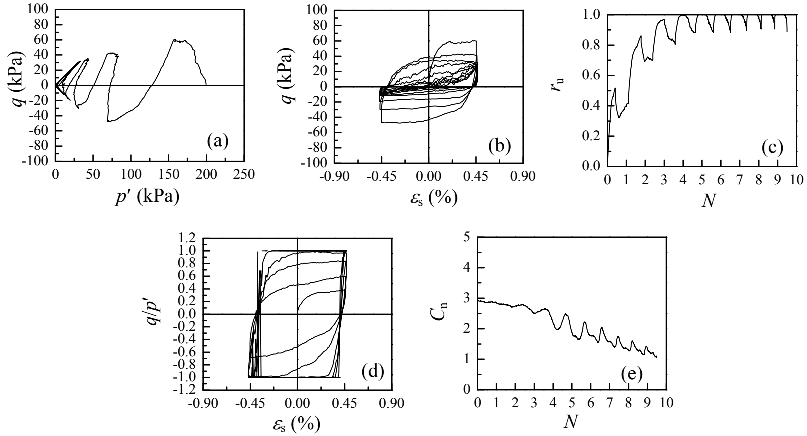

FIG.3. Results of numerical simulation

Effect of cyclic strain amplitude

According to the findings of previous experimental studies, the magnitude of cyclic strain amplitude will significantly affect the liquefaction resistance of sand deposits. Vasquez and Dobry (1988) carried out a series of strain-controlled cyclic torsional tests on saturated loose sand and found that the higher the magnitude of strain amplitude, the greater is the liquefaction potential.

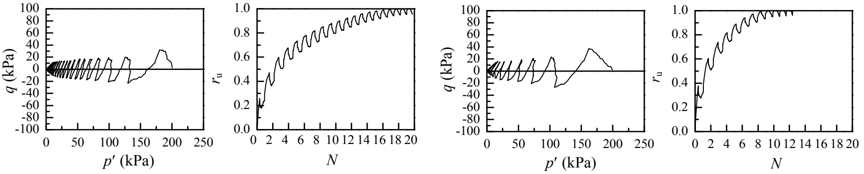

(a) ε_{sm}=0.05% (b) ε_{sm}=0.1%

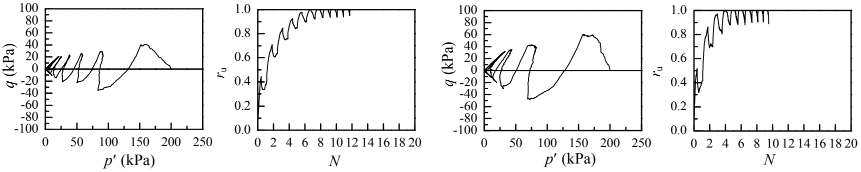

(c) ε_{sm}=0.2% (d) ε_{sm}=0.45%

FIG.4. Effect of cyclic strain amplitude

In this study, numerical tests at 0.05, 0.1, 0.2 and 0.45% deviatoric strain amplitude (ε_{sm}) were conducted. Fig.4 shows the response of effective stress path and excess pore water pressure of numerical samples at different strain amplitude level. As shown in Fig.4, the number of cycles to liquefaction failure (N_f) are 17, 8, 6 and 4 cycles at ε_{sm}=0.05, 0.1, 0.2 and 0.45%, respectively.

Fig.5(a) shows the liquefaction resistance curve (ε_{sm}~N_f) of numerical samples. In order to compare with laboratory tests, the experimental results of anisotropically consolidated loose sand achieved by Vasquez and Dobry (1988) are plotted in Fig.5(b). By comparison of numerical and experimental results, it is seen that numerical simulations can qualitatively capture the decreasing tendency of liquefaction resistance with the number of cycles as typically exhibited in laboratory tests.

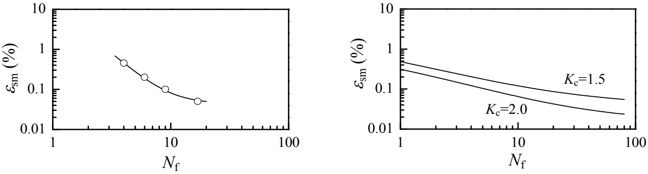

(a) numerical results (b) experimental results (after Vasquez and Dobry, 1988)

FIG.5. Plots of ε_{sm} versus N_f

Effect of confining pressure

Numerical tests at different confining stress levels were carried out, and the results were shown in Fig.6. It can be seen from Fig.6 that the number of cycles to trigger liquefaction increases as confining pressure increases. For further analysis of the effect of strain amplitude and confining pressure, a set of numerical tests at different strain amplitude (ε_{sm}=0.05, 0.1, 0.2 and 0.45%) were conducted at three stress levels (σ'_{30}=100, 200 and 300kPa). As in a stress-controlled cyclic loading test, the definition of cyclic stress ratio (CSR) was commonly used to describe the liquefaction resistance of the sample. It is recommended by Uchida and Stedman (2001) that CSR can also be

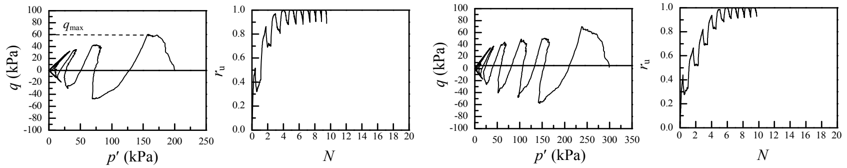

(a) σ'_{30}=200kPa (b) σ'_{30}=300kPa

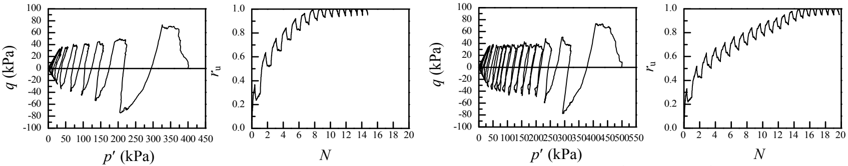

(c) σ'_{30}=400kPa (d) σ'_{30}=500kPa

FIG.6. Effect of confining pressure

used in a strain-controlled cyclic loading test, and the definition of CSR in a strain-controlled test is

$$\mathrm{CSR} = \frac{q_{\max}}{\sigma'_{30}} \tag{5}$$

Where $q_{\max}$ is the value of shear stress during compression in the first loading cycle, as indicated in Fig.6(a).

The plot of CSR versus N_f achieved from numerical tests is shown in Fig.7(a). Fig.7(b) shows the experimental results of stress-controlled cyclic triaxial tests on Hangzhou river sand performed by Ke et al (2004). The figures showed that, with the decrease of CSR, the number of cycles to initiate liquefaction increases. The relationship is more linear in the physical tests by Ke. In numerical modeling, CSR reached to a higher value of 0.33 at the confining pressure of 100kPa. This might due to the reason that in numerical modeling, the density of samples is easier to control than in physical tests. Another reason might due to the difference of the material used in the two tests.

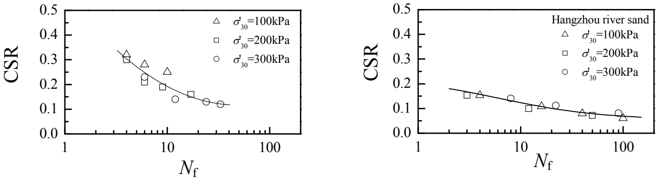

(a) numerical results

(b) experimental results (after Ke et al, 2004)

FIG.7. Plots of CSR versus N_f

CONCLUSIONS

The results of this investigation showed the power of DEM technique in simulating the liquefaction behavior of saturated sand. Some distinctive features observed in laboratory tests on sand, such as the excess pore water pressure buildup to initial liquefaction, hysteresis loop degradation and the "phase transformation" behavior, can all be well reproduced by numerical simulations. The regularities of the influences of cyclic strain amplitude and confining pressure on liquefaction resistance previously found in laboratory tests on actual sand can be also qualitatively achieved from numerical simulations. The micromechanical information such as the variation of average coordination number can be well presented with DEM. This research provides a basis for further quantitative research on sand liquefaction by DEM.

ACKNOWLEDGMENTS

The authors appreciate the support from the National Nature Science Foundation of China (No. 50909057, 90815008).

REFERENCES

Cundall, P.A. (1971). "A computer model for simulating progressive large scale movements in blocky rock systems." *ISRM Symp.*, Nancy, France, Proc.2: 129-136.

Ishihara, K., Tatsuoka, K. and Yasuda, S. (1975). "Undrained deformation and liquefaction of sand under cyclic stresses." *Soils Found.*, Vol. 15 (1): 29-44.

Jensen, R.P., Edil, T.B., Bosscher, P.J., et al. (2001). "Effect of particle shape on interface behavior of DEM-simulated granular materials." *Int. J. Geomech.*, Vol. 1 (1): 1-19.

Ke, H., Chen, Y.M., Zhou, Y.G. and Zhang, M.Q. (2004). "Evaluation of liquefaction resistance by means of dynamic triaxial tests with shear wave velocity measurement." *China Civil Eng. J*, Vol. 37 (9): 48-54. (in Chinese)

Koseki, J., Yoshida, T. and Sato, T. (2005). "Liquefaction properties of Toyoura sand in cyclic torsional shear tests under low confining stress." *Soils Found.*, Vol. 45(5): 103-113.

Ng, T.T. and Dobry, R. (1994). "Numerical simulation of monotonic and cyclic loading of granular soil." *J Geotech. Eng.*, Vol. 120 (2): 388-403.

Seed, H.B. and Lee, K.L. (1966). "Liquefaction of saturated sands during cyclic loading." *J Soil Mech. Found. Div.*, Vol. 92 (SM6): 105-134.

Sitharam, T.G. (2003). "Discrete element modeling of cyclic behavior of granular materials." *Geotech. Geol. Eng.*, Vol. 21 (4): 297-329.

Uchida, K. and Stedman, J.D. (2001). "Liquefaction behavior of Toyoura sand under cyclic strain controlled triaxial testing." *Proc. Int. Offshore Polar Eng. Conf.*, Stavanger, Norway, Vol2, 530-536.

Vasquez, H.A. and Dobry, R. (1988). "Pore pressure buildup and liquefaction failure of anisotropically consolidated sand due to cyclic straining." *Hydraulic Fill Structures (GSP 21)*, ASCE, Reston/VA: 346-366.

Wang, W. S. (2005). "Distinction and interrelation between liquefaction, state of limit equilibrium and failure of soil mass." *Chinese Geotech. Eng. J*, Vol. 27(1): 1-10. (in Chinese)

Zhou, J. and Shi, D.D. (2007). "Numerical simulation of mechanical response on sand under monotonic loading by particle flow code." *J Tongji Uni.*, Vol. 35(10): 1299-1304. (in Chinese)

Study on the Deformation of Loose Sand Under Cyclic Loading by DEM simulation

Minyun Hu[1,2], Catherine O'Sullivan[3], Richard R Jardine[3], Mingjing Jiang[1]

1 Key Laboratory of Geotechnical and Underground Engineering of Ministry of Education, Tongji University, China

[2] Zhejiang University of Technology, Hangzhou, China, huminyun@zjut.edu.cn

[3] Imperial College London, UK

ABSTRACT: The extensive use of granular materials as roadbeds accelerates the study of sand behavior under cyclic loading. While several studies have been done on sand deformation under cyclic loading, little information is available on the explanations for this behavior**.** By discrete element method (DEM) simulation, this paper offered a preliminary insight into particles interaction of loose sand which controls the material's stress-strain behavior. A 2-D 'sample' of 896 'quartz' disks, with diameters of 0.20, 0.25 and 0.30mm, was produced by self-gravity sediment. Then it was K_0 loaded to t' = 127 kPa, at which point, the sample started to be cyclically loaded for 5000 cycles when t' kept constant. Cyclic amplitudes varied from 0.02 to0.04 t'. Increasing strain accumulation with increased number of cycles was observed. For smaller cyclic amplitude, strain accumulation increased smoothly, but for larger one, strain accumulation increased erratically after a large number of cycles. The coordination number variation during cycling load was considered to be responsible for this phenomenon. Induced anisotropy was observed, and it could be explained by deviatoric fabric analysis.

INTRODUCTION

Deformation of foundation upon loading depends on the plastic behavior of soils which build up the foundation. For granular materials, it involves particle rearrangement and the consequent fabric changes. While contributions have been done to the mechanical properties of soils at both macro- and microscopic level, the extensive use of granular materials as roadbeds gives a strong impulse to study and understand the effects caused by repeated, cyclic loading on sand.

Laboratory tests are commonly used to study soil's behavior under appointed load paths, and several experiments by triaxial apparatus have been carried out to study sand's behavior under cyclic loading (Dupla JC et al. 2003; AnhDan LQ et al. 2004; Toyota H et al. 2004; Masayuki Koike et al.2003; T.Wichtmann et al. 2006; N.Khalili et al. 2005; Liu HL et al. 2003). They have been intended to investigate the elasto-plastic response of granular materials as well as calculate parameters which can be applied in constitutive laws. An alternative approach is the simulation of the system by discrete element method (DEM). In DEM, the evolution of a single sand particle is caught by calculating the interaction forces between particles. Then, the system evolution is obtained by integrating the equations of motion. By using DEM, Kuhn and Mitchell (1992,1993) modeled the creep in granular materials. Their study primarily focused on the development of a visco-elastic contact constitutive model, which was testified to be satisfying in simulating sand creep under different stress level. David et al (2005) considered the effect of cyclic loading on the development of strain within a granular material. They found that there was a significant increase in strain accumulation with increasing number of cycles. In order to explain the shape of the stress-strain curves obtained in simulations of cyclic loading, S.McNamara et al (2005) established an analytical relationship between the number of sliding contacts over one cycle and changes in stiffness of the assembly by requiring the work done on the sample to be equal to the energy stored or dissipated at the contacts.

While several studies have been done on sand deformation under cyclic loading, little information is available on sand deformation under loading with large number of cycles, neither on the explanations for this behavior. The purpose of this study was to investigate the strain accumulation of sand under cyclic loading with large number of cycles. Then, we linked sand behavior during cyclic loading of different amplitude with the change of void ratio, coordination number and soil fabric.

METHOD

a) Sample Preparation

Disks, with diameters of 0.20, 0.25 and 0.30mm, settled at self-gravity into a "box" to build up a sand sample of h×b=23×10mm, as shown in Fig. 1. The disks distribution was designed to simulate Ham River sand, which is used as standard sand in geotechnical laboratory in Imperial College, and produced by Gaussian generation method according to PFC2D. The sample was produced as two-dimensional and loose in order that we may see clearly the changes in the fabric as a consequence of stress perturbation. Because of the limit of the computer storages and running time, the selected sample was much smaller than a real one prepared in laboratory.

After the sample has settled to static equilibrium, the "box" was removed. Then, two rigid walls were placed on both top and bottom in order to simulate loading and bearing plate, respectively. It keeps shape by a "membrane", which was composed of the outside disks with stipulated connections.

b) Model and Parameters

The simple viscoelastic contact law, which was built in PFC2D and commonly used in DEM analysis, was adapted in this study. According to the contact law, the interaction force is related to the overlap of two particles. Thus, particles interact only if they are in contact, and the force between them can be decomposed into a normal and a tangential part. The normal and tangential spring stiffness between particles are $k_n = k_s = 2\times10^7$ N/m. The damping coefficient is 0.7. Friction angle of $\varphi = 18°$ was testified by "triaxial compression". Interaction forces also exist between particles and loading/bearing plates. The normal and tangential stiffness used are $k_{nw} = k_{sw} = 1.94\times10^7$ N/m, while the friction coefficient is $f_s = 0.0875$.

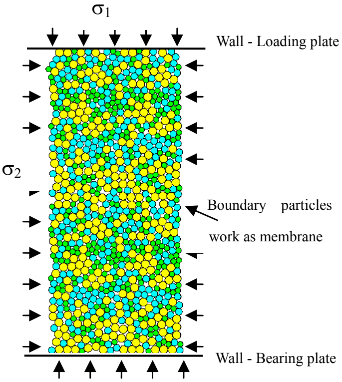

FIG. 1 Sample for DEM analysis

c) Test Procedure and Project

In order to examine the effects of cyclic loading on deformation of particle assembly, different amplitudes were investigated.

After the disk assemblies settled down with a all-round pressure $\sigma_2 = 50$kPa, the samples were "normally consolidated" to t' $(=(\sigma_1+\sigma_2)/2) = 126.75$kPa with $K_0 = 0.69$ ($K_0 = 1-\sin\varphi$, according to Jaky's equation, but need further verifying in 2-D condition). At this point of stress state, while t' kept constant, samples were loaded with three different cyclic amplitude: Δs（$=(\sigma_1-\sigma_2)/2$) = (2%, 3%, 4%) t', respectively, for 5000 cycles. Typical load path was shown in Fig. 2. The cyclic loading was strain-controlled, with the top wall moving with a constant velocity of 0.01mm/s up and down. All tests were performed under drained conditions, which produced both deviator and volumetric deformations.

NUMERICAL RESULTS

Fig. 3 shows the variation of axial strain with the number of cycles. It was seen that the axial strain tended to accumulate with cycle number. For the cyclic amplitude of 2% and 3%t', smoothly ongoing strain accumulation, i.e., ratcheting, was observed even after 4000 cycles. It is consistent with what was found in David's (2005) simulation with a larger 3D system. As well, it is accordant with laboratory test (AnhDan LQ et. al. 2004). That we can get similar results with a much smaller 2D system may be due to the different selected parameters and contact model. For the cyclic amplitude of 4%t', the increasing of axial strain accumulation displayed a stepwise development, and in higher level of cycles, steeper steps were observed. The unstable development of axial strain indicates the adjustment of the inner fabric under violent cycles.

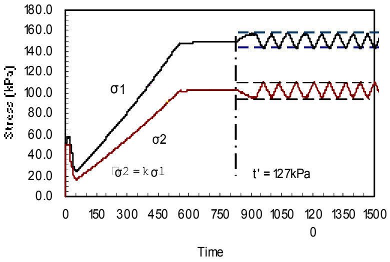

FIG. 2 Typical load path of cyclic loading

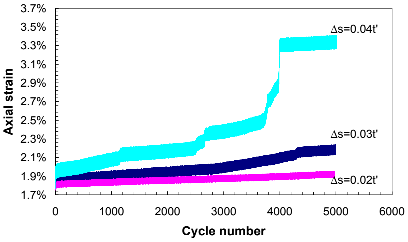

FIG. 3 Axial strain curves of cyclic loading

Fig. 4 shows the change of deviator strain with the number of cycles. Deviator strain is defined as the difference between axial strain and radial strain (i.e., horizontal strain in 2D). From the figure, we could clearly see that the deviator strain not only varied with deviator stress, but also tended to accumulate with cycle number. This means the vertical (axial) stain and horizontal (radius) stain develop differently although the t' keeps constant in cyclic loading. With a lower amplitude, i.e., Δs=0.02 or 0.03t', the deviator strain increased with cycle number but was in negative value. However, with a larger amplitude, i.e., Δs=0.04t', the deviator strain increased sharply into positive value after 4000 cycles. It suggests that the material develop anisotropy after a large number of cycles, especially when the amplitude increases.

Porosity can represent the degree of density of granular materials. The simulation results of porosity variation during cyclic loading are illustrated in Fig. 5. Although there is a big difference between the values in 2D and 3D cases, the curves make sense. In cyclic loading with smaller amplitude, i.e., Δs=0.02 or 0.03t', the sample was quickly compacted after a small number of cycles. Then the porosity changed gently over the long period of cycles. However, for the amplitude of 0.04t', the sample's porosity decreased incessantly before 4000 cycles, and decreased sharply around 4000 cycles, but after that, the porosity showed a trend to increase. The results presented here suggest that loose sand could be compacted by cyclic loading, but special attention should be given to larger amplitude, for sample may undergo unstable development after certain number of cycles. It need to point out that since the sample was composed of disks but not spheres, the void ratio in 2D simulation is not equivalent to that in 3D state. The values of void ratio in 2D are much smaller than those in 3D samples.

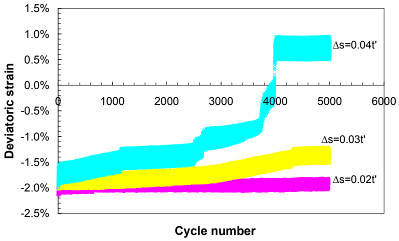

FIG. 4 Deviator strain curves of cyclic loading

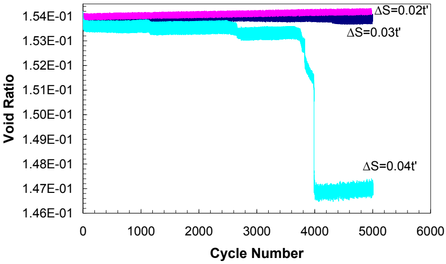

FIG. 5 Porosity variation with cycle number

DISCUSSION

Coordination number (Rothenburg and Bathurst, 1989), which indicates the average normal contacts between particles, appears to be responsible for the cyclic response of granular materials. Fig. 6 gives the variation of coordination number during cycling. It was shown that, for the smaller cyclic amplitude of 0.02t' and 0.03t', the coordination number increased during the initial number of cycles, indicating that the contact forces was adjusting. Then, after a large number of cycles, the sample set up a stable network of contacting particles to sustain the cycling load while the coordination number keep very gently increasing. During the process, the specimen was gradually compressed and strengthened. However, the curve for 0.04t' amplitude was different. In 4% amplitude, the coordination number increased in low level cycles, suggesting particles rearranging to produce overall material compaction. In succession, the coordination number fluctuated, associating with unstable strain development, as was observed in Fig. 3 and Fig. 5.

In order to analyze the anisotropy of contact fabric, we give the fabric tensor for 2D analysis as below (Cowin, S.C., 1985).

$$\Phi_{ij} = \frac{1}{N_c} \sum_{N_c} n_i n_j \tag{1}$$

where Φ_{ij} = fabric tensor; N_c = number of contacts; n_i = unit vector normal to contact. The matrix form of fabric tensor is

$$\Phi = \frac{1}{N_c} \begin{bmatrix} \sum_{N_c} n_1 n_1 & \sum_{N_c} n_1 n_2 \\ \sum_{N_c} n_2 n_1 & \sum_{N_c} n_2 n_2 \end{bmatrix} \tag{2}$$

Similar to stress tensor, $\boldsymbol{\sigma}$, eigenvalues of this matrix give principal values of fabric: Φ_1 and Φ_2. Φ_1-Φ_2, which is defined as deviatoric fabric, indicates anisotropy of material, and for isotropic material $\Phi_1 = \Phi_2$.

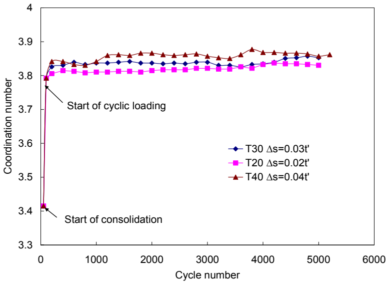

FIG. 6 Coordination number change

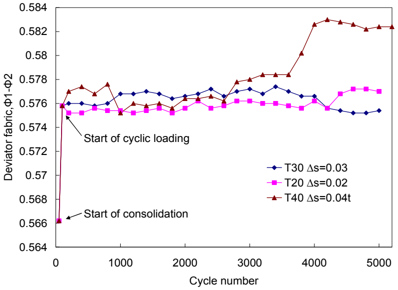

FIG. 7 Deviatoric fabric (Φ_1- Φ_2) variation

CONCLUSIONS

A 2-D ‘sample’ of 896 ‘quartz’ disks, with diameters of 0.20, 0.25 and 0.30mm, was produced by self-gravity sediment. DEM simulation was carried out to investigate the change of strain accumulation, void ratio and coordination number during cyclic loading of different amplitude.

With smaller cyclic amplitude, ongoing axial strain accumulation during cyclic loading was observed. The deviator strain smoothly increased with cycle number but was in negative value. The porosity changed gently over the long period of cycles after initially decreased. By checking the variation of coordination number during cycles, we can conclude that after the contact forces between particles adjust during early cycles, the sample can set up a stable network of contacting particles to sustain the cycling load.

With larger cyclic amplitude, axial strain accumulated erratically. This could be seen through the coordination number fluctuation with cycle number. The deviator strain increased sharply into positive value after a large number of cycles, which can be explained by anisotropy induced by cyclic loading. From here, we would suggest that, although the granular material can be compacted by cyclic loading, cares should be taken when using larger cyclic amplitude in order to avoid unstable deformation.

The results presented in this paper are assumed to be dependant on the selected contact model and parameters. As well, the size of the samples may affect the simulation outcomes. These aspects should be taken into account in successive study.

REFERENCES

AnhDan LQ and Koseki J. (2004). "Effects of large number of cyclic loading on deformation characteristics". *Soils and Foundations,* Vol.44(3):115-123.

C.T.David, R.Garcia-Rojo and H.J.Herrmann (2005). "Hysteresis and creep in powders and grains." *Powders and Grains – García-Rojo, Herrmann and McNamara (eds),* 2005 Taylor&Francis Group, London: 291-294

Cowin, S.C. (1985). "The relationship between the elasticity tensor and the fabric tensor." *Mechanics of Materials,* Vol.4(1):137-147.

Dupla JC and Canou J. (2003). "Cyclic pressuremeter loading and liquefaction properties of sands." *Soils and Foundations*, Vol.43(2): 17-31.

Liu HL, Zhou YD and Gao YF. (2003). "Laboratory test on volumetric characteristics of saturated sea sand under cyclic loading." *China Ocean Engineering,* Vol.17(1): 93-100.

Masayuki Koike, Toru Kaji and Prathuang Usaborisut. (2002) "Several contributions to soil compactibility induced by cyclic loading test." *Journal of Terramechanics,* Vol.29(3): 127-141.

Matthew R. Kuhn and James K. Mitchell. (1993). "New Perspectives on soil creep.[J]." Journal of Geotechnical Engineering, Vol.119(3):507-524.

N.Khalili, M.A.Habte and S.Valliappan. (2005). "A bounding surface plasticity model for cyclic loading of granular soils." *International Journal for Numerical Methods in Engineering*, 63: 1939–1960.

Rothenburg,L. and Bathurst, R.J. (1989). "Analytical study of induced anisotropy in idealized granular material." *Geotechnique,* Vol.34(4):601-614

S.McNamara, R.García-Rojo and H.J.Herrmann. (2005). "The stress-strain curve of cyclic loading: microsopic, analytical results." *Powders and Grains – García-Rojo, Herrmann and McNamara (eds),* 2005 Taylor&Francis Group, London: 295-298

T.Wichtmann, A.Niemunis and Th.Triantafyllidis.(2006). "Strain accumulation in sand due to cyclic loading: Drained cyclic tests with triaxial extension." *Soil Dynamics and Earthquake Engineering*, 4:1-7。

Tang-Tat Ng and Ricardo Dobry. (1994). "Numerical simulations of monotonic and cyclic loading of granular soil." Journal of Geotechnical Engineering, Vol.120(2): 388-403.

Toyota H, Nakamura K and Kazama M.(2004). "Shear and liquefaction characteristics of sandy soils in triaxial tests. "*Soils and Foundations*, Vol.44(2):117-126.

Three-Dimensional DEM Modeling of Triaxial Compression of Sands

Ye Lu [1], and David Frost [2]

[1]Graduate Research Assistant, School of Civil & Environmental Engineering, Georgia Institute of Technology, 210 Technology Circle, Savannah, GA 31407, USA. Email: ylu31@gatech.edu.
[2]Professor, School of Civil & Environmental Engineering, Georgia Institute of Technology, 210 Technology Circle, Savannah, GA 31407, USA. Email: david.frost@ce.gatech.edu.

ABSTRACT: The three-dimensional discrete element method code (PFC3D) was used to model triaxial compression tests on sands and the results were compared with physical laboratory tests. The sand particles were modeled by unbreakable 2-sphere clumps, so that interlocking between particles, which yielded more stable and efficient force chains, could take place. This was confirmed by comparing the results modeled by 2-sphere clumps with the results of tests where particles were modeled by single spheres. In addition to global stress and strain response, void ratios and coordination numbers were monitored at different locations within the specimens throughout the shearing process, and their evolution was evaluated to see whether localization existed within the specimens.

INTRODUCTION

In contrast to continuum modeling, the discrete element method (DEM) assumes that the soil mass is composed of discrete particles which can displace independently from one another and interact only at contact points (Cundall and Strack 1979). Considering the discrete nature of soils, DEM can conceptually provide better simulations of particulate behavior at the microscopic scale than continuum models. Consequently, DEM has been used by many researchers to model both laboratory and field behavior (e.g. Cundall, 1989; Iwashita and Oda, 1998; O'Sullivan and Cui, 2009). Much of the early research work was completed using 2D modeling due to various reasons, including computational capacity. However, as actual soil masses are subjected to 3D loading in most laboratory and field conditions, 2D modeling is not always sufficient for simulation. One such case is the triaxial compression test where the intermediate principal stress plays an important role in the stress-strain behavior. Some researchers have developed insight into triaxial tests using 2D DEM simulations (e.g. Wang and Leung 2008), nevertheless, 3D DEM simulations potentially provide a superior solution (e.g. Thornton, 2000; Maynar and Rodríguez, 2005; Belheine et al., 2009). The basic element in 3D DEM is a spherical particle, but more complex shapes can be formed by overlapping two or more spheres. Such structures are called clumps in most

DEM programs. Application of clumps to 3D DEM models can reduce large-magnitude rotations and enhance interlocking between particles (Yan, 2009). Notwithstanding this important consideration, application of clump logic to modeling triaxial tests using 3D DEM has only been published in the literature on a limited basis to date.

In this paper, the response of dry sands subjected to drained triaxial compression loading was investigated. A series of numerical experiments were performed using the commercial 3D DEM code PFC3D (Itasca Consulting Group, 2008). Two-sphere-clump logic was used to simulate the irregularly shaped sand particles, and the modeling results were compared with physical experiment results as well as modeling results using single-sphere logic to assess the degree to which clump logic can create force chains which make the general stress-strain response of the specimen less erratic and better match laboratory data. Finally, void ratios and coordination numbers captured during the numerical experiments were analyzed to gain insight into the evolution of soil fabric.

PHYSICAL SPECIMEN TESTS

Two triaxial tests previously reported in the literature were used as the basis for the present study (Yang, 2005). The material tested was ASTM graded Ottawa sand. Based on sieve analysis results, the median grain size, D_{50}, was 0.35 mm, and the coefficient of uniformity, C_u, was 1.65. Two different preparation methods, air pluviation and moist tamping, were used to prepare the specimens to similar initial void ratios (0.579 for air pluviation and 0.583 for moist tamping) but with different soil fabrics. Both specimens were sheared to global axial strains of about 14% under an initial confining stress of 50 kPa.

NUMERICAL SPECIMEN TESTS

Four stages were employed for the numerical specimen tests: (1) specimen preparation; (2) clump creation; (3) consolidation; and (4) specimen shearing. The first stage, specimen preparation, provided the preliminary frame for the assemblage. Care was taken to select numerical parameters that were consistent with real triaxial tests. Cylindrical specimen dimensions of 70 mm in diameter and 140 mm in height were selected. Rigid plates were placed on the top and bottom of the specimen as loading plates, and a less rigid cylinder wall was used as a membrane to confine the specimen. The sphere radii were selected to be uniformly distributed between 0.125-0.225 mm, resembling the grain size distribution of the test sand. To reduce the calculation time, the radii were scaled 12 times to reduce the number of spheres and allow the step time to be increased. Consequently, 8791 single spheres, with sphere radii uniformly distributed between 1.5-2.7 mm, were generated for the specimen. The normal stiffness of the spheres, k_n, was calculated based on Hertz-Mindlin theory at small strains (Santamarina et al., 2001). Additional material properties are provided in Table 1. The specimens were prepared to an initial void ratio of 0.580, and the inter-particle friction was initially set to zero until the last test stage to produce a dense specimen for shearing.

Table 1. Material properties of the numerical experiments

Parameters	Experimental	Numerical
Specimen Height	140 mm	140 mm
Specimen Width	70 mm	70 mm
Particle Radii Range	-	1.5-2.7 mm
Mean Particle Size	0.35 mm	4.2 mm
Initial Void Ratio	0.579 (AP)* 0.583 (MT)*	0.580
Particle Normal Stiffness, kn	-	$1.5\text{x}10^6$N/m
Particle Shear Stiffness, ks	-	$1.5\text{x}10^6$ N/m
Particle Friction Coefficient	-	0.27, 0.31
Specific Gravity	2.67	2.67
Platen Stiffness	-	$1\text{x}10^8$ N/m
Membrane Stiffness	-	$1\text{x}10^7$ N/m
Number of Particles	-	8791

*AP – air pluviation, MT – moist tamping

The second stage was to replace each individual sphere with an arbitrarily oriented two-sphere clump, while maintaining its volume, centroidal position and material properties. The two-sphere clump was comprised of two identical spheres overlapping each other such that the aspect ratio was 1.5:1, and it was set as unbreakable for later modeling stages. After all the sphere replacement was finished, the specimen contained 8791 clumps, with mean particle size of 5.3 mm in the long axis and 3.5 mm in the short axis. The assemblage of 2-sphere clumps is shown in Figure 1(a). An enlarged view of a coupon of the assemblage is shown in Figure 1(b).

The third stage was to isotropically load the specimen with 50 kPa confining pressure. A servo-controlled mechanism was applied so that constant pressure on the membrane and the top and bottom plates could be maintained. After the desired isotropic state was reached, inter-particle friction was assigned to the clumps. Then, the specimen was sheared to a global axial strain of 14% during the final test stage.

Modeling Results

Two numerical tests, with friction coefficient of 0.27 and 0.31 respectively, were performed to simulate the laboratory triaxial tests. The modeled stress-strain responses and volumetric strains are compared with experimental data in Figure 1(c). For the air-pluviated specimen, the numerical data reached higher peak strength (approximately 3 kPa) at smaller peak strain (approximately 1% different) than the experimental data. After the peak, the numerical data matched well with the experimental data until the axial strain exceeded about 12.6%. For the moist-tamped specimen, the numerical data reached the same peak strength, 186 kPa, at almost the same peak strain, 2.2%, as the experimental data. After the peak, the numerical data decreased more slowly than the experimental data, but better matched the experimental data at 14% axial strain. It is noted that the volumetric strains were not monitored during the lab tests, and that the volumetric strains at 14% global axial strain were calculated from the image analysis results. Both the numerical tests showed very small volume contraction in the beginning followed by continuous volume dilation. The simulated volumetric strain matched well with the experimental data at 14% axial strain.

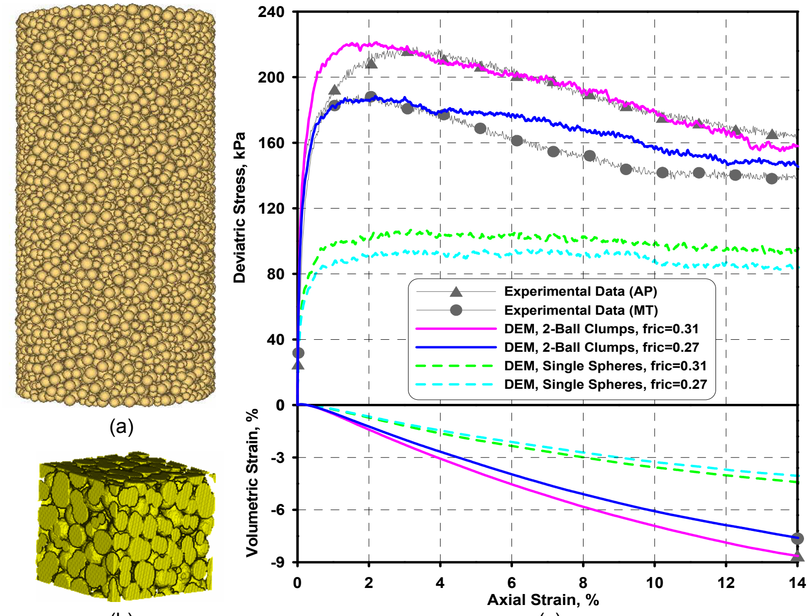

(a)

(b)

(c)

FIG. 1(a). Assemblage of clumps for numerical triaxial tests. (b). Enlarged portion of the assemblage. (c) Stress-strain and volumetric strain vs. axial strain of the numerical tests.

Two additional numerical tests were performed using single-sphere logic to compare with the 2-sphere-clump logic. The material properties and experimental stages for the sphere logic were all the same as with the clump logic, except for stage two. The modeling results are also presented in Figure 1(c). The clump models displayed higher peak strength and larger strength decrease after peak. The reason is that for single spheres, the applied pressures are mainly sustained through rolling and sliding between spheres, while for clumps, interlocking plays an additional but important role in resisting the applied pressures. Because of its irregular shape, one clump can be interlocked with another one, which consequently creates force chains. The irregular shape of the clumps also caused the specimen to dilate more than the specimen with only single spheres.

EVOLUTION OF VOID RATIOS AND COORDINATION NUMBERS

In order to monitor the evolution of void ratio and coordination number during shearing, 8 measurement spheres were defined within the specimen as shown in Figure 2. The radii of measurement spheres 1-7 were 10 mm, and each of them contained approximately 13 clumps. The radius of measurement sphere 8 was 34 mm, and contained approximately 530 clumps. Based on their locations and radii, measurement spheres 1-7 would capture local changes while measurement sphere 8 would allow for a generalized evaluation of the parameters.

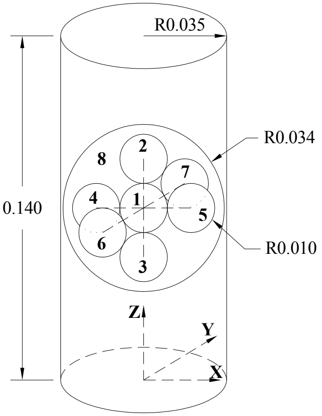

Meas. Sphere	X	Y	Z	R
1	0	0	0.070	0.010
2	0	0	0.100	0.010
3	0	0	0.040	0.010
4	-0.020	0	0.070	0.010
5	0.020	0	0.070	0.010
6	0	-0.020	0.070	0.010
7	0	0.020	0.070	0.010
8	0	0	0.070	0.034

Note: all the dimensions are in meters

FIG. 2. Coordinates and radii of the measurement spheres.

One test using clump logic and one using sphere logic are selected for presentation in Figure 3. The friction coefficients of the selected tests were both 0.31. It can be noted that the development of void ratio is different for the two models. For the clump model, although the generalized change of the void ratios was smooth, the local changes fluctuated, and can be attributed to the shape of the clumps. The local void ratios deviated from the generalized value until the axial strain reached 6%. After that, local void ratios resumed deviating. The maximum deviation, 10%, took place in measurement sphere 7 at 9.7% axial strain. For the sphere model, both the local and generalized changes were smooth, and the local void ratios kept deviating from the generalized value throughout the test. The maximum deviation, 7.4%, took place in measurement sphere 5 at 13.8% axial strain. The development of the coordination numbers was similar for both the clump model and sphere model. The coordination numbers of the clump model started around 10, followed by a sharp decrease to somewhere between 5.7 and 5.8 until axial strain reached 1.6%, at which stage they stabilized until the end of the test. The coordination numbers of the sphere model started around 6, decreased to 4.2-4.3 at 0.9% axial strain, and then also stabilized until large strains at the end of the test.

CONCLUSIONS

Three dimensional numerical tests using 2-sphere clumps were performed to simulate laboratory triaxial tests. The results were analyzed and the following conclusions reached:

1. The 2-sphere clump is a better match to soil particles than the single sphere, as interlocking and consequent force chains can be enforced. Therefore, theoretical or measured parameters can be directly assigned to the model.
2. Although the confining membrane was simulated by a rigid cylinder wall, localization of void ratio still occurred within the specimen. This proves the numerical model presented in this paper can be used for future research involving image analysis of localized materials.
3. 3D discrete element method is an advance to 2D discrete element method when simulating triaxial tests.

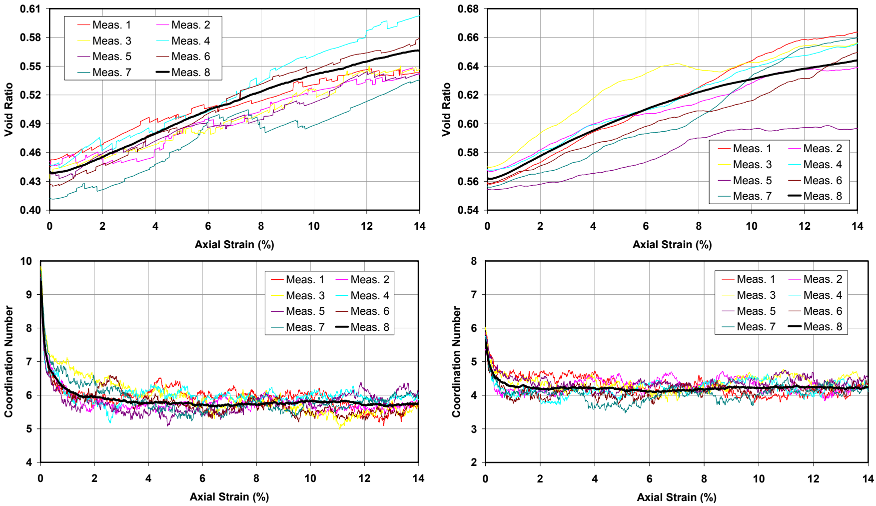

(a) (b)

FIG. 3(a). Void ratios and coordination numbers of the clump model test. 3(b). Void ratios and coordination numbers of the sphere model test.

REFERENCES

Belheine, J.P., Plassiard, J.P., Donzé, F.V., Darve, F., and Seridi, A. (2009). "Numerical simulation of drained triaxial test using 3D discrete element modeling." *Computers and Geotechnics*, 36: 320-331.

Cundall, P.A., and Strack, O.D.L. (1979). "A discrete numerical model for granular assemblies." *Géotechnique*, 29(1): 47-65.

Cundall, P.A. (1989). "Numerical experiments on localization in frictional materials." *Ingenieur-Archiv*, 59: 148-159.

Itasca Consulting Group. (2008). "PFC3D: Particle Flow Code in Three Dimensions." 4.0.

Iwashita, K., and Oda, M. (1998). "Rolling resistance at contacts in simulation of shear band development by DEM." *Journal of Engineering Mechanics, ASCE*, 124(3): 285-292.

Maynar, M.J.M., and Rodríguez, L.E.M. (2005). "Discrete numerical model for analysis of earth pressure balance tunnel excavation." *Journal of Geotechnical and Geoenvironmental Engineering*, ASCE, 131(10): 1234-1242.

O'Sullivan, C., and Cui, L. (2009). "Micromechanics of granular material response during load reversals: combined DEM and experimental study." *Power Technology*, 193: 289-302.

Santamarina, J.C., Klein, K.A., and Fam, M.A. (2001). *Soils and Waves*. John Wiley and Sons, West Sussex, England.

Thornton, C. (2000). "Numerical simulations of deviatoric shear deformation of granular media." *Géotechnique*, 50(1): 43-53.

Wang, Y.H., and Leung, S.C. (2008). "A particulate-scale investigation of cemented sand behavior." *Canadian Geotechnical Journal*, 45: 29-44.

Yan, W.M. (2009). "Fabric evolution in a numerical direct shear test." *Computers and Geotechnics*, 36: 597-603.

Yang, X. (2005). "Three-dimensional characterization of inherent and induced sand microstructure." PhD thesis, Georgia Institute of Technology, School of Civil and Environmental Engineering, Atlanta.

3D Modeling of Piping Mechanism Using Distinct Element Method

ZHOU Jian[1,2], ZHOU Kai-min[1,2]

[1]Department of Geotechnical Engineering, Tongji University, Shanghai ,China;
[2]Key Laboratory of Geotechnical and Underground Engineering of Ministry of Education, Tongji University, Shanghai, China, 200092 ; zhoukm30@126.com

Abstract: A 3D coupled continuum-discrete hydromechanical model was utilized to simulate the pore fluid flow and solid particle transport during piping in a micro scale. The fluid phase was implemented using the “fixed coarse-grid” fluid scheme based on Navier-Stokes equations and the solid phase which consists of an assemblage of discontinuous particles can be modeled effectively using DEM. Numerical simulations were conducted to investigate the mechanisms of macro-meso response of fluid and grains during piping in the presence of increase hydraulic gradient. The fluid velocity, loss fraction of eroded particles, pathway of moving particles, and etc are traced and recorded. The outcome of these simulations was consistent with experimental observations and revealed valuable information on the micro-mechanical characteristics of piping in sandy soil.

INTRODUCTION

Piping erosion has long been recognized as a serious harm in dam and embankment engineering projects (Ding LQ, 2007). From a phenomenological point of view, the piping erosion customarily indicates the detachment of fine particle from the soil structure and then transports and collides under the mechanical action of fluid flow in the form of internal seepage force. A progressive erosion and transportation of fine particles along a flow path will result in a large flow channel, which may lead to the phenomenon of piping (Sterpi D, 2003).

Although much experimental and numerical work has been conducted to investigate piping erosion phenomenon for various soil materials, relatively few attempts have been made to describe the fundamental particle transport and fluid flow mechanisms of piping in sandy soil from the microscopic view (Sherard, 1984b; Skempton, 1994; Indraratna, 1997; Hajra, 2002). Especially for numerical simulation, piping erosion is often addressed by researcher using intricate continuum formulation. Indeed, these piping soils involve different constituents whose behavior is governed by dissimilar physics and consequently exhibit a high non-linear behavior. Based on the constitutive material considerations, a effective tool for studying the mechanism of piping in sandy soil is the discrete element method (DEM) developed by Cundall and Strack (1979), which is based on discrete mechanics.

In this paper, a comprehensive analytical 3D piping erosion model is described, based on the particle flow code theories. The flow of water through the particulate medium is modeled using the Navier-Stokes equations which are discredited using the finite difference method. And the discrete element method (DEM) is employed to model granular solid grains assemblage. A coupled fluid-particle response using explicit algorithm is addressed based on the established semi-empirical relationships (Shamy, 2007). The model can be used to predict the characteristics of fine particle transport and micromechanical mechanisms during piping.

PIPING TEST MODEL

The apparatus (Fig. 1) designed by the authors (Zhou J, 2007), consists of a 60cm ×50cm×10 cm tank with a transparent front wall, so that the phenomenon occurring in the casing could be observed. Before laying the soils, a 10cm thick gravel (grain sizes 5-10 mm) filter was placed at the bottom to ensure uniform flow across the soil samples. Soil samples were wetted and laid evenly in four layers into the tank to a thickness of 20 cm and width of 10cm.The soil samples were subjected to upward controllable water pressure.

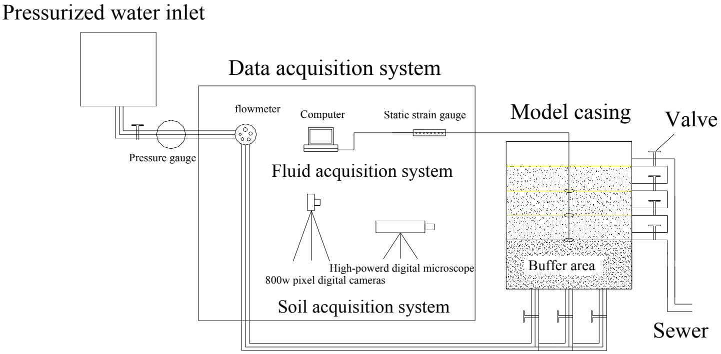

FIG.1 Arrangement of experimental apparatus for piping tests.

PIPING DEM MODEL

Specimen Generation

Due to the computation capacity of personal computers, a numerical modeling with PFC3D on a prototype model (Zhou J, 2007) was hard. Therefore similarity theory was adopted to improve the efficiency of computation. Related parameters are as following. Similarity: 2; Model size: 100×50×50 mm; Total number of particles: 19,785. Distributions of grain size used in the experimental and DEM analyses are specified in Table 1.The grain size of 5-10mm represents the skeleton particles and grain size of 0.5-2mm stands for the erosion fine particles. The particles which smaller than 0.5mm diameters are negligible for the purpose of saving computational time.

Table 1. Distribution of grain size

Sample	Porosity	Distribution of grain size (mm)				
-	n	10-5	5-2	2-0.5	0.5-0.25	0.25-0.075
Experiment	0.35	81%	4.4%	13.4%	0.8%	0.3%
DEM	0.36	82.5%	2.3%	15%	0.25%	0%

Micro-parameters adopted in model are shown in Table 2, in which the particles parameters are determined based on hypothetical real sand particles (Zhou J, 2008). No bonding model is adopted for simulating the cohesionless sand in DEM. The linear contact model and the slip model are also used in solid phase. The walls utilized PFC3D standard wall are almost the same stiffness and friction parameters as those of particles (Itasca, 2003).

Table 2. Characteristics of conducted simulations parameters during piping

Particles					Computation parameters	
Diameter	**Friction coefficient**	**Density**	**Normal stiffness**	**Tangent stiffness**	**Time steps for DEM**	**Time steps for CFD**
0.075-10.0 mm	0.5	2650 kg/m^3	1.00E+07 N/m	1.00E+07 N/m	2.00E-07 s	2.00E-05 s
g-level	**Walls**			**Fluid (water at 20 C)**		
-	**Normal stiffness**	**Tangent stiffness**	**Friction coefficient**	**Density**	**Viscosity**	**Finite volume cell**
2	1.00E+07 N/m	1.00E+07 N/m	0.5	1000 kg/m^3	1.00E-03 Pa.s	5×5×5 mm

SIMULATION PROCEDURE

The procedure in PFC3D is similar to the lab tests. The numerical modeling followed the following steps: prepare the soil sample in the container and then fill with water; apply an upward pressure on the bottom of container to create a small hydraulic gradient in the soil sample; increase the bottom pressure gradually to initiate piping. When the external bottom pressure reaches about 100kPa, critical hydraulic gradient of piping erosion can be measured and the law of particle transport and particle erosion of the sample can be investigated.

ANALYSIS OF RESULTS

Fluid Velocity

The variation of fluid velocity measured by PFC3D fluid cells with the increase of hydraulic gradient imposed on the sample is present in figure 2. From the figure, with the increase in hydraulic gradient, the seepage fluid velocity rises slowly, but when the critical hydraulic gradient reaches (i=0.42), the velocity of fluid has a tremendous increase. That denotes the fine particles start to loss uninterruptedly, and piping damage occurs. Additionally, the critical hydraulic gradient in DEM (i=0.42) is almost the same as that determined in the model test (about i=0.41), which proves that PFC3D is a effective tool to simulate the piping erosion.

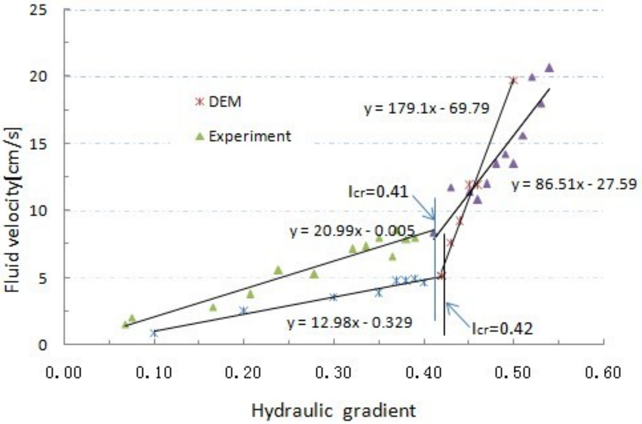

FIG. 2 Variation of Fluid Velocity with Increase in Hydraulic Gradient

Flow Velocity and Pore Water Pressure

Water pressure and flow velocity have a significant impact on the response of saturated granular soils subjected to external seepage conditions, as defined in Fig. 3. From Fig. 3(a), pressure difference between the middle and bottom sections is always higher than that between the middle and top sections during piping erosion, which results in the velocity of fluid flow in lower location is larger than that of upper location (Fig 3(b)). In a word, the magnitudes of fluid velocity are directly decided by pressure difference of fluid flow.

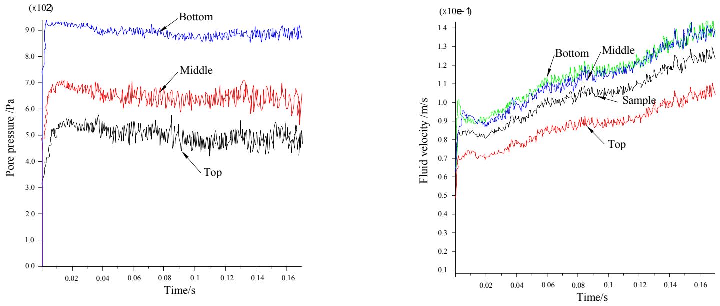

(a) water pressure (b) Mean fluid velocity of piping passage

FIG.3 Time history of Fluid Velocity and Pore Pressure During Piping

Loss Fraction of Eroded Particles

The change of loss fraction of eroded particles during piping can be recorded with Fish function via PFC3D, as been shown in Table 3. The 0-5cm means the top location of piping sample. Table 3 shows that the loss fraction of eroded particles in the lower section is slightly larger than that in the upper section of sample. This is because the hydraulic gradient of the lower part is greater than that of upper part. It is worth noting that the loss fraction at the depth of 10-15cm in DEM is not eroding but minor increasing after piping. The increase of fine particles is supplied from the lower part of sample under critical hydraulic gradient.

Table 3 Comparison of loss fraction of eroded particles

	Sample	**Averaged**	**0-5 cm**	**5-10 cm**	**10-15 cm**	**15-20 cm**
Lose fraction of fine particles (%)	Experiment	21.1	34.2		50	
	DEM	30.4	5.1	37.2	-6.2	55.4

Pathway of Particle

Figure 4 depicts the evolution of particle position during piping, which can clearly observe the particle transport and entrapment at the different stage of piping. The particles are assumed to become unstable and erode continuously when the applied hydraulic gradient exceeds a critical value (about 0.42 from Fig.2). At this time, the eroding particles keep moving, and the pathways of particles are always in the process of dynamic adjustment. When the original pathway is blocked by the movable fine particle, fluid velocity becomes smaller in this channel. Additionally, as particles move upwards, some larger fine particles are obstructed by skeleton particles and cannot go through the inter voids of particles; they will stay at certain stable position.

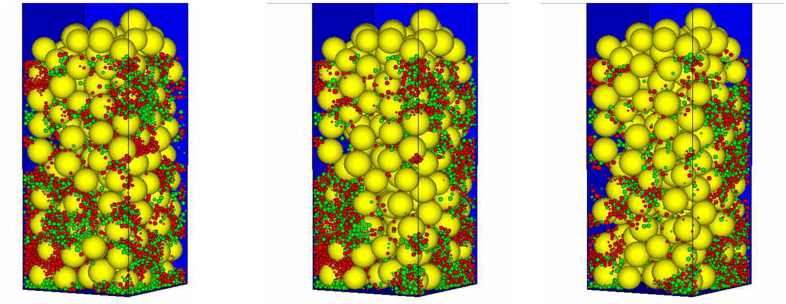

(a) 0.15 million step (b) 0.81 million step (c) 1,17 million step

FIG.4 Three-Dimensional View of Particle Evolution During Piping

CONCLUSIONS

The utilized 3D coupled continuum-discrete model was shown to be an effective tool to simulate the micro-mechanical mechanisms of piping in sandy soil. The loss fraction of eroded particles is determined by both hydraulic gradient and fluid velocity. The magnitudes of fluid velocity are directly decided by pressure difference of fluid flow. The piping passages are formed randomly, which are the outcome of the complicated interaction between fluid and grains.

ACKNOWLEDGMENTS

The research is supported by the Chinese National Natural Science Foundation, Grant numbers 50379037. This support is gratefully acknowledged.

REFERENCES

Cundall, P.A. and Strack, O.D.L. (1979). “The distinct numerical model for granular assemblies.” *Geotechnique*; 29 (1): 47-65.

Ding, L.Q., Zhang, Q.Y., and Yao, Q.L. (2007). “Analysis on characteristics of risk from piping in levee projects within Yangtze river basin during 1998.” *Chin J Water Resources and Hydropower Engineering*, Vol. 38 (2): 44-46.

Hajra, M.G. and Reddi, L.N. (2002). “Effects of logic strength on fine particle clogging of soil filters.” *J. of Geotech and Geoenv Eng*; Vol. 128 (8): 631-639.

Indraratna, B. and, Vafai F. (1997). “Analytical model for particle migration within base soil-filter system.” *J. of Geotech And Geoenv Eng*, Vol. 123 (2): 100-109.

Itasca (2003). “Particle Flow Code, PFC3D, Release 3.1.” *Itasca Consulting Group*, Inc., Minneapolis, MN.

Shamy, U.El. and Zeghal, M. (2007). “A micro-mechnical investigation of the dynamic response and liquefaction of saturated granular soils.” *Soil Dynamics and*

Earthquake Engineering; Vol. 27: 712-729.

Sherard, J.L., Dunnigan, L.P. and Talbot, J.R. (1984b). “Basic properties of sand and gravel filters.” *J. Geotech. Eng;* 110 (6): 701-718.

Skempton, A.W. and Brogan, J.M. (1994). “Experiments on piping in sandy gravels.” *Geotechnique*; 44 (3): 449-460.

Sterpi, D. (2003). “Effects of the erosion and transport of fine particles due to seepage flow.” *Inter. J. of Geomech,* Vol.3 (1): 111-122.

Zhou, J., Yao, Z.X. and Zhang, G. (2007). “Meso-laboratory study on initiation and evolution of piping.” *Chin J Under Space Eng*; Vol. 5 (3): 842-848.

Zhou, J. Yao, Z.X., Bai, Y.F., Zhang, J. (2008). “Meso-mechanical study on piping in sandy soils”. *J Tongji University (Natural Science)*; Vol. 36 (6): 733-738.

A Coupled Micro-Macro Method for Pile Penetration Analysis

Weifeng Jin[1] and Jian Zhou [2]

[1]Ph.D. Candidate, Department of Geotechnical Engineering, Tongji University, Shanghai 20009, China; jinweifenga@163.com
[2]Professor, Department of Geotechnical Engineering, Tongji University, Shanghai 20009, China; tjuzj@163.vip.com

ABSTRACT: This paper presents a coupled macro-micro method for numerically simulating pile penetration. In order to properly describe a set of particles experiencing large deformation, during the penetration process, Particle Flow Code (PFC), which is based on discrete element method, is introduced here to simulate sands near the pile as interacted balls. Thus the discrete properties of the sands nearly around the pile can well be depicted. In order to overcome the deficiency of particles during the simulation process, the domain containing particles away from the pile is simulated as continuous media by FLAC program, given that this set of particles exhibits linear elastic properties. Thus all the sands around the pile are divided into two domains, and the interface between them is treated as force boundary for the continuous domain and velocity boundary for the other domain simulated as a set of balls. It is shown that the coupled method can well depict the pile penetration process without loosing the discrete properties of the sands near the pile and efficiently reduce particle numbers during the simulation.

INTRODUCTION

Material consisting of discrete particles exhibits complex behaviours. During most numerical pile and cone penetration tests, granular materials were characterized by continuum models (Shuttle and Jefferies 1998; Salgado et al. 1997; Van et al. 1996; Kiousis et al. 1988). Thus the discrete properties of granular materials were not taken into account, and it was difficult to have an insight into the penetration mechanism on the microscopic scale. From another perspective, it is very convenient to model such materials by using the discrete element method, since the discrete element model gives a realistic description of granular material on the microscopic scale. The discrete element method was useful for simulating macroscopic parameters derived from discrete simulations (Masson and Martines 2000), and numerical cone penetration tests (Hiroakit and Masatoshi 2000; Jiang et al. 2005; Zhou et al. 2007). However, these problems solved by discrete element method are very time consuming. Due to the limit of computer capacity, it is impossible to simulate the zone containing too many particles by discrete element method.

The aim of this research is to establish a coupled macro-micro method. That is, in the concerned zone around the pile, the discrete element method can be utilized to simulate granular material, while the other zone exhibiting linear behaviours can be depicted by the continuum model. The coupled model provides a way to reduce particle numbers without loosing granular properties in the concerned zone.

COUPLED SIMULATION MODEL

The discrete model and the continuum model

The code, which is based on the discrete element method and used here, is Particle Flow Code (PFC). Particles are treated as circular balls, and the motion of each ball is traced. Interaction of ball/ball is dominated by Newton's second law. Ball/wall contacts can be used as the velocity boundaries confining balls. This approach provides a perspective on the microscopic mechanism of granular material behaviours.

The finite difference method code used is FLAC. The granular material away from the pile is treated as continuous media characterized by a linear elastic model. This model contains two macro parameters: Young's modulus E and Poisson's ratio v.

Coupled pile penetration model

The domain analyzed is divided into two zones. The concerned zone is characterized by the discrete element method, and the other zone is depicted by the continuum model. The essence of the model is that, the interface between the two zones gets ball/interface contact forces from the discrete element method, and obtains interface velocities from the continuum model. Then the contact forces are applied to the continuum model, while interface velocities are applied to the discrete element model as velocity boundaries.

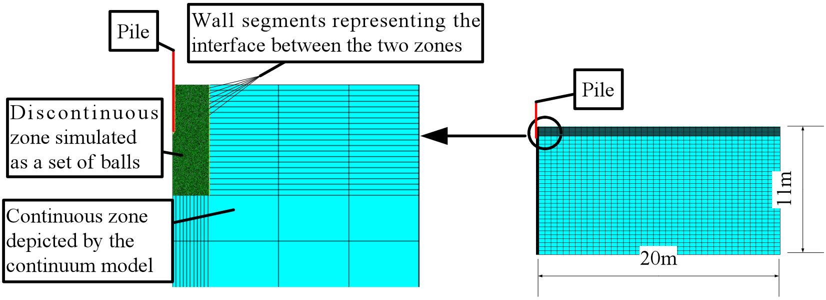

FIG. 1. Schematic view of the coupled approach.

As shown in Figure 1, the coupled model is illustrated with a numerical pile penetration test, and only the right-half of the rectangular domain in the horizontal direction is chosen. The numerical pile penetration test consists of pushing a pile into the discrete zone filled with balls simulated by PFC, and calculating the linear elastic zone away from the pile by FLAC, while interchanging unbalanced wall forces in PFC and grid point velocities in FLAC. The interface between the discrete and continuous zones is divided into segments. These segments are treated as velocity boundaries in PFC, while such segments corresponding to FLAC's grid sides are applied forces in the FLAC program.

SIMULATION OF PILE PENETRATION

Determination of microscopic parameters

In the discrete model, circular particles obey uniform distribution. The radii of the particles range from 1mm to 3mm. The microscopic parameters are as follows: the solid density of the particles ρ_s, the particle/particle friction coefficient f_c, the particle/particle contact stiffness k_n for the normal direction and k_s for the shear direction, and the porosity e. Table 1 shows the microscopic parameters.

Table 1. Values of Micro Parameters of Numerical Samples

Micro Parameter	ρ_s (kg/m^2)	f_c	k_n (N • m^{-1})	k_s (N • m^{-1})	e
Value	2650	1	1×10^6	1×10^6	0.2

By using a discrete particle simulation of biaxial compression tests, the macro parameters of the granular material on the macroscopic scale can be obtained from the knowledge of the particle properties and the microscopic distribution of the particles.

Numerical pile penetration test

The geometry of the pile penetration model is shown in Figure 1. The pile's geometry is cylindrical with a diameter of 3.5 cm and a conical point with apex angle of 60^0, the constant penetration velocity is 20 mm/s. The rectangular domain has dimensions 20× 11m, and the discrete zone filled with balls has dimensions 0.25×0.8m. The left side of the two-dimensional discrete zone is simulated as stiff walls in PFC. Zero velocity boundaries during penetration are applied to the right, left and bottom sides of the rectangular continuous zone. Numerical simulation includes two stages: making an assembly of particles and applying a constant velocity to the pile.

Results

Pile tip resistance

Pile tip resistance obtained by discrete element method is shown in Figure 2. The fluctuation of the development of tip resistance, which is caused by random impacts of particles, well depicts the characteristics of penetration into discrete granular material.

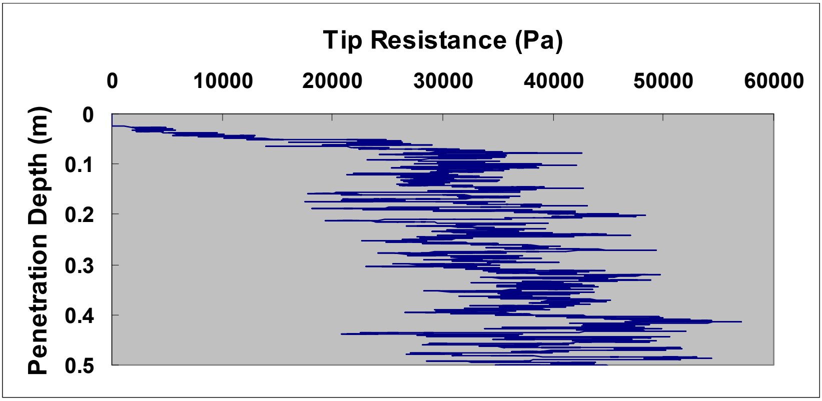

FIG. 2. Pile tip resistance

Particle displacements in the discrete zone around the pile

In order to analyze the variations of particle displacements on the microscopic scale, during penetration simulation, each particle is colored according to the ratio of its own displacement to the maximum of all particles. Tracing particle displacements provides a microscopic perspective on the mechanism of pile penetration.

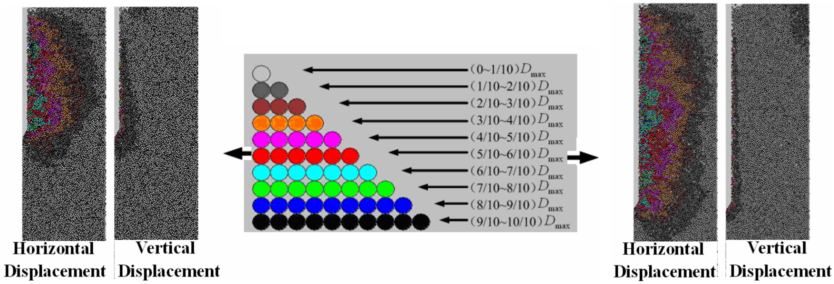

(a) Depth=0.4m (b)Colours for different displacements (c)Depth=0.6m

FIG. 3. Particle displacement fields around the pile

Let D_{max} be the maximum of all particle displacements, then the color each particle obtains according to its own displacement is provided in Figure 3.

Fig 3 also shows the horizontal and vertical displacement fields. According to the figure shown, during penetration, the zone where horizontal displacement field develops is much larger than the zone where the vertical displacement field is.

Stresses in the discrete zone

During the penetration simulation, measure circles are set around the pile in the discrete zone. Each measure circle measures average stress components and the porosity within itself. Figure 4 shows the stress fields during pile penetration.

(a)Depth=0.4m (b)Depth=0.6m

FIG. 4. Contours of the stresses around the pile at different depths

Figure 4 shows that the maximum stresses exist in close proximity to the pile tip, and the magnitude of the maximum vertical stress around the pile is larger than that of the maximum horizontal stress. In the horizontal direction, the vertical stress decreases more quickly than the horizontal stress does. It is obvious that high stress gradients exist around the pile tip. In the zone close to the pile tip, granular material exhibits nonlinear properties and it is convenient to simulate penetration in this zone by discrete element method.

Displacement fields in the zone governed by the continuum model

Figure 6 shows displacement components in the zone away from the pile. The vertical displacement fluctuates along the horizontal direction. The propagation of vibration, which is depicted by this fluctuation and is caused by random impacts between pile/particle boundaries during the penetration process, reflects that pile penetration is a dynamic process and how the granular material has an effect on the pile.

(a) Horizontal displacement (b) Vertical displacement

FIG. 5. Contours of displacement fields in the Continuous Zone

CONCLUSIONS

In this research, a coupled macro-micro method is established and applied in simulating pile penetration. This method couples discrete analysis in the concerned zone with continuum analysis in the outside zone. The discrete model provides a perspective on discerning the microscopic mechanism of penetrating into granular assemblies. The continuum model governing the zone away from the pile efficiently reduces particles. This reduction conduces to saving computation time.

It is shown that this coupled method can efficiently reduce particle numbers and well characterize the effect granular material has on the penetration process.

ACKNOWLEDGMENTS

This coupled method is a partial work of the research funded through grants 90815008. The authors appreciate the support of the National Science Foundation in China.

REFERENCES

FlAC User Manual, version 3.4, (1998), Itasca Consulting Group Inc., USA.

Jiang, M.J.; Yu, H.S and Harris, D.(2006). "Discrete element modelling of deep penetration in granular soils." *International Journal For Numerical and Analytical Methodsin Geomecanics*, Vol. 30 (4): 335-361.

Hiroakit, H. and Masatoshi, M.(2000). "Simulation of soil deformation and resistance at bar penetration by the distinct element method." *Journal of Terramechanics*., Vol. 37 (1): 41–56.

Kiousis P.D. and Voyiadjis G.Z. and Tumay M.T. (1988). "A large strain theory and its application in the analysis of the cone penetration mechanism." *International Journal for Numerical and Analytical Methods in Geomechanics*, Vol.12 (1):45–60.

Masson, S. and Martinez, J. (2000). "Multiscale simulations of the mechanical behaviour of an ensiled granular material" *Mech. Cohes.-Frict. Mater.*, Vol. 5 (26): 425-442.

PFC User Manual, version 3.1, (2004), Itasca Consulting Group Inc., USA

Shuttle, D. and Jefferies, M. (1998). "Dimensionless and unbiased CPT interpretation in sand" *International Journal for Numerical and Analytical Methods in Geomechanics*., Vol. 22 (5): 351-391.

Salgado, R. Mitchell, J.K. and Jamiolkowski, M. (1997). "Cavity expansion and penetration resistance in sand." *Journal of Geotechnical and Geoenvironmental Engineering*, ASCE, Vol. 123 (4): 344-354.

Van, D.B. De, B.R. and Huetink H. (1996). "An Eulerean finite element model for penetration in layered soil." *International Journal for Numerical and Analytical Methods in Geomechanics*, Vol. 20 (12): 865-886.

Zhou, J. and Cui, J.H. (2007). "Numerical simulation of cone penetration test by discrete element method" *Chinese Journal of Geotechnical Engineering*, Vol. 29 (11): 1604-1610.

Model Test and PFC^{2D} Numerical Analysis on Soil Arching Effects Surrounding Passive Laterally Loaded Piles

J. Jiang[1], B.Qi[2], J.Zhou[3] and Q.Y.Zeng[4]

[1]Ph.D., Dept. of Geotechnical Engineering; Key Laboratory of Geotechnical and Underground Engineering of Ministry of Education, Tongji University, Shanghai , China, 200092; rebecca1201@126.com
[2]Ph.D., Wuxi Communication and Transportation Bureau, Wuxi, China, 214031; qibin1212@126.com (Corresponding author)
[3]Professor, Dept. of Geotechnical Engineering, Tongji University, Shanghai , China, 200092; tjuzj@vip.163.com
[4]Ph.D., Fujian Communication Planning & Design Institute, Fuzhou, China, 350004; zengqy1688@163.com

ABSTRACT: This article uses a model test and PFC^{2D} discrete element simulation for systematic research on the mechanism and behavior of soil arching around passive piles in sand. In the model test, soil arching effects with different pile spacing was studied. In the discrete element simulation, the influence of pile spacing on soil arching was revealed at the meso-level. The model test indicates that pile spacing influences soil arching effects significantly. Numerical analysis also shows that pile spacing is the most significant factor on soil arching surrounding passive laterally loaded piles. From this study, the meso-mechanism and behavior of soil arching are discovered further.

GENERAL INTRODUCTION

Soil arching effects have been observed and applied by geotechnical engineers for years. Soil arching is caused by the non-homogeneous displacement in soil. The stress transferred from a geo-structure (such as a pile) to the surrounding stable medium forms an arch. The arching effect between passive piles is significant and should not be ignored.

Roberts (Janssen, 1895) found the “silo effect” in 1884. The pressure at the bottom of the silo was a maximum and remained constant when the silo packing height came to a limiting value. This is the arching effect. Terzaghi (1943) also verified that the same arching effect existed in soil with the trap door test. Analytical research and numerical simulation are two main tools for investigating soil arching (Ladanyi and

Hoyaux, 1969, Koutsabeloulis and Griffiths, 1989). Later research verified the result of the trap door test and further extended the original findings. However, most published works focus on macroscopic aspects such as the formation of soil arching and the influence of various soil parameters on it. Little has been reported on the meso-mechanism of soil arching in piles (especially passive piles).

This paper presents the results of a model test of double passive piles in different pile spacing settings and the discrete element numerical simulation (using PFC^{2D}) of soil arching in passive piles. In the model test, effects of different pile spacing on soil arching were investigated. With the validation of model testing results, the numerical simulation (using PFC^{2D}) further examined some factors influencing the soil arching, such as the pile spacing.

MODEL TEST OF DOUBLE PASSIVE PILES

Description of test

A laboratory model test has been conducted in order to investigate the influence of several parameters on soil arching effect. In the model test, a jacking mechanism is adopted to apply lateral loading on a rigid retaining wall to squeeze the sand and transfer the loads to passive piles. Figure 1 shows a sketch of this model test of passive piles. The model box is made of glass with a dimension of 600mm×400mm×370mm. The two model piles were fabricated from square wood, with a dimension of 30mm×30mm×270mm. The piles are installed behind the rigid retaining wall at a distance of 100mm. Five soil pressure cells are set on the pile body (the location is shown in Figure 1). The test soil is PingTan Sand, which is made of dense sand sample (porosity ≈0.602, relative density ≈0.748, density ≈1650Kg/m^3). A non-target digital photography deformation measure system has been introduced to accomplish this objective (Li, 2003).

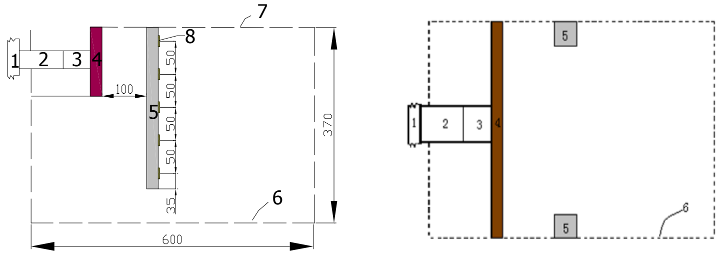

(a) Front view (b) Top view

1 reaction frame, 2 jacking apparatus, 3 load transducer, 4 retaining wall, 5 passive pile, 6 model box, 7 surface of sand, 8 soil pressure cells

FIG.1. Sketch of model test of passive piles

Loads on the retaining wall are applied as step loading in the test. When the displacement of the retaining wall reaches 2mm, the next load increment is applied. If the load applied by the jacking apparatus cannot be increased, the model test is terminated. Lateral wall displacement of the retaining wall and the passive pile head are measured by dial indicators. Soil arching in two different types of pile spacing, 2 times and 6 times of width of the pile, respectively noted as 2D and 6D, is studied.

Analysis of model test results

Figure 2 shows the displacement of the pile head and the loads on the retaining wall in the 2D and 6D pile spacing model tests. To generate the same displacement of the retaining wall, a larger load must be applied to the wall in the 2D model than in the 6D model. This means that effects of suppresses development of retaining wall is large in the smaller pile spacing (2D) model. In 6D model, the larger spacing between the two passive piles decreased the soil-pile interaction, which shows similar character to a single pile. For 2D, the coefficient of group pile interaction is larger than 1.0. Note the 2D model displacement increases continuously; the 6D curve is "S" shaped, which is nearer to the curve for a single pile.

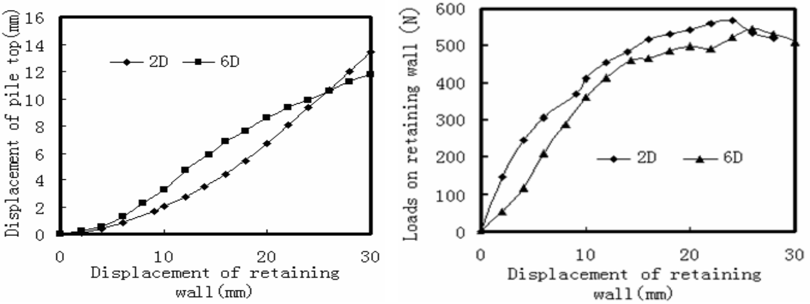

FIG.2. Displacement and load on retaining wall in model test

Distribution and developing of displacement field on sand surface

Figure 3 shows the displacement contours of the sand surface in model 2D and 6D at the maximum displacement of the retaining wall. Note that in model 2D, not only the two passive piles themselves held the sand development, but also the interaction of these two passive pile suppressed displacement of sand also. And the limit degree to sand deformation is larger at the soil between piles. The limit to sand deformation at model 6D is reduced significantly because of the pile spacing increasing. Sand seemed to "leak out" in the large pile spacing, which is similar with sand deformation in the single pile model. Apparent "arching effect" was found in smaller pile spacing. This soil displacement due to soil arching is larger than that of single pile, which means the coefficient of pile interaction is larger than 1.0.The deformation development mode agrees well with the relation of loads on the retaining wall versus displacement and the relationship of displacement of pile head versus that of retaining wall (see Figure 2.)

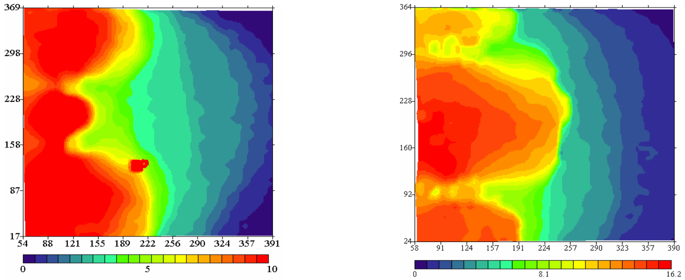

(a) Pile spacing =2D (b) Pile spacing =6D

FIG.3. Displacement field of passive pile parallel to loading (2D and 6D respectively)

PFC^{2D} ANALYSIS OF PILE-SOIL

Generating the PFC model

In numerical analysis model, the dimension of the model box is 650 mm in height and 1260 mm in width. It contains about 50,000 circular particles. The circular particle is adopted in the numerical calculation because the shape of the sand grains is approximately round. In addition, using circular particles can improve the calculation speed and obtain the sufficient accuracy. A smooth "standard wall" is adopted to simulate the boundary, and the left wall is the servo-mechanism wall. The pile body (section shape) is simulated by "general wall", whose section shape and coefficient of friction could be changed. The behavior of the two above walls (standard wall and general wall) is described in the PFC^{2D} manual. The parameters used in the PFC^{2D} model are listed in Table1. The density and radius of the particles are based on the properties of the actual test material. The stiffness and friction coefficient of the particle in Table1 are derived from fitting curves from laboratory plane strain tests and numerical biaxial tests for sands. According to the properties of the actual material of pile and box, parameters of pile and box are obtained through trial calculation.

Table1. Parameters of PFC^{2D} Model

Parameters	Density kg/m^3	Radius mm	Shear stiffness N/m	Normal stiffness N/m	Coefficient of friction μ
Particle	2650	0. 7～2.0	2.00E+06	2.00E+06	2.0
Pile	1000		3.00E+06	3.00E+06	1.0
Box			5.00E+07	5.00E+07	

As well as passive pile model test, displacement of wall is specified. The wall moved 1 mm due to each loading step. When the numerical system balanced well with the step loading, result files were saved and the next step load could be applied. In order to obtain soil pressure of concern zone, many measure circles should be laid out along pile two sides.

Pile spacing effects on interaction of soil-pile in PFC^{2D}

Figure 4 depicts the calculated relation of loads on the retaining wall and stress on the pile versus displacement of it. Note that generating same displacement, the loads on the wall increased with decreasing pile spacing, which is the reverse of that in active piles (Zhou et al, 2007). When the pile spacing is larger than 6D, the maximum stress on the pile concentrates in a small range at the displacement to 10mm, which is the limiting lateral resisting force. With the continuous developing of displacement, the lateral resisting stress decreased.

The curve of pile spacing of 4D dropped sharply then increased to the former value when displacement reached 15mm stress on pile. The reason may be that particles between piles came to and exceeded the limit state of stability and lost the stability. Release of stress occurred then new soil arching was generated after rearrangement of particles. Curve of 2D was nearly a straight line, which means that particles between retaining wall and piles were compacted and only a few particles moved around the pile. Soil arching in this pile spacing was the most stable. Pile spacing is an important and progressive factor to generate soil arch. Stable arch could be generated when the pile spacing is small. Soil arch may be generated in larger pile spacing but the stability of it decreased with increasing loads on it. If the pile spacing is too large, no soil arch could be generated.

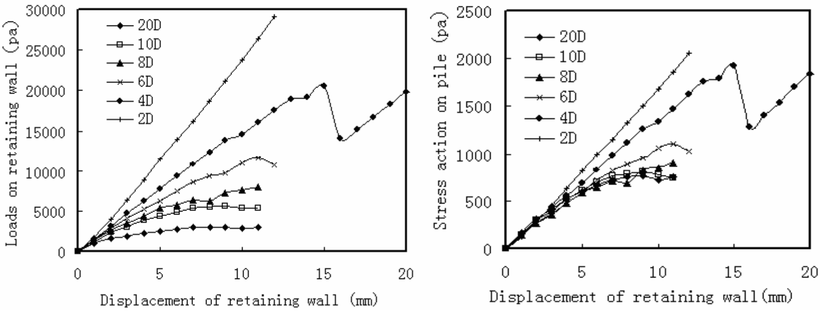

FIG. 4. Load and stress on retaining wall in PFC^{2D}

Figure 5 is the displacement of the particles and the contact force of the particles for pile spacing of 4D and 20D, respectively. From the particle flow, particles moved right at the force of left retaining wall and deflected near or at the pile. A relatively rigid triangular zone was formed behind the pile (see left diagrams in Figure 5). In this zone the contact force of particle is largest. Note that contact forces in 4D are larger than in 20D (see right diagrams in Figure 5). The direction of the particles deflected after they passed the pile and came to horizon moving state. There was a smaller triangle zone before the pile, in which the stress was smallest in the whole plane.

The displacement of the particles around the pile decreases significantly with decreasing pile spacing, which means if the pile spacing is small, the pile limits the lateral movement of the soil. Soil arching enhances the action of pile to particles and contact forces to particles around the pile are also enhanced significantly. When pile spacing is small, squeezing on pile caused by soil is increased significantly, so leaking out of soil from piles is difficult, then soil arching effects is enhanced.

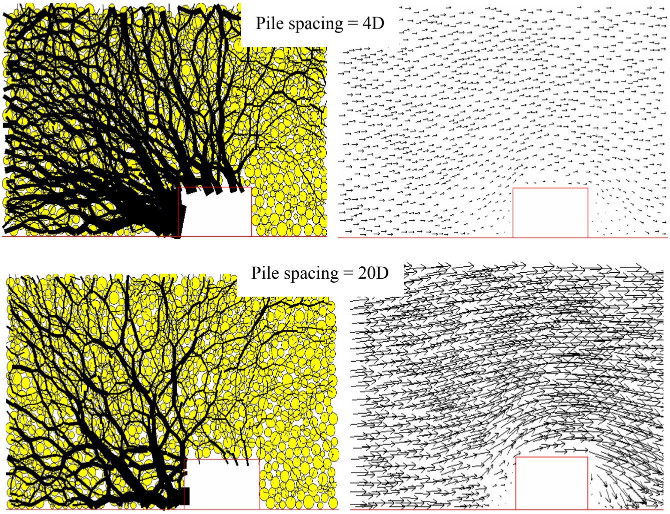

FIG. 5. Displacement around pile due to 4D and 20D pile spacing

CONCLUSIONS

(1) Meso-mechanism investigation indicates that soil arching was a complex combination of many factors. The pile spacing had a significant effect on soil arching surrounding passive laterally loaded piles.

(2) Results of the model test show that pile spacing affected the generation of soil arching and pile-soil interaction. Soil arching effect in 2D pile spacing model was larger than that in 6D pile spacing model. Hence, smaller pile spacing limited “leaking out” of sand between passive piles.

(3) Analysis of PFC^{2D} indicates that the influence of pile spacing on soil arching was significant but gradual. Comparing soil arching in six different pile spacing, soil arching in 2D pile spacing was the most stable. When the pile spacing exceeded 6D, the maximum stress on pile concentrated in a small range. The lateral resisting stress decreased when the displacement on retaining wall exceeded 12mm.

ACKNOWLEDGMENTS

The authors would like to acknowledge the National Natural Science Foundation of China (Fund No: 50578122) for financial support.

REFERENCES

Janssen H.A. (1895). "Vereins Z.Versuche tiber Getreidedruck in Silozellen." *Deutsch Ing*.39(25):1045-1049.

Koutsabeloulis N. C. and Grifiths D. V. (1989). "Numerical modeling of the trap door problem." *Geotechnique*.39(1):77-89.

Ladanyi B. and Hoyaux B. (1969). "A study of the trap door Problem in a granular mass." *Canadian Geotechnical Journal*.6(1):l-l4.

Li,Y,H.(2003). "Study on digital photography-based deformation measurement technique and its application in geo-physical model experiment." *PhD thesis*, Tongji University, Shanghai, China.

Terzaghi, K. (1943). "Theoretical Soil mechanics." *New York：JohnWiley & Sons.*

Vardoulakis, I. and Graf, and B. (1981). "Trap door problem with dry sand：a statically approach based upon model kinematics." *Int J NamerAnaly Mech Geomech*.5:57-58.

ZH, J. ZH, G. and Z Q.Y. (2007). "Model tests and PFC^{2D} numerical analysis of active laterally loaded piles." *Chinese Journal of Geotechnical Engineering*.29 (5):650-656.

Method to Evaluate the Shear Strength of Granular Material with Large Particles

Wei Hu[1], Etienne Frossard[2], Pierre-Yves Hicher[1], Christophe Dano[1]

[1] Research Institute in Civil and Mechanical Engineering, UMR CNRS 6183, Ecole Centrale de Nantes, 44321 Nantes, France, wei.hu@ec-nantes.fr
[2] Coyne-et-Bellier Bureau d'Ingénieurs Conseils, 9 Allée des Barbanniers, 92632 Gennevilliers, France, etienne.frossard@coyne-et-bellier.fr

ABSTRACT: Because of the lack of experimental devices for testing granular materials with large particles, the mechanical behaviour of rockfill is not very well known. This lack of knowledge can lead to improper design of rockfill dams, and as a consequence, to severe accidents including dam failures. A method has been developed by Frossard (2005) for evaluating the shear strength of rockfill based on the estimation of size effect in granular materials, affected by grain breakage. Comparison between experimental results and numerical predictions shows that this method can estimate with good accuracy the strength of granular materials made of large particles.

INTRODUCTION

Because of the lack of experimental devices suitable for testing granular materials with large particles, an attractive way is developed to predict their shear strength from the behaviour of a finer fraction of the same material. An important outcome is to improve the design of rockfill dams and, as a consequence, to prevent severe accidents of such hydraulic structures. Nevertheless, the mechanical behaviour of granular assemblies depends on the amount of particle breakage during loading, itself related to particle size. The authors have developed a method to evaluate the shear strength of granular assemblies containing large particles from the shear strength of assemblies with small particles. This method results from an in-depth review of previous experimental results on rockfill materials at the light of present knowledge in mechanics of materials (Frossard, 2005).

SIZE EFFECT IN GRANULAR MATERIALS

Size effect is encountered in many fields of engineering, involving concrete, rocks or soils. For granular materials, it has been found that the shear strength and more particularly the friction angle decrease whereas the particle size increases (Barton & Kjaernsli, 1981; Charles & Watts, 1980). Marachi et al. (1969) performed a series of triaxial experiments on three kinds of granular materials. For each of them, specimens of different sizes were reconstituted assuming parallel grain size distributions and grain sizes in proportion to the specimen sizes. The specimens were respectively about 70 mm, 305 mm and 915 mm in diameter. The height-to-diameter ratio was greater than 2. Test results showed that the friction angle decreases whereas the confining pressures increase (Figure 1). More, largest samples exhibit a lower value of the friction angle for a given cell pressure. Those features were clearly related to grain crushing, more intense if large particles are tested and if greatest cell pressures are used. In fact grain crushing involves a more compressible behaviour of the material: the reduction of dilatancy causes the non-linear decrease of the friction angle, as shown in Figure 1.

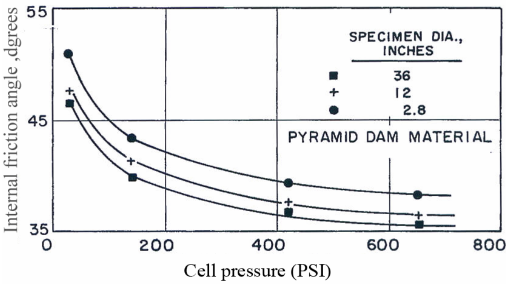

FIG.1. Friction angle vs. cell pressure for different sample size (Marachi et al., 1969)

METHODOLOGY TO DETERMINE THE SHEAR STRENGTH OF COARSE SOILS

Particle crushing test

The first step of the methodology consists in establishing the relationship between the particle size d_m and the maximum crushing load $\overline{P_a}$, as done by Marsal (1967) (Figure 2). The average experimental crushing load $\overline{P_a}$ can be fitted by a power function of the particles average diameter d_m:

$$\overline{P_a} = \eta . d_m^{\lambda} \tag{1}$$

where η and λ are experimental constants. The breakage feature can also be described by a Weibull distribution considering the probability of survival within a population of fragile objects, exposed to loading conditions:

$$P_s(V) = \exp\left[-\frac{V}{V_0}\left(\frac{\sigma}{\sigma_0}\right)^m\right] \tag{2}$$

where V is the volume, σ the applied stress, m the Weibull modulus, V_0 and σ_0 are respectively the volume and the stress corresponding to a probability of 37 %.

The theories by Marsal (Eq.1) and Weibull (Eq. 2) can be connected through a relationship between the parameter λ and Weibull modulus m. Indeed, as the grain volume V is proportional to the cube of its diameter d_m, this approach leads for a given level of survival probability P_s to an average strength proportional to a power function of the diameter d_m:

$$\sigma \propto d_m^{-3/m} \tag{3}$$

The mean stress σ is assumed proportional to the applied force during loading divided by the mean section of the grain, itself proportional to the square of the diameter:

$$\sigma \propto \frac{\overline{P_a}}{d_m^2} \tag{4}$$

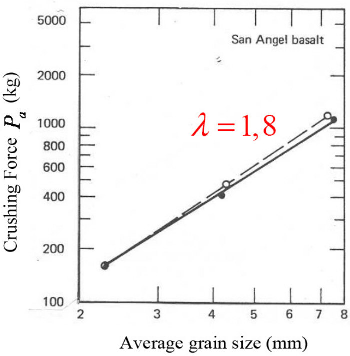

FIG.2. Experimental results of the relationship between the average grain size and particle crushing force (Marsal, 1967)

Equations 1, 3 and 4 are connected to state that:

$$\lambda = 2 - \frac{3}{m} \text{ or } m = \frac{3}{2-\lambda} \tag{5}$$

In the range of materials investigated by Marsal (1967), the parameter λ was between 1.2 and 1.8 corresponding to Weibull moduli m between 4 and 15, with a central value of λ about 1.5 corresponding to a Weibull modulus m equal to 6. Such a value is typical of many materials encountered in civil engineering.

Failure envelopes for rockfill materials

The shear strength of a compacted rockfill material can be determined by carrying out drained triaxial compression tests. The shear strength measured in such a test at a particular confining pressure can be represented by the friction angle:

$$\phi = \sin^{-1}\left[\frac{\left(\sigma_1'/\sigma_3'\right)_f - 1}{\left(\sigma_1'/\sigma_3'\right)_f + 1}\right] \tag{6}$$

where $(\sigma_1'/\sigma_3')_f$ is the maximum principal stress ratio during the test. As previously mentioned, there is a marked decrease of the friction angle when the confining pressure σ_3' is increased. Therefore, a curved failure envelope is chosen (De Mello, 1977):

$$\tau_f = A\left(\sigma'\right)^b \tag{7}$$

Introduction of size effect in the expression of the failure envelope

Size effects provide an efficient rule, as derived by Frossard (2005, 2009), to predict the strength failure envelope for a given rockfill material with large particles of grading $G_1(D_1 = D_{max})$, from the measured shear strength of a similar rockfill materials with small particles of grading $G_0(D_0 = D_{max})$. One important assumption states that the coarse and fine fractions are issued from the same homogeneous mineral stock, that they have parallel gradings and same porosities (Figure 3). In that frame, size effects can be integrated in the shear strength envelope, like De Mello's parabolic criterion (Eq. 7). If the general failure envelope for the material G_0 is given by the following formula:

$$\tau_{G_0} = f\left(\sigma_n, D_0\right) \tag{8}$$

the failure envelope for material G_1 is given as follows:

$$\tau_{G1} = \left(\frac{D_1}{D_0}\right)^{\frac{-3}{m}} \cdot f\left\{\sigma_n \cdot \left(\frac{D_1}{D_0}\right)^{\frac{3}{m}}, D_0\right\} \tag{9}$$

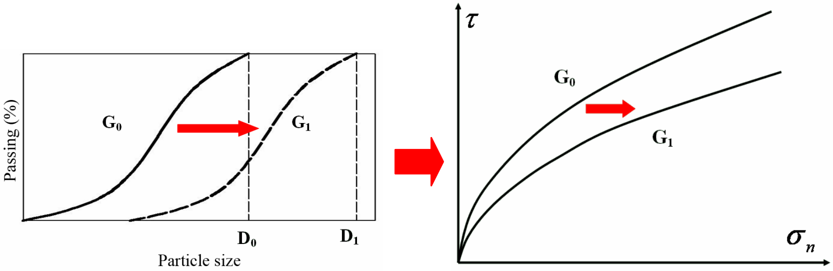

FIG.3. General scheme of the size effect rule

The substitution of Eq. 7 into E. 9 leads to the shear strength envelope for the material G_1:

$$\tau_{G_1}=\left(\frac{D_1}{D_0}\right)^{\frac{-3(1-b)}{m}}\cdot\tau_{G_0}=A_{G_0}\cdot\left(\frac{D_1}{D_0}\right)^{\frac{-3(1-b)}{m}}\cdot\sigma_n^b \tag{10}$$

VALIDATION OF THE METHOD

In order to validate the method, experimental results by Lee (1992) on two kinds of oolitic limestone from Greetham (UK) subsequently named MOLS and POLS, with parallel gradations (Figure 4), are considered. MOLS is the limestone with comparatively small particles and POLS is the material with larger particles. The ratio between the respective mean diameters of MOLS and POLS grains is about 10.

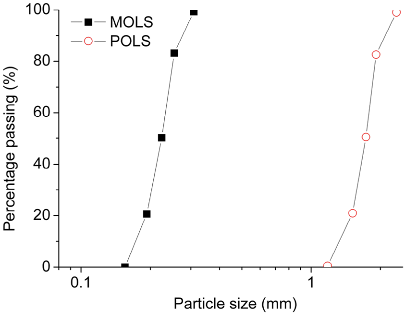

FIG.4. Original gradations for materials MOLS and POLS (after Lee, 1992).

Crushing tests on individual particles were performed: they exhibit a typical decrease of the crushing load as a function of the particle size (Figure 5). According to Marsal's formula (Eq. 1), the crushing function for the limestone is:

$$\overline{P_a}=4.508d_m^{1.65} \tag{11}$$

The values of the two parameters can also be calculated: λ= 1.65 and m = 8.57.

In order to obtain the failure envelope of the materials MOLS and POLS, several triaxial tests were also performed by Lee (1992). In the range of cell pressures 40 kPa – 320 kPa, the shear strength envelope for the granular soil with smaller particles MOLS can be fitted:

$$\tau_M(\sigma_n)=0.71\sigma_n^{0.89} \tag{12}$$

According to Eq. 10, the size effect rule allows to predict the shear strength envelope of the POLS materials containing large particles, from the experimental observations on the soil with smaller particles. Then:

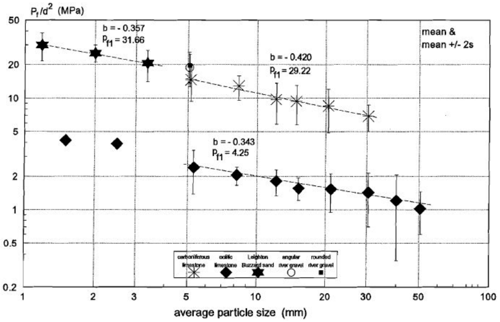

FIG.5. Relationship between average particle size and crushing stress (Lee, 1992)

$$\tau_P(\sigma_n) = \left(\frac{D_P}{D_M}\right)^{\frac{-3(1-b)}{m}} \cdot \tau_M(\sigma_n) = A_M \cdot \left(\frac{D_P}{D_M}\right)^{\frac{-3(1-b)}{m}} \cdot \sigma_n^b \tag{13}$$

The parameter m was identified from crushing tests (m = 8.57) and the parameter b from triaxial tests on MOLS material (b = 0.89). $D_M = 0.3$ mm and $D_P = 2.5$ mm are the maximum particle diameters of materials MOLS and POLS, respectively. Substituting Equation 12 into Equation 13, the failure envelope for POLS can be predicted:

$$\tau_P(\sigma_n) = 0.657\sigma_n^{0.89} \tag{14}$$

That theoretical shear strength envelope can now be compared to the shear strength envelope determined by triaxial compression tests, in the range of cell pressures between 40 kPa and 160 kPa (Figure 6). Theoretical predictions and experimental results fit very well. However, because of the relatively small contrast in the mean diameters of the grains, size effect is not so much marked, due to the particularly high values of both parameters m and b (in Equation. 13, it may be shown that when *b* tends towards a value of 1, size effect vanishes as the shear strength envelope tends towards the Coulomb failure criterion).

A similar approach has been used on Marsal (1967)'s results. Triaxial tests by Marsal (1967) show more contrast between grain size distributions and size effect. However, the rule developed in this paper enables to predict the behaviour of coarse granular soils from a finer fraction with good accuracy. Because of limitations of space, those results can not be presented here.

The prediction of the shear strength degradation because of grain crushing can finally be involved in classical slope stability analysis. It causes the slope to be increased to keep the safety factor at a same level.

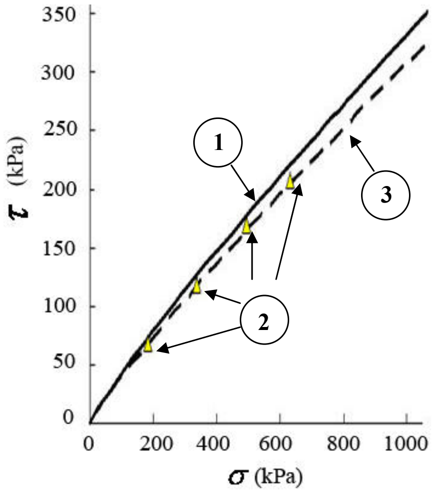

(1) Experimental shear strength envelope for MOLS
(2) Experimental shear strength envelope for POLS
(3) Shear strength for large size material extrapolated from MOLS, through the size effect rule

FIG.6. Comparison of experimental and predicted shear strength envelopes

CONCLUSION

A new method for the evaluation of the mechanical behaviour of rockfill materials based on size effects has been presented. In this method, the Weibull theory and experimental observations by Marsal about the rupture of granular particles have been connected through the relationship between Weibull's modulus m and the parameter λin Marsal's formula. Basically, these two parameters give an indication on the "rupture capability" of particles. Size effects have also been introduced and used in the method for connecting the strength of specimens with comparatively large particles and that of specimens with small particles. A series of crushing tests and triaxial experiments on limestone granular assemblies have been used to validate the method. Comparison of model prediction and experimental results demonstrates that the method is able to predict with very good accuracy the maximum strength of coarse granular materials.

ACKNOWLEDGEMENTS

This work is a part of the French research Project ECHO (Scale effects in fill works in Civil Engineering), sponsored by the French National Agency for Research, targeted to validate the method exposed above and explore its limitations, through a wide experimental testing program, including 1m diameter triaxial tests on granular fills.

REFERENCES

Barton, N. and Kjaernsli B. (1981). “Shear Strength of Rockfill”, *Journal of Geotechnical Engineering* ,Vol. 107 (136): 873-891.

Charles, J.A and Watts K.S. (1980). “The influence of confining pressure on the shear strength of compacted rockfill”, *Géotechnique,* Vol. 30 (4) :353-367.

Charles, J.A .and Soares, M.M. (1984). “Stability of compacted rockfill slopes” *Géotechnique,* Vol. 34 (1):61-67.

De Mello V.F.B. (1977). “Reflections on design decisions of practical significance to embankment dams”, *Géotechnique,* Vol. 27 (3):281-355.

Frossard, E. (1979). “Effect of sand grain shape on interparticle friction: indirect measurements by Rowe’s stress-dilatancy theory”, *Géotechnique,* Vol. 29 (3): 341-350.

Frossard, E. (2005). “Macroscopic behaviour of granular materials used in dam construction”, *Coyne et Bellier Report on Investigation Program on Micromechanics in Rockfill Dams (sponsored by French Ministère de la Recherche)*

Frossard, E. (2009). “On the structural safety of large rockfill dams”, Proceedings XXIII° International Conference on Large Dams, Brasilia.

Lee, D.M. (1992). “The angles of friction of granular fills”, PhD thesis, Cambridge University.

Marachi, N.D., Chan C.K., Seed H.B. and Duncan J.M. (1969). “Strength and deformation characteristics of rockfill materials”, Report No. TE-69-5, Department of civil engineering, University Of California, Berkeley.

Marsal, R.J. (1967). “Large-scale testing of rockfill materials”, *Journal of the Soil Mechanics and Foundation Engineering Division*, ASCE, Vol. 93 (SM2): 27-44.

Weibull, W. (1951). “Statistical distribution function of wide applicability”, *Journal of Applied Mechanics*, ASCE, Vol.18 (2) :293-297.

Experiments on a Calcareous Rockfill Using a Large Triaxial Cell

Hu Wei, Christophe Dano, Pierre-Yves Hicher

Research Institute in Civil and Mechanical Engineering, UMR CNRS 6183, Ecole Centrale de Nantes, 44321 Nantes, France ; wei.hu@ec-nantes.fr

ABSTRACT: Granular materials with large particles have been widely used to construct embankments or rockfills dams. However, due to limitations in the size of experimental set-ups, their behavior remains relatively less investigated than the behavior of sands for instance. A new large triaxial apparatus, with a maximum specimen diameter of 1000mm, has been designed to study the behavior of such coarse granular materials. This device is described in this paper. The results of a triaxial test on calcareous particles with a maximum particle size of 160 mm are presented. Special attention has been paid on grain crushing under shear loading.

INTRODUCTION

The study of granular materials containing large particles (rockfills, ballast …) requires suitable laboratory facilities whose dimensions must be in proportion of the grains maximum size. Since the pioneering works using very large triaxial cells at the University of Berkeley, California and at the University of Mexico in the 1960's and 1970's (Marsal, 1967; Marachi et al., 1972; Leps, 1970), few experimental developments have been done. Some cells smaller than Marsal's device have been nevertheless constructed and have provided interesting results about the behavior of unsaturated gravels and rockfills (Chavéz & Alonso, 2003), about the dynamic behavior of ballasts (Indraratna et al., 1998; Lackenby et al., 2007) or about the pseudo-static behavior of rockfills (Charles & Watts, 1980; Barton & Kjaernsli, 1981; Indraratna et al., 1993;). Nowadays, only few cells in the world are able to reproduce Marsal's experiments (Verdugo & de la Hoz, 2006) and to pursue the research on the behavior of rockfills at the light of the current geotechnical knowledge. In this paper, a new large triaxial cell is presented.

CELL DESIGN

Contrary to the peculiar design of Marsal's spherical cell, the new large apparatus described in this paper looks like a smaller conventional cylindrical triaxial cell. The cell could support a vertical load of 2000 kN. The full cell (Figure 1) lies on a pre-stressed concrete slab. The cell base is a 1.60 x 1.60 x 0.145 m steel element lying on a steel frame. Depending on the sample size and the material nature, a suitable inner load cell is placed between the cell base and the sample. Three submersible and specifically designed load cells of respective capacities 500 kN, 1000 kN or 2000 kN are thus available in addition to an external measurement of the vertical load given by the hydraulic jack. Their linearity is lower than ±0.5 % of the measure scale. The sample bottom platen is screwed on the load cell. At the present time, the cell may host samples either 1 m in diameter and 1.5 m in height (height-to-diameter ratio: 1.5) or 0.5 m in diameter and 1 m high (height-to-diameter ratio: 2). An intermediate stiff steel piece is placed below the 0.5 m in diameter sample to keep the top surface of the sample at the same altitude than the top surface of the largest sample. Additional sample sizes can be added (all the pieces for samples of 300 mm in diameter and 700 mm in diameter were designed but have not been constructed until now). A similar platen, then named top platen, is put on the top of the sample. Those steel circular platens are 120 mm thick and 1100 mm in diameter for 1 meter samples and 100 mm thick and 600 mm in diameter for 0.5 meter samples. Concentric grooves in the inside face of the platens acts as drains. A screen on which two fine layers of geo-membrane are placed acts as a porous stone and a filter to avoid penetration of fine particles in the drainage network. No lubrication is used to prevent boundary effects on the platens.

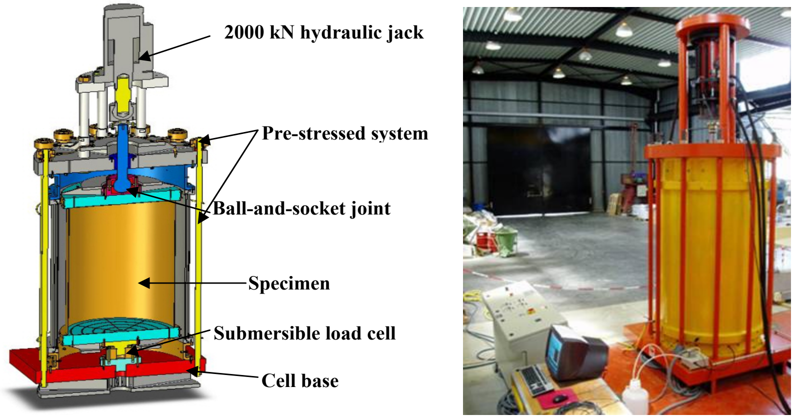

FIG. 1. First configuration (right) and second configuration (left) of the large triaxial cell.

The lateral steel envelope is in fact a 2 meters high double-wall chamber. The double-wall chamber filled with water as confining fluid is composed of a steel outer cylinder, 12 mm thick and 1256 mm in diameter, and a high density polyethylene (HDPE) inner cylinder, 8 mm thick, 1200 mm in diameter and 1718 mm high. The chamber can theoretically withstand a confining pressure of 1.5 MPa but it is limited to 1 MPa for safety. A servo-valve connecting the two parts is used to balance the pressure in inner and outer chamber, so that the HDPE cylinder remains undeformable.

The functional capability of the cell has been proved by comparing triaxial test results on sand samples of different sizes (100 mm, 500 mm, 1000 mm). Those tests are not presented here. However, it has been shown that the pre-failure behavior of sand samples reconstituted at a same density is not dependent on the sample size, as expected in a representative volume of a granular material which was not subjected to grain crushing.

TRIAXIAL EXPERIMENT ON A CALCAREOUS ROCKFILL

Sample Preparation and testing procedure

The experiment presented in this paper has been carried out to calibrate subsequent tests for an on-going project. The tested material is a calcareous rockfill from a quarry located in Prefontaines (center of France). The initial gradation is slightly modified so that the minimum grain size is 25 mm and the maximum grain size is 160 mm. The uniformity coefficient U_c is close to 2 and the mean grain diameter to 90 mm. The angularity of the particles is classified as sub-angular (ASTM D2488-10). The material is first dried by natural evaporation in a covered hall: the water content initially equal to 11 % decreases until a value of 0.3 % is reached.

Membranes are made of PVC. Two membranes, 1.4mm each in thickness, are superimposed to avoid possible tears by angular grains. The second PVC membrane is free to slide on the first outer membrane. About 17 layers of material, 100 kg each, are deposited in the mold. Each layer is then compacted using a vibration spear which is inserted into layer of particles.

The unit weight finally obtained is 14.05 kN/m^3. However, uncertainty about the volume remains since the diameter cannot be accurately determined. Planarity of the sample top surface is also quite difficult to obtain because of the grain size. A slight planarity default was thus observed. Initial sample shape is shown in Figure 2.

(a) Before test (b) After test

FIG.2. Calcareous rockfill sample aspect, before and after shearing.

Test results

The test was conducted at a confining effective stress of 200 kPa. The shearing rate was 30mm/h. The deviatoric stress vs. axial strain curve and the volumetric strain vs.

axial strain curve are presented in Figure 3. The axial strain was technically limited to 20 %. Volumetric strains are deduced from water volume changes measured on a electromagnetic flowmeter placed at the exit of the cell inner volume.

At the end of the test, the membrane was cut at its base and gradually opened over the height. Contrary to an uncemented sand mass which immediately flows, the rockfill mass did not collapse and photos of the final structure can be taken (Figure 4). Observations particularly show intact grains even of large diameters, some grains deeply crushed and some grains which split in two parts. Grain size distributions have been compared before and after the test (Figure 5). A relatively large amount of ruptures occurred during shearing.

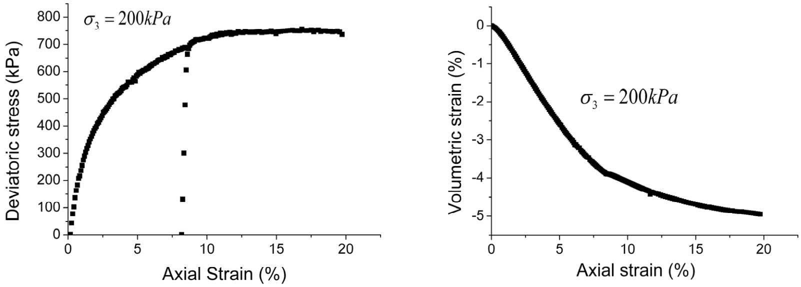

FIG. 3. Test results.

The opportunity to test coarse soils offers great advantages. First, the behavior of granular materials containing large particles can be directly measured instead of being extrapolated from the behavior of a finer fraction of soil. More, it is well known that large particles statistically crush more easily than small particles, and it becomes possible to establish scale effects on granular materials. Such an approach is presented in a second paper by the same authors.


(a) *(b)*

FIG. 4. Grain assembly at the end of the test.

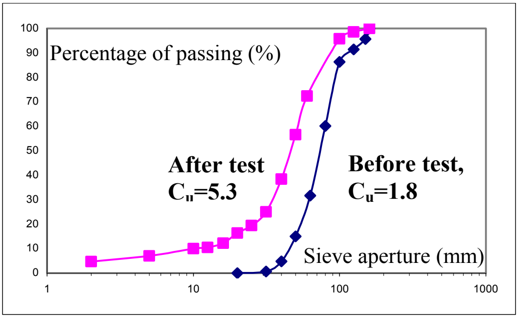

FIG. 5. Grain size distributions before and after triaxial experiment.

CONCLUSION

This paper presents a large triaxial cell designed for the investigation of coarse soil behavior. The main characteristics of the cell and the main difficulties in the use of this facility have also been introduced. The most recent evolutions allow the users to apply confining pressures in the range 100 – 1000 kPa and axial loads up to 2000 kN, monotonically or cyclically with adapted frequencies in the range 0 – 5 Hz. The original features of the cell, beyond its dimensions, result from the different possible sample sizes and the double-walled cylindrical envelope designed to accurately measure the volume changes of the sample during testing. A drained triaxial test on a calcareous rockfill shows the capability of the cell to experiment coarse soils and to quantify the amount of grain ruptures.

ACKNOWLEDGEMENTS

This work is a part of the French research Project ECHO (Scale effects in fill works in Civil Engineering), sponsored by the French National Agency for Research, targeted to make research on the size effect of the granular materials through a wide experimental testing program, including 1m diameter triaxial tests on granular fills.

REFERENCES

Baldi, G. and Nova, R. (1984). “Membrane penetration effects in triaxial testing.” *Journal of Geotechnical Engineering.*, Vol. 110: 403-420.

Barton, N. and Kjaernsli, B. (1981). “Shear Strength of Rockfill.” *Journal of Geotechnical Engineering.,* Vol .107 (7) : 873-891.

Biarez, J. and Hicher, P.Y. (1997). “Influence de la granulométrie et de son évolution par ruptures de grains sur le comportement mécanique de matériaux granulaires. ” *Revue française de génie civil*, Vol. 1 (4) : 607-631.

Charles, J. A., Watts, K. S. (1980). “The influence of confining pressure on the shear strength of compacted rockfill.” *Géotechnique,* Vol .30 (4):353-367.

Chávez, C. and Alonso, E.E. (2003). “A constitutive model for crushed granular aggregates which include suction effects.” *Soils and Foundations*., Vol.43

(4) :215-227.

Georgopoulos, I.O. and Vardoulakis, I. (2005). “Corrections on the specimen volume changes and axial force in the Wykeham Farrance triaxial cell.” Internal report, NTU Athens, Greece.

Hardin, B.O. (1985). “Crushing of soil particles.” *Journal of Geotechnical Engineering,* Vol. 111(10):1177-1192.

Indratatna, B., Ionescu, D. and Christie,. H.D. (1998). “Shear behaviors of railway ballast based on large-scale triaxial tests.” *Journal of Geotechnical and Geoenvironmental Engineering,* Vol. 124 (5): 439-449.

Lackenby, J., Indraratna, B., McDowell, G. and Christie, D. (2007). “Effect of confining pressure on ballast degradation and deformation under cyclic triaxial loading.” *Géotechnique*, Vol. 57 (6) :527-536

Leps, T.M. (1970). “Review of Shearing Strength of Rockfill.” *Journal of the Soil Mechanics and Foundations Division*., Vol. 96 (4):1159-1170

Marachi, N.D., Chan, C.K., Seed, H.B. and Duncan, J.M. (1969). “Strength and deformation characteristics of rockfill materials.” Report No.TE-69-5, Dept. of Civil Engineering., Univ. of California, Berkeley.

Marsal, R.J. (1967). “Large-scale testing of rockfill materials.” *Journal of the Soil Mechanics and Foundation Engineering Division*, Vol. 93 (SM2): 27-44.

Verdugo, R. and de la Hoz, K. (2006). “Strength and stiffness of coarse granular soils.” Geotechnical Symposium “Soil Stress-Strain behaviour: measurement, modelling and analysis, Rome, 16-17/03/2006, Hoe I. Lings et al. (eds), Springer: 243-252.

Investigation of Mechanical Response Induced in Dynamic Compaction of Sandy Soils with PFC^{2D}

Mincai Jia[1] and Jian Zhou[2]

[1]Lecturer, Key Lab. of Geot. & Underground Engrg, Ministry of Education, Dept. of Geot. Engrg., Univ. of Tongji, Shanghai 200092, China. E-mail: mincai_jia@tongji.edu.cn
[2]Professor, Lecturer, Dept. of Geot. Engrg., Univ. of Tongji, Shanghai 200092, China. E-mail: tjuzj@vip.163.com

ABSTRACT: The paper discusses the main aspects involved in numerical modeling of large deformation, rigid body impacts in sandy soils. The modeling was performed for the study of dynamic compaction of sandy soils induced by repeated drops of a rigid tamper. A two-dimensional discrete element model, written with PFC^{2D} code (Particle Flow Code in two dimension), has been developed to carry out simulation of dynamic compaction process on a sandy soils. Comparisons were made of the dynamic contact stress of tamper bottom, dynamic stress with depth, displacement fields with depth and crater depth. A preliminary assessment of the reliability of these numerical curves was conducted using results from the laboratory model tests. The results show that the mechanical response of sandy soils induced by tamper dropping could be well simulated with PFC^{2D} during dynamic compaction, and the change of dynamic stress and dynamic strain with depth can be real-time traced and recorded.

INTRODUCTION

Dynamic compaction is a well-established ground improvement technique which is particularly effective for sandy soils and loose unsaturated soils. This heavy tamping is achieved by dropping a heavy weight of 10-40t from a height of 10 to 25m in a grid pattern across the treatment area (Menard and Broise 1975). Over the past decades, simple analytical model (Mayne and Jones 1983; Chow et al. 1992), FEM simulation (Poran and Rodriguez 1992; Gu and Lee 2002) and field tests(He et al. 2007) are commonly suggested to study the soil behavior during heavy tamping. Because of the discrete properties of soils and its complexity of dynamic response under impacting, it was difficult to have an insight into the macro-micro mechanism of dynamic compaction by the common FEM or field tests.

PFC^{2D} (Particle Flow Code in 2 Dimensions), based on the discrete characteristics of granular media, provides a powerful and flexible environment to simulate actual static and dynamic problems and to explore the unknown meso-characteristics of granular media. The feasibility of using PFC^{2D} to conduct static and dynamic nature has been verified by many scholars (Powrie et al. 2005; Zhou et al. 2007).

The aim of this research is to establish a PFC2D numerical model, written with FISH language, in order to simulate the behaviors of sandy soils under dynamic compaction. This paper focuses on the transmission of particle contact force, dynamic stress under the hammer, and the distribution of dynamic stress field and displacement field. The findings contribute to a correct understanding of relation between the meso-mechanical response of sand particles and the macro-compacting of sands under dynamic impact.

Numerical model written with PFC2D

Contact model of particles

Determination of the particle contact model is essential to the numerical results when setting up the dynamic compaction model with PFC^{2D}. In order to explore the dynamic response of sands under dynamic compaction effectively, the advantages and drawbacks of three types of contact model (Linear Elastic model, Hertz Model and Hysteretic Damping Model) are compared, and the Hysteretic Damping Model is ultimately selected. As Shown in Fig. 1, the Hysteretic Damping Model could truly reflect the change of soil stiffness and instantaneous compaction during impacting.

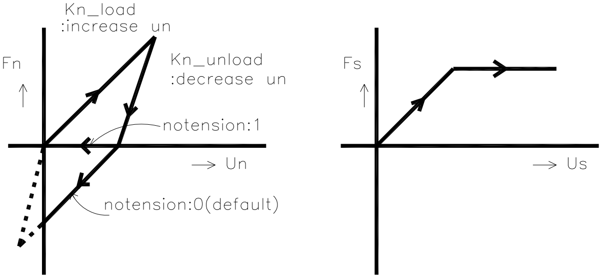

FIG. 1. Hysteretic Damping Model

Particles box and its meso-scale parameters

The semi-model is adopted to accelerate the computing speed based on the symmetry (Fig. 2). The size of the model box is 60 cm × 60 cm, which is determined based on the principle of similarity and the influence area of the actual dynamic compaction. The particles box is modeled with the definition of smooth left, right, and bottom wall. The parameters of the box are shown in Table 1.

Meso-scale parameters of sandy soils and hammer

As shown in Fig. 2, blocking partition principle is adopted in the model to reduce the computation time. In area 1, the main influence area of impacting, 20362 particles are generated in the 0.232 m × 0.3 m area. 18814 larger particles are generated in areas 2 and 3, the weak influence area of the impact loading. The meso-scale parameters of numerical sand particles shown in Table 1 are determined based on the results of the biaxial tests by means of fitting the numerical stress-strain curves with the test results.

The CLUMP block consisted of 84 particles with diameter of 1cm is generated to simulate the 4 cm × 6.75 cm hammer, as shown in Fig. 3. Meso-scale parameters of the hammer are shown in Table 1.

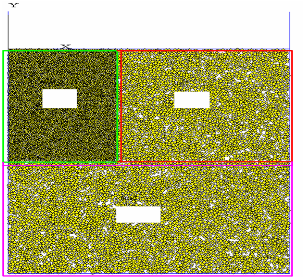

Fig. 2. Particles and Box

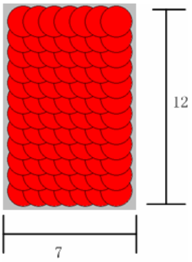

Fig. 3. Tamper

Table 1. Meso-scale parameters of PFC^{2D} model

Particles	Normal Stiffness	5×10^6N/m
	Tangent Stiffness	5×10^6N/m
	Density	2600 kg/m^3
	Quality Damping Coefficient	0.0
	Friction Coefficient	0.1
	Hysteretic damping coefficient	0.1
Walls (Except the left)	Normal Stiffness	1×10^9N/m
	Tangent Stiffness	1×10^9N/m
	Friction Coefficient	0.0
Hammer	Normal Stiffness	1×10^9N/m
	Tangent Stiffness	1×10^9N/m
	Density	7800 kg/m^3
	Quality Damping Coefficient	0.0

NUMERICAL SIMULATION ANALYSIS

Propagation of contact force

The propagation of dynamic contact force is radiating from the tamping point to the surroundings, similar to the wave source. While considering the space and symmetry, the shape of its propagation is similar to an hemisphere, as shown in Fig. 4. With the increasing of contact time, the radius of the hemisphere is increasing and the dynamic contact force is gradually decreasing in the effect of damping until the system unbalanced forces has totally dissipated close to zero. When the system re-achieves equilibrium state and the contact force under the hammer are approximately equivalent to the weight of the hammer.

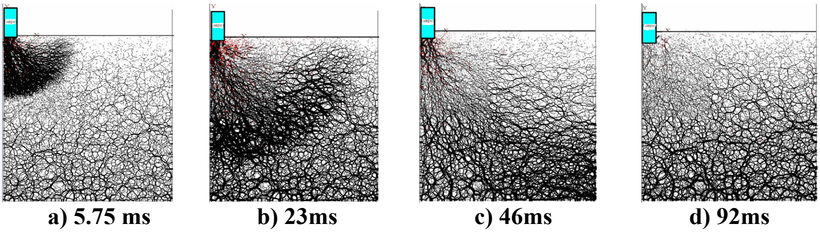
a) 5.75 ms b) 23ms c) 46ms d) 92ms

Fig. 4. Propagation of Contact Force During 1st Impacting

Dynamic stress in sandy soils

As shown in Fig. 5, the vibration inside the sands caused by the dynamic compaction is a transient vibration, the increasing and attenuation process of the vertical and horizontal dynamic stress occurs within 40ms to 60ms. The vertical dynamic stress under the hammer is significantly greater than the horizontal dynamic stress at the same depth, which indicates that the sands under the hammer to dynamic compaction mainly occur the vertical compressive deformation. Vertical peak dynamic stress has the same phase with the horizontal peak dynamic stress without lag, but along the depth there is an obvious lag.

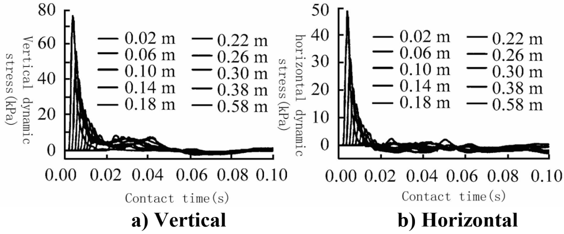

a) Vertical b) Horizontal

Fig. 5. Dynamic Stress in Crater vs Time

Dynamic stress-time curve in different depths and different distances away from the tamping point are shown in Fig. 6 to Fig. 7. The dynamic stress of sand particles away from the tamping point at different distances has a single peak, and the time of the process is about 40ms to 60ms. At the same depth but different positions, the nearer to the tamping point, the greater the dynamic stress is. In addition, the peak vertical dynamic stress at the surface is less than that of the horizontal stress and the range of attenuation level of the vertical dynamic stress is significantly greater than the horizontal stress with the increasing distance from the tamping point. This phenomenon initially reflects why the soil surface becomes loose after several impacts.

As shown in Fig. 8, the vertical peak dynamic stress under the tamping point at different depth has shown a decreasing trend, and the maximum, which becomes larger with the increasing distance from the outside line of the hammer, appears in the contact surface with the hammer. The vertical peak dynamic stress increases at first and then decreases. Along with the distance further from the outside line of the hammer, the occurrence of the maximum peak position of the six curves of the vertical stress is also moving downward. All these trends confirm that the transmission of the dynamic stress of soil under tamping is in accordance with a certain proliferation angle downward.

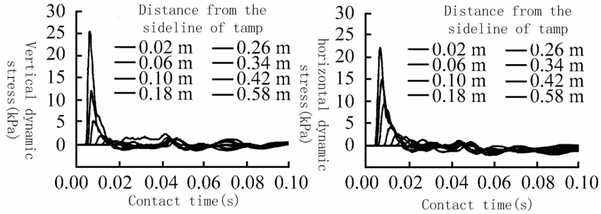

a) Vertical **b) Horizontal**

Fig. 6. Dynamic Stress at Depth 8 cm vs Time

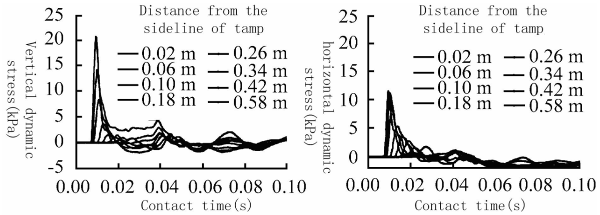

a) Vertical **b) Horizontal**

Fig. 7. Dynamic Stress at Depth 24 cm vs Time

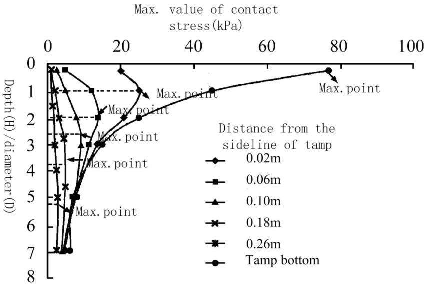

Fig. 8. Dynamic Stress Peak vs Depth

Distribution of displacement fields and settlements

In order to analyze the variations of particle displacements on the meso-scale during impacting, each particle is colored according to the ratio of its own displacement to the maximum of all particles. Tracing particle displacements provides a meso-scale perspective on the mechanism of dynamic compaction. The relationship between the colors and the displacement values is shown in Fig. 9.

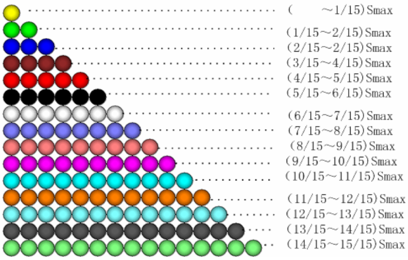

Fig. 9. Color Scale

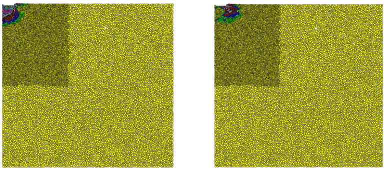

vertical displacement (S_{max} = 5.99 mm)

horizontal displacement (S_{max} = 0.56 mm)

Fig. 10. 5.75 ms after 1st impact

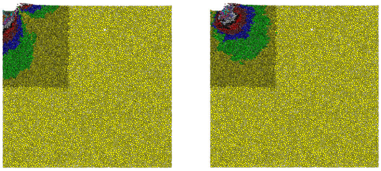

vertical displacement (Smax = 19.60 mm)

horizontal displacement (Smax = 1.85 mm)

Fig. 11. 23 ms after 1st impact

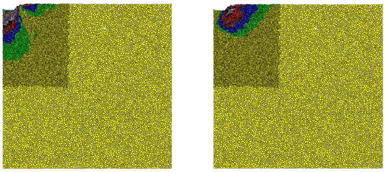

vertical displacement (Smax = 22.35 mm)

horizontal displacement (Smax = 2.4 mm)

Fig. 12. 92 ms after 1st impact

As shown in Figs. 10-12, the scope and value of the deformation of sand particles due to the impact is increasing to the maximum after 46ms, which has an apparent lag to the emergence of dynamic stress maximum. The displacement values decrease slightly because of the dissipation of dynamic stress wave and unloading rebound. The shape of the tamping pit is similar to the pit in the actual engineering situation. The shape of vertical influence area under tamping is similar to an oval, and the long axis of the ellipse at any time is 2 times of the short axis, which indicates that the influence area of vertical displacement is about 2 times of the level of the horizontal influence area. The shape of horizontal displacement of the influence area is an oval, but the long axis of the ellipse with the time has a rotating trend heading to the horizontal direction.

VERIFICATION WITH LABORATORY MODEL TEST

Model test introduction

Model box size of 60 cm × 60 cm × 60 cm, is made by the five ordinary transparent glass. Pulley would be fixed in one translation guide poles, and heavy hammer would drop down the vertical orbit. Heavy hammer is semi-model with 8 cm diameter, 6.75 cm height, and 1.232 kg weight. Model test device and its testing equipment layout are shown in Fig. 13. In order to observe change of particles fabric at different positions, the semi-model test is adopted to read the displacement of soils by means of staining sands. Particles fabric would be measured with stereoscope and image analysis software.

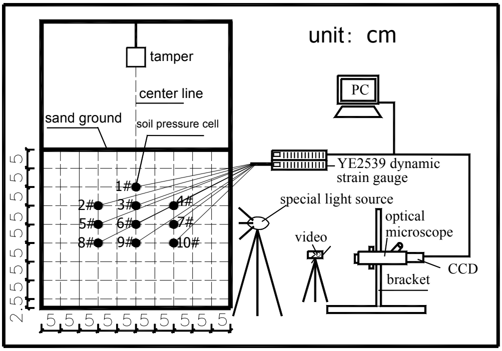

Fig. 13. Layout of model box

Based on the images of marked staining sand under the blow of different number, the Dataread is introduced to get the coordinates of each grid point to draw the vertical displacement contour map, which are shown in Fig. 14. While considering symmetry, the shape and distribution of particles in the contour map are similar to the results of numerical simulation shown in Figs. 10-12.

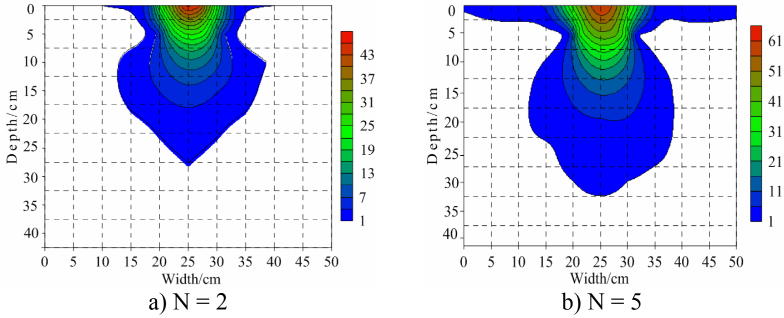

a) N = 2

b) N = 5

Fig. 14. Contour of Vertical Displacement

Test results and analysis

As shown in Fig. 15, vertical dynamic stress-time curve was received by means of soil pressure cells. Compared with the foregoing results from the numerical simulation, the dynamic stress change of sands under the hammer in different depth has the same trend both single-peak response and no second peak, as shown in Fig. 15.

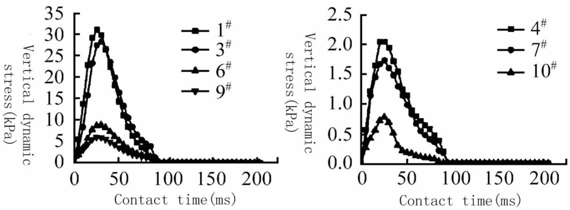

a) under the tamper b) 0.06 cm away from tamper

Fig. 15. Vertical Dynamic Stress vs Time

5. CONCLUSIONS

Based on the theory of discrete element, A numerical model of dynamic compaction was founded with PFC^{2D}, and the dynamic response characteristics of sands under impacting has been studied from the meso-mechanical point of view.

Compared the numerical simulation results with the laboratory test results, the feasibility and effectiveness of using PFC^{2D} to research the compacting mechanism of sandy soil has been preliminary verified. The dynamic stresses of the sands surface and the soils at different positions induced by the tamping both have one peak and no clear second stress wave. The asymmetry between the stress increasing and attenuation process occurs, and the increasing time is less than the decay time. The transmission of the dynamic stress of soils under tamping is in accordance with a certain proliferation angle downward.

REFERENCES

Chow, Y.K., Yong, D.M. and Lee, S.L. (1992). "Dynamic compaction analysis". *Journal of Geotechnical engineering*, Vol.118(8): 1141-1157.

Gu, Q. and Lee, F.H. (2002). "Ground response to dynamic compaction of dry sand". *Geotechnique*, Vol. 52(7): 481-493.

He, C.M., Zou, J.F. and Li, L. (2007). "Field tests on measurement of dynamic stress of dynamic compaction". *Chinese Journal of Geotechnical Engineering*, Vol. 29(4): 628－632.

Mayne, P.W. and Jones, J.S. (1983). "Impact stresses during dynamic compaction". *Journal of Geotechnical engineering*, Vol. 109(10): 1342-1346.

Menard, L. and Broise, Y. (1975). "Theoretical and practical aspects of dynamic consolidation". *Geotechnique*, Vol. 25(1): 3-18.

PFC User Manual, version 3.1, (2004), Itasca Consulting Group Inc., USA

Poran, C.J. and Rodriguez, J.A. (1992). "Finite element analysis of impact behavior of sand". *Soils and Foundation,* Vol. 32(4): 68-80.

Powrie, W., Ni, Q. and Harkness, R.M. (2005), "Numerical modeling of plane strain tests on sands using a particulate approach". *Géotechnique*, Vol. 55(4): 297-306.

Zhou, J., Shi, D.D. and Jia, M.C. (2007), "Meso-mechanical simulation of liquefaction behavior of saturated sand under cyclic loading". *Chinese Journal of Hydraulic Engineering*, Vol. 38(6): 697-703.

Local Deformation of Compacted Soil in Triaxial Compression Tests Using PIV Analysis

Y. Nakade[1], Y. Nakata[1], M. Hyoudo[1] and H. Qiao[1]

[1]Yamaguchi University; n042vn@yamaguchi-u.ac.jp

ABSTRACT: Due to many cases of embankment failures reported in recent years, our society requires high-level stability of embankments. For this reason, it is necessary to make a detailed examination on deformation and strength characteristics of compacted soil used for soil structures. Authors have developed a triaxial testing apparatus for the rotated specimen method (RSM), thereby developing a system that enables us to measure volume changes and local deformations of partially saturated soil. In this paper, we examined the effects of variations in degrees of compaction and in compacted soil layers on local deformation and strength characteristics of the compacted soil in a systematic and experimental manner.

INTRODUCTION

A test sample used for this study is the Ube Masado. The test specimen was adjusted to a degree of compaction, or Dc=80%, and then prepared for 3-layer, 5-layer, and 10-layer compacted soil, and for unified 3-layer soil. Their degrees of compaction were made to Dc=80%, 90% and 95%, respectively. In this test, after being isotropically consolidated for 1 hour, these compacted soil layers were sheared at a strain rate of 0.1 mm/min until an axial strain reached 15%. During shearing, these test specimens were shot with a digital camera from 8 directions and for each axial strain of 1%. A testing apparatus used for this test, which has a structure for simultaneous rotation of an axis and the test specimen as show in Fig. 2, is a triaxial testing system that can shoot all-round surface of the test specimen with one digital camera. A gauge point with a diameter of 2 mm as shown in Fig. 1 is placed at an interval of 5 mm on a rubber membrane for the easiness of image analysis. If images obtained from 2 directions for the same gauge point are analyzed, a three-dimensional coordinate for this point can be determined. Considering a rectangle made up of 4 gauge points on the surface of this test specimen as one element, a strain after the deformation of the specimen was measured. A mean value of strains in 30 elements located at the same height was considered as a representative strain in the layer. The test specimen with a height of 10 cm has 20 layers.

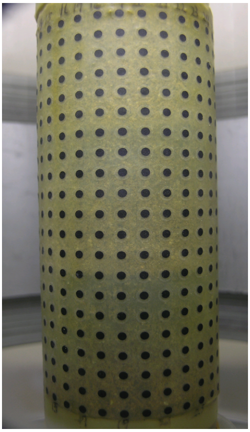

Fig. 1. Original image

Fig. 2. Test equipment

TEST RESULTS

Fig. 3 shows an average relation between a deviator stress and axial or volumetric strains in the whole test specimen for a unified degree of compaction of Dc=80% and for 3-layer, 5-layer, and 10-layer compacted soil. Since all strain levels have an almost equal value of deviator stress, it is seen that the average stress-strain relation is not affected by the number of compacted soil layers. Fig. 4 shows local axial strains at a shear axial strain of 14% for a height (mm) of a specimen. From this figure, it is seen that values of local axial strains are distributed in a sawtooth waveform and the number of peaks responds to the number of compacted soil layers, that an average trend found in this distribution shows large values near the center, slightly smaller values in the lower figure than in the center, and smaller values in the upper than in the lower, and that this trend doest not depend on the number of the layers.

With a focus on difference in degrees of compaction, a test for the specimens with Dc = 80%, 90% and 95% that were prepared with 3 compacted soil layers was conducted. Summarizing the results of the test in the same way as Fig. 4, Fig. 5 shows a distribution of local axial strains in the Dc = 80% specimen. A soil layer with a large axial strain represents 9th and 15th layers and is located directly above the compacted surface. Due to that the compacted surface is a boundary of the compacted soil layer, compaction energy transmits hard directly above the layer boundary, which lowers the density of the compacted soil near the boundary. In the result, an axial strain is considered to become large near the compacted surface. On the other hand, a soil layer with a small axial strain represents 7th and 13th layers and is located directly below the compacted surface. A compacted soil directly below the boundary is conversely affected by compaction energy, resulting in a high density of the soil. This is said to cause a clear variation in local axial strain at the boundary of the compacted soil layer. A difference between maximum and minimum values of this local axial strain reached 12.57% at the completion of shearing.

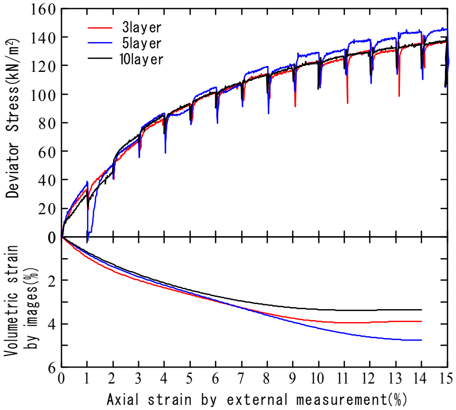

Fig. 3. Dc = 80% 3, 5, 10-layer Axial Strain, Deviator Stress, Volumetric Strain

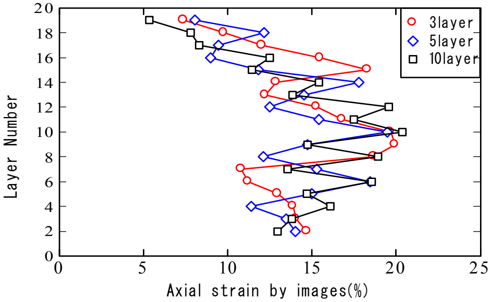

Fig. 4. Dc = 80% 3, 5, 10-layer (ex-axial strain 14%) Distribution of Axial Strain

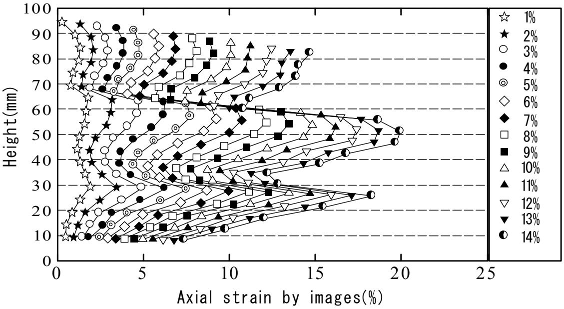

Fig. 5. Dc = 80% 3-layer Distribution of Axial Strain

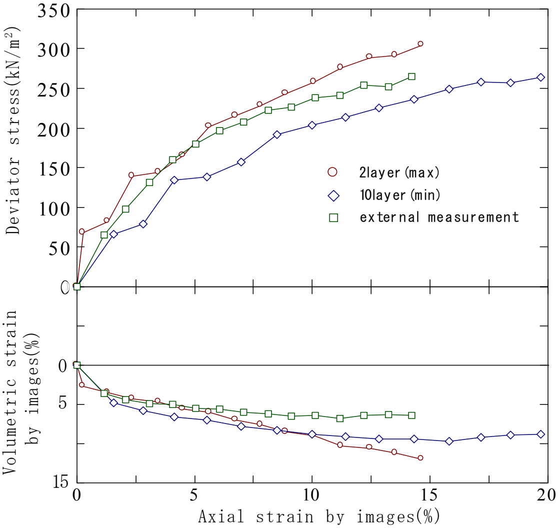

Fig. 6. Dc = 80% Axial strain, Deviator Stress and Volumetric Strain

Fig. 6 shows a relation between a deviator stress and axial or volumetric strains that were calculated based on section areas of different layers determined from the image analysis. A section area at a height of each gauge point was also calculated from 3-dimensional displacement. Fig. 7 shows a distribution of axial strains on each layer with Dc=90%. Also in Fig. 7, as shown in Fig. 5, an axial strain becomes large directly above the compacted surface while becoming small directly below the surface. A difference between maximum and minimum values of an axial strain on each layer reached 25.22% at the completion of shearing.

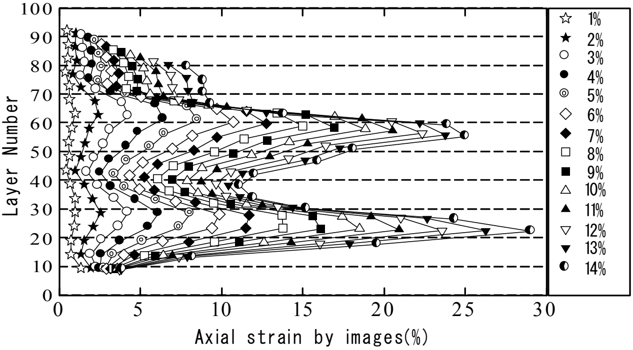

Fig. 7. Dc = 90% 3-layer Distribution of Axial Strain

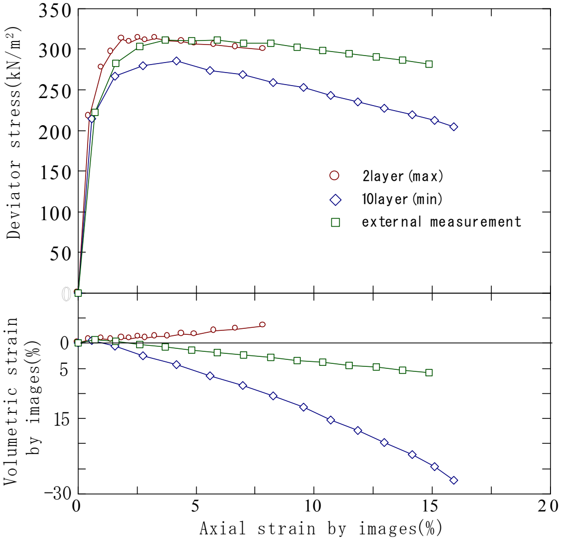

Fig. 8. Dc = 90% Axial Strain, Deviator Stress, Volumetric Strain

Fig. 9 summarizes the results when the average deviator stress reached a peak. These results show a ratio of local deviator stress obtained after the local deviator stress was divided by the average deviator stress, concerning each degree of compaction. Concerning a degree of compaction of 80%, ratios of local deviator stress on the 2th layer, on the 10th layer, represented 114.93% and 99.92%, respectively. Concerning a degree of compaction of 90%, ratios of local deviator stress on the 2th layer and on the 10th layer represented 100.26% and 91.65%, respectively. Concerning a degree of compaction of 95%, ratios of local deviator stress on the 2th layer and on the 14th layer represented 100.73% and 93.00%. It was also concluded that a difference between maximum and minimum values of axial strains became larger with more densely compacted soil. Furthermore, it is seen that layers with a small ratio of local deviator stress exist with a larger degree of compaction. This indicates that a higher degree of compaction increases an average strength of soil while strength uniformity of soil is decreased.

CONCLUSIONS

Using the Ube Masado, we empirically identified the effects of difference in degrees of compaction and in the number of compacted soil layers on local deformation and strength characteristics of the compacted soil. In the result, it was found that the characteristics of local deformation were affected by the number of compacted soil layers. It was also revealed that strength uniformity of soil was reduced with more densely compacted soil

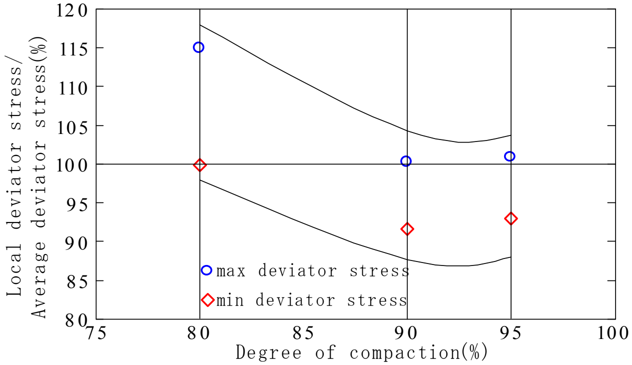

Fig. 9. Ratio of Degree of Compaction and Local Deviator Stress

ACKNOWLEDGMENTS

The authors appreciate the support of the International Engineering Foundation.

REFERENCES

Kikkawa,N., Nakata,Y., Hyodo,M., Murata,H. and Nisio,S.(2006).Three-dimensional measurement of local strain using digital stereo photogrammerty in triaxial test, Proceeding of Geomechanics and Geotechnics of Particlate Media,pp.61-67

Qiao,H., Nakata,Y. and Hyodo,M.(2008).Triaxial compression test for unsaturated sandy soil using image processing technique, Deformational Characteristics of Geomaterials volume2 pp.529-534

The SEM Analysis of Rock-Soil Mini-Structure After Saturation

Zhen Liu[1], S.M. ASCE, Hecheng Liang[2], Jie Zhang[3], M. ASCE, Ph.D., P.E.

[1]Graduate Student, Department of Engineering , China University of Geosciences, Wuhan 430074, China; Department of Civil Engineering, New Mexico State University, P.O. Box 30001, MSC-3CE, Las Cruces, NM 88003-8001; zhenliu@nmsu.edu
[2]Lecturer, School of Environmental Studies, China University of Geosciences, Wuhan 430074, China; hchliang@cug.edu.cn
[3]Assistant Professor, Department of Civil Engineering, New Mexico State University, P.O. Box 30001, MSC-3CE, Las Cruces, NM 88003-8001; jzhang@nmsu.edu

ABSTRACT: In reservoir areas, due to the change of water environment, the properties of rock/soil change. Therefore, it is necessary to study the changed rock/soil properties due to watering and develop necessary forecasting models. In this study, saturation experiments were performed in the laboratory using rock/soil samples from a bank-slope located in the Three Gorges Reservoir and water samples from the Yangtze River. By SEM (Scanning Electron Microscope) analysis, the mini-structures of undisturbed samples were studied. It shows that the mini-structure of rock/soil changes after a 9-day saturation period in flowing water. Before saturation, the soil structure was of good integration and mainly composed of piled and accumulated prothallus. After saturation, the structure changes to be flocculent and there are many scattered prothallus which connect to each other mainly by edges and angularities. Compare to the unsaturated samples, there are more pores in the saturated samples caused by corrosion.

INTRODUCTION

It is well-known that water is one of the active key factors causing slope failure. It has also been recognized since the 1960s that water-rock interaction cannot be treated just by the effective stress principle but should be recognized as a complicated process of stress corrosion (Logan and Blackwell, 1983; Dieterich and Conrad, 1984; Feucht and Logan, 1990; Dunning et al., 1994).

According to the report from the China Ministry of Land and Resources, there are about 1153 large-scale landslides and rockfalls, and 299 deformed rock/soil masses along the Yangtze River from Yichang to Jiangjin in the Three Gorges Reservoir area in China. Because of the impoundment of the Three Gorges Reservoir, many slopes are and will be influenced by the changes of water level and have potential slope failure. Through extensive research, it was found that the impoundment and fluctuation of water level is the main factor of bank-slope failure (Tang et al., 2002; Yuan and Tang, 2003; Yin and Hu, 2004). However, very little research has been done on the mechanism of water-rock interaction.

It is noted that the engineering properties of soil change with a variation of soil structure. Therefore, it is meaningful to do some research about the structure changes of rock/soil under the condition of saturation in the Three Gorges Reservoir. In this paper, saturation experiments were performed in the laboratory using rock/soil samples from Shiliushubao slope in Badong, the Three Gorges Reservoir in China.

CLASSIFICATION OF SOIL STRUCTURE

Depending on the purpose of the research, the classification of soil structure varies. There are two commonly-used classification systems: (1) dividing soil structure into macro-structure and micro-structure; and (2) dividing soil structure into macro-structure, micro-structure, and mini-structure (Yi et al., 2008). The macro-structure, which can be seen by the naked eye, a magnifier or an optical microscope, is related to the soil state and the relative position of soil masses with different characteristics; the micro-structure refers to the crystal structure and mineral composition; and the mini-structure is about the interaction and structure of granules in the soil mass (Wu et al., 1999, 2000; Yi et al., 2008).

For loose soil masses, the skeleton of soil mainly consists of single granules, clots of granule and cement, and so forth. Usually, under the circumstance of normal temperature, atmospheric pressure and ordinary solubility, the crystal lattice of the minerals is not broken or not totally broken when failure of the soil mass occurs. However, the structural strength of the soil mass is depleted. So it can be concluded that the failure of the soil mass is caused by the loss of bond between the granules or the clots but not by the breakage of the granules when the soil mass fails (Yang, 2000). Therefore, water-rock/soil interaction mainly causes a change in the soil mini-structure. At this point, it is beneficial to investigate the changes of mini-structure for the study of the mechanism of soil property changes.

SUMMARY OF EXPERIMENT

The objective of the laboratory saturation experiment is to investigate the changes of mini-structure in loose rock/soil masses. In this experiment, undisturbed soil samples from Shiliushubao slope and water samples from the Yangtze River are used. Fig. 1 is the experiment flowchart, which consists of:

- Free expansion rate test: to estimate the expansion characteristic of samples.
- Permeability test: to give an indication of the water rock/soil interaction.
- Scanning electron microscope (SEM) test: to investigate changes of mini-structure in the samples.

In the process of saturation, undisturbed samples were kept in a permeameter and water from the Yangtze River was introduced by a peristaltic pump at a steady rate of 48 r/m in order to maintain a water-flowing environment. The saturation process did not end until the hydraulic conductivity became constant. After saturation, SEM analysis was conducted on the samples using the scanning electron microscope Quanta 200. The experimental facility is shown in Fig. 2.

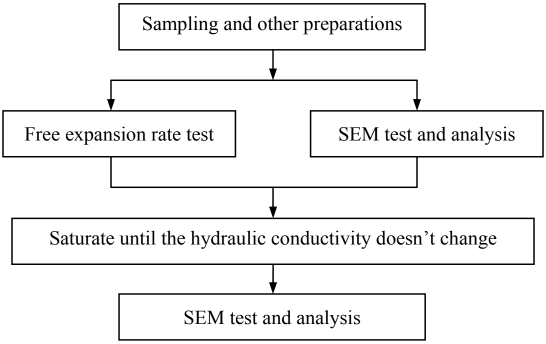

FIG. 1. Experiment flowchart.

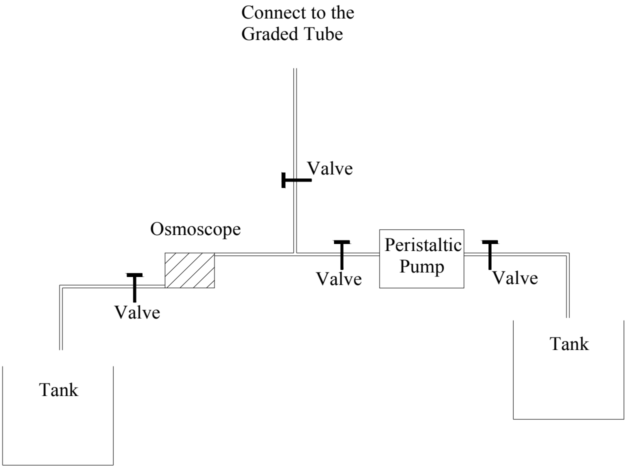

FIG. 2. Illustration of the experimental facility.

EXPERIMENT RESULTS AND ANALYSIS

In this experiment, the samples were tested under the magnifications of 120, 600, 800, 1000, 1200, 1500, 3000, and 5000 using the scanning electron microscope Quanta 200. In order to analyze the changes of soil mini-structure effectively, choosing an appropriate magnification is very important.

Fig. 3 shows SEM pictures of undisturbed soil samples before saturation under different magnifications. Under magnifications of 120, 600 and 800, it is hard to see the bonds of granules in the samples. Under very large magnifications, such as 3000 and 5000, what can be seen are just some crystals. The best magnifications for the analysis are 1200 and 1500, under which the whole structure of the sample and the bonds of granules can be seen well. It means that the pictures under magnifications of 1200 and 1500 represent the mini-structure of samples very well.

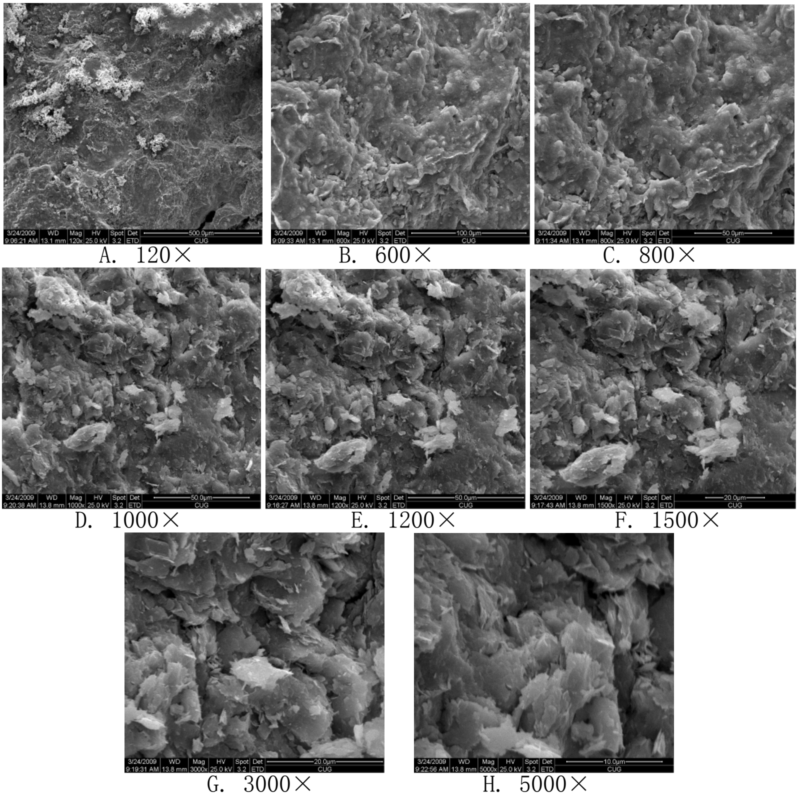

A. 120× B. 600× C. 800×

D. 1000× E. 1200× F. 1500×

G. 3000× H. 5000×

Fig. 3. SEM pictures of unsaturated samples under different magnifications.

Fig. 4 shows that the mini-structure of the sample changed after a 9-day saturation period. From the figure, it can be seen that:

- Before saturation, the mini-structure of the sample was of good integration and mainly composed of piled and accumulated prothallus; the layers in the structure were of good integrity and well bonded by plane. There was no coccode.

- After the 9-day saturation, the mini-structure changes to be flocculent and there are many scattered prothallus which connect each other mainly by edges or angularities; the contact area is very small and it may cause the decrease of connection strength.
- Comparing with unsaturated samples, there are more pores in the saturated rock/soil samples caused by corrosion.

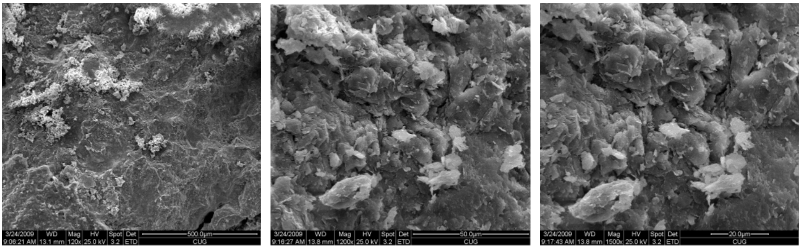

A.unsaturated（120×） B. unsaturated（1200×） C. unsaturated（1500×）

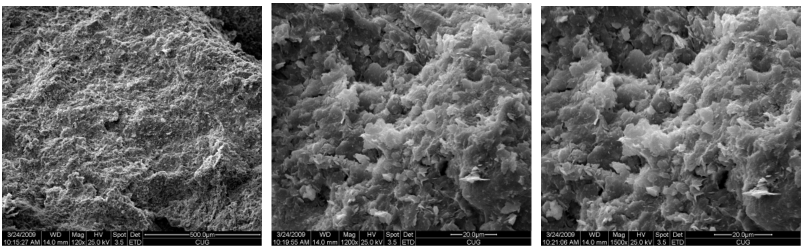

D. saturated（120×） E. saturated（1200× ） F. saturated（1500× ）

FIG.4. Changes of mini-structure after saturation.

The free expansion test was also performed. It shows that the soil samples are not expansive soils, which means that the changes of mini-structure are mainly caused by the water-rock/soil interaction not by the expansion of the samples.

CONCLUSION

It is noted that in reservoir areas a lot of geo-hazards are caused by the change of water environment. Even though much research has been done on the water-rock/soil interaction, most of the achievements are in the area of mechanical property changes of rock/soil, very few are about the mechanism of rock/soil property changes. Therefore, it is very important to study how and why the properties of rock/soil change under the new water environment in order to develope necessary forecasting models for potential geo-hazards.

This paper compares the mini-structures of unsaturated and saturated samples based on SEM analysis. It shows that the mini-structure of soil mass changed under the water-flowing environment and the changes are mainly caused by the water-rock/soil interaction. However, the mini-structure and the mechanical property changes in the saturation process are also very important for studying the water-rock/soil interaction mechanism. Therefore, more comprehensive research should be done in the future.

ACKNOWLEDGMENTS

The authors appreciate the support of the Chinese NSF (40702059) and the NSF of Hubei Province (2007ABA148).

REFERENCES

Dieterich, J.H. and Conrad, G. (1984). "Effects of humidity on time and velocity dependent friction in rocks". *J. Geophys. Res.*， Vol. 89: 4196-4202.

Dunning, J., Douglas B., Miller M., et al. (1994). "The role of the chemical environment in frictional deformation: stress corrosion cracking and comminution." *Pure Appl. Geophys.*, Vol. 143(1/3): 151-178.

Feucht, L.J. and Logan, J.M. (1990). "Effects of chemically active solutions on shearing behavior of a sandstone". *Tectonophysics*, Vol. 175: 159-176.

H. Liang, P. Li, A. Zhou & D. Yuan(2007). "Chemical characteristics of saturated loose rocks in Badong, Three Gorges reservoir", *Proceedings of the 12th International Symposium on Water-Rock Interaction WRI – 12*, 1399 -1402.

Logan, J.M. and Blackwell, M.I. (1983). "The influence of chemically active fluids on the frictional behavior of sandstone". EOS， *Trans. AM. Geophys. Union*, 64: 835.

Tang, H.M., Ma, S.Z., Liu, Y.R. et al. (2002). "Stability and control measures of Zhaoshuling landslide, Badong County, Three Gorges Reservoir." *Earth Sciences – Journal of China Univ. of Geosciences*, Vol. 27(5): 621-625.

Wu, H., Zhang, X.G., Han, L.H. (1999). "The change of ground water chemical field affect properties of soil mass." *Journal of Guangxi Univ.*, Vol. 24(2): 85-88.

Wu, H., Zhang X.G., Yi, N.P. et al. (2000). "Research on water-soil interaction and meso-structure of soil mass." *Chinese Journal of rock mechanics and engineering*, Vol. 19(2): 199-204.

Yang, Q.S. (2000). "The mini-structure mechanics and design of complex material." China Railway Publishing House, Beijing, China.

Yi, N.P., Zhang, X.G., Li, M.Y. et al. (2008). "SEM test for soil mini-structure in groundwater variation." *Journal of Guilin Univ. of Technology*, Vol. 28(1): 43-47.

Yin, Y.P. and Hu, R.L. (2004). "Engineering geological characteristics of purplish-red mudstone of middle Tertiary formation at the Three Gorges Reservoir." *Journal of engineering geology*, Vol. 12(2): 124-135.

Yuan, Z.Y. and Tang, X.C. (2003). "The influence of sluice and water level fluctuation on landslides and rockfalls of the Three Gorges Project and principles of prevention." *Tropical Geography*, Vol. 23(1): 30-34.

Author Index

Page number refers to the first page of paper

Subject Index

Page number refers to the first page of paper